Faculty of Science and Engineering
Department of Physics and Astronomy

Wind Prediction Modelling and Validation Using Coherent Doppler LIDAR Data

Muhammad Omer Mughal

This Thesis is presented for the degree of
Doctor of Philosophy
of
Curtin University

July 2016

DECLARATION

To the best of my knowledge and belief this thesis contains no material previously published by any other person except where due acknowledgement has been made.

This thesis contains no material which has been accepted for the award of any other degree or diploma in any university.

Muhammad Omer Mughal

Signature……

Date 30/11/2016

Table of Contents

Acronyms

A2C	Atmospheric-to-CFD
ABL	Atmospheric Boundary Layer
ACM2	Asymmetrical Convective Model version 2 PBL scheme
ADM	Atmospheric Dynamics Mission
AFWA	Air Force Weather Agency
AGL	Above Ground Level
ARW	Advanced-Research WRF
ASL	Above Sea Level
ALVPT	Advanced LIDAR data volume processing technique
CAPS	Center for Analysis and Prediction of Storms
CC	Correlation Coefficient
CDL	Coherent Doppler LIDAR
CFD	Computational Fluid Dynamics
CFL	Courant–Friedrichs–Lewy
CFSR	Climate Forecast System Reanalysis
CRC CARE	Cooperative Research Centre for Contamination Assessment and Remediation of the Environment
DER	Department of Environment Regulation
DEM	Digital Elevation Model
DNS	Direct Numerical Simulation
ECMWF	European Centre for Medium-Range Weather Forecasts
ERA	ECMWF Interim Reanalysis
ESA	European Space Agency
FAA	Federal Aviation Administration
FDDA	Four-Dimensional Data Assimilation
FFT	Fast Fourier Transform
FNL	Final Operational Global Analysis
GAMG	Generalised Geometric-Algebraic Multi-Grid
GFS	Global Forecast System
GNU	GNU's Not Unix
GPU	Graphical Processing Unit
GRIB	General Regularly Distributed Information in Binary form
GRADS	Grid Analysis and Display System

GUI	Graphical User Interface
GWh	Giga Watt Hour
hPa	Hecta Pascal
Hz	hertz
IDV	Integrated Data Viewer
IEC	International Electrotechnical Commission
IGBP	International Geosphere-Biosphere Programme
IWES	Institute for Wind energy and Energy Systems
LASI	Langrangian-Averaged Scale-Independent Dynamic Smagorinsky
LBC	Lateral Boundary Condition
LES	Large Eddy Simulation
LIDAR	Light Detection and Ranging
LSM	Land-Surface Model
LST	Land Surface Temperature
LTWPC	Lake Turkana Wind Power Project Consortium
LW	Long Wave
MAE	Mean Absolute Error
MEASNET	International Measuring Network of Wind Energy Institutes
MERRA	Modern-Era Retrospective Analysis for Research and Applications
MHz	Megahertz
MM5	Fifth-Generation Penn State/NCAR Mesoscale Model
MODIS	Moderate Resolution Imaging Spectroradiometer
MRF	Medium Range Forecast Model PBL scheme
MVAD	Modified Velocity Azimuth Display
MW	Megawatt
NASA	National Aeronautics and Space Administration
NCAR	National Center for Atmospheric Research
NCEP	National Centers for Environmental Prediction Remediation of the Environment
NCL	NCAR Command Language
NOAA	National Oceanic and Atmospheric Administration
NOAH	**N**CEP-**O**regon State University-**A**ir Force-**H**ydrology Lab
NMC	National Meteorology Center
nm	Nanometre

NMM	Non-Hydrostatic Mesoscale Model
NNRP	NCEP/NCAR Reanalysis
NREL	National Renewable Energy Laboratory
NS	Navier-Stokes
NWP	Numerical Weather Prediction
OBSGRID	Objective Analysis
PBL	Planetary Boundary Layer
PBICG	Preconditioned (Bi-) Conjugate Gradient
PCG	Preconditioned Conjugate Gradient
PDF	Probability Distribution Function
PISO	Pressure Implicit with Splitting of Operators
PIMPLE	Pressure Implicit Method for Pressure-Linked Equations
PPI	Plan Position Indicator
PRF	Pulse Repetition Frequency
PX	Surface Layer PleimeXiu Scheme
RANS	Reynold's Average Navier Stokes
RHI	Range Height Indicator
RMSE	Root Mean Square Error
RNG	Re-Normalisation Group
RRTM	Rapid Radiative Transfer Model
RSSRG	Remote Sensing and Satellite Research Group
RVFT	Radial Velocity Feature Tracking
SGS	Sub-Grid Scale
SIMPLE	Semi-Implicit Method for Pressure-Linked Equations
SL	Surface Layer
SNR	Signal -to-Noise Ratio
SODAR	Sonic Detection and Ranging
SOWFA	Simulator for On/Offshore Wind Farm Applications
SRTM	Shuttle Radar Topography Mission
SW	Short Wave
TSO	Transmission System Operator
UKMO	United Kingdom Meteorological office
USGS	United State Geological Survey
UTC	Coordinated Universal Time

UTM	Universal Transverse Mercator
UPC	Unidata Program Center
VAD	Velocity Azimuth Display
VVP	Volume Velocity Processing
WA	Western Australia
WASP	Wind Atlas Analysis and Application Program
WMO	World Meteorological Organization
WPS	WRF Pre-processing System
WRF	Weather Research and Forecast Model
WSDSA	Wind Speed and Direction Sensitivity Analysis
WWEA	World Wind Energy Association
YSU	Yonsei University PBL scheme
2D	Two Dimensional
3D	Three Dimensional
3DVAR	Three Dimensional Variational Data Assimilation
4DVAR	Four Dimensional Variational Data Assimilation

List of Figures

List of Tables

Abstract

The stochastic nature of wind makes it challenging to predict and to utilize as a management tool. Modelling thus has to be predicted utilising an appropriately short temporal scale for grid integration. Due to the lack of actual descriptive variables representative of the terrain, the conventional wind modelling approaches sometimes generates unrealistic outcomes. The key objective of this research is therefore, improving the modelling of the boundary layer wind field in a complex terrain and validating against *in situ* and Coherent Doppler LIDAR (CDL) observations. Since atmospheric models present a broad spectrum of configuration options and parameters, a sensitivity study is required for selecting the best configuration. Therefore, a physical technique is introduced in current research that optimises a mesoscale model via wind speed and direction sensitivity analyses (WSDSA) and validates it with *in situ* and CDL observations. The optimised wind speed and direction serve as boundary conditions to a micro scale model for understanding the details of local flow in the atmospheric boundary layer that is critical to both siting wind power infrastructure and making short term predictions of wind variability, hence supporting accurate short term forecasting.

A physically-based wind model is applied to determine wind speed and direction and to conduct a model sensitivity analysis. The focus is the East African site of the Lake Turkana Wind Farm, characterized by complex terrain and high diurnal variability that creates a nocturnal jet of typically 15 m/s. Observations from three tall meteorological masts are compared with Weather Research and Forecast (WRF) model outputs. WRF is configured with four domains nested down to 900 m spatial resolution. The model is tested with initialization fields from two different sources, optimised using different grid configurations and parameterization schemes. Comparing model and data from 3 tall masts A, B and C yields RMSE of 1.6, 1.7 and 1.9 m/s for wind speed and correlation coefficients (CC) 0.69, 0.57 and 0.48 respectively. The wind direction RMSE for mast A and B are 12° and 13° and CCs are 0.44 and 0.24 respectively. Prior to undertaking research at the wind farm, WRF's performance was evaluated over a 16-day period in a well-defined meteorological environment in Western Australia (WA) yielding a wind speed RMSE of 1.27 m/s and CC 0.70 while the wind direction RMSE was 32° and CC was 0.78. These results show that WRF model is able to

predict wind speed acceptably well when provided with sufficient observational data and in for a less complex terrain. Additionally, a 40 % reduction in error between observed and modelled wind speed is achieved, using European Centre for Medium-Range Weather Forecasts (ECMWF) Interim reanalysis (ERA-Interim) data instead of National Center for Environmental Prediction (NCEP) data. This change would correspond to an estimated potential annual power generation difference of 285GWh for a 1625GWh per annum wind farm at Lake Turkana. Further research at the Lake Turkana wind farm includes CDL data refinement with improved NCL code provided 25% improvement in wind prediction and a 22% improvement in the correlation coefficient (against *in situ* mast observations).

The microclimatic modelling reduced RMSE to 1.07 m/s at the location of mast A, 1.25 m/s at the location of mast B and mast C, even with its associated problems, showed and improvement of 1.77 m/s.

The research thus has established methodology of determining the optimised configuration of the WRF software through a sensitivity analysis. The integration of microclimatic model with WRF and validation with CDL has improved the short term wind prediction in a complex terrain and provided a pathway for clean and economic power generation.

Acknowledgements

This whole endeavour would not have been possible without blessing of Almighty Allah who guided me through thick and thin and to whom I owe all my success.

I would like to express deepest gratitude and appreciation to my supervisor, Professor Mervyn Lynch for his invaluable guidance and encouragement throughout this study. His exquisite knowledge and experience helped me in understanding various critical issues involved in the research. His approach towards understanding the environment numerical modelling proved to be the major breakthrough in this research. I also feel obliged to Dr Brendan McGann who helped me with various academic issues and through various theoretical and mathematical modelling issues. I feel indebted to Mr John Sutton who helped in paving a smooth way for my research and providing me with opportunity to work with the members of the Department of Environment Regulation (DER) especially Dr Peter Rye. Dr Peter Rye's vast experience in computational fluid dynamic (CFD) modelling codes both compressible and incompressible and their applications in the field helped to solve major problems of the research. In addition, his original code for extracting output data files from the WRF also helped to solve various research issues.

Most important of all I would like to express my appreciation to Dr Frank Yu whose continuous help in numerical modelling, experience with CDL and experience in the field not only helped me to understand the crux of this research but also helped in generating various valuable outputs which otherwise would have not been impossible in his absence.

The effort on meso and micro scale coupling was supported by Matthew J. Churchfield, Senior Engineer, National Wind Technology Centre; NREL. Matthew support remained throughout 2015 and helped to solve the most intricate part of the thesis. Matthew has a strong background in CFD and its application to the wind farm modelling and analysis.

I would like to give recognition to Cooperative Research Centre for Contamination Assessment and Remediation of Environment (CRC CARE) Australia and Curtin University Western Australia for providing me with this invaluable research

opportunity and allowing me to work on state-of-the-art LIDAR and with such dynamic team of researchers.

The Pawsey Supercomputing Centre (Perth) is acknowledged for the provision of computer time.

Finally, I would like to thank my parents whose extreme efforts allowed me to come to this stage and achieve this opportunity. They have been extremely patient when I relocated from my home country to Perth, Australia. They had to bear the impact of departure and supported me continuously even though I and they themselves were faced with various financial problems. I would like to thank my brother for taking care of my parents in my absence and also to my lovely and the only sister whose extreme love and supplications through day and night has made the hardships of this endeavour much easier to bear.

List of Publications

1. M. O. Mughal, M. Lynch, F.Yu, B. McGann, F. Jeanneret & J.Sutton, Wind Modelling, Validation and Sensitivity Study Using Weather Research and Forecasting model in Complex Terrain (submitted December 2015 to the Journal of Environmental Modelling and Software).
2. M. O. Mughal, M.Lynch, F.Yu, B. McGann, F. Jeanneret & J.Sutton, "Numerical Modelling for Optimization of Wind Farm Turbine Performance", in Proceedings 12th DEWEK International Conference, DEWEK 2015, Bremen, Germany May 19-20, 2015
3. M. O. Mughal, M.Lynch, F.Yu, B. McGann, F. Jeanneret & J.Sutton, State of the art micrositing and forecasting of winds in a complex terrain in East Africa: validating coupled Meso and Microscale models (abstract submitted February 2016 to the Journal of Wind Engineering and Industrial Aerodynamics)

Chapter 1 Introduction

Wind power generation is a challenging and an active and evolving research field in the current era. The most intricate fact is the stochastic nature of wind which makes it difficult to predict and hence the associated power generation facilities a complex to manage compared with geothermal and hydroelectric power plants. The energy generated by wind, without supporting infrastructure cannot be reserved economically (as yet) and therefore it needs to be accurately predicted on the shortest possible time scales for balancing supply and demand. Integrating wind energy into a national grid demands appropriate forecasting tools to predict the wind power ramps and to obtain the attractive market price incentives associated with correctly predicting the energy imbalance.

The range of wind power forecasting requirements can be specified depending upon the applications. Very short term (few seconds to 30 minutes ahead) are usually employed in electric power markets associated with clearing and regulation actions while short term forecasts (30 minutes to 6 hours ahead) are used for economic load dispatch planning and load increment/decrement decisions (Soman et al., 2010). Generally, short term forecasting may be associated with a prediction horizon of about 8 hour ahead (Wang et al., 2011). Hence, in order to attain an economic edge both in the national and international markets, it is incumbent on the transmission system operators (TSO) to focus on the methods and techniques required to improve short term forecasting.

There exist various approaches for predicting wind speed for various time scales comprising of physical, statistical and hybrid methods. The physical methods utilize meteorological data to predict the wind speed which then is converted to output power forecasts. The statistical techniques employ historical data in conjunction with neural networks and fuzzy logic without considering meteorological conditions. The hybrid techniques involve the combination of statistical and physical approaches with an emphasis on weather forecasts and time series analysis. Statistical methods are preferred in the case of short term forecasting due to them being less time demanding, their flexibility and ease of operation. But since such approaches are based on historical data and they lack real time physical information, such as atmospheric temperature and humidity profiles, especially the separation effects. Consequently,

results obtained are usually approximations to the real wind field. Hence, such results are sometimes unrealistic and TSOs endure significant economic losses through losing market share. It is therefore necessary to apply research effort to develop techniques that are more representative of the terrain's variability (cover, surface roughness, soil temperature, soil moisture), that properly account for the forcing field and, at the same time, are cost effective.

Scientific approaches for advancing wind prediction include (a) enhancing the density of local meteorological measurements [surface, remotely sensed information and upper air observations] and (b) the assimilation of these observations into a numerical prediction model. In the current research the approach adopted is the coupling of the output of a mesoscale model with a microscale model and constraining the model output by ingesting three dimensional observations from a CDL.

WRF is a mesoscale model that is widely used in the international meteorological community, especially in short term forecasting due to its flexibility and robustness to act as a regional scale model. In fact, it has the capability not only to run global simulations at spatial resolutions of several kilometres but it can also be nested down to a resolution as low as a few hundred meters. The efficiency of WRF could be improved further in short term forecasting by avoiding its "cold start" and optimizing it through the WSDSA. Further refinement can be achieved by augmenting WRF with a micro scale model and then using observation data from a CDL or, if WRF itself is sufficiently accurate to match *in situ* observations, the likelihood of using a microscale model is reduced.

Conventionally, *in situ* instruments like cup and vane or 3-axis acoustic anemometers on tall masts are used for wind and turbulence measurements but since these masts give measurements at a point and are unable to provide area measurements, have inherent inflexibility and cost issues therefore the industry is looking towards alternative state of the art techniques and instruments. The methods for measuring the wind spatial variability both horizontally and vertically require improvement (Hannon et al., 2008). One such instrument is CDL, which because of its three dimensional (3D) scanning capability, is gaining popularity. The 3D scanning strategy embedded in CDL has the potential to improve both wind farm site planning, (e.g. site selection, design) and optimization of the subsequent operational performance. Such a strategy

can serve to form the platform for real-time adaptive control of wind turbines and hence can profile the incoming wind field, measure the velocity deficit downstream, of a turbine as well as observe the accumulated wakes leaving an array of wind turbines (Laks et al., 2009; Retallack et al., 2010). CDL instruments may have a range of 10-20 km and can sample 2π sr (the upper hemisphere). These instruments may be utilized for determining complete wind field structure comprising mean wind and turbulence profiles, time series and atmospheric boundary layer characteristics.

Since numerical weather prediction (NWP) models at the synoptic scale generally have a coarse spatial resolution and sparse supporting meteorological observational data, they are unsuitable for short term forecasting. The WRF model initialized via NWPs may be able to generate short term forecasts for wind farms in a hybrid scenario but might not be sufficiently precise and may requires the input from a local observation source sufficiently capable to capture the complete wind scenario both vertically and horizontally.

Several methods have been used to couple mesoscale- and microscale models, typically using the results of a mesoscale model as the boundary conditions for a microscale model. The issue to be addressed is how a mesoscale model can provide instantaneous boundary values to a microscale model as turbulence in mesoscale models are just represented as average fields. Another coupling technique is to use a single model for both the mesoscale and microscale modelling in which the variations of the mesoscale model are reflected at the microscale and the results are returned to the mesoscale by a two-way nesting method (Nicholls et al., 1993; Yamada, 2004). There is also a hybrid approach where a mesoscale model provides boundary conditions to a modified microscale model that includes the capabilities of a mesoscale model. The problem is that this approach is immature because an appropriate method for linking these models has not been established. This approach also requires significant computational resources. The validation of these models is also difficult because the supporting validation measurements typically available are limited (Yamada and Koike, 2011).

The availability and integration of CDL data into mesoscale models for studying the wind field in a microscale model using CFD code exists. Several methods have been applied to couple mesoscale and microscale models, one of which is to use the results

of the mesoscale model as the boundary conditions for the microscale model. Liu et al. (2011) coupled WRF with Large eddy simulations (LES) to simulate a two-day case study at a wind farm in northern Colorado. The issue to be addressed was how a mesoscale model can provide instantaneous boundary values of turbulence to LES since in mesoscale models these are just average fields.

Another coupling technique is to use a single model for both mesoscale and microscale models in which the variations of the mesoscale model are reflected into the microscale model and the results are returned to the mesoscale model variables by two-way nesting method (Nicholls et al., 1993; Yamada, 2004). There is also a hybrid approach where a mesoscale model provides boundary conditions to a modified microscale model that includes the capabilities of a mesoscale model. Yamadaa and Koikeb (2010) coupled atmospheric-to-CFD (A2C) scheme with WRF where WRF provided the boundary conditions to the A2C code. The problem is that these models are still immature and appropriate methods for linking these models have not been established. These schemes also require significant computational resources. The validation of these modelling approaches is also difficult as the measurement data available is limited (Yamada and Koike, 2011).

The wind farm numerical modelling and prediction techniques that are in vogue are somewhat immature in their ability to provide a complete description of the wind field. Most of the existing techniques (Strack, 2004) are using vertical wind profilers that measure velocity along one direction and therefore have limited applications and are in that sense similar to metrological masts. Parkes and Tindal (2004) lack the use of CFD and LIDAR while Strack (2004) lacks access to LIDAR data. Quail (2012) compared CFD and LIDAR but his research didn't extend to forecasting. Tapia (2009) compared the performance of two CFD software packages for wind modelling but does not specifically address wind forecasting. The current research on the other hand has a broader prospective and is not limited to wind profiling but spatially samples the wind field, captures the wind's evolution, as well as atmospheric turbulence and its transport.

1.1 Status of Wind Energy Modelling and Management

The pressing need to implement emission free energy resources and the economic advantage of wind power caused the worldwide wind capacity to reach 336,327 MW by the end of June 2014, out of which 17,613 MW were added in the first six months of 2014 (WWEA, 2014). It is expected to reach 100,000 MW by the end of 2020 (Stefan and Jean-Daniel, 2013).

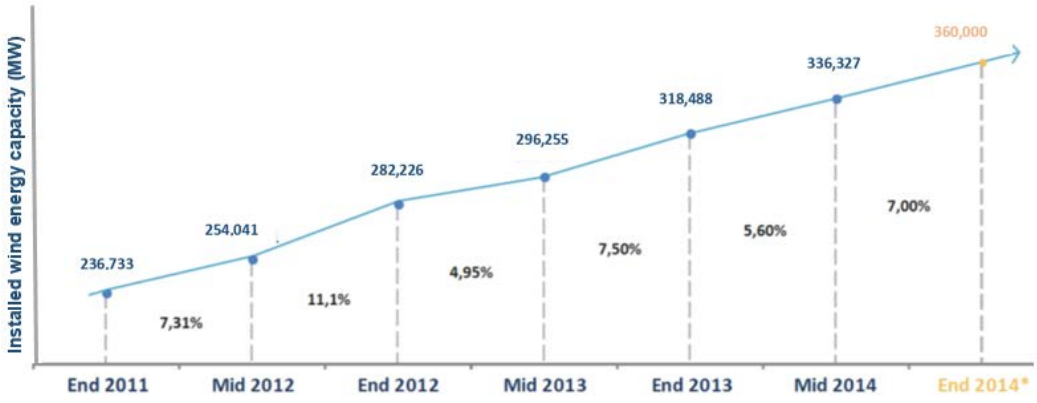

Figure 1.1 Total installed capacity 2001-2014 [MW] (WWEA, 2014)

This rapid growth has encouraged researchers to investigate more sophisticated methods for improving the power output from wind farms. The preliminary information about the wind energy entering a wind farm helps TSO make important decisions on electricity market clearing, real-time grid operations and regulation actions. According to Chang (2014) this falls into the category of ultra-short-term forecasting (i.e. from few minutes to 1 hour ahead), while for economic load dispatch planning and load increment/decrement decisions, short term forecasts are used. In the past decades, research efforts have been made to develop sound short-term forecasting methods. In this regard, Giebel (2003) and Costa et al. (2008) provide a summary of the developments pertaining to short-term wind power forecasting methods and techniques, including physical models, conventional statistical models, hybrid physical-statistical models, artificial intelligence based models, and others. This research uses a hybrid technique where a mesoscale model is coupled to microscale model and improvements in the forecast are achieved via improved initialization fields provided to the model through CDL.

NWPs serve as a base for most forecasting systems and therefore the effort to increase their accuracy provides a major challenge in short term forecasting. There are two major requirements for improved numerical weather prediction: better observational data and better methods for data assimilation. These improvements are very computationally intensive, and thus advances in computational power, coupled with the trend toward local modelling efforts, has allowed for concentrated study of both historical and local real-time mesoscale structures and dynamics, resulting in extensive evaluation, optimization, and improvement in these three key areas of NWP that continue today (Kalnay et al., 1998).

Kalnay et al. (1998) trace the history and improvements of operational NWP at NCEP. The review is inclusive of improvements at all major NWP operational centers. NWP has evolved from the 381 km resolution of the National Meteorology Center (NMC) 1 level barotropic model of the 1950's, running on a then state-of-the-art IBM 704 supercomputer, to United Kingdom Meteorological office (UKMO) operational mesoscale model, with 1.5 km resolution and 70 vertical levels, running on today's state-of-the art massively parallel computer system (Mylne, 2013). But since most of the topographic features and atmosphere's behaviour within complex terrain occurs on a smaller spatial scale than the commonly used synoptic-scale forecasting models can simulate, so near-surface model accuracy is compromised. A mesoscale model is quite similar to a global model but is generally limited to an area of some hundred square kilometres. Therefore, precision can be increased, without demanding too much additional computing time. The initial and boundary conditions necessary for input to the mesoscale model are given by a global NWP model. Higher resolution mesoscale models, such as the WRF model, are better suited for resolving the near-surface atmospheric behaviour in complex terrain. WRF was developed jointly by National Center for Atmospheric Research (NCAR), National Centers for Environmental Predictions (NECP) and several other agencies and laboratories. It is freely available online and is used world-wide by scientists as well as companies and individuals. WRF evolved from Fifth-Generation Penn State/NCAR Mesoscale Model (MM5) and serves as a replacement for MM5. WRF is now available in two separate forms: WRF-NMM (Non-hydrostatic Mesoscale Model) and WRF-ARW (Advanced-Research WRF). WRF-NMM is mainly used for operational weather forecasting while

WRF-ARW (more complex so slower to run) is aimed at stimulating atmospheric research.

Remote Sensing instrumentation for wind energy purposes has developed rapidly in the past few years, with ongoing changes being made to hardware and the associated software elements. The (2009) performance (against cup anemometers) of the two types of LIDAR then available commercially (ZephIR and Windcube) was reported for flat terrain (Courtney, 2009) and for complex terrain (Foussekis et al., 2009).

Computational fluid dynamics (CFD) modelling is now being employed as a means of correcting the observed bias in complex terrain (Harris et al., 2010). In Boquet et al. (2010) CFD and LIDAR have also been applied together, in order to better understand LIDAR wind profile measurements in complex and rough terrain.

1.2 The Research Opportunity

In order to balance supply and demand on a national grid and to satisfy customers needing the energy at a particular time, variability in wind power output has to be within a suitable range. The RMSE for most modelling exercises is usually 10% of installed capacity. Wind farm operators have quoted individual wind farm modelling accuracy to be in the range of 10-20% of installed capacity (Foley et al., 2012). The management issue associated with wind energy is that it cannot be directly integrated into the electric grid due to its intermittency so an approach that forecasts future values of wind power production will be very advantageous. Fossil fuel saving of 10 to 25 % could be achieved by combining NWP models with physical flow models and statistical models as a forecasting strategy. Higher wind forecast errors may lead to increased payment to wind farms for their reactive power service due to increased lost opportunity cost (Soman et al., 2010).

Power forecasts of a wind farm require accurate modelling of wind speed. Time series plots of wind speed can be used to judge the accuracy of forecast from models. It has been shown by Castro et al. (2010) that using WRF alone has a horizontal wind speed prediction error of 26% but coupling it with a CFD code reduces this figure to 3%. The associated RMSE was reduced from 2.93 m/s to 1.8 m/s for November 2007.

Mesoscale atmospheric models give an almost complete description of the atmospheric properties but they have low resolution and therefore can't capture turbulence generation and its propagation. Microscale models (e.g. CFD), on the other hand, have high spatial resolution and thus can capture turbulence due to small topographic features. Further the turbulence intensity calculated depends on the model used. Castro et al. (2010) plotted the daily turbulence intensity for November 2007 and found that turbulence intensities are well predicted by the coupling approach as compared to using a mesoscale model independently.

The importance of CDL in short term forecasting was studied by Frehlich (2013) who concluded that CDL provides the high resolution weather observations necessary for improving forecasts made by NWPs. The WindTracer® CDL, considered in this study, proved to be the most advantageous in short term forecasting, as it is equipped with high resolution and range due to its low divergence laser beam. This feature allows it to best match the high resolution of NWP models over a large domain compare to *in situ* instruments. The wind speed measured several kilometres upstream by CDL is useful for making real time operation improvements by wind farm operators. In order to optimize the utilization of wind for power generation and to create a reliable, clean energy source, more accurate wind measurements and forecasts are needed. The primary contribution of this present study to the broad wind energy sector will be the provision of accurate wind measurements and accurate wind forecasts. This will ensure sustainability of both the wind farm and its power delivery to Kenyan people and its industry.

1.3 The Numerical Modelling Strategy for Wind Forecasting

This research intends to follow a physically based modelling approach for achieving accurate power forecasts for Lake Turkana wind farm. The overall research methodology is elucidated in Figure 1.2 and the major steps of the work flow are stated below:

a. Coupling WRF or a simplified WRF model with CFD for prediction of microscale wind for estimation of wind turbine energy output.
b. Integrate LIDAR radial velocity measurements into WRF-CFD for improving fidelity in resolving localized winds.

c. Evaluate model performance with meteorological mast measurements and the LIDAR observations themselves.

Figure 1.2 shows that the WRF pre-processing system (explained later in chapter 4) is initialized using boundary conditions from NCEP or ERA-Interim data. This data is passed on to the WRF ARW core for processing. The processed data then flows through two paths to obtain improved wind speed and direction. In the first path WRF modelled wind speed and direction at a point in the simulation domain is compared with *in situ* and LIDAR data. The deviations are noted between the modelled and observed wind speed. The modelled wind speed from WRF is flowed through the second path for further improvement where it serves as the boundary condition for the CFD module. The CFD module comprises of TOOF_Points, WRFTOOF and ABLTerrainSolver (explained later in chapter 6). The TOOF_Points converts WRF geographical coordinates to OpenFOAM readable Cartesian coordinates. The WRFTOOF program generates boundary conditions for OpenFOAM from WRF. The ABLTerrainSolver generates the output in terms of improved wind speed. The modelled wind speed is then compared with that observed by LIDAR.

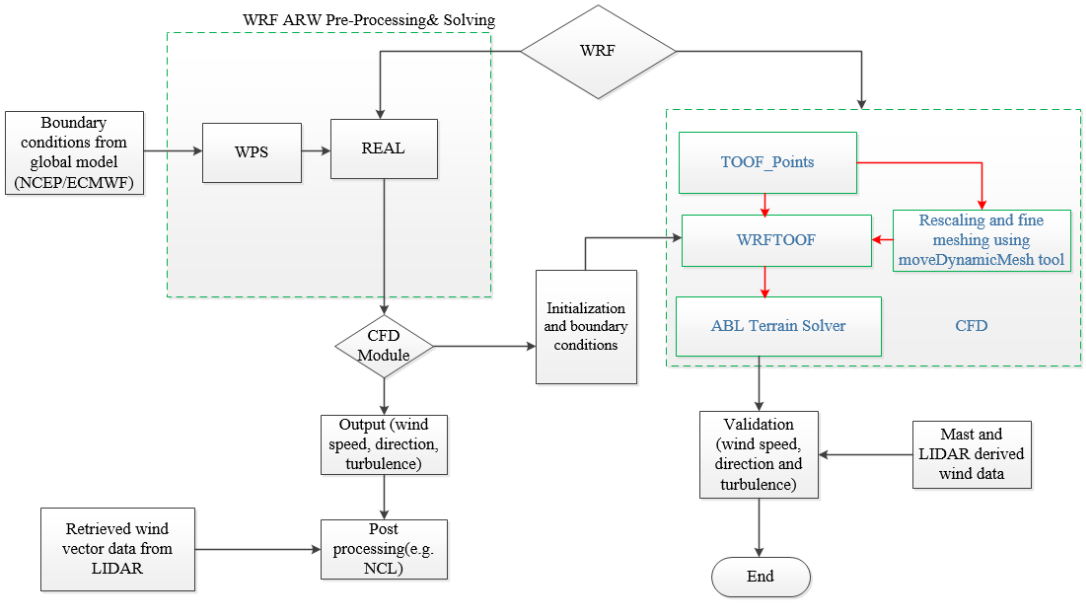

Figure 1.2 Research Methodology

1.4 Field Measurements and Verification Program

The site at Lake Turkana is characterised by three elevated masts installed at Sirima, Nyiru, and Kalkumpei (see Figure 3.6) each of which was used for model validation. The data were measured at a height of 38 m at Sirima and Kalkumpei and 46 m at Nyiru during a period ranging from a maximum of almost two years (2008 to 2010) for Sirima to a minimum of 14 months (since October 2008) for Nyiru and Kalkumpei. The measured average wind speed was 10.2 m/s for Sirima, 9.9 m/s for Kalkumpei and 10.5 m/s for Nyiru. These masts gathered wind speed and direction data having a sampling temporal resolution of 10 min. Model temporal resolution is also averaged to 10 min to permit a direct comparison with the measurements. The nearest model grid point approach is used to compare measured data at the sites with that of the simulations. The stations are located within approximately 20 km of each other.

The data recorded at the three masts must satisfy the validation criteria mentioned in Bailey et al. (1997). Missing data that does not pass the validation criteria and is rejected can be replaced by values observed by redundant sensors at other heights as long as the redundant sensor's data pass all validation criteria. Missing wind speed and direction data at the 38.5 m, 49 m and 40 m for all of Kalkumpei, Nyiru and Sirima masts respectively were synthesised from wind speed and direction measurements at 20 m and 21 m.

The CRC CARE WindTracer® CDL was employed in the field measurement campaign at Lake Turkana wind farm in 2009 under Lake Turkana Wind Power Consortium (LTWPC) due to its long range capabilities, sensitivity and portability. WindTracer® is developed by the Lockheed Martin Corporation and is a 1.6 µm Doppler-LIDAR. It is state of the art eye safe technology with a range of 8-12 km with 250 km^2 areal coverage for winds.

The LIDAR was transported to site by road and positioned on a high point within the landscape (latitude 2.48333°N, longitude 36.84835°E, at height 788 m above sea level). The site provided excellent 360° line of sight for the laser with clear views to all locations within the proposed wind farm (see Figure 3.1). The LIDAR was located approximately 20 km to the south east of Lake Turkana. The field measurement was conducted over two periods in mid and late 2009. Approximately six weeks data was

collected during the field program with the first period running over the 15 days from July 10 to 24. The second measurement period ran over a 5-week period between 28 September and 8 November, 2009. The second period was punctuated by instrument downtime which resulted in three distinct data collection periods. In most cases the LIDAR was operated over a full 24-hour period. The separation in time between the July and October campaigns provided an opportunity to refine the measurement strategy in the second phase, and to examine seasonal differences in meteorological conditions on site.

The principal output from investigation is a terrain-following wind speed map which illustrates the relative velocity differences across the study domain over the measurement period. The map comprises 10 min average wind speed estimates at a height of 45 m above the ground. Additional outputs include information of the structure and dynamics of the vertical wind profile, the LIDAR derived wind speed probability distribution function (PDF) and the uncertainty analysis.

The location near Perth WA is a relatively simple coastal location 41 m above sea level. The site is characterized by single automatic wind measuring station that gathers wind speed and direction. The data gathered for this mast is for March 2011 and the sampling interval for this mast is 5 minutes and the average wind speed measured at this site is 4.8 m/s. The data from this instrument is regularly provided to the World Meteorological Organization (WMO) at 12 hour and 6 hour intervals

1.5 Problem Definition

The basic objectives of this research project are to:

a. Develop approaches for improving the detailed forecasting of wind field at a wind energy farm.
b. Investigate the methods for assessing the performance of both spatial and temporal predictions of the structure of the boundary layer wind field.
c. Direct particular attention at the generation and propagation of turbulence and the relationship to regions of complex terrain.
d. Investigate improvements to forecast fields that result from assimilation of additional *in situ* knowledge.

The four key wind farm forecasting approaches used today include persistence, physical, statistical and hybrid modelling methods (Soman et al., 2010). Physical approaches are more reliable for predicting the power outputs from a new or existing wind farm. These approaches utilize the outputs of a mesoscale model which, if combined with statistical regression, can develop power generation forecasts for a wind farm (Parkes and Tindal, 2004) There is also research carried out on coupling meso- and microscale models for detailed wind field analysis. These coupling techniques are still somewhat immature and need to be validated via on-site measurements (Yamada and Koike, 2011). Further improvement can be obtained if on-site observations are somehow integrated / assimilated into the model. Henceforth, there is significant opportunity left for improving the detailed forecasting approaches. This forms one of the objectives of this research.

Recent approaches for prediction are generally only optimal for non-turbulent, steady state conditions and become uncertain for unsteady condition (Zehnder, 2011). Since these predictions are in the form of point forecasts they have errors that may be reduced by assimilating additional observations or by refining the resolution of physical models.

The turbulence and turbulence transport are difficult to simulate and predict in a complex terrain due to wind evolution in the inner boundary layer. However, microscale models have the capability to resolve turbulence due to small changes in topographic height because of their fine spatial resolution (Strack, 2004). The generation of turbulence by topographic features and its transport may be simulated, in principle, by using a robust k-ε model or by using a combination of K-ε, K-ε Re-Normalisation Group (RNG) and Reynold's Stress model (Satngroom, 2004). The model can be adjusted with a variable wall function to ingest the changes in the topography in a given terrain.

Prior to assimilation, data from *in situ* and remote sensing instruments require certain refinements. Advance forecasting assimilation algorithms predict wind fields into the future using previous observations and they must produce the analysis in a time step of between 5 and 60 min within a few hours of the observations being taken (Barker et al., 2012). Recently, much effort has been applied to developing NWPs but little has been gained (Barker et al., 2012). In order to optimize the use of input

observational and prior forecast data, data assimilation requires accurate estimates of observation and forecast error. To encompass this objective an advanced assimilation tool is implemented in this research.

1.6 Research Questions

This research being taken in this project will try to address the following matters

a. How does one develop a robust and reliable short term forecasting system (2 hours to 30 mins or less)?
b. How to assimilate most appropriate regional and local climatic information to achieve an acceptable forecast accuracy?
c. How to determine wind magnitude and direction sensitivity to the assimilated climatic information?
d. What is the level of accuracy required for modelling near surface wind speed and direction?
e. Investigate factors determining this accuracy specification i.e. the energy management plan of the wind farm
f. What is the decisive wind farm design criteria?
g. How to reduce the forecast error and validate using CDL data?

1.7 Summary

In this chapter an introduction and the review of the approach to be adopted towards solving the several research issues is described. The current status of wind energy modelling and management is explained in detail and is compared with the current research. A brief description of the objectives of the project is explained along with the information on research methodology. The data collection procedure used for the meteorological masts and LIDAR is discussed in section 1.4. The significance of this research is explained in section 1.2.

Chapter 2 Progress in Wind Energy Numerical Modelling and Validation

2.1 Introduction

In today's competitive market scenario, short term wind forecasting has been a vital part of business planning, particularly in areas characterized by a high concentration of wind generation and a limited capacity. The aim of this chapter is to present a critical literature review and an up-to-date bibliography on wind forecasting technologies utilised around the world. It is intended to describe various forecasting aspects concerning the wind speed and power generation. The technologies based on NWP methods, statistical methods, mesoscale modelling approaches will be discussed.

Studies in Piwko et al. (2005) have shown that wind energy will not impact energy reserves significantly if wind power forecasting can be improved. The financial benefits of good forecast are referenced in Wu and Hong, (2007) who have claimed that advanced forecasting techniques are required and are important for increasing wind penetration (percentage of demand covered by wind energy in a certain region on annual basis) in the marketplace. According to Zhang et al. (2014), short term forecasting provides TSOs with information that contributes to wind turbine and power system frequency control improving grid reliability. Projections on this time-scale contribute to improved electrical grid scheduling of power sources and reserve requirements (Zhang et al., 2014) to optimize power capture and ensure wind power decreases are balanced. Therefore, this research focuses on improving short term forecasting technique that are currently in vogue.

2.2 Predicting the Wind

The wind energy industry needs reliable tools for estimating mean wind speeds at selected heights for locations and wider areas where data are sparse. However accurate methods are required to ensure confidence that the actual power generation will be close to the prediction. Computational modelling via a physical approach is one such technique used in this study and these models are either diagnostic or prognostic as described in section 2.2.1 and 2.2.2. Data assimilation techniques used to improve initial conditions of NWP are discussed in section 2.2.3.

2.2.1 Diagnostic Modelling

Diagnostic models are also referred to as mass-consistent models. These models contain no time derivative and therefore specify the balance of quantities at a particular moment in time. Starting with some upper level and surface wind data, mass-consistent models firstly reconstruct the three-dimensional wind fields by interpolation. The interpolated wind fields are then adjusted to satisfy the laws of mass conservation caused by topographic forcing or by other physical constraints. Mass consistent models are therefore specifically designed to predict the effects of orography on steady mean wind flow. One advantage of diagnostic models, especially in the past, is their lesser computational demand. The Wind Atlas and Analysis Program (WASP) is an example of a diagnostic model. In contrast WASP, which calculates wind statistics by parametrizing the influence of topography, roughness and obstacles, CFD modelling computes the three dimensional wind flow field (Cattin et al., 2006).

2.2.2 Prognostic Modelling

Prognostic modelling is the method used by weather forecasting models. Prognostic model (also known as 'predictive' or dynamic models) are used to forecast the time evolution of the atmospheric system through the integration of conservation equations for mass, motion, heat and water, and if necessary, other substances like gases and aerosols (Finardi et al., 1997).

Prognostic models can be used for a range of scales of motion from microscale, 2 mm-2 km (cumulus cloud structure or pollution dispersion), to mesoscale, 2-2000 km (thunderstorm or urban pollution), to synoptic scale, 500-10000 km (for weather fronts and hurricanes), to planetary scale, greater than 10000 km (global wind patterns and ozone) (Jacobson, 2005).

Prognostic models can be used to investigate the effects of synoptic scale weather systems on local scale airflow, and provide the ability to simulate such events for extended time periods. While synoptic scale weather systems are driven primarily by large-scale dynamic and thermal processes, mesoscale processes are governed more by orography and irregularities of the surface energy balance (Lalas et al., 1996).

Therefore, computer codes or models can be constructed so that atmospheric phenomena may be simulated at the scale at which they occur.

Prognostic mesoscale models are often used with nested grids, which range from a coarse to a finer scale. The outer grid can obtain boundary or initial conditions from global scale models (low resolution grid data). In the nesting procedure, output of the larger domain is used as the prescribed boundary condition for the next level inner grid. This process may be repeated until the required resolution is achieved. Output from global models is usually computed six hourly, so that the boundary conditions can be 'nudged' at these times to maintain the accuracy of the simulation. Most prognostic mesoscale models now use terrain following co-ordinate systems. This allows for easy reconstruction and analysis of the wind field features at a local scale. The WRF is an example of a prognostic model.

2.2.3 Model Selection

There has been much research into the best ways of simulating the airflow close to the Earth's surface, especially in complex terrain, and many questions still remain. Prognostic models also have limitations with simulating airflow near the Earth's surface, but with increased computing power, these limitations should also become less. Some hybrid modelling techniques introduced in this study combines both prognostic and diagnostic techniques.

Non-hydrostatic source codes are considered to be the new generation models. In computer modelling, the hydrostatic approximation resulted in significant reductions in computing time and expense. Effectively, this approximation neglects non hydrostatic effects, and thus localised dynamical vertical accelerations. Models adopting this approach could not be applied for horizontal scales less than about 10 km, because in this case non-hydrostatic effects should not be neglected (Lalas et al., 1996). In non-hydrostatic diagnostic and prognostic models, mesoscale pressure differences can be computed, and hence wind fields can be evaluated at a higher resolution. With greater computing capabilities, non-hydrostatic models are not only accessible to the research field, but also for more practical applications, such as in the wind energy field.

2.2.4 Data Assimilation

The method of combining all available information on the atmospheric state in a given time window producing an estimate of atmospheric conditions valid at a prescribed analysis time is known as an assimilation system. The information sources used for producing analysis include observations, previous forecasts (the background or first-guess state), their respective errors and the laws of physics. This analysis may be used for

1. Initializing or providing initial condition for a numerical weather forecast.
2. Analysing climate through the merging of observations and numerical models (reanalysis).

The significance of accurate initial conditions to the success of an assimilation/forecast NWP system is renowned. The forecast error due to error in initial conditions depends on various factors e.g. resolution, domain, data density, orography however research communities devoted to data assimilation consider better initial condition vital for a whole range of NWP applications.

Variational Data Assimilation

Variational data assimilation (VAR) produces an optimal estimate of the true atmospheric state at the analysis time through iterative solution of prescribed cost function (Barker et al., 2003). Lions (1971) describes the underlying optimal control theory of this process while its application to meteorology is explained in DIMET and Talagrand (1986). The summary of the VAR problem is given by iterative solution of equation 2.1

$$J(x) = J^b + J^\circ = \frac{1}{2}(x - x^b)^T B^{-1}(x - x^b) + \frac{1}{2}(y - y^\circ)^T (E + F)^{-1}(y - y^\circ) \tag{2.1}$$

where $J(x)$ is minimized to find the analysis state x. The solution represents the maximum likelihood estimate of the true state of the atmosphere given the two sources of a priori data: the background (previous forecast) and x^b observations y° (Lorenc, 1986). The fit to individual data points is weighted by estimates of their errors: *B, E*

and F are the background, observation (instrumental) and representivity error covariance matrices respectively. Representivity error is an estimate of inaccuracies introduced in the observation operator H used to transform the gridded analysis x to observation space $y=H(x)$ for comparison against observations. This error will be resolution dependent and may also include a contribution from approximations (e.g. linearizations) in H.

The quadratic ***cost function*** given by equation 2.1 assumes that observation and background error covariances statistically are described using Gaussian probability density functions with zero mean error. Alternative cost functions maybe used which relax these assumptions. Equation 2.1 additionally neglects correlations between observation and background errors.

The use of ***adjoint*** operations, which can be viewed as a multidimensional application of the chain-rule for partial differentiation, permits efficient calculation of the gradient of the ***cost function***. Modern minimization techniques (e.g. Quasi-Newton, preconditioned conjugate gradient) are used to efficiently combine ***cost function***, gradient and the analysis information to produce the "optimal" analysis.

Equation 2.1 represents three-dimensional variational data assimilation (3DVAR) that creates a full 3D structure of the atmosphere. A better way to introduce the time dimension into the simulation i.e. four-dimensional variational data assimilation (4DVAR). The difference between the two is that the former largely ignores the information present in the temporal distribution of the observations while the latter makes use of it. The time dimension is added with the introduction of M in $y=H(x)$ such that it becomes $y=MH(x)$ where M is the model forecast from t_1 to t_2. Equation 2.1 becomes

$$J(x) = J^b + J^\circ = \frac{1}{2}(x - x^b)^T B^{-1}(x - x^b) + \frac{1}{2}(MH(x) - y^\circ)^T (E + F)^{-1}(MH(x) - y^\circ) \tag{2.2}$$

The ***adjoint*** of M is M^T where M^T is the Jacobian of M and propagates this gradient information back in time from t_2 to t_1. The gradient becomes

$$\nabla J(x) = B^{-1}(x - x^b) - M^T H^T (E + F)^{-1}[y^\circ - HM(x)] \qquad (2.3)$$

4DVAR is better than 3DVAR because it uses observations at the correct time, calculates analysis at the correct time and implicitly generates flow-dependent B.

ERA-Interim prognostic forecasting products utilize both 4DVAR and 3DVAR while the NCEP products utilize 3DVAR[1]. The difference between the two is that NCEP provides forecast 4 times a day while ERA-Interim provides twice a day hence NCEP model can recover quickly from a bad forecast while in case of ERA-Interim a long time is required for recovery as it is computationally expensive. However, ERA-Interim system in contrast to a hydrostatic model is non-hydrostatic utilizing altitude as opposed to a pressure as vertical coordinates in the forecast and therefore more accurately accounts for topographic effects in high resolution[2].

2.2.5 Employing 4DVAR to Retrieved Wind from CDL

Atmospheric boundary layer (ABL) is turbulent in nature and its true representation in the numerical weather prediction models is the key aspect of short term wind forecasting for wind farms. A dynamically consistent approach towards retrieval of spatially and temporally resolved velocity and thermodynamic field within ABL is fitting the outputs of a prognostic model to the CDL measurements (Newsom and Banta, 2004). If the model's boundary conditions are prescribed in some manner than the solution would be uniquely determined by the initial conditions. Thus these initial conditions are adjusted to optimize the agreement between the CDL observations and the model's predicted radial velocity. The retrieved fields are obtained when the optimal initial state is determined. This procedure, referred to as 4DVAR forms the basis of the retrieval technique. The retrieval algorithm uses a forward model that simulates dry, shallow incompressible flow with the Boussinesq approximation. The adjoint method is used to find the initialization of the forward model that gives the best fit to radial velocity measurements from a CDL. Measurements are obtained by repeatedly scanning a 3D volume of the ABL.

[1] https://reanalyses.org/atmosphere/comparison-table
[2] https://www.quora.com/What-is-the-difference-between-the-ECMWF-GFS-and-other-weather-forecasting-models

2.2.6 The Wind Profile Power Law

The power law is used in wind power assessments where near surface observations (such as that from CDL) are used to estimate wind speeds at a certain height (wind turbine hub height). This law was first proposed by Hellmann (1916), according to Simiu and Scanlan (1996). Generally, this law is represented by equation 2.4

$$\frac{V_2}{V_1} = \left(\frac{z_2}{z_1}\right)^{\alpha} \tag{2.4}$$

where V_1 and V_2 are simultaneous steady wind speeds over level terrains at elevations z_1 and z_2, respectively. The exponent, α is derived experimentally, and according to Golding (1956), it varies with height, time of the day, season of the year, topography, wind speed and temperature gradient. Kármán (1921) showed that α is equivalent to 1/7 or 0.143 for neutral stability conditions.

In wind resource assessments, the value of 0.143 is commonly used because introduction of substantial errors into estimates, due to differences between the z_1 and z_2, are insignificant (usually < 50 m). In cases where constant α is used, it does not account for the roughness of the surface, zero-plane displacement (the displacement of calm winds from the surface due to the presence of obstacles), or the stability of the atmosphere (Touma, 1977) (Panofsky, 1976). The use of constant 0.143 exponent may yield quite erroneous estimates in places where trees or structures impede the near-surface wind[3], therefore, log wind profile is preferred. Further details on the estimation of wind power potential for the flow over heterogeneous terrain can be found in Peterson and Hennessey (1978).

2.3 Evolution of Forecasting Methodologies

2.3.1 Development and Current Trends

As stated earlier Soman et al. (2010) has classified wind forecasting methodologies into four basic types i.e. persistence method, physical approach, statistical approach and hybrid approaches. Soman et al. (2010) further classified them into four time scales i.e. very short term, short term, medium term and long term forecasting. Short term forecast predicts wind 30 minutes to 6 hours ahead in time, medium forecasts

[3] https://en.wikipedia.org/wiki/Wind_profile_power_law

predict from 6 hours to 1 day ahead while long term forecasts last from a day to a week ahead The present study is concerned with a physically based approach to improving existing short term forecasting techniques since the current wind forecasting methods are limited. Wind forecasting errors arise from timing significant weather fronts incorrectly. Large power error can occur since the passing of such fronts can be associated with the changes in wind speed. Data assimilation can be used to correct wind forecasting errors. The observations integrated with the model will however be unable to correct the forecast if the prediction of weather fronts is mistimed. For example, if a change that is forecast to arrive at a particular time arrives an hour early or late, then models produce erroneous results. While the forecast is wrong, trying to correct it with a single observation or a small number of local observations tends to produce a very misleading picture of the wind field

It is interesting to note that the industry is still using persistence models and they are effective in very short term forecasting due to their unbelievable accuracy (Potter and Negnevitsky, 2006; Wu and Hong, 2007). Persistence models are the benchmark to judge the improvement in a newly developed short term forecasting model (Milligan et al., 2003).

The physical approaches concentrate on using detailed physical description for modelling on-site conditions at wind farm location (Kariniotakis et al., 2004). A number of physical approaches have been introduced till now (Lei et al., 2009). The physical approaches are based on the models using the fundamental physical principles of conservation of mass, momentum, and energy in air flows. Roulston et al. (2003) demonstrated that NWP model output can be used directly for wind speed predictions. NWP models are sometimes naive with respect to physical conditions such as topography and are not satisfactory for wind farm applications. Many of the topographic features and atmospheric behaviours within complex terrain occur on a smaller spatial scale than the commonly used synoptic-scale forecasting models can simulate, resulting in limited near-surface model accuracy (Reid and Turner, 2001). The NWP models can therefore be downscaled in three different ways to act as input to other models to make them more suitable for wind farm applications.

In the first method the initialization fields from NWPs can be used as an input to a mesoscale model such as WRF. These mesoscale models are better suited for resolving

the near surface atmospheric behaviour in complex terrain (Jiménez et al., 2010; Rife et al., 2004). However, these models frequently differ in physical parameterizations, numerical schemes, data assimilation, and coordinate systems (Lee and Fernando, 2004). Studies like Byrkjedal and Berge (2009), Soares et al. (2011) and Soare et al. (2010) support the interest of the use of meteorological models, and specifically the WRF model, for wind simulation and wind energy purposes.

The second technique refines the NWP data taking into account on-site conditions via downscaling methods based on the physics of the lower atmospheric boundary layer. The downscaling method used depends on the detailed physical description of the wind farm and the associated terrain. Typically, refined wind speed data from NWP at hub height is fed into the corresponding wind power curve for calculating the wind power production. Statistics are performed via online data to reduce forecast error. Landberg (1999) first introduced the concept of utilizing the NWP models as an input field and then applied corrections on the wind speed predictions using various programs such as WASP and PARK (Landberg, 1999).

There are also many CFD models available. They are all based on the same basic physical principles but they may differ in how the grids are structured and scaled, and how the numerical computations are performed (Jung and Broadwater, 2014). Mesoscale models have been coupled in the past by Boutanios et al. (2010) where WRF is coupled with OpenFOAM. In another technique, Perivolaris et al. (2006) coupled the mesoscale model COAMPS with the CFD model VANE. Also Nakayama et al. (2011; 2012) coupled WRF with CFD code developed by (Nakayama et al., 2011) for urban areas.

The third technique is to refine the outputs from the synoptic model by integrating LIDAR data and then running the mesoscale model based on the updated boundary conditions. Such techniques are presented in Liu et al., (2011) and Carpenter et al., (2013).

2.3.2 Future Prospective

In a review presented by Jung and Broadwater (2014) a foundation is provided to guide future research. It is recommended that combinations of different forecasting approaches will help to reduce forecast errors. The current research presented in this

dissertation is a combination of two approaches and an improvement in forecast error has been achieved. Archer and Caldeira (2009) assessed the potential of high altitude winds for energy generation and outlined how these winds may be utilized to generate electricity in future. A summary of options for improving wind forecasting is presented with respective time frames in Table 2.1.

	Resource assessment and siting	**Time frames**
1.	International wind atlases: develop publicly accessible databases of land based and offshore wind resources and conditions.	Complete by 2015
2.	Remote sensing techniques: high spatial resolution sensing technology and techniques for use in high-fidelity experiments and siting wind power plants.	Complete by 2015
3.	Siting optimisation of turbines in a wind power plant: develop tools based on state-of-the-art models and standardised micro-siting methods; refine and set standards for modelling techniques for wind resource and micro-siting.	Complete by 2020
	Improve short-term forecasting accuracy	**Time frames**
1.	Wind forecasts: meteorological wind forecasts, with feed-back loop from wind power plant online data to weather forecasting.	Complete by 2020. Weather forecasting takes input data from wind power plants.
2.	Power production forecasts: for use in power system operation, with storm and icing forecasts.	Complete by 2020

Table 2.1 Future prospective of wind energy forecasting (Philibert and Holttinen, 2013)

2.4 Status of LIDAR Technology for Wind Field Assessment

2.4.1 Development and Current Trends

A study by Krishnamurthy (2013) showed how measurements derived from LIDAR can represent the wind field and how predictions of the wind at the wind farm can be used as an input for control methods to meet the needs of wind farm operators. The current work described in this dissertation adopts physical approach where the LIDAR

measurements are assimilated into a synoptic model's output through FDDA (four-dimensional data assimilation) for closely representing the actual wind experienced at the wind farm.

Parks et al. (2011) conducted a study for ameliorating wind power forecasting and establishing the reliability of wind power integrating into the grid. It was found that for common wind forecast models used at wind farms, significant ramp (an event of a certain duration that in magnitude is several standard deviations in excess of the mean wind) events are often poorly predicted or not predicted at all as a result of imprecision in the meteorological conditions. The study shows that WRF may capture large-scale ramps, such as cold fronts, but often incorrectly predicts their time of arrival by minutes to hours. This error, of course, depends upon the amount of locally and regionally assimilated *in situ* wind information (both spatially and temporally). It misses smaller scale events, for example, outflows due to convective activity. In order to balance unexpected changes in power due to less accurate prediction for magnitude and timing of ramps grid operators schedule wind power output conservatively to avoid unexpected changes in generated power. Xcel Energy (Parks et al., 2011) developed a method, which applies a mesoscale ensemble prediction model to provide a probabilistic wind prediction through NWP modelling as the core forecasting system. In order to avoid errors in forecasts, Doppler radar and public meteorological data near the wind farm are added. This helps to provide successful warnings of ramp events with 0-2 hours lead time.

A comparison between LIDAR profiles and meteorological tower measurements was presented by Frehlich and Kelley (2008). This paper discussed the need for accurate measurements of turbulence profiles due to the effects of turbulence on wind energy generation shown in previous studies. The authors noted that, with the improved statistical accuracy of the volume-averaged profiles provided by Doppler LIDAR measurements, sudden changes in wind conditions may be monitored, making appropriate wind farm control possible. The authors concluded that

a. Measurements with smaller LIDAR range gates would give more accurate estimates of turbulence statistics.
b. Wind speed and direction changes, based on the use of angular subsectors, which are different azimuthal sector sizes, reveal spatial variability.

c. Statistical properties of the profiles need further study for quantification (Krishnamurthy, 2013).

Two WindTracer® LIDARs were used in a study by Carpenter et al. (2013), one of which was located at a wind farm (Glacier wind farm, Montana, USA) and the other to the west at a higher elevation on a mountain and, further upstream. To measure the conditions at higher levels of the atmosphere, the methodology used 5 Plan Position Indicator (PPI) sweeps at low elevations separated by 1° and a sixth PPI at a 45° elevation to measure the conditions at higher levels of the atmosphere. The radial velocity was measured with a sector Velocity Azimuth Display (VAD) method. By propagating the wind vectors ahead to predict the future wind field, the researchers found that a direct advection model provided improved power prediction compared to a persistence model that, the procedure often used as a baseline for prediction evaluation. The advection model therefore had the best result in the 10-15-minute range and provided a 40% reduction in prediction error as far as 45 minutes in advance.

Forecasting for isolated wind farms located on the Canary Islands was studied by Treinish et al. (2013). It was concluded most ramp events at the Islands were missed by NWP forecasts. The importance of predicting ramp events for an isolated grid, where the large power output variations that ramps can cause are not easily balanced, was emphasized by the authors and a need for turbulence-scale modelling to capture the flow due to the Islands' complex topography was recognised. LES were applied to get output every 5 minutes and to capture transients and integrated it with a WRF (version-ARW 3.3.1). No observational system existed so no data assimilation studies were possible.

Another project was performed at the Glacier Wind farm by Wilde (2012). The goal was applying off-site measurements to create short-term predictions of ramps. Ramps were defined as a change in hourly average wind farm power generation by at least 15% of installed capacity over a 3-hour period. Real-time data was used with the WRF model and additional measurement stations were setup at upstream locations. The pressure differential with other locations was useful to predict the ramps that would occur at the wind farm. North and North-western winds seemed to interrupt the more predictable and stable westerly winds from the Marias Pass. The model proved better than persistence, but was not much better than existing models used at the site already.

They did prove that off-site measurement stations do improve forecasting for sites with complex terrain.

2.4.2 Future Prospective

Forecast failures of high-impact weather systems are often due to lack of observations over data sparse areas, such as the Southern Hemisphere, the Tropics and Northern Hemisphere oceans, over a prolonged period prior to the extreme events. The meteorological observing systems still lacks acceptable global coverage of wind profile observations despite the upper air network (radiosondes and radiosondes are highly non-uniform in their spatial coverage of the globe) and continuous progress in the observation of meteorological variables from space by satellites. The European Space Agency (ESA) Atmospheric Dynamics Mission (ADM), featuring the satellite named ADM-Aeolus3, is a first step to fill in this gap and will provide wind profiles in otherwise data sparse areas (Figure 2.1) and thus may reduce the number of forecast failures. ADM-Aeolus is a demonstration mission scheduled for launch in 2017 and will be operational for three years.

Figure 2.1 Artist impression of the ESA earth explorer mission ADM-Aeolus that will provide a global coverage of wind information for the first time in history Marseille (2014)

2.5 Summary

This chapter provided an in-depth review of the recent advances and developments in the short term forecasting with a concentration on physical approaches. The chapter focusses on the latest information available for short term forecasting and its improvement regarding the usage of NWPs, mesoscale models such as WRF, LES CFD and integration of CDL. The future prospects in the technology are also discussed in detail. The statistical methods involving artificial neural networks are not discussed as the focus of the study is physically based approaches. However, their importance cannot be neglected in short term wind power forecasting.

Chapter 3 Lake Turkana Wind Energy Farm

3.1 Introduction

Electricity, wood fuel, petroleum and renewable resources are the main sources of energy in Kenya. Of the total energy requirements in Kenya, the majority (68%) of the country's primary energy consumption relies on fossil fuel sources. This is followed by petroleum (22%), electricity (9%) and other sources (1%). Approximately 14 % of the Kenyan population uses electric power and economic growth requires increased access and distribution. Most of the electric power generation (50%) comes from hydro-turbines but the continuing droughts in the region like the one in 1999-2002, reduces the reliability of hydropower (Gabisch and Duru, 2011). This situation forced the Kenyan government to consider alternative power generation resources that would reduce uncertain reliance on hydropower and fossil fuel (Theuri, 2008).

The Lake Turkana Wind Power project is of potentially significant strategic benefit to Kenya, and is one of the largest private investments in Kenya's history. It aims to provide 325 MW of reliable, low cost wind energy to the national grid, equivalent to over 20% of the current installed electrical generation capacity. The wind farm site is located in the Marsabit District in northern Kenya, approximately 50 km north of South Horr township and 8 km east of Lake Turkana.

The Kenyan government joined with its global partners and identified the potential wind resource at Lake Turkana and thus formed LTWPC. The strategy involves the construction and operation of a 300 MW wind power farm which comprises of 367 turbines (850 kW capacity each). In October 2008, LTWPC approached CRC CARE through its participant organisation; DER to assist in the measurement of wind fields using CDL. This involved a field monitoring program in mid and late 2009 to map the wind field at the site and support validating the accuracy of wind modelling where appropriate (Sutton et al., 2010).

This chapter provides a brief description of the topography and climatology of the Lake Turkana Wind Farm. The data collection via conventional and remote sensing instruments is discussed in detail along with the uncertainties involved in wind resource assessment. The instruments involved in measurements campaigns and their

statistics are also covered in this chapter in order to provide an indication of the quality of data acquired.

3.2 Topography and Climatology

Lake Turkana region has diverse topographic features that include the Ethiopian highlands to the northeast and Kenyan highlands to the southwest (Figure 3.1). In between the Ethiopian highlands and the East African highlands lies a low-level region. This valley is referred to as the Turkana channel (Kinuthia and Asnani, 1982). It is above 500 m from the mean sea level and has a depth that varies between 610 and 1524 m, and a width that varies about 140 to 700 km. The channel is approximately 700 km long and oriented from southeast to northwest (Kinuthia, 1992). It has been observed by (Kinuthia, 1992; Kinuthia and Asnani, 1982) that the NE and SE monsoon near the equator branches off from the Indian Ocean, enters the Turkana channel and intensifies, maintaining an average speed of 11 ms^{-1} (Figure 3.1). Their observations showed quite distinct low-level jet in the channel (Turkana easterly low-level jet) that persists throughout the year. They further postulated that the configuration of the Ethiopian highlands and the East African highlands could be playing a critical role in the development and maintenance of the Turkana low-level jet through the orographic channeling effect.

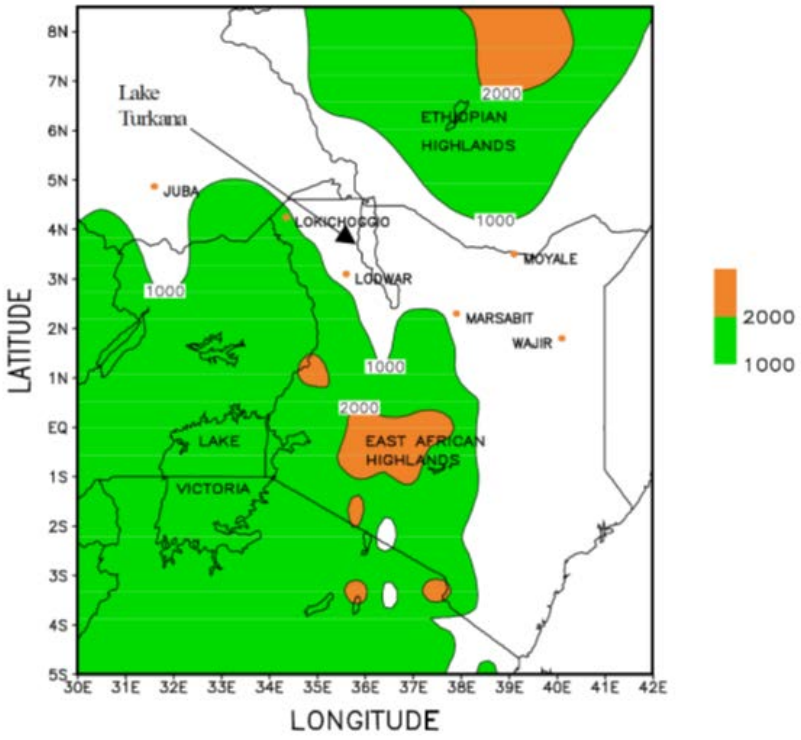

Figure 3.1 Topography over the Turkana Channel. Terrain height values greater than 1000 m are shaded (Indeje et al., 2001)

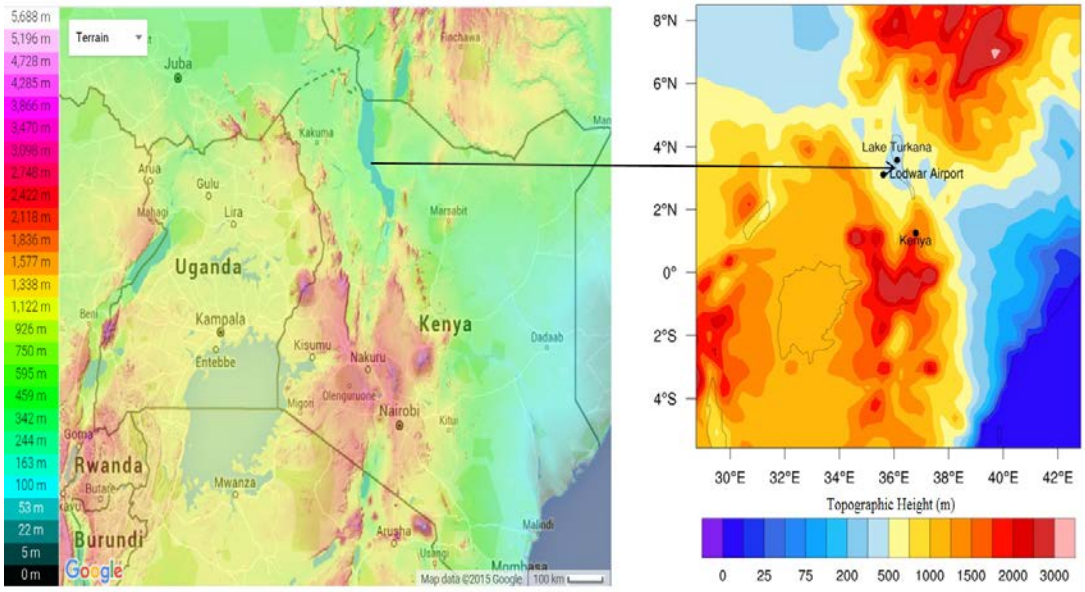

Figure 3.2 Topography of the Lake Turkana

The detailed topography of Lake Turkana region is shown in Figure 3.2. The East African site is a hilly terrain, with elevations ranging between 700 m and 900 m above sea level. It is uninhabited, rocky, arid desert area. The area has unique geographical conditions in which daily temperature fluctuations support the generation of strong but very predictable winds. The climate is very hot and dry and the mean monthly

temperatures are in the range of 27–29 °C. The mean minimal lie around 13–20 °C and the mean maxima are 26–35 °C. The coolest months are July and August while February, March and October are the hottest. The average wind speed is 11 m/s from a consistent SE sector. The wind is accelerated locally between Mt. Kulal (2300 m above sea level (a.s.l)) and the Mt Nyiru Range (2750 m a.s.l). Due to thermal effects, the wind decreases around mid-day and is at full force during the night (Kinuthia, 1992).

3.3 Conventional Wind Resource Assessment

Bailey et al. (1997) delineates the basic principles of wind resource assessment at a site. The conventional instruments used for wind speed and direction are cup anemometers and wind vanes respectively. These instruments are installed on tall tubular towers known as meteorological mast which are 40- 60 m in height. Because wind varies inter-seasonally and inter-annually, long term resource assessment campaigns are essential for the correct estimation of the wind power at hub height (Lackner, 2008). The approximate price of a measurement campaign ranges from $20,000- $30,000 depending on the labour cost (Gardner et al., 2004).

The flow of air near the anemometers is significantly affected by the masts used in wind resource measurement. This effect is known as the “tower shadow”, and it becomes pronounced when the anemometer is in wake of the mast. Tower shadow effect can be reduced by selecting the higher reading of two anemometers at each height as the value of the measured wind speed for each averaging period.

Cup anemometers have an accuracy of 0.1 m/s based on wind tunnel tests (Pedersen, 2004). They are characterized by the distance constant (Manwell et al., 2010) (typically< 5 m) which determines the sensitivity of the anemometer. In general, cup anemometers with small distance constants can be classified as “point measurements” of the wind speed, and so they measure the instantaneous wind speed at a given point in space and a given time. Currently, only three models of anemometer are approved by the International Electrotechnical Commission (IEC) and International Measuring Network of Wind Energy Institutes (MEASNET) for power curve calculation – the Risø P2546A, Thies First Class 4.3350.10.000 (used in this study), and a Vector A100 model anemometer.

3.4 Conventional Wind Assessment Uncertainty

The uncertainty due to conventional methods of wind measurement can be influenced by various factors. These are generally classified into four categories as explained in Table 3.1

Uncertainty	**Cause**	**Types**	**Cause**
Wind Speed Measurement Uncertainty	Arises when measuring the actual wind speed at a site.	Calibration Uncertainty	The uncertainty arises from variations between anemometers of a given model
		Dynamic Over Speeding	It is caused by over speeding of anemometer due to turbulence intensity
		Vertical Flow Effects	This uncertainty is due to different anemometers responding differently to flow which is not purely horizontal induced by terrain effects.
		Vertical Turbulence Effects	Consequence of overestimation in wind speed due to turbulence in vertical direction
		Tower Effects	Also known as shadow effect arises when

			anemometer is in the wake of tower
		Boom Effects	Arises due to tilted anemometer on boom and distance between boom and anemometer is <12 boom diameters
Long-term Resource Estimation Uncertainty	Arises when the measured wind resource data are used to estimate the long-term wind resource at a site		
Wind Resource Variability Uncertainty	Long term resource assessment depends on yearly data potential of random errors and the uncertainty is less if longer reference site data set is used to estimate the long-term parameters		
Site Assessment Uncertainty	Is due to a. Wind shear model used to extrapolate the estimated long-term wind resource to the hub height. b. Tower location and complex topography between towers at a large site		

Table 3.1 Explanation of conventional wind assessment uncertainty (table compiled from (Bailey et al., 1997), (Lackner, 2008) and (Lackner et al., 2007))

3.5 Wind Resource Assessment using Active Remote Sensing

Due to high costs associated with the conventional methods of resource assessment including the installation of towers, advanced anemometers, data loggers etc. and restrictions to height of towers and increasing size of the rotor diameter researchers are now looking for alternative methods of resource assessment. The most popular is remote sensing due to its relatively low cost and increased flexibility.

Wind speed and direction at several heights is determined through remote sensing techniques using a ground-based instrument which operates via the transmission and detection of light (LIDAR) or sound (SODAR). This will reduce the uncertainty related to the power curve by considering the flow over the whole height of the turbine rotor (Antoniou et al., 2007). SODARs have been used intermittently in wind energy applications rather than meteorological applications. Crescenti (1997) shows that large differences occur in practice between different SODAR measurement systems which suggests a need for a new and more generic SODAR calibration procedure. The LIDAR on the other hand is a more recent development (Albers, 2006) which had complications in the past with cost, size, cooling, eye safety. However, all such problems have been offset with the emergence of coherent lasers.

3.5.1 Implementation of CDL in Wind Resource Assessment

The adoption of advanced instrumentation and measurement technologies is motivated by the stochastic nature of the wind resources, the high initial capital cost, and the increasing structural flexibility of modern turbines. Scanning CDL systems are able to measure real-time wind conditions between 5- 15 kilometres upwind of wind farm and are therefore suited to providing preview information of flow disturbances before they impact the wind farm.

Studies by (Albers, 2006; Jaynes et al., 2007; Kindler et al., 2007; Smith et al., 2006) showed the importance of CDL in wind energy applications and concluded that error between the measured and observed wind field can be reduced to about 3% with the use of CDL compared to meteorological masts. A recent study was conducted using a 2 μm LIDAR at a test site in Bremerhaven, in the northern Germany and it concluded that CDL is a convenient tool for wind energy research (Käsler et al., 2010). A more

detailed view on the application of LIDAR profilers for wind energy is provided in Courtney (2009). A very interesting study was presented by Aitken et al. (2012) which provided guidance for determining the utility of LIDAR for deployments at wind farms in order to characterize turbine performance.

3.5.1.1 Wind Tracer CDL

The data for the wind farm site at Lake Turkana was collected using the state of the art WindTracer® CDL manufactured by US Defence contractor Lockheed Martin Coherent Technologies. This eye safe infrared technology with 1.6 μm laser source not only helps to detect wind vectors but serves as an evaluation tool for verifying numerical meteorological prediction models that support wind farm planning through turbine siting, and subsequently wind energy production management. It possesses the ability to measure winds and aerosol levels with high temporal and spatial resolution. It can scan hemispherical volumes specifically with radii of 8-12 km within minutes. Single cross-sections, for example a vertical cross-section (or Range Height Indicator (RHI)), can be completed in seconds, allowing measurement of transient atmospheric processes. The range capabilities of the LIDAR are strongly influenced by atmospheric backscatter conditions (aerosol levels), and as such will vary between locations.

3.5.1.1.1 Operating Principle

The CDL WindTracer® measures wind velocity through a very simple procedure. It basically illuminates a target of interest e.g. atmospheric aerosol in case of wind speed measurement a small portion of this beam is backscattered into the receiver. A change in the light's frequency via a Doppler shift due to the motion of the particles along the beam direction. This frequency shift is accurately measured by mixing the return signal with a portion of the original beam (the reference beam, or local oscillator), and sensing the resulting beats at the difference frequency on a photodetector. The Doppler shift is induced by the component of the velocity of the particle directly towards or away from the laser. By analysing the frequency shift, a direct measurement of the radial component of velocity of the aerosol particle is made. It is assumed that aerosol move with a speed and direction identical to that of the surrounding air and so an estimate of the radial wind speed is obtained.

Figure 3.3 highlights the basic principles of operation. The complete specifications of the instrument are given in Table 3.2. The length of the pulses transmitted by the WindTracer® system is approximately 90 m and pulses are transmitted 500 times per second (i.e. a pulse repetition frequency, or PRF, of 500 Hz). This means that the beam may be thought of as a series of 'pencils' that are emitted every 2 milliseconds that measure 90 m long by 10-30 cm wide, depending on the distance away from the system and the laser divergence. However, some WindTracer® systems use a PRF other than 500 Hz. The system used in this study uses PRF of 600 Hz. The Doppler frequency shift is $\Delta v=-2v_r/\lambda$, where v_r is the radial velocity and λ is the operating wavelength. For a 1.6 μm operating wavelength, the frequency shift is roughly 1.25 MHz per meter/second of particle velocity.

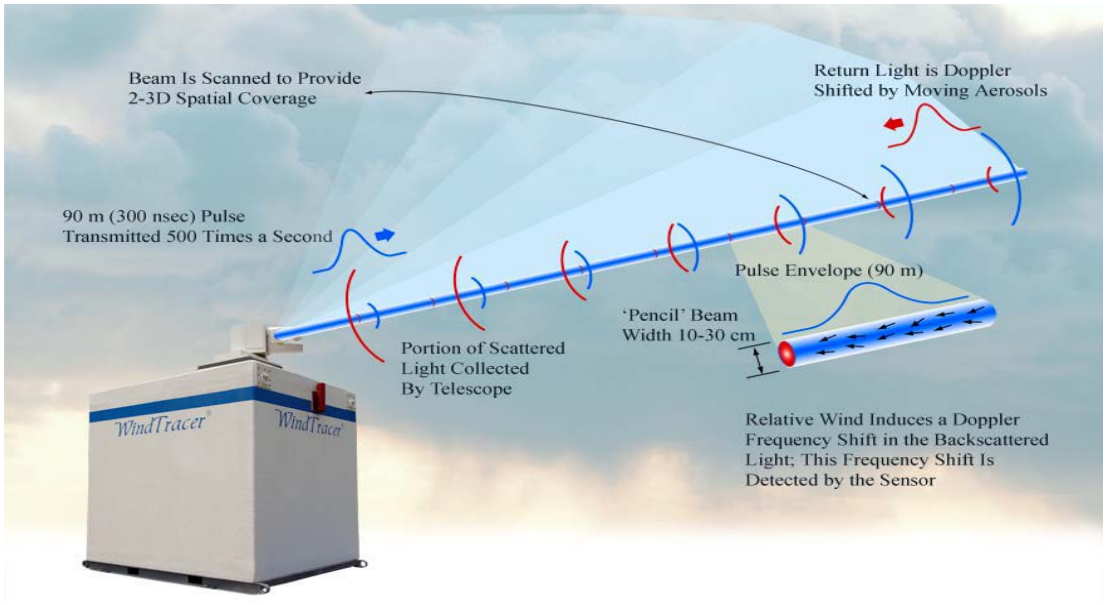

Figure 3.3 CDL operating principle (Sutton et al., 2010)

Measurement	
Typical Range	400 m to 18 km
Maximum Range	33 km
Radial Wind Velocity Range	±38 m/s
Minimum Range Resolution	100 m
Scanner	
Azimuth Range	0 to 360 °
Elevation Range -	5 to 185 °
Resolution	0.001 °
Pointing Accuracy	±0.1 °
Optical Clear Aperture	12 cm
Transceiver	
Laser Wavelength	1617 nm
Pulse Energy	2.5 ± 0.5 mJ
Pulse Duration	300 ± 150 nsec

Pulse Repetition Frequency	750 Hz
Beam Diameter	9.6 cm
Shelter	
Environment	All weather
Weight	2600 kg
Dimensions	197x244x329 (H) cm
Power Specification	200-240 VAC single phase, 50 or 60 Hz 50A

Table 3.2 Specifications of the WindTracer® CDL
(http://www.lockheedmartin.com.au/us/products/windtracer.html)

3.5.1.1.2 Data Acquisition

A trigger signal (T=0) is received by the data acquisition system from the laser slightly before the laser pulse is transmitted to the atmosphere. As it is transmitted, a "copy" is recorded to analyse and determine the precise frequency and timing of the pulse as it left the system. This recorded copy is called the Monitor pulse, because it "monitors" the frequency of the laser. After a small time period, atmospheric returns are then recorded in what is called the Signal Block. This data can be analysed to determine the speed and distance of a group of aerosol particles.

The receiver system samples every 4 nanoseconds (corresponding to a 250 mega sample per second rate). In spatial coordinates, the 4 nanoseconds correspond to 0.6 meters of round-trip distance (sample spacing). The signal block is divided in range gates of a chosen number of samples for velocity retrieval.

The velocity algorithm utilizes the Fast Fourier Transform (FFT) algorithm to transpose the temporal return signal to the frequency domain for each gate to produce range-resolved estimates of the radial wind velocity. The highest peak of the FFT spectrum gives the predominant signal frequency, and therefore the prevailing radial wind speed, in each gate. A Graphical User Interface (GUI) enables selection of the number of range gates and the size (number of samples) of each gate. A typical range gate size of 256 samples results in a range resolution of 153.6m (256 * 0.6m = 153.6m). The dilemma in the LIDAR signal FFT processing is that the frequency resolution (and accuracy in wind speed retrieval) is proportional to the length of the signal while the range resolution is inversely proportional: the longer the gate, the better the wind speed accuracy and the worse the range resolution. CDL wind speed measurement is a compromise between spatial resolution and velocity accuracy.

Various retrieval techniques have been developed to obtain two-dimensional (2D) and 3D wind field estimates based on radial velocity measurements. These include the VAD, Modified Velocity Azimuth Display (MVAD), Volume Velocity Processing (VVP) and Radial Velocity Feature Tracking (RVFT). These techniques are potentially suitable for many applications including vertical wind profiling at airports and wind farms, military applications, atmospheric science and air pollution transport studies.

3.5.1.2 Elements Affecting Precision of CDL

Several elements affect the performance of CDL for wind resource assessment which are elucidated in Table 3.3

Uncertainties	**Types**	**Cause**
CDL hardware uncertainty	Sensing range error (Range gate trigger, Focusing, Range gate distortion)	Since the wind speed on average increases significantly with height an error in sensing distance will introduce a measurement bias. An average error of 5 m in the sensing height can easily introduce a bias of 0.2 m/s in typical shear conditions (Lindelöw-Marsden, 2009)
	Cone angle and Tilted mounting	This is uncertainty in the intended cone angle, φ (Figure 3.4) which causes an error in the sensed horizontal wind speed linearly proportional to the wind velocity. An error of 0.5° will affect

		the constant sensing range by -1.5%
	Tilted mounting (from horizontal)	A tilted LIDAR will experience significant cone angle and limited sensing range errors which are different for the different sensing directions which produce biases in wind speed and direction.
Uncertainties connected to atmospheric phenomena	Turbulence over the scan perimeter	Is both due to spatial turbulence and that the radial measurements are taken at different times
	Inhomogeneous aerosol scatter distribution	Is due to assumption that the weighting function used to set the sensing range is calculated for a homogeneous aerosol distribution.
	Clouds and rain	Clouds affect the weighting function of a sample volume due to non-homogeneous backscatter distributions hence horizontal wind speed bias is introduced since clouds predominantly are above and the wind thus typically stronger at the

		cloud height than at the set sensing height
	Sheer	This is due to difference in the radial wind velocity for different shear conditions even if the wind velocity at the set measurement height is the same
	Veer	The measured radial wind velocity distribution depends on the wind veer, directional change with sensing range, over the sample volume in a similar manor as for shear. The estimator might therefore make the same kind of errors in strong veer

Table 3.3 Uncertainties affecting CDL performance

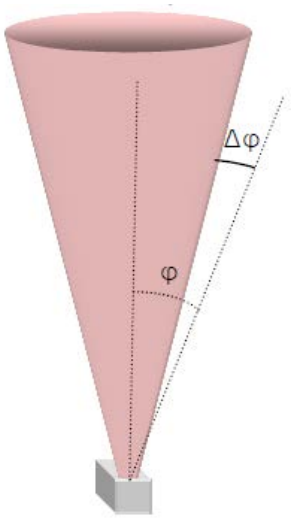

Figure 3.4 Illustration of the cone angle error. The intended cone angle is shown as a dotted line

3.6 Meteorological Mast Measurements

Three masts equipped with cup anemometers and wind vanes have been positioned at Kalkumpei, Nyiru and Sirima locations in Lake Turkana wind farm region to carry out high quality wind measurements. The stations provide measurements at 10-minute intervals throughout the day. Table 3.4 shows the meteorological masts locations as well as the measured wind data. The actual erected masts are shown in Figure 3.5 while their relative positions are shown in Figure 3.6 respectively.

At all masts, the anemometers are mounted on horizontal booms approximately 7.5 mast face widths long, and the cups of the anemometers are at least 15 boom diameters above the booms in each case. The booms supporting the top and lower anemometers on Sirima mast are orientated to 38° and 31° respectively. The top wind vane is orientated to 222°and the lower vane to 125°. On Nyiru mast, the boom supporting the top anemometer is orientated to 38 degrees while the lower anemometer is on a boom orientated to 42°. The top and lower wind vanes are on booms orientated 213° and 127° respectively. The booms for the top and lower anemometers on Kalkumpei mast are orientated to 18° and 22° respectively. The boom supporting the top wind vane is orientated to 209° while the boom for the lower wind vane is orientated to 118° (Claveri, 2010). These mounting arrangements are consistent with the recommendations provided by IEC (Quarton, 2004).

Masts	Latitude	Longitude	Height above sea level (m)	Anemometer height above ground level (m)	Wind vane height above ground level (m)
Kalkumpei	2.53115	36.85693	843	38.5, 20	39, 21
Sirima	2.47445	36.83806	832	46, 20	49, 20
Nyiru	2.46035	36.80324	872	38, 20	40, 20

Table 3.4 Locations and heights of the three masts used in the measurement campaigns at Lake Turkana site Kenya East Africa

Figure 3.5 Meteorological masts at Lake Turkana site Kenya East Africa

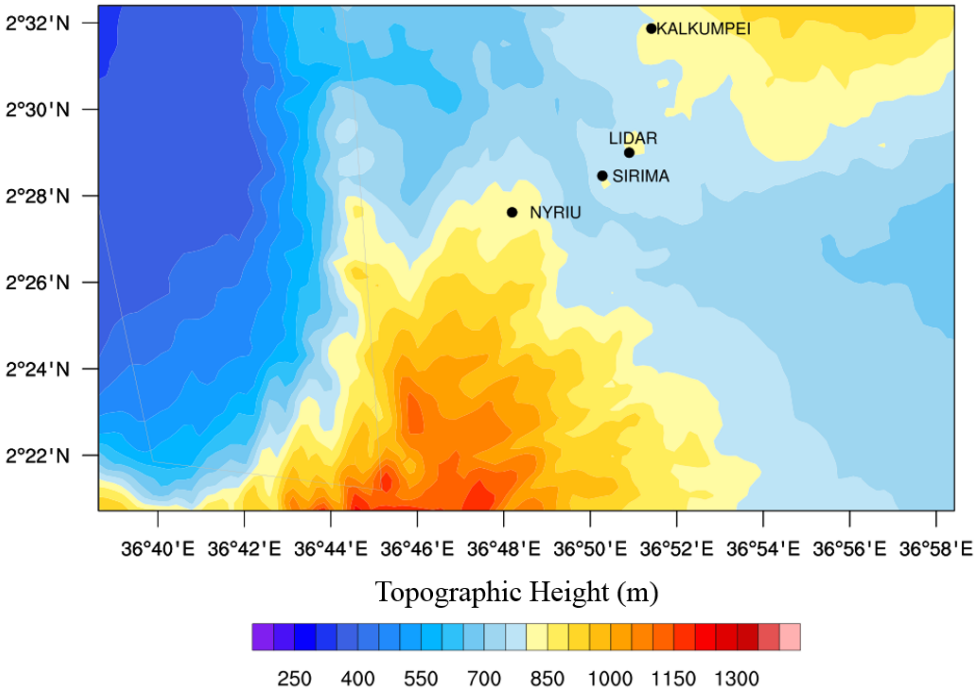

Figure 3.6 Wind speed and direction meteorological measuring stations designated Kalkumpei, Sirima and Nyriu and the CDL located on the Lake Turkana Wind Farm

3.6.1 Data Quality Control

The WMO recommends the standard for the wind speed and direction measurement as shown in Table 3.5

Variable	Range	Reported resolution	Required measurement uncertainty	Output averaging time
Wind Speed	0-75 m/s	0.5 m/s	0.5 m/s for ≤ 5 m/ s 10% for > 5 m/ s	2 and/or 10 min
Wind Direction	0-360°	1°	5°	2 and/or 10 min

Table 3.5 Operational Measurement Uncertainty Requirements and Instrument Performance (Jarraud, 2008)

Before data analysis, there was a need to examine data quality. This is necessary if correct statistical inferences are to be made from the data. The quality of data may be compromised by inconsistencies in records and data gaps. Inconsistent data can occur due to several reasons, for example change of location of observing stations and/or in instruments, and also due to human error. WMO standard recommends that a climate dataset for which more than 10% is missing, is not good. The wind data was subject to a quality checking procedures to identify records which were affected by equipment malfunction and other anomalies. The main periods for which valid wind data were doubtful are summarised below, together with details of the errors identified:

Kalkumpei mast:

9th November to 23 November 2009: Erroneous data, 38.5 m anemometer

Nyiru mast:

14th November to 31st December 2009: Sensor setup fault, 49 m wind vane

Sirima mast:

17th April to 31st December 2009: Erroneous data, 40 m wind vane

Missing and erroneous wind speed and direction data at the 38.5 m, 49 m and 40 m levels for Kalkumpei, Nyiru and Sirima masts respectively were synthesised from wind speed and direction data at 20 m and 21 m respectively.

3.6.2 Measured Wind Statistics

The measured wind statistics for Kalkumpei, Nyiru and Sirima are presented and discussed in the following sections.

3.6.2.1 Kalkumpei Mast

Wind speed data recorded between 9th November 2009 and 23st November 2009 at 38.5 m was below 1 m/s and hence declared erroneous. During this period wind speed data at 20 m anemometer was used to replace the doubtful data at 38.5 m height. The measured mean annual wind speed for Kalkumpei 38.5 m is 10.44 m/s while the mean wind direction at 39 m is 117.25° respectively. The mean annual temperature is 28.3° C. These measurements were made between 01-01-2009 to 31-12-2009. Table 3.6 shows the mean monthly wind speed, wind direction and temperature at Kalkumpei mast.

Month	**Mean Speed at 38.5 m (m/s)**	**Mean wind direction at 39 m (degrees)**	**Mean temperature (°C)**
January	10.33	119.95	28.6
February	11.37	120.70	29.2
March	10.59	120.19	30.3
April	9.28	116.33	29.3
May	9.36	117.26	28.8
June	10.64	112.21	28.1
July	11.50	112.99	26.7
August	11.86	113.82	26.9
September	11.29	113.79	28.4
October	10.31	119.03	27.9
November	10.05	116.48	28.4
December	8.79	124.22	27.8

Table 3.6 Mean monthly wind speed, wind direction and temperature at Kalkumpei mast

3.6.2.2 Nyiru Mast

Wind direction data recorded between14th November to 31st December 2009 at 49 m was erroneous due to wind vane setup fault. During this period wind direction data recorded by the 20 m wind vane was used to replace the doubtful data at 49 m height. The measured mean annual wind speed for Nyiru at 46 m 10.75 m/s while the mean

wind direction at 49 m is 121.21°. The mean annual temperature was not computed because 4 months (June, July, August and September) data is missing. These measurements were carried between 01-01-2009 to 31-12-2009. Table 3.7 shows the mean monthly wind speed, wind direction and temperature at Nyiru mast.

Month	**Mean Speed at 46 m (m/s)**	**Mean wind direction at 39 m (degrees)**	**Mean temperature (°C)**
January	10.55	127.85	29.1
February	11.38	127.31	29.7
March	10.92	124.36	30.9
April	9.75	121.74	30.0
May	9.74	121.76	29.3
June	10.86	115.51	28.4
July	11.77	112.85	missing
August	12.17	113.25	missing
September	11.63	118.57	missing
October	10.65	120.81	missing
November	10.67	122.19	28.9
December	8.93	133.51	28.5

Table 3.7 Mean monthly wind speed, wind direction and temperature at Nyiru mast.

3.6.2.3 Sirima Mast

Wind direction data recorded between17th April to 31st December 2009 at 40 m was erroneous. During this period wind direction data recorded by 20 m wind vane was used to replace the doubtful data at 40 m height. The measured mean annual wind speed for Sirima at 38 m is 11.10 m/s while the mean wind direction at 40 m is 110.73°. The mean annual temperature is 28.0°C. These measurements were carried between 01-01-2009 to 31-12-2009. Table 3.8 below shows the mean monthly wind speed, wind direction and temperature at Nyiru mast.

Month	Mean Speed at 46 m (m/s)	Mean wind direction at 39 m (degrees)	Mean temperature (°C)
January	10.80	118.18	28.0
February	11.87	117.08	28.7
March	11.26	115.47	30.0
April	10.15	119.81	29.1
May	10.11	116.84	28.5
June	11.24	107.25	27.7
July	11.97	94.49	26.3
August	12.42	94.94	26.6
September	11.94	94.99	28.1
October	11.11	105.70	27.6
November	11.15	118.44	28.0
December	9.31	126.06	27.6

Table 3.8 Mean monthly wind speed, wind direction and temperature at Sirima mast

Figure 3.7 and 3.8 show the monthly mean wind speed variation and air temperature (measured 1.5 m above ground) for Kalkumpei, Nyiru and Sirima mast locations respectively. The period between June and October has the highest mean wind speed hence the prime period for electricity generation. The windiest month is August with mean wind speed varying between 11.86 m/s and 12.42 m/s for the Kalkumpei, Nyiru and Sirima mast locations. December records the least mean wind speed varying between 8.79 m/s and 9.31 m/s for the 3 mast locations.

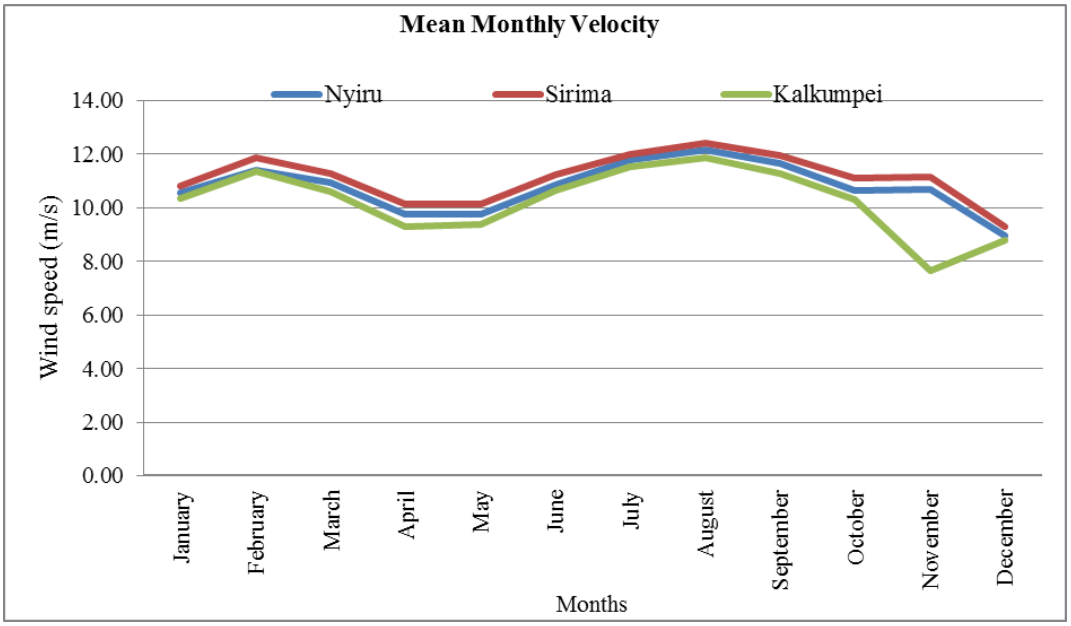

Figure 3.7 Mean monthly wind speed variation for Kalkumpei, Nyiru and Sirima mast locations.

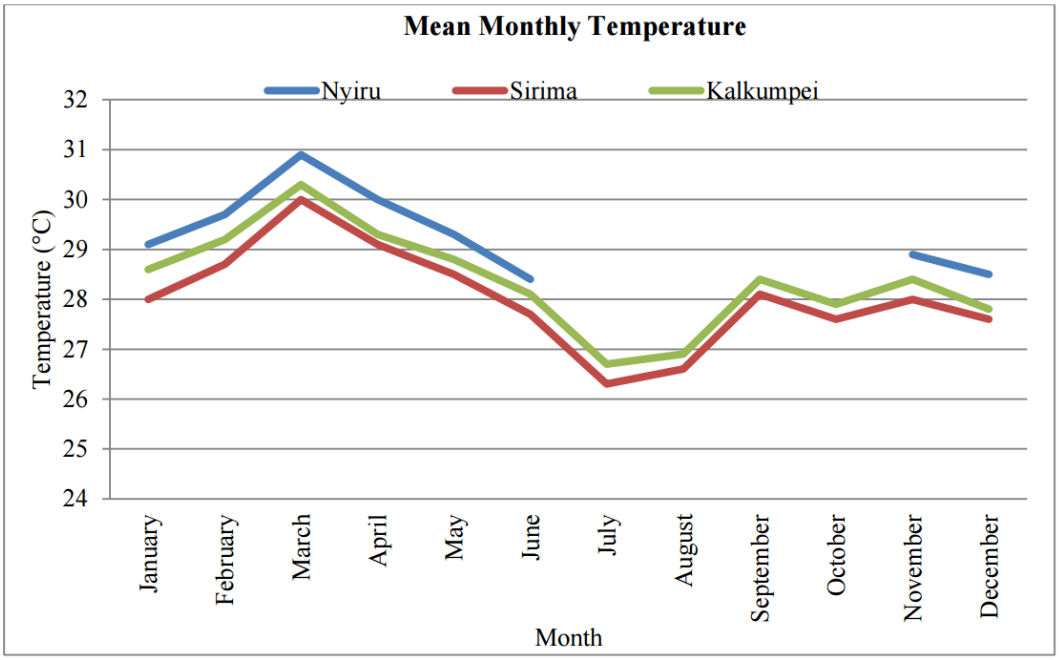

Figure 3.8 Mean monthly temperature (measured 1.5 m above ground) variation at elevated heights for Kalkumpei, Nyiru and Sirima mast locations.

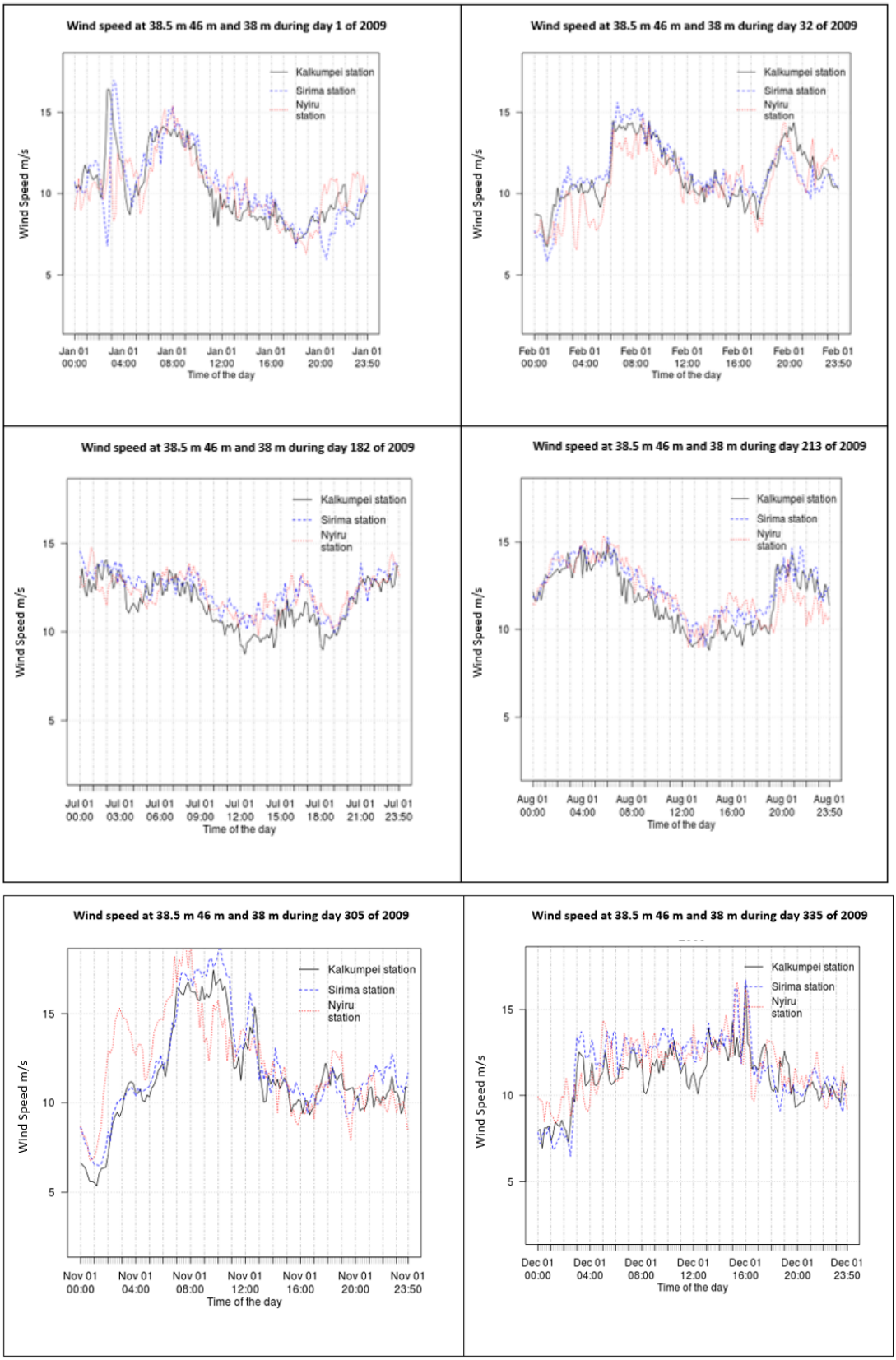

Figure 3.9 Diurnal variation in wind speed at Lake Turkana wind farm site (all observations are in Kenyan local time)

Table 3.9 shows Annual Mean Absolute Error (MAE), CC and RMSE while Table 3.10 shows monthly MAE, CC and RMSE between the 3 masts for wind speed. The statistics presented in these two tables confirm that the 3 mast locations are within the same wind speed climatology. This further corroborates the hypothesis that the wind farm is located within an area of fairly consistent wind climatology.

Statistics/Mast locations	**Kalkumpei vs Nyiru**		**Kalkumpei vs Sirima**		**Nyiru vs Sirima**	
	38.5 m	**46 m**	**38.5 m**	**38 m**	**46 m**	**38 m**
MAE (m/s)	1.09		0.97		1.01	
CC	0.825		0.906		0.851	
RMSE (m/s)	1.453		1.229		1.358	

Table 3.9 Annual MAE, RMSE and CC for wind speed between the three mast locations

Month/Mast	**Kalkumpei vs Nyiru**			**Kalkumpei vs Sirima**			**Nyiru vs Sirima**		
	38.5 m	**46 m**		**38.5 m**	**38 m**		**46 m**	**38 m**	
	MAE (m/s)	**RMSE (m/s)**	**CC**	**MAE (m/s)**	**RMSE (m/s)**	**CC**	**MAE (m/s)**	**RMSE (m/s)**	**CC**
January	1.17	1.53	0.75	0.97	1.22	0.87	1.15	1.48	0.87
February	1.32	1.77	0.72	0.98	1.26	0.89	1.34	1.74	0.89
March	1.14	1.50	0.77	1.00	1.24	0.89	1.11	1.43	0.89
April	1.16	1.50	0.85	1.08	1.34	0.92	1.00	1.34	0.92
May	1.16	1.56	0.82	1.02	1.30	0.91	0.99	1.36	0.91
June	1.05	1.41	0.82	0.90	1.15	0.89	0.96	1.35	0.89
July	0.83	1.04	0.84	0.74	0.93	0.89	0.73	0.98	0.89
August	0.87	1.10	0.79	0.78	0.98	0.87	0.78	1.02	0.87
September	0.94	1.20	0.76	0.86	1.09	0.85	0.85	1.15	0.85
October	1.14	1.48	0.79	1.02	1.28	0.89	1.02	1.35	0.89
November	1.17	1.54	0.64	1.26	1.56	0.77	1.04	1.36	0.77
December	1.18	1.61	0.84	0.98	1.24	0.92	1.13	1.53	0.92

Table 3.10 Monthly MAE, RMSE and CC for wind speed between the three mast locations

It is observed in Table 3.10 that during the month of July lowest MAE (0.83 m/s) and RMSE (1.04 m/s) are observed between Kalkumpei and Nyriu, MAE (0.74 m/s) and RMSE (0.93 m/s) between Kalkumpei and Sirima and MAE (0.73 m/s) and RMSE (0.98 m/s) between Nyriu and Sirima. The CC are not the best but very close to the best in the month of July for the three masts. It is concluded that the month of July

contains the best observation data particularly useful for validation of WSDSA and therefore it is used in this research.

3.7 LIDAR Wind Measurements

A major part of material presented in this section is taken from Sutton et al. (2010). LIDAR measured wind speed and direction from 11th July to 24th July 2009 are used in this study.

3.7.1 Scanning Strategy

The radial wind field to a distance of approximately 10 km from the LIDAR was retrieved using a series of 360° horizontal (azimuth) scans. Each scan took approximately 10 minutes to complete providing data consistent with the averaging period of the masts' anemometers. The scans were configured to scan between -1 degree and 1 degree in vertical elevation to achieve radial wind velocity data above and below the 45 m height across the landscape. Data across 10 or 11 horizontal layers were typically used to produce terrain-following wind speed maps. A direct comparison was required between the LIDAR and mast measurements; therefore, the scanning pattern of LIDAR was configured to complete each set of scans in approximately 10 minutes without considering the optimization of the averaging period.

Figure 3.10 shows the location of the closely spaced laser beams (brown lines) along a horizontal plane radiating from the LIDAR. A LIDAR scanning rate of 6~8-degree azimuth per second was typically used to achieve the required data averaging period. The Lidar performance is improved by accumulating the signal from many Lidar shots for each range gate. The resulting range uncertainty is decreased by a factor of $(N)^{-1/2}$, where N is the number of shots. For an accumulation of 100 pulses (July period) the range uncertainty is reduced to 4.5 m.

Radial wind speed estimates were recovered from each beam at a radial spatial resolution (range gates) of 150 m. The LIDAR is effectively "blind" for the first 500 m in range along the laser beam's path due to electro-optical constraints within the receiver. The "blind" area is indicated by the grey region surrounding the laser measurement location.

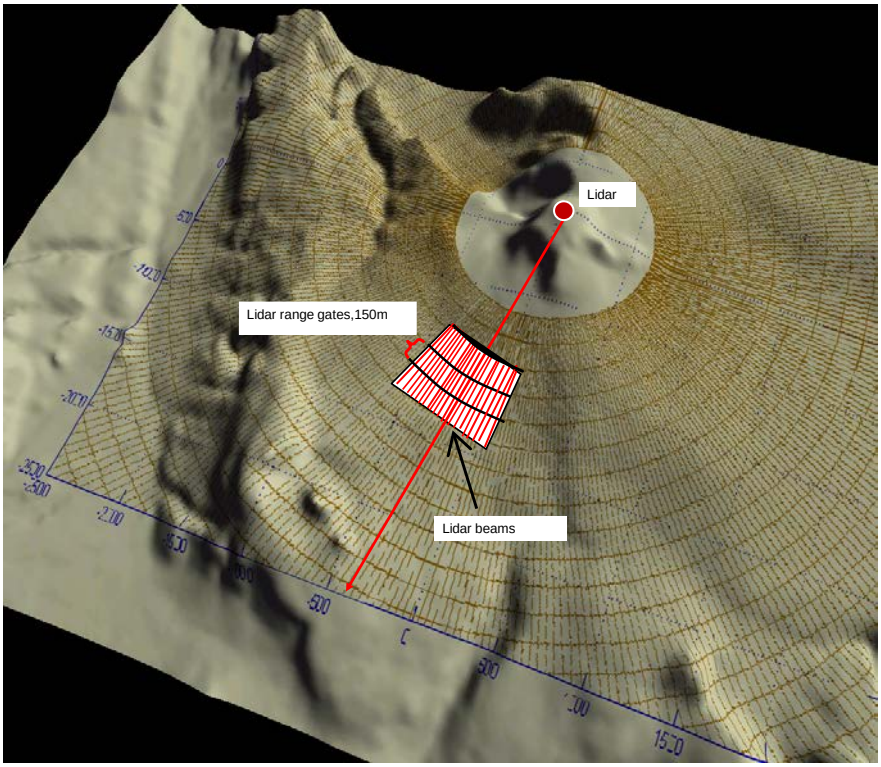

Figure 3.10 LIDAR scanning pattern in the South Western Sector of the study site (Sutton et al., 2010)

Figure 3.11 is a 15-degree sector representation of the scan in the vicinity of the Sirima mast. Data collected within the 15-degree sectors of all layers of the 360 degree horizontal scans are used to recover the full wind vector at each range gate. Figure 3.11 also shows two layers of the horizontal scanning planes within a 15-degree sector. It can be seen that the two horizontal scanning planes lie either side (above and below) of the anemometer. The positioning of the vertical scans permits the use of interpolation techniques for deriving the 45 m terrain- following wind speed maps.

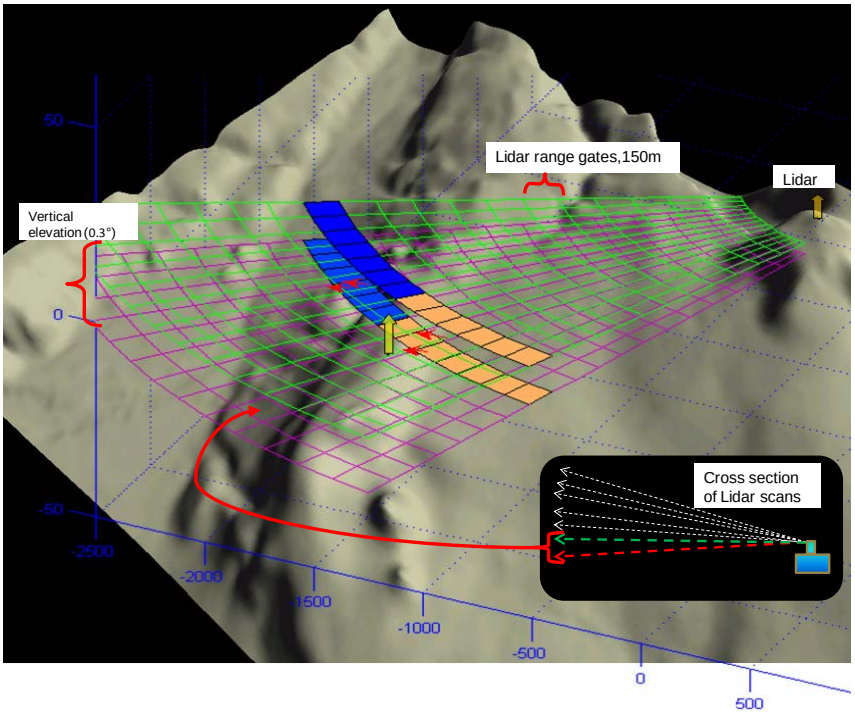

Figure 3.11 Two LIDAR scanning planes within a 15-degree horizontal sector (Sutton et al., 2010)

3.7.2 Filtering Poor Quality data

Prior to the analysis, data filtering is performed. The first step in data filtering is the removal of data with signal-to-noise ratio (SNR) below -10 db. The reason for this step is that the accuracy of the LIDAR measurements decreases with increasing range due to decreasing SNR. The second filtering step involves comparing a sudden rise (jump) in radial velocity compared with previous and following data points. The data point is not considered for analysis if the jump recorded in any direction is more than a threshold value of 5 m/s. The threshold value must be subjectively determined because of the individual variations associated with different datasets and is generally used to separate the noise from the data. The third step considers removing hard target returns i.e., when the laser pulse hits an opaque object such as terrain. The hard target returns were removed on the basis of high SNR (> 20 dB).

3.7.3 Wind Vector Retrieval

An advanced LIDAR data volume processing technique (ALVPT) developed by the Remote Sensing and Satellite Research Group (RSSRG), based at Curtin University in Perth, Western Australia was used to retrieve the wind vectors. The technique categorises the available LIDAR data into several concentric conical layers and

subsequently subdivides each layer into many small analysis volumes (Figure 3.12). The fundamental theory of this technique was derived from the general Doppler radar data processing scheme called VVP. This type of scheme is considered to be a more straightforward way of resolving wind velocity directly from the LIDAR radial velocity data (Boccippio, 1995; Crook et al.; Hannon et al., 2008; Koscielny et al., 1982).

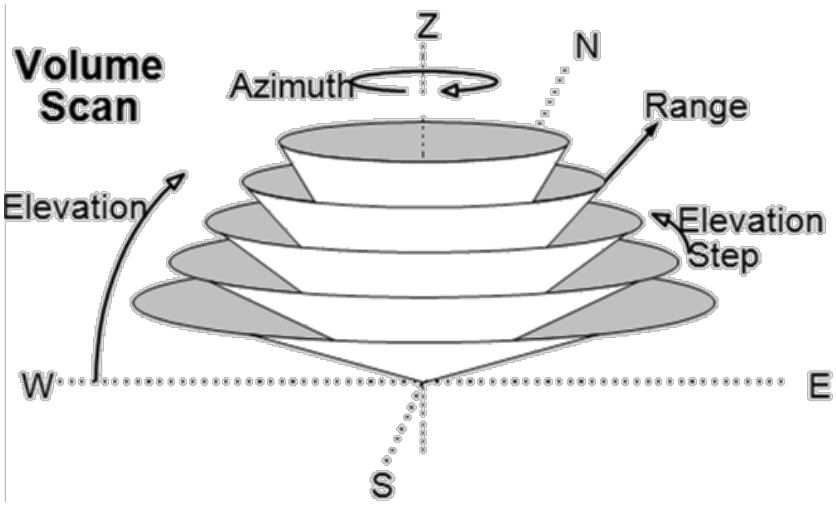

Figure 3.12 Basics of the technique developed at RSSRG

In each analysis volume, an optimised wind vector is obtained after filtering through all data points included in the volume (Figure 3.12). A constraint that uses the VAD retrieved mean wind is applied in order to control the instability in the processing, especially at the perpendicular area (orthogonal to the mean wind direction, i.e. at the north-east and southwest direction from the LIDAR site). After each layer of the wind speed values is retrieved, the processing algorithm interpolates these values to 45 m above ground level to permit the comparison with the mast instrumentation.

3.7.4 Volume Velocity Processing Algorithm

The advanced VVP algorithm, is an improved version based on the traditional VVP analysis scheme (Waldteufel and Corbin, 1979). It has improvements in retrieval stability and solution quality control. The direct measurements of wind by Doppler LIDAR are restricted to the radial component of the wind. To resolve the tangential components, LIDAR beam measurements of the radial component of the wind are used from other directions. By taking adjacent or lateral radial velocity measurements

at defined range gates, the VVP algorithm is then used to estimate wind vector that represents the localised mean wind at the specified range gate location.

The VVP algorithm firstly groups the obtained LIDAR data from the volume of scans into small conical analysis volume elements. Each of these volumes uses 10 to 20 radial velocity data points, depending on the size of the conical analysis volume. As more radial velocity data points are included in the analysis volume, the larger the analysis volume needs to be. This would mean a reduction in the retrieved wind field resolution. On the other hand, with less radial velocity data points, the retrieval of the wind becomes ill-conditioned and unstable, which leads to errors in the retrieved wind field. It is therefore important to understand the trade-off between these two factors in order to produce a quality controlled retrieval.

The size of the analysis volume element used in the field investigation of the Lake Turkana wind field is defined by the LIDAR scanning mode with $\Delta\varphi=10°$, $\Delta r=150$ m and $\Delta\alpha=0.4°$ (Figure 3.13). For the given analysis volume element, the VVP algorithm automatically loops through all analysis volumes, applying a least squares minimization scheme to obtain solutions

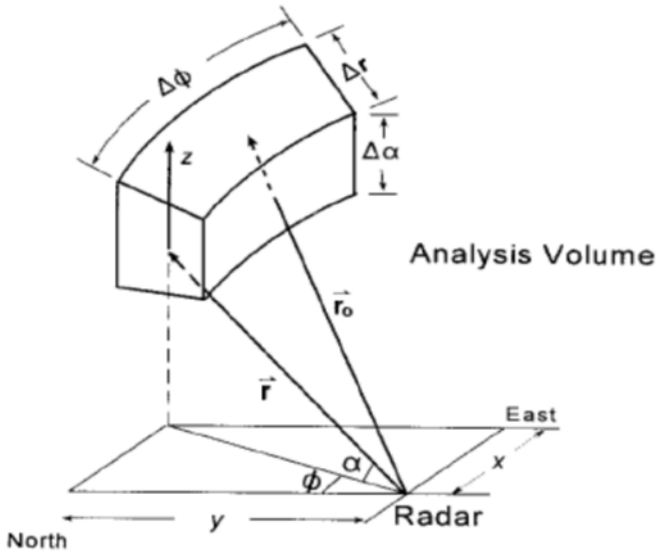

Figure 3.13 Unit conical analysis volume for CDL at Lake Turkana

Once the solutions are obtained, a quality check is performed to filter out solutions that are not considered to be reasonable. The solutions retrieved are then registered at the centre of each volume element and further gridded to a rectangular mesh of 150 m

x 150 m resolution. While the VVP algorithm requires more processing time than the tradition VAD approach, it produces the more detailed output required for this project.

3.7.5 Generation of Wind Map

With the acquired layers of rectangular meshed wind velocity solutions, it is possible to generate a 45 m terrain-following wind map. At each grid point, there are normally five velocity values at different heights that can be used to interpolate speeds to the 45 m level. However, due to the terrain-blocking at lower levels of the LIDAR scans and noise caused by atmospheric conditions (possibly wind-generated surface aerosol), the required scan levels always may not be available. To overcome this problem, three different approaches were used to complete the interpolation:

a) Interpolation method: At the grid point where there are at least two available LIDAR measurements at different heights and the 45 m level is at the level in between these measurements, the wind profile power law fit (equation 2.3) (with exponent value of 0.143 under a neutral atmospheric condition assumption) is used to obtain the wind speed at the 45 m level.

b) Interpolation method: At the grid point where there are at least two available LIDAR measurements at different heights and the 45 m level is below these measurements, the linear interpolation is implemented to a reference height (between heights of these available data). The 45 m level wind speed is then obtained applying the theoretical wind power law (with the same 0.143 exponent value) under a neutral atmospheric condition assumption.

c) Extrapolation method: At the grid point where there is only one available measurement along the vertical, the 45 m level is simply obtained by applying the wind profile power law with the same exponent as above.

LIDAR analysed wind speeds are obtained for several different layers (Figure 3.14, labelled in green lines at different elevations). Each of these layers of wind speed is retrieved by algorithms provided with LIDAR observations two or three layers of PPI scans (labelled in red lines, Figure 3.15). Each layer of derived wind speed is then interpolated to the 150 m by 150 m horizontal grid. These layers of wind speed on grid mesh are eventually interpolated or extrapolated vertically to the required level for

producing terrain following wind map and or comparing with the mast measurements as described above.

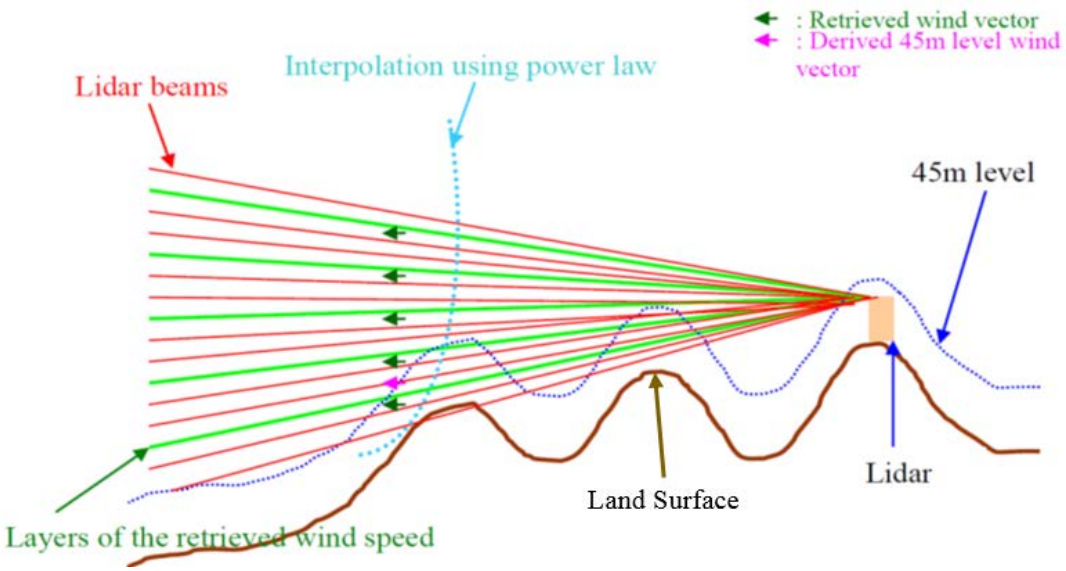

Figure 3.14 Schematic drawing of the interpolation of the LIDAR derived wind speed applied (Sutton et al., 2010)

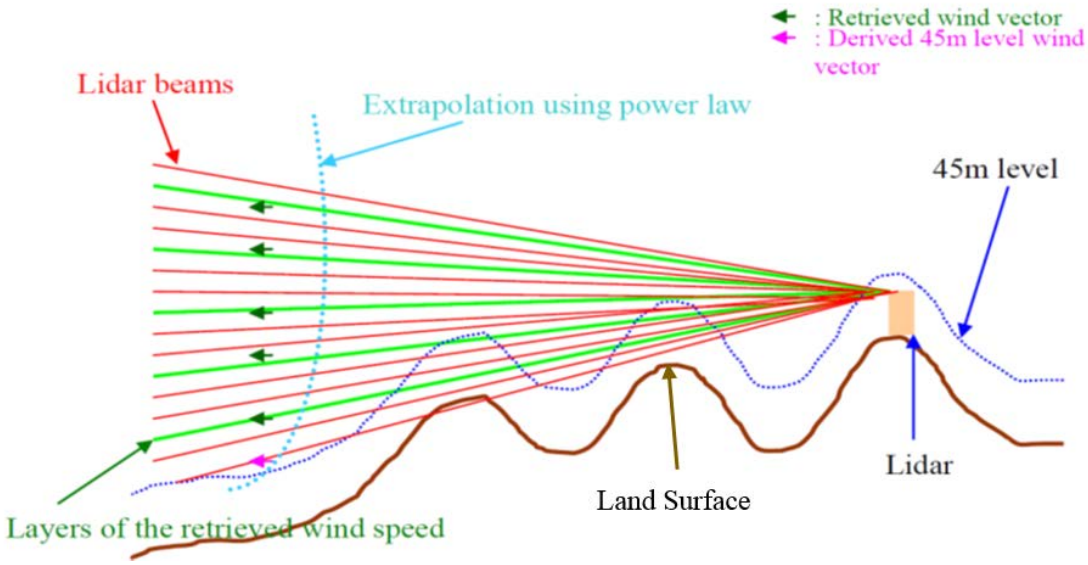

Figure 3.15 Schematic drawing of the extrapolation of the LIDAR derived wind speed applied (Sutton et al., 2010)

3.8 LIDAR Measured Wind Characteristics

The LIDAR analysed wind speed is compared to masts measurements at three locations from 11th to 24th of July 2009 after removal of poor quality LIDAR data (section 3.7.2). Each LIDAR scanning volume is composed of several 360º PPI scans, which approximately take 9~10 minutes duration, ranging from -1º to 1º elevations.

These analysed time series of wind speed values are compared to the mast 10 minute averaged measurements. It is shown in Table 3.11 that the difference between the two means (mast and LIDAR 45 m level wind speed) are small and the standard deviations from the mean in both instruments are in close agreement. The standard deviation is the time series of wind speed deviation of each instrument to its own mean over 10-minute interval. It represents the degree of variability of the time series wind speed data.

Mast locations	**Height**	**Mean (m/s)**	**Standard Deviation (m/s)**	**RMSE (m/s)**	**CC**
Kalkumpei	Mast (38 m)	11.03	1.90	0.93	0.9
	LIDAR (45 m)	10.5	1.65		
Nyiru	Mast (46 m)	11.2	1.92	1.05	0.84
	LIDAR (45 m)	11.19	1.79		
Sirima	Mast (38 m)	11.44	1.71	1.14	0.86
	LIDAR (45 m)	10.85	1.72		

Table 3.11 Wind speed statistics between the CDL and mast 10-minute average winds for a period from11th to 24th of July 2009 at the Lake Turkana site, Kenya

The comparison of wind speed variations over a two-week period time of *in situ* mast measurements and the CDL observations are presented in Figure 3.16. It can be seen that the LIDAR and mast measurements are in close alignment with the mean wind differences between two instruments less than 0.5 m/s.

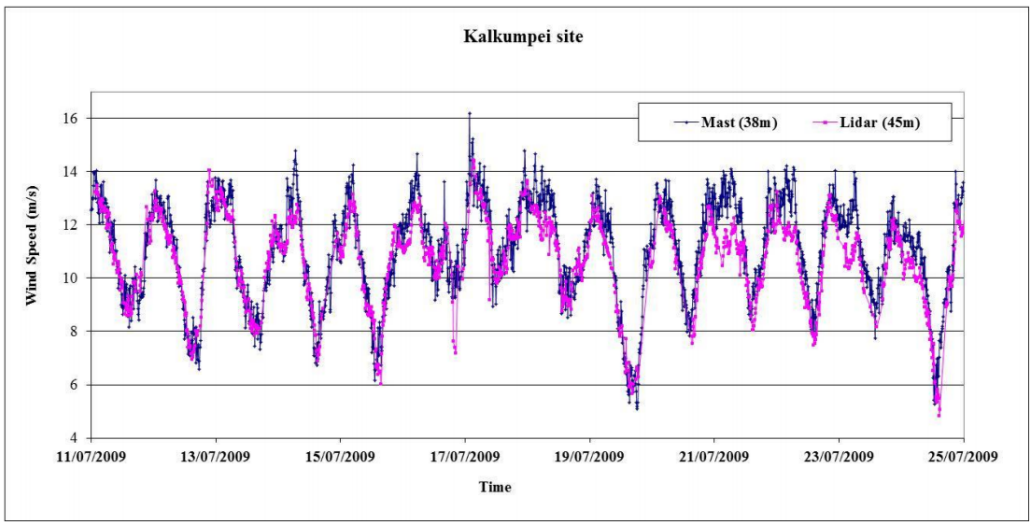

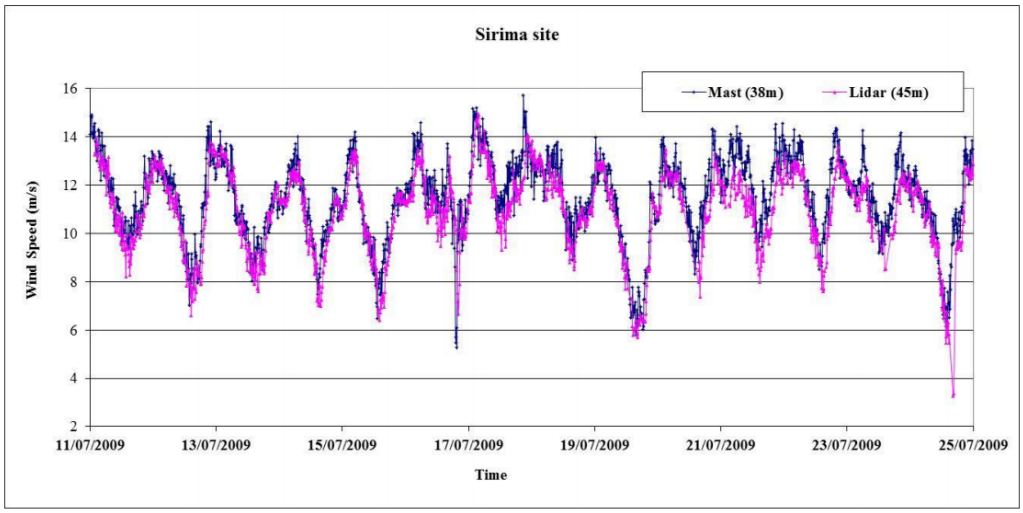

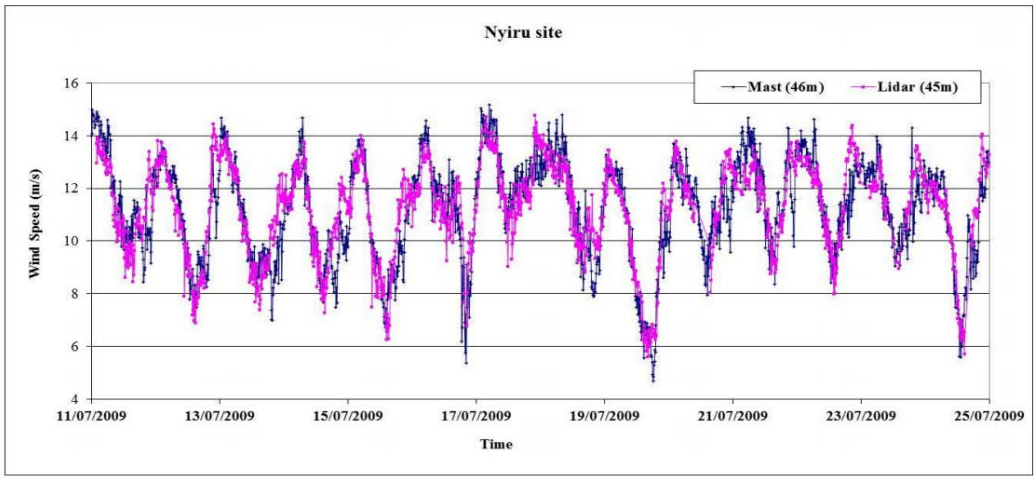

Figure 3.16 Compassion of wind speed between the mast measurements (10 minute averages) and the CDL observations for the period from 11th to 24th of July 2009 at Lake Turkana site, Kenya

3.8.1 CDL and Mast Observed Wind Speed Comparison Uncertainties

CDL and meteorological masts observe wind speeds using different technologies and their spatial and temporal dimensions may also be different. Kelley et al. (2007) stated the following key issues, comparing the relative accuracy of wind speeds derived from a pulsed Doppler Lidar, a SODAR and four levels of tower mounted sonic anemometers up to a height of 116 metres above ground:

- Sampling volume considerations- CDL and sonic anemometers have different sampling volume. Sonic anemometers assume that the wind vector is being sensed within a spherical volume of having a diameter of 46 cm or an estimated volume of 0.05 m^3. CDL in the study however, samples volume over an effective beam diameter of 8 cm rendering a physical volume of 0.23 m^3. The CDL in Lake Turkana has larger effective beam diameter of 120 cm therefore, differences in the size of the sampling volumes of the sonic anemometers employed by DER at Lake Turkana and 1.6 um Lidar will be more significant.
- Sampling time considerations- CDL employed at Lake Turkana averages wind speed roughly 9-10 minutes while masts average wind speed at 10 minutes. This is due to the scanning pattern used for sampling the 'volume' covering - 1 to 1 degree of elevation does not finish exactly within 10 minutes. Better comparison can be achieved if CDL is actually configured to stare at the mast point instrument during the time periods.
- Reliability of anemometer measurements- Instrument design, sensitivity, tower vibration etc. can influence the accuracy of the tower mounted cup anemometers The relationship between flow angle approach and variations in speed and direction biases adds a level of complication in the uncertainty analysis.

It may be reasonable to believe that these considerations contribute to the uncertainties in the wind speed measured at mast and that observed by the CDL at Lake Turkana site.

3.8.2 Terrain-Following Wind Speed Plots

The CDL derived wind speed data was output into a 20 km x 20 km grid domain and overlayed on a digital terrain model. The data was adjusted using equation 3.1 (Sutton et al., 2010) to remove bias arising from an uneven distribution of 10-minute sample periods within the data set. Lidar measurements were conducted over two periods; a 15-day period July 10 to 24, 2009 and a 5 week periods between September 28 and November 8, 2009. Regardless of the difference in the wind field characteristics between the July and October periods, there is also difference in the number of wind speed data observations available for producing averaged wind speed at each hour. As a result, the final averaged wind speed map produced can be affected due to the uneven number of data taken for averaging between day and night. The number of wind speed data available for averaging is relating to the measured data (radial velocity data) density after noise filtering and the instrument down time. These are the factors that results in uneven hourly distribution of the wind speed data.

$$\overline{V}_{(x,y)} = \frac{\left[\sum_{i}^{24} \frac{\left(\overline{V^i}_{p1} n^i_{p1} + \overline{V^i}_{p2} n^i_{p2}\right)}{n^i_{p1} + n^i_{p2}}\right]}{24} \tag{3.1}$$

where

$\overline{V}_{(x,y)}$ is the averaged wind speed at each grid point labelled by (x, y).

$\overline{V^i}_{p1}$ is the averaged wind speed at the ith hour during the first period of LIDAR measurements.

$\overline{V^i}_{p2}$ is the averaged wind speed at the ith hour during the second period of LIDAR measurements.

n^i_{p1} is the number of wind speed data at the ith hour during the first period of LIDAR measurements.

n^i_{p2} is the number of wind speed data at the ith hour during the second period of LIDAR measurements.

The resultant map covers a geographic area of 400 square kilometres and comprises approximately 18,000 data points along the 45 m height terrain- following plane. Figure 3.17 and Figure 3.18 contain two plots, the first being a 3D image of the wind field; the second providing the same information in 2D, enhanced with terrain-following vector fields.

The maps show that the 10-minute averaged wind speed on the relatively flat landscape to the east of the measurement domain approximately 6 m/sec. The average wind speed gradually increases as the flow moves west to approximately 10 m/sec near the LIDAR site. Maximum velocities occur on the higher ridges on the western boundary with wind speed reaching over 14 m/sec. Wind shadow effects from topography are also evident in the maps.

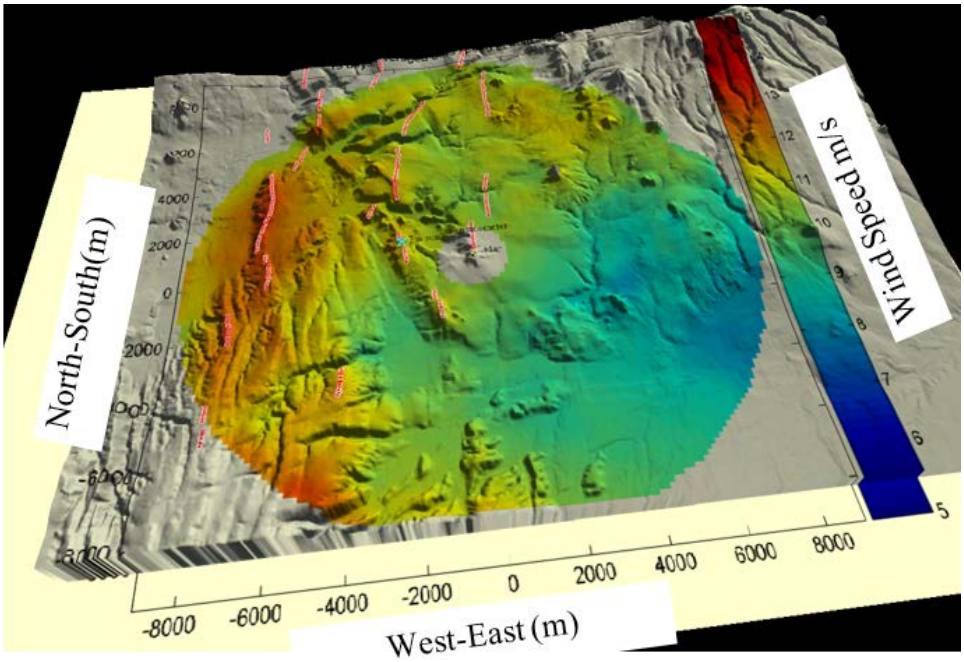

Figure 3.17 Three dimensional horizontal wind speed at Lake Turkana wind farm site (Sutton et al., 2010)

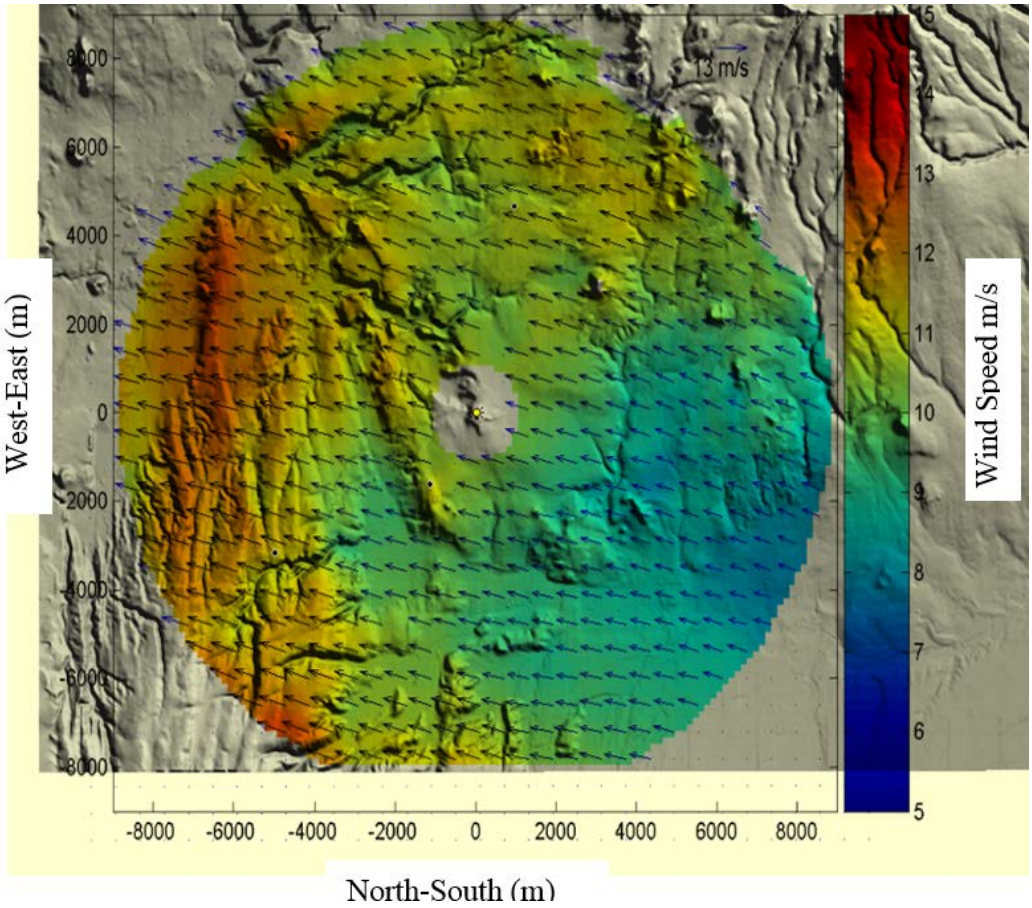

Figure 3.18 Two dimensional horizontal wind speed with terrain-following vector fields at Lake Turkana wind farm site (Sutton et al., 2010)

3.9 Summary

This chapter explains the complete 2009 measurement campaign at the Lake Turkana site, Kenya. It also describes the meteorological conditions onsite and the topography. It takes an in depth look into the conventional wind measurement instrumentation with the associated uncertainties. It illuminates the significance of the remote sensing strategy, in particular, the use of CDL for the purpose of resource assessment. Measurement of the uncertainties with CDL are also addressed. Since the region is a complex terrain accurate measurement and understanding of surface winds is necessary for accurate prediction. The choice of models and their understanding is necessary for these predictions and therefore diagnostic and prognostic models have been discussed. These models will be discussed in detail in chapters to follow.

This chapter further discusses the data recorded by three *in situ* instruments on the masts and also the CDL. These observations will be used for comparing with the

outputs of the numerical models. The *in situ* instruments on the masts have recorded data for the whole year (2009) while CDL provided data sets for a two-week period. The discrepancies in the data have also been pointed out.

It has been observed that the local winds are generally characterized by high annual mean wind speed with values over 10.3 m/s and relatively large diurnal variability. The mean diurnal cycle is characterized by stronger winds during night-time and early morning than during daytime. Nicholson (2015) explained that these strong winds in the lower atmosphere or the low level jet is due to nocturnal decoupling of the surface and boundary layers at Lake Turkana. The existence of highlands on either side of the jet may also contribute to the acceleration of the flow in the core of the jet due to katabatic wind resulting from cooling of slopes at night.

The ALVPT has been described and applied to CDL data. It is suggested that due to differences in vector averages of wind speed extracted from in CDL data and averages of wind speed from point measurements used by anemometers, the recorded wind speed may be different in both cases though each itself may be measuring correctly.

Excellent agreement exists between CDL data and *in situ* measurements. In the chapters to follow the CDL measurements will be compared with WRF modelled outputs at different locations. Finally, CDL derived winds will be assimilated into WRF to improve short term forecasting.

Chapter 4 Wind Forecasting (WRF) Model

4.1 Introduction

The aim of this study is to apply an optimised configuration of the WRF model to a unique wind farm site in East Africa. The intention is to achieve an accurate simulation and prediction of near-surface winds. Since current atmospheric models present a broad spectrum of configuration options and parameters, selecting the best configuration among these options has its own inherent challenges (Nossent et al., 2011). The importance of the sensitivity of a model to changes in its configuration settings has been emphasized by Hirabayashi et al. (2011). Various model configurations and parameter settings along with different initialization fields have been evaluated in this study. Modelling results are presented for a final optimised configuration.

WRF, developed by the NCAR (Skamarock et al., 2008) is a mesoscale model that is widely used by the international meteorological community, especially for short-term forecasting, due to its flexibility and robustness as a regional scale model (Carpenter et al., 2013). In this research, WRF version 3.6.1 has been used to conduct the simulations. It has the capability not only to run global simulations at spatial resolution of several kilometers but it may also be nested down to a few hundred meters Skamarock et al. (2008) describes numerous physical parameterization schemes available for microphysics, radiation (long wave and short wave), and clouds as well as boundary layer schemes including

- The surface layer (SL)
- The planetary boundary layer (PBL)
- A land surface model (LSM)

Such schemes interact non-linearly with each other and with the dynamical core of the model; and therefore it becomes challenging to optimise the model due to these complex relationships. Further, certain assumptions used in these schemes may result in an erroneous analysis (Awan et al., 2011), so caution is required. Besides physical parameterization schemes and unconfined empirical parameters within these schemes, there are other sources of errors in the numerical model. Such model errors include

the dependence on different numerical solvers, domain sizes, site location, initial and boundary conditions, grid resolution (both horizontally and vertically), and terrain and vegetation characteristics (Awan et al., 2011). Topography may also affect the climate by influencing the heat flux and the radiation reflected from the ground. In addition, the separation effects due to topographical features influence the wind speed and direction significantly. Since model accuracy is accomplished by comparing simulated and observed atmospheric conditions at the same time and observations are point recordings, while model simulations represent spatial means determined by a model's horizontal and vertical grid spacing (Hanna and Yang, 2001), differences are expected between observed and simulated conditions simply due to the differences of time and volume averages that each represents.

Many of the topographic features and atmospheric behaviours within complex terrain occur on a smaller spatial scale than the commonly used synoptic-scale forecasting models can simulate, resulting in limited near-surface model accuracy (Reid and Turner, 2001). However, higher resolution mesoscale models, such as the WRF are better suited for resolving the near-surface atmospheric behaviour in complex terrain (Jiménez et al., 2010).

Mesoscale models have been used in various types of wind regimes for studying energy applications, particularly when they are combined with the statistical tools or microscale models in short-term forecasting for wind farm energy production. They are helpful for power grid planning and for assessing potential sites for future wind farms. WRF has been used extensively in wind energy applications. Its efficiency could be improved further in short-term forecasting by avoiding its cold start and optimizing it through a WSDSA [see Chapter 5]. In addition, since model sensitivity studies with respect to near surface winds, have not been in vogue for meteorological studies (Yamadaa and Koikeb, 2010), this study may provide an attractive pathway for TSO. In conclusion, we demonstrate that, with *in situ* verification observations, appropriate optimisation for a specific site can lead to significant improvements in wind prediction.

It should be noted here that the meteorological mast at Kalkumpei will be designated as mast A, Sirima's as mast B and Nyriu's as mast C for simplicity in the sensitivity analysis that is employed.

4.2 WRF Model Description

[4]WRF is a numerical weather prediction and atmospheric simulation system designed for both research and operational applications. WRF is supported as a common tool for the university/research and operational communities to promote closer ties between them and to address the needs of both. The development of WRF has been a multi-agency effort to build a next-generation mesoscale forecast model and data assimilation system to advance the under- standing and prediction of mesoscale weather and accelerate the transfer of research advances into operations. The effort has been a collaborative one among the NCAR's Mesoscale and Microscale Meteorology (MMM) Division, the National Oceanic and Atmospheric Administration's (NOAA) NCEP and Earth System Research Laboratory (ESRL), the Department of Defence's Air Force Weather Agency (AFWA) and Naval Research Laboratory (NRL), the Center for Analysis and Prediction of Storms (CAPS) at the University of Oklahoma, and the Federal Aviation Administration (FAA), with the participation of university scientists (Skamarock et al., 2008).

The ARW dynamics solver integrates the compressible, non-hydrostatic Euler equations. The equations are cast in flux form using variables that have conservation properties, following the philosophy of Ooyama (1990). The equations are formulated using a terrain-following mass vertical coordinate (Laprise, 1992).

4.3 WRF Software

WRF basically comprises two major components WPS (WRF pre-processing system) and the WRF model itself. The inter-relationships in this modelling system is shown in Figure 4.1.

[4] It is declared that the description in this paragraph is used from Skamarock et al (2008).

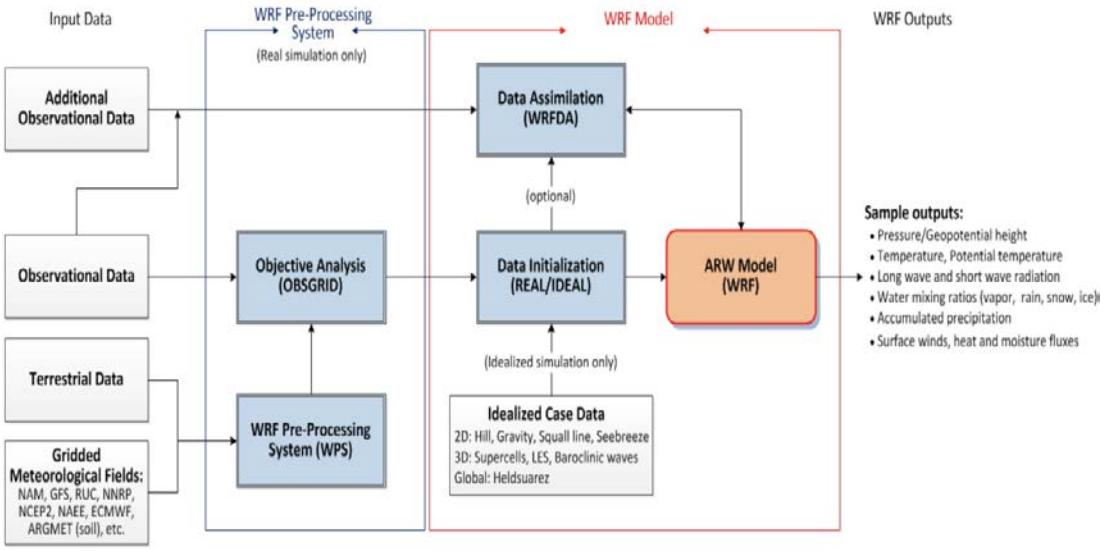

Figure 4.1 Detail of WRF Modelling and Processing System

The WRF has two pre-processing programs i.e. WPS and Objective Analysis or OBSGRID. The WPS is a set of programs that takes terrestrial and meteorological data and transforms them for input to the ARW pre-processor program for real-data cases while OBSGRID is used for adding more observations to the analysis.

The WRF model further has two cores the ARW and the NMM. For this study WRF was installed with the ARW core. The ARW solver is the key component of the modelling system, which is composed of several initialization programs for the idealized and real data simulations, and numerical integration programs. The detail of the processing system for the WRF modelling system is described below.

4.3.1 WPS

The WPS program pre-processes data for WRF. It defines the location and grid spacing of the desired model domain including nests. Nests are grids with increasing resolutions that can be placed within the coarse grids, either with or without feedback to the coarse grids. The WPS also interpolates static data (i.e., terrain, landuse, soil types) to the desired grid spacing. The model domains are defined and static geographical data is interpolated to the grids through GEOGRID program of WPS system. It should be noted that static data is available in different resolutions and higher resolution data will be ineffective in a coarse grid resolution. The pre-existing meteorological initialization fields from another model or data are horizontally interpolated to model domain through two programs, UNGRIB and METGRID which

are also part of the WPS system. Data available from other models is usually large therefore it is compressed into GRIB (General Regularly Distributed Information in Binary form) format. The UNGRIB program extracts meteorological fields from GRIB-formatted files and degribbs them. Degribbing is the process is the process of unfolding GRIB formatted data sets and writing them into an intermediate format. The METGRID program horizontally interpolates these fields to the model grids defined by GEOGRID. These processed files are then passed on to the REAL program which vertically interpolates the meteorological fields to WRF eta (η) levels. The REAL program creates the initial and boundary condition files for the WRF model itself. Once all of the input data is processed by WPS system and REAL program, the ARW solver is implemented. The connection between these programs is explained in Figure 4.2 and their complete description is given from section 4.3.5 to 4.3.8.

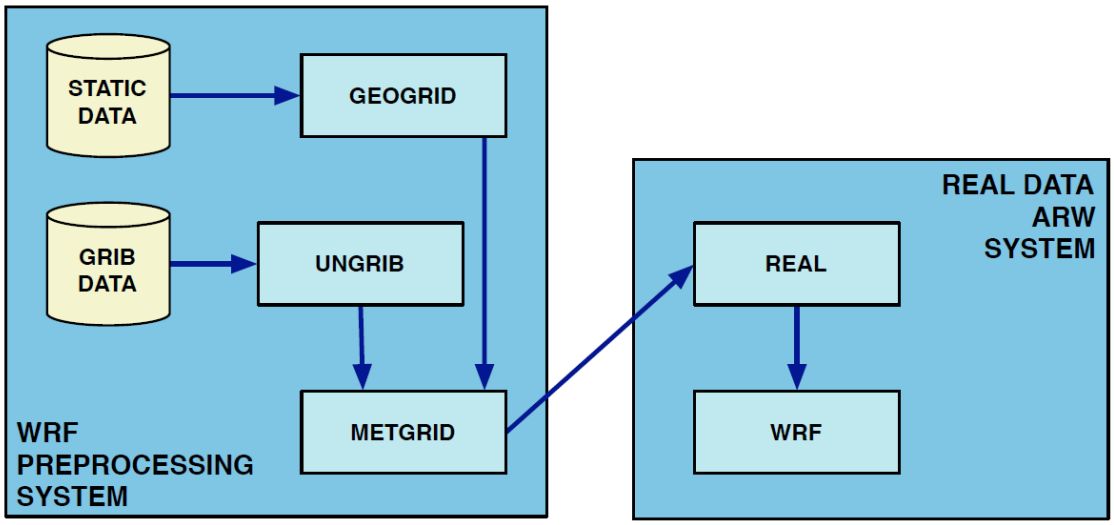

Figure 4.2 Schematic showing the data flow and program components in WPS, and how WPS feeds initial data to the ARW

4.3.1.1 Projections and Domain Resolution

Since the Earth is an ellipsoid and WRF computational domains are defined by rectangles in a plane, ARW is provided with 4 projection methods including Mercator, Lambert conformal, polar stereographic and latitude longitude projections. Mercator is suitable for low latitudes and hence is utilized in the current study. Each choice of map projection and associated parameters distorts distances at a given point on the globe differently. Geographic grid distance in WRF at a point is given by

$$\Delta x_{geographical} = \Delta x_{nominal}/m \quad (4.1)$$

where m is a map scale factor. Maximum stable time step in WRF is determined by geographic grid distance, not nominal (i.e., NAMELIST) grid distance. How the domains are arranged in WRF-ARW core is shown in Figure 4.3.

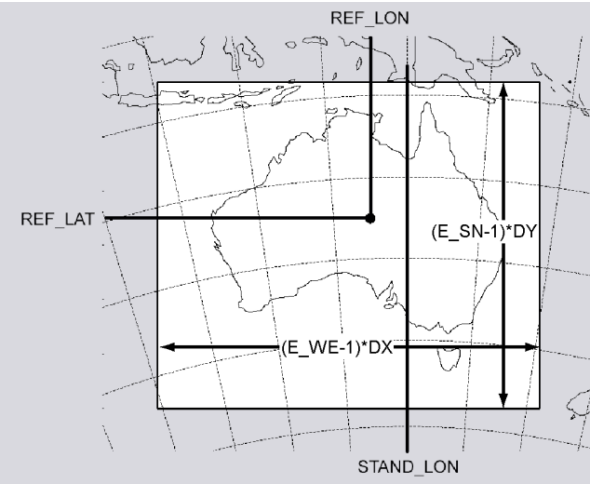

Figure 4.3 Parameters for defining domains in WRF (a) E_WE and E_SN is the number of velocity points in west-east and south-north direction (b) DX and DY are grid distances where map factor = 1 (c) REF_LAT, REF_LON: The (lat, lon) location of a known location in the domain(d) STAND_LON is the meridian parallel to y-axis

The spatial resolution (or grid spacing) is an important parameter that has a large influence on the model execution time. Indeed, dividing the grid spacing by two implies four times more cells but also divides the simulation time-step by two, which in the end multiplies the computing time by about 8.

Skamarock (2004) showed that the kinetic energy spectrum of a mesoscale model with a grid spacing "Δx" matches well with reality over wavelengths of 7 Δx but rapidly deteriorates below this limit. This means that features smaller than about 6 to 7 times the grid spacing (called the "effective resolution") are not adequately resolved. So a 10-point grid (10 times grid resolution) is too small compared to this effective resolution. Consequently, a balance must be found between grid size, resolution and computing time.

4.3.2 Nesting

A nested domain is an area wholly contained within its parent domain. It receives information from its parent, and it may also feed information back to its parent. A

nested domain has exactly one parent while a domain may have one or more children. Nesting is important because

- Large areas of high resolution produce model executions that are expensive.
- Lateral boundary conditions (LBC) from other sources are not adequate in time (less frequent) and space (may lack of vertical resolution), and may not be consistent with the WRF model.
- There are no boundary conditions for microphysical variables and vertical motion. Consider using the parent domain as a provider of LBCs for the nest.

The disadvantages of nesting however include:

- Nesting uses more memory.
- Requires nest input information (esp. for chem).
- Generates lateral boundaries on multiple domains.
- Solutions may not be smooth across nested domain boundaries.

The parent grid ratio determines the nominal grid spacing for a nest in relation to the grid spacing of its parent and is explained in Figure 4.4.

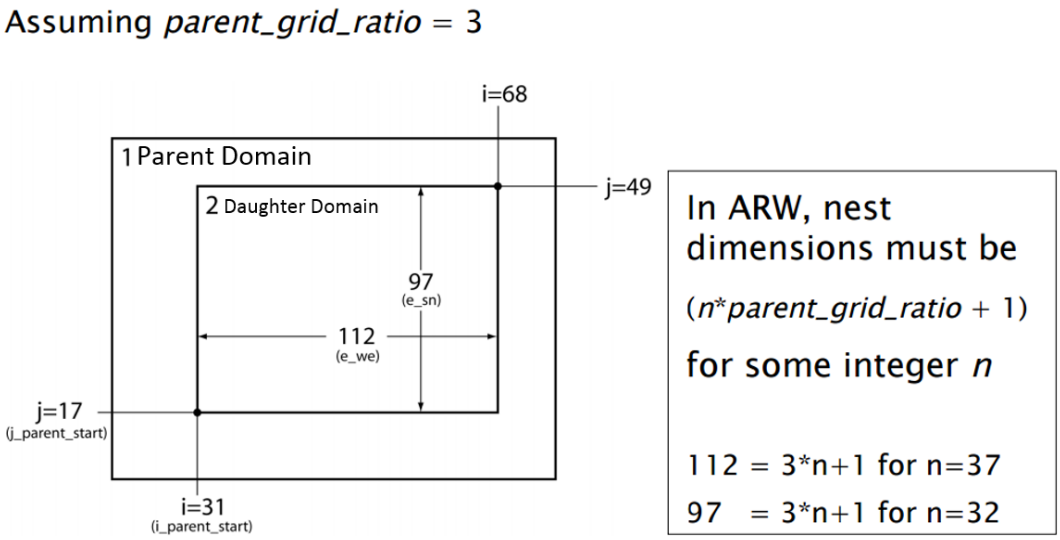

Figure 4.4 Formula for placement of nest in ARW Domain 2 has boundaries shown by indexes I and j. So, Domain 2 is of size 37 by 32 in the coordinates of the parent domain. It is nested into a sub-grid that is 112 by 97 which is the “daughter

The nests are arranged having a minimum distance equal to the product of inflow velocity and time step. The minimum distance should be four grid cells between the

nest and parent boundary, while it is recommended to use 1/3rd of coarse grid surrounding each side of the nest. The magnitude of time step (in seconds) should be prescribed at least 6 times the magnitude of coarsest grid distance (in kilometres). The size of the inner grids should be small to increase the speed of simulation.

4.3.2.1 One Way Nesting Its Restrictions and Applications

Two separate one-way nested options are supported by WRF. In the first option, one-way nesting is defined as a finer-grid resolution run, performed as a subsequent run after the coarser-grid-resolution run, where the NDOWN program is run in-between the two simulations. The initial and lateral boundary conditions for this finer-grid run are obtained from the coarse grid run, with input from higher resolution terrestrial fields (e.g. terrain, landuse, etc.), and masked surface fields (such as soil temperature and moisture). The program that performs this task is NDOWN.EXE. The one-way nesting is turned on by selecting the feedback option to "0".

The advantage of this method is that the nest's boundary conditions are updated frequently. The disadvantage, however, includes the solutions in the nest and parent may drift apart[5] and that is why this option is avoided in the current study.

In the second option, one-way nested simulations are performed by the running nest concurrently with the parent domain.

[5] http://ruc.noaa.gov/wrf/WG11/wrf_tutorial_2012_brazil/WRF_nesting.pdf

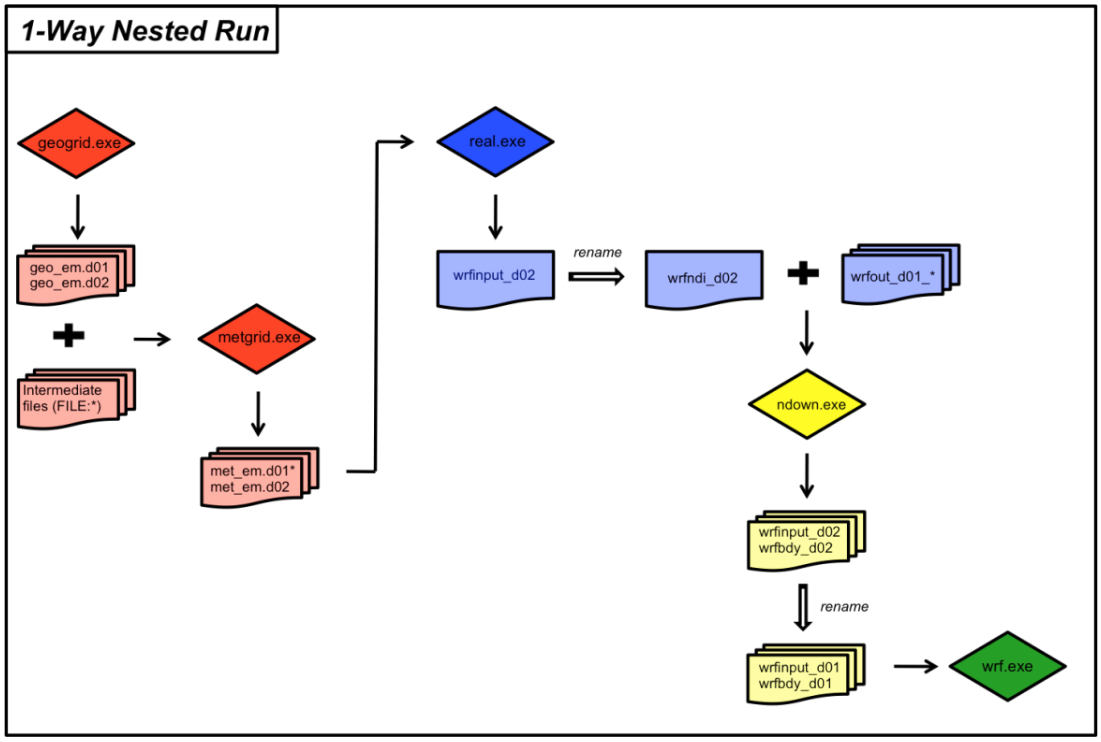

Figure 4.5 Illustration of one-way nesting procedure in WRF (option 1)

4.3.2.2 Two-Way Nesting its Restrictions and Applications

A two-way nested run is a WRF execution in which multiple domains at different grid resolutions are run simultaneously and communicate with each other: The coarser domain provides boundary values for the nest, and the nest feeds its calculation back to the coarser domain. The model can handle multiple domains at the same nested level (no overlapping nest), and multiply nested levels (telescoping).

Two-way nesting can either be implemented with a single or two input files. Running with the single file has the advantage that the nested domain may initiate at a different time. The disadvantage is that the nested domains may not benefit from the higher resolution static fields. All static and meteorological data are interpolated from coarse resolution to the nested grid value and no input is needed for the nested domains. The program flow for this case is shown in Figure 4.6.

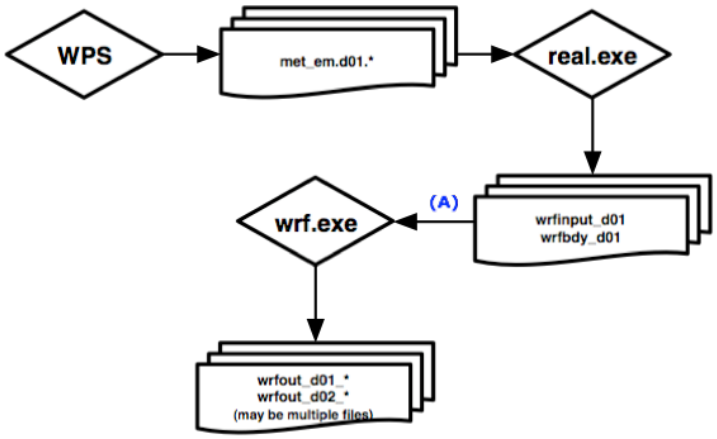

Figure 4.6 Illustration of two-way nested execution with one input file

The procedure for a two-way nested execution with two nested files is different and here one can either chose to use all the meteorological and static data from nested domains as input, or use only the static data for nested domains as input. The former method is however recommended[6] and is therefore utilized in this study. The program flow for this method is illustrated in Figure 4.7.

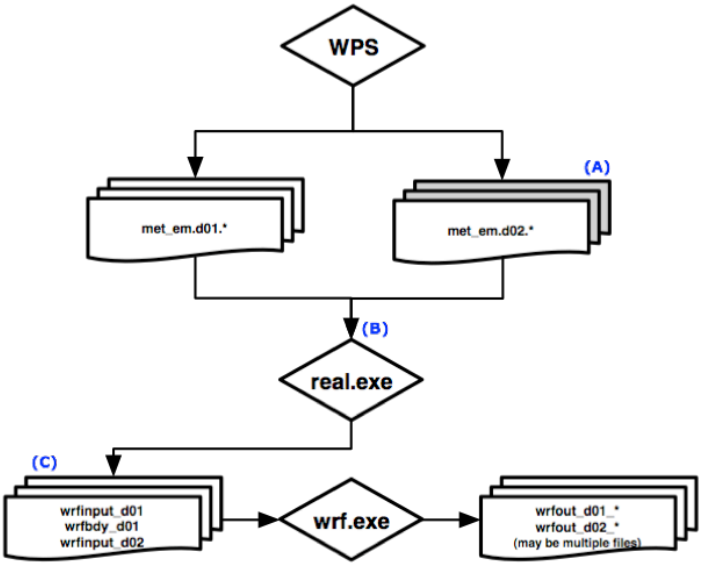

Figure 4.7 Illustration of two-way nested execution with two input files. (A) WPS can be set up to generate multiple met_em. d02. * files for the nested domain, but only the initial time is required. (C) The nested domain will always acquire its boundary conditions from the coarse domain, so the file wrfbdy_d02 will not be created.

[6] http://www2.mmm.ucar.edu/wrf/OnLineTutorial/CASES/NestRuns/2way2inputs.htm

4.3.3 Terrestrial Data (Static Data)

These are time-invariant initialization fields and includes soil categories, land use category, terrain height, annual mean deep soil temperature, monthly vegetation fraction, monthly albedo, maximum snow albedo, and surface slope category. Global data sets for each of these fields are available in different resolutions of 30'', 2', 5', and 10' though various sources, and, because these data are time-invariant, they only need to be downloaded once. All of the available resolutions for the site of interest in Kenya have been downloaded from NCAR and have been used at different nested levels in this study. The resolution of these data used in the numerical experiments will be referred as "Geographic Resolution" from here onward. In addition, a few tests have been performed using the Digital Elevation Model (DEM) from the Advanced Spaceborne Thermal Emission and Reflection Radiometer (ASTER) data base.

By default, the geogrid program will interpolate land use categories from United States Geological Survey (USGS) 24-category data[7]. However, an alternative set of land use categories based on the Moderate Resolution Imaging Spectroradiometer (MODIS) land-cover classification of the International Geosphere-Biosphere Programme[8] and modified for the NOAH (**N**CEP-**O**regon State University-**A**ir Force-**H**ydrology Lab) land surface model is also possible. MODIS contains 20 categories of land use which are not a subset of 24 USGS categories.

4.3.4 Meteorological Initialization Fields (Dynamic Data)

WRF provides the option for obtaining meteorological initialization fields from different sources. The ERA-Interim data having a horizontal resolution of 70 km with 60 model levels and 6 hourly temporal resolution has been used to define the final analysis in the current research. The NCEP FNL (Final) Operational Global Analysis data on 1° by 1° grid prepared operationally every six hours, has been used for most of the experiments performed and for the test case in WA.

[7] http://www2.mmm.ucar.edu/wrf/users/download/get_sources_wps_geog.html

[8] http://www2.mmm.ucar.edu/wrf/users/docs/user_guide_V3/users_guide_chap3.htm#_Land_Use_and

4.3.5 GEOGRID

This program defines the simulation domains, and interpolates various terrestrial data sets to the model grids. It is controlled by the NAMELIST.WPS file and in addition to computing latitude and longitudes for every grid point; it interpolates soil categories, land use category, terrain height, annual mean deep soil temperature, monthly vegetation fraction, monthly albedo, maximum snow albedo, and slope category to the model grids. GEOGRID interpolates available resolution data sets onto the user's selected grid spacing. Therefore, if the model domain has a spatial resolution of 12 km, there is no benefit of selecting 30" over the 2' data since the higher details of the 30" will be smoothed out. On the other hand, if the horizontal resolution of the domain is a fine scale (e.g., 1 km or less), the static high resolution data is beneficial. If a nested higher resolution domain exists inside a coarser grid, different static resolution data sets can be used appropriately.

New and additional data sets may be interpolated to the simulation domain through the use of the table file, GEOGRID.TBL. This file defines each of the fields that will be produced by geogrid; it describes the interpolation methods to be used for a field, as well as the location on the file system where the data set for that field is located.

4.3.6 UNGRIB

The functions of this program is to read and degrib the data (GRIB files) from regional or global model, such as NCEP's NAM or GFS models and write it in an intermediate format to be read by the METGRID program. UNGRIB uses specific tables of codes called VTABLES to extract fields from GRIB files and writes them to an intermediate format. Various types of VTABLES are available and UNGRIB is capable of writing the output in three types of formats.

4.3.7 METGRID

The intermediate-format meteorological data that are extracted by the UNGRIB program onto the simulation domains defined by the GEOGRID program are horizontally interpolated by METGRID. The program REAL can then ingest this interpolated data from METGRID. Since the work of the METGRID program, like

that of the UNGRIB program, is time-dependent, METGRID is run every time a new simulation is initialized.

Control over how each meteorological field is interpolated is provided by the METGRID.TBL file. The METGRID.TBL file provides one section for each field, and within a section, it is possible to specify options such as the interpolation methods to be used the particular field, the field that acts as the mask to be used for masked interpolations, and the grid staggering (e.g., U, V in ARW; H, V in NMM to which a field is to be interpolated.

4.3.8 REAL

The output from WPS is passed to the REAL-data pre-processor in the ARW— program REAL— which generates initial and lateral boundary conditions. This program vertically interpolates the meteorological fields produced by metgrid.exe to the defined eta levels within WRF. The REAL program also generates the required input variables for WRF initialization and creates a base state for ARW. It also vertically interpolates the soil levels. It further initializes water and sea ice and creates a Land/Water mask. It has a special role during nesting (increase of WRF grid resolution) as it may read multiple input files from METGRID and creates an initialization file for each processed domain while it creates only a lateral boundary file for the coarsest domain in the case of two-way nesting.

4.3.9 ARW Solver

WRF ARW is a fully compressible Euler non-hydrostatic (with a hydrostatic option) model. The time integration employs a 3rd order Runge-Kutta scheme, with smaller time steps for the acoustic and gravity-wave modes. The spatial discretization in the horizontal and vertical may be selected anywhere between a 2nd and 6th order advection option (Skamarock et al., 2008). Figure 4.8 is a schematic representation of atmospheric processes simulated by WRF.

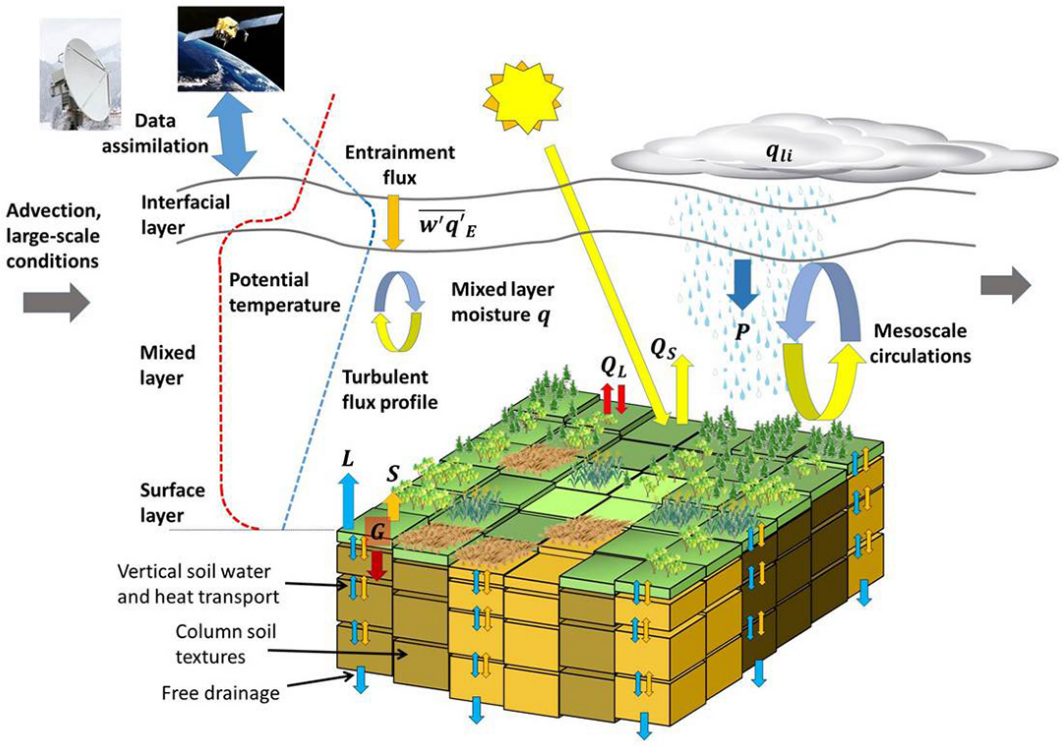

Figure 4.8 A schematic representation of atmospheric processes simulated by WRF[9]

WRF also offers turbulent mixing filters. These include a subgrid scale turbulence formulation in both coordinate and physical space. Divergence damping, external-mode filtering, vertically implicit acoustic step off-centering, with an explicit filter option are also available. The diffusion options select how the derivatives used to estimate diffusion are calculated. This is accomplished by selecting two parameters within WRF, the "diffusion" and "K" options. If the diffusion option is not turned off, the K option selects how the diffusivity coefficients are calculated. Since a PBL scheme is utilized throughout this study, the K option only evaluates the horizontal diffusion, as the vertical diffusion is performed by the PBL scheme.

WRF uses an Arakawa C-grid, which is a staggered grid (Figure 4.9). The mass variables are defined in the middle of the grid, while the wind components are defined on the edges of the grids. To compute the wind speeds for the centre of the grid (where the 10 m wind and 2 m temperature, etc. variables are defined), the U and V variables are interpolated onto the centre of the grid. The vertical grid also uses the staggered grid (Figure 4.9). The WRF model uses a terrain-following hydrostatic-pressure

[9] http://www.gauss-centre.eu/gauss-centre/EN/Projects/EnvironmentEnergy/2015/bauer_WRFCLIM.html?nn=1345670

vertical coordinate denoted by η (Figure 4.10). This coordinate is referred as the σ coordinate which is used in many hydrostatic atmospheric models. η varies from a value of 1 at the surface to 0 at the upper boundary of the model domain The coordinates are defined as:

$$\eta = \frac{(P_h - P_{ht})}{\mu} \tag{4.2}$$

where $\mu = P_{hs} - P_{ht}$ and P_{hs} is the hydrostatic pressure at the surface and P_{ht} is the hydrostatic pressure at the top of the model domain. The heights selected to be used can either be specified by giving the desired η levels or by selecting how many vertical levels the user requires. If the user does not specify the η levels, then an automated algorithm is used to select the placement of these levels. This algorithm will not place more than 7 levels within the lowest 2 km. Since the model output is reported on the η levels, the heights relative to ground level are calculated from the geopotential heights. The grid spacing of the vertical levels is also not constant; rather, it increases with height.

This vertical coordinate is also called a mass vertical coordinate. But μ(x, y) in equation 4.2 represents the mass per unit area within the column in the model domain at (x, y). The appropriate flux form variables are

$$V = \mu v = (U, V, W), \Omega = \mu\dot{\eta}, \Theta = \mu\theta \tag{4.3}$$

where v = (u, v, w) are the covariant velocities in the two horizontal and vertical directions, respectively.

Using the variables defined above, the flux-form Euler equations may be written as

$$\partial_t U + (\nabla \cdot V u) - \partial_x(p\varphi_\eta) + \partial_\eta(p\varphi_x) = F_U \tag{4.4}$$

$$\partial_t V + (\nabla \cdot V v) - \partial_y(p\varphi_\eta) + \partial_\eta(p\varphi_y) = F_V \tag{4.5}$$

$$\partial_t W + (\nabla \cdot V w) - g(\partial_\eta p - \mu) = F_W \tag{4.6}$$

$$\partial_t \Theta + (\nabla \cdot V \theta) = F_\Theta \tag{4.7}$$

$$\partial_t \mu + (\nabla \cdot V) = 0 \tag{4.8}$$

$$\partial_t \varphi + \mu^{-1}[(V \cdot \nabla\varphi) - gW] = 0. \tag{4.9}$$

The diagnostic relations for the inverse density is,

$$\partial_\eta \varphi = -\alpha\mu \tag{4.10}$$

while the equation of state is,

$$p = p_0 \left(\frac{R_d \theta}{p_0 \alpha}\right)^\gamma \tag{4.11}$$

where the subscripts x, y and η denote differentiation,

$$\nabla \cdot V\, a = \partial_x (U\, a) + \partial_y (V\, a) + \partial_\eta (\Omega a) \tag{4.12}$$

and

$$V \cdot \nabla a = U\, \partial_x a + V\, \partial_y a + \Omega \partial_\eta a \tag{4.13}$$

where a in 4.12 and 4.13 represents a generic variable. $\gamma = cp/cv = 1.4$ is the ratio of the heat capacities for dry air, Rd is the gas constant for dry air, and p0 is a reference pressure (typically 105 Pascal). The right-hand-side (RHS) terms F_U, F_V, F_W, and F_Θ in equations 4.4 to 4.7 represent forcing terms arising from model physics, turbulent mixing, spherical projections, and the Earth's rotation respectively. For further details of the WRF model refer (Skamarock et al., 2008).

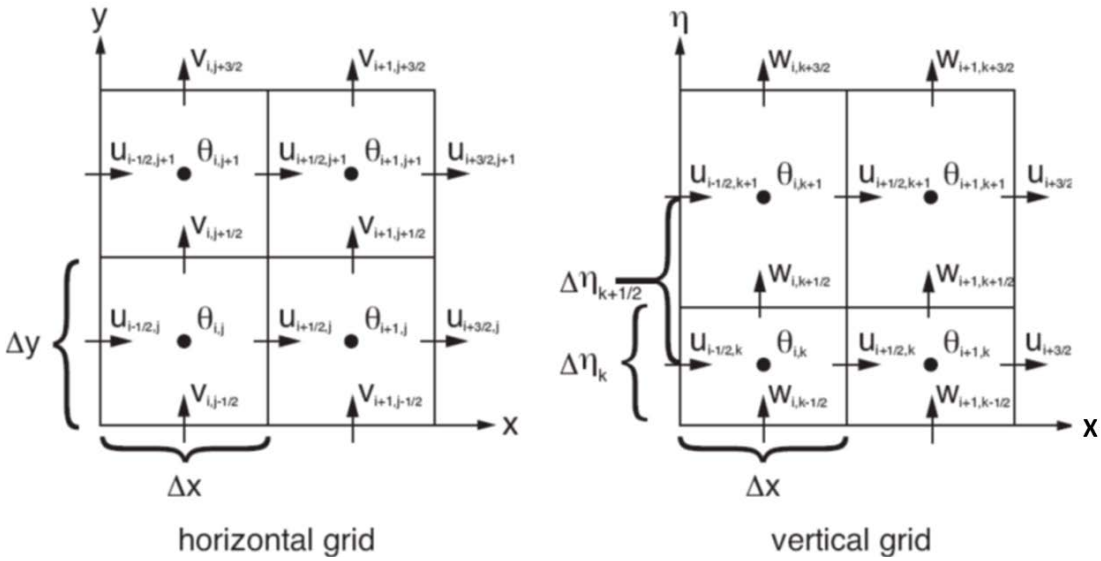

(a)

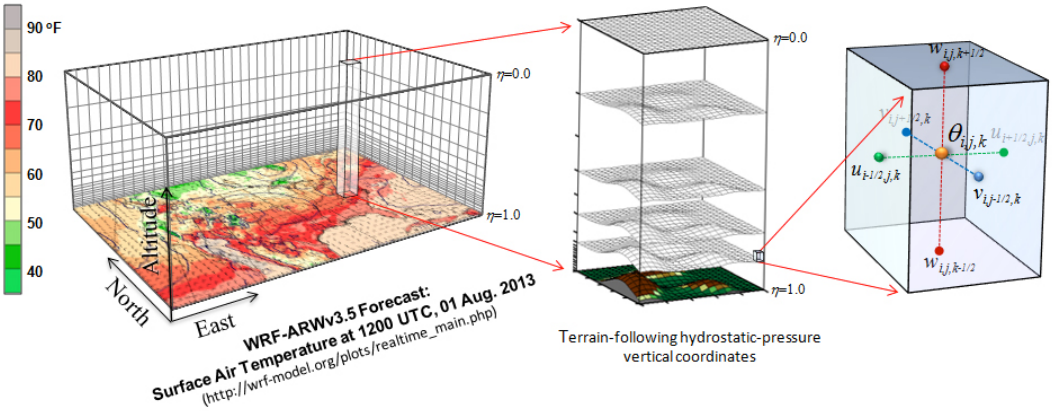

(b)

Figure 4.9 2D (a) and 3D (b) representation of horizontal and vertical grids of the ARW WRF

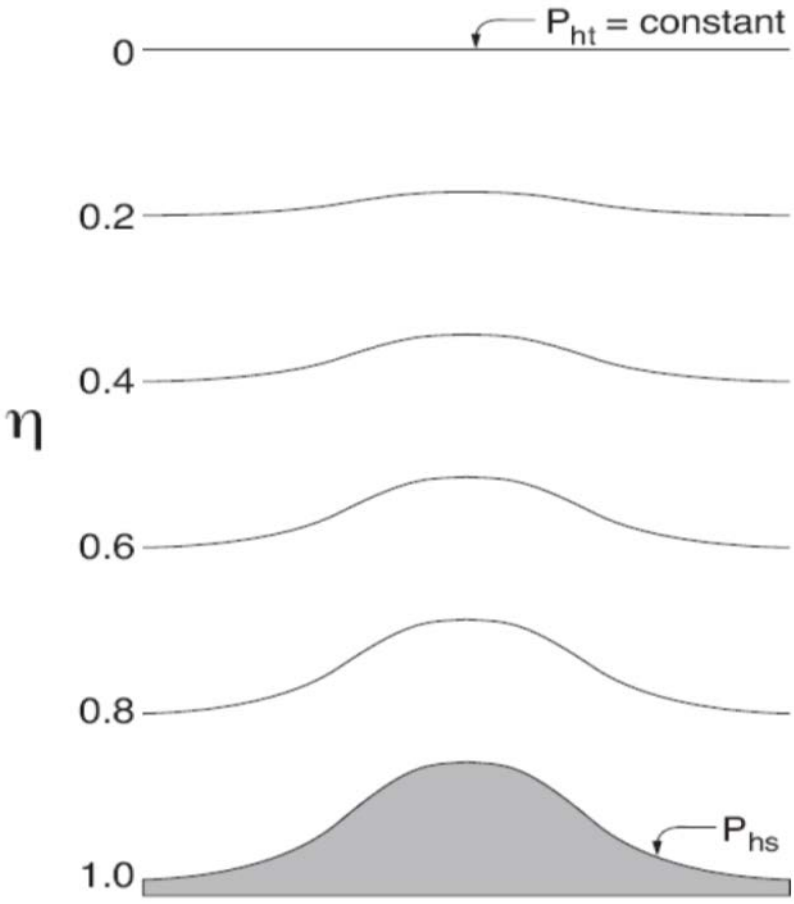

Figure 4.10 WRF ARW η coordinate

4.3.9.1 ARW Solver Control File

The user is provided with the flexibility in the WRF software to choose different physical and parametrization options at the time of the commencement of the simulation using the control file NAMELIST.INPUT. This list can be divided into three main sections for normal runs. Primarily the first section of the list provides the option for the time of start of simulation for parent domains and nests. It also provides control over the average interval of the output produced from each WRF domain. It also allows the user to select the size of the output file and either the user wants to restart a simulation or not.

The details regarding configuration and resolution of the domains are handled more specifically in the NAMELIST.WPS as described in section 4.3.1. A few of these are relisted in the second portion of the NAMELIST input file. This section also allows the user to select the mode of nesting and the parent grid ratio. The most important function of this list is to provide control over the time coverage of the simulation in terms of the time step (limited by the courant number; criteria for convergence while solving hyperbolic partial differential equations numerically) and defines the stability of the simulation. Thus, for 3D applications the time step should satisfy equation 4.14,

$$\Delta t_{max} < \frac{Cr_{theory}}{\sqrt{3}} . \frac{\Delta x}{u_{max}} \tag{4.14}$$

where u_{max} is the maximum possible velocity from the simulation and Cr_{theory} should be obtained from Table 3.1 in (Skamarock et al., 2008). It also allows to select the number of vertical levels (the eta levels) to vertically divide the atmosphere into computation cells. Those levels are neither altitude-fixed nor pressure-fixed. The vertical coordinate η is pressure-dependent. It is always 1 at the Earth's surface (it follows the topography) and decreases towards 0 at the top of the atmosphere according to equation 4.15,

$$\eta = \frac{(p - p_{top})}{(p_{surf} - p_{top})} \tag{4.15}$$

where p is the hydrostatic component of the pressure, varying between:

- psurf at the surface of the Earth
- ptop at the top of the atmosphere (a constant pressure fixed by the model, typically at 50hpa)

If the user only defines the number of levels, a default set of eta-coordinates will be provided by the program REAL. But the user may also give explicit values for the set of eta-levels which will be used. It should be noted that these values provided to WRF will correspond to the levels dividing the computational cells (i.e. the cells' bottom and top boundaries). In the output files, most variables will be given, not on these eta-levels but at the cell centres between these levels.

This section further allows selection of the number of METGRID levels and soil levels which are used for the meteorological initialization field. For NCEP data METGRID levels are 27 in number while for ERA-Interim data these are defined to be 38 levels.

The physical and parametrization options are handled in the third section of the file. There are 5 groups of physical schemes available in WRF:

1. The microphysics scheme explicitly solves for the distribution of water in the atmosphere between vapour, clouds, rain and snow.
2. The cumulus parameterization adds the sub-grid-scale effects of convective clouds (for domains whose grid spacing is greater than 5 km).
3. The planetary boundary layer scheme represents the vertical fluxes from sub-grid-scale turbulence.
4. The short-wave and long-wave radiation schemes take into account the presence of clouds, carbon dioxide and ozone to calculate the absorption, reflection, emission of radiation, and therefore the heating or cooling of the surface and the atmosphere.
5. The surface and land-surface models are the key point, taking into account the information from the other schemes to compute heat and moisture exchanges at the surface and the friction velocity. Some of them take into account some vegetation processes and temperature and moisture profiles in the soil.
6. The topographic correction for surface winds to represent extra drag from sub-grid topography and enhanced flow at hill tops can be also be modelled using TOPO_WIND option.

7. Number of the soil layers in the land-surface model and the number of land use categories in the input data is also specified in this section.

For each scheme, WRF allows choices between several models. The details of selecting these models and their interrelationships are described in detail in section 4.3.11 below.

The other sections of NAMELIST.INPUT data deal with the grid, observational and spectral nudging using FDDA, controlling the dynamics of the model involving diffusion, damping and advection options, boundary condition control and an option for asynchronized I/O for MPI applications.

4.3.10 Domain Configuration

WRF has been tested in the current research with various grid configurations (level of nesting, grid resolution and spacing, spatial resolution of the time invariant data etc.) and geographical shifts in domain centres. The geographical projection scheme used for all the domains was Mercator while the nests were arranged having a minimum distance equal to the product of inflow velocity and time step. The minimum distance of the nested system should be four grid cells from parent boundary (Wang et al., 2010). For computational stability, the magnitude of time step (in seconds) should be prescribed at least 6 times the magnitude of coarsest grid distance (in kilometres) (Skamarock et al., 2008). The size of the inner grids should be reduced to increase the speed of simulation. The final configuration of the domains for the East African site is presented in Figure 4.11 while configuration details and related parameters are shown in Table 4.1. The domain configuration used for WRF's performance validation is presented in Table 4.2 and in Figure 4.12.

Configuration 4 domains 36 model levels	**Domain size (km x km)**	**Geographic resolution**	**Grid resolution (km)**	**Time step (s)**
1	1593 x 1593	10'	27	30
2	918 x837	5'	9	10
3	459 x 297	2'	3	3.33
4	126 x 82	30"	1	1.11

Table 4.1 Domain configurations and associated parameters for WRF model executions used in East Africa

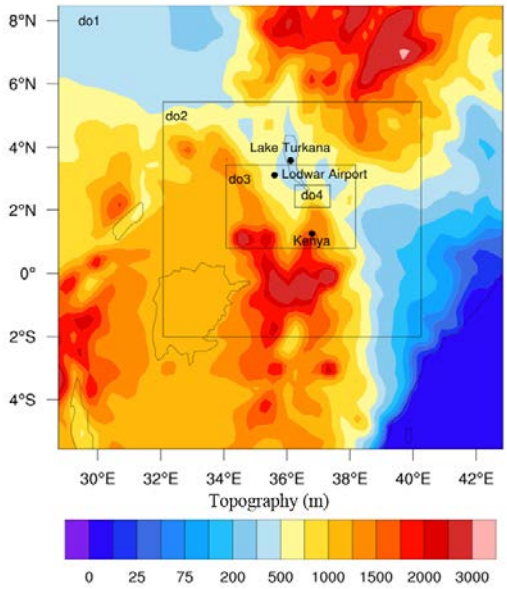

Figure 4.11 Domains (do) showing the nesting configurations detailed in Table 1 overlaid on the regional topography for the East African terrain

Configuration 3 domains 53 model levels	**Domain size (km x km)**	**Geographic resolution**	**Grid resolution (km)**	**Time step (s)**
1	295 x 295	5'	5	30
2	94.6 x 94.6	2'	1.66	10
3	23.1 x 23.1	30"	0.55	3.33

Table 4.2 Domain configurations and associated parameters for WRF execution used for performance verification at the Western Australia site

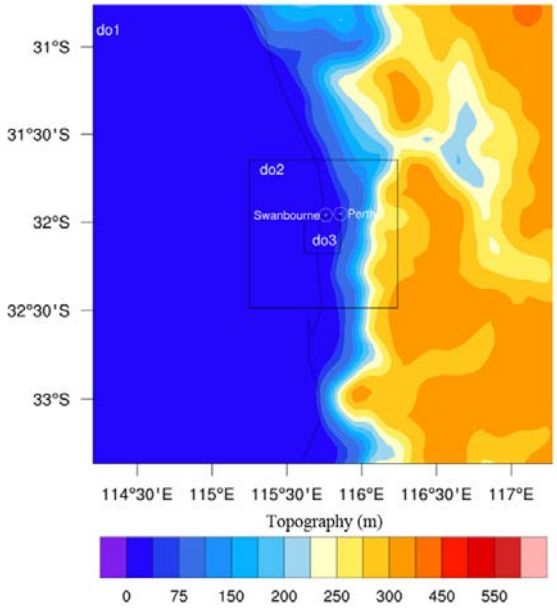

Figure 4.12 Domain (do) configurations detailed in Table 4.2 for WRF performance verification at the Western Australian site

4.3.11 Physical Options

Typically, WRF's fields are influenced significantly by the boundary layer parameterizations especially for the case of near-surface wind simulations (Carvalho et al., 2012). Since regional models cannot resolve smaller spatial and temporal scales, such unresolved physical processes are accounted for using physically-based parameterization schemes. These include the surface layer (SL), planetary boundary layer (PBL) and the land-surface model (LSM) parameterization schemes. According to (Nossent et al., 2011), it is not necessary to include all the model configuration options in the sensitivity analysis for obtaining the correct model configuration. Momentum, moisture and heat transfer between the surface and the atmosphere are represented by SL, PBL and LSM schemes in mesoscale models (Gilliam and Pleim, 2009). Particularly, since the wind changes according to the stability and baroclinic instability of PBL, it plays a significant role in the accuracy of the forecast state and flow. In addition, other factors such as thermal stability, height of PBL, infiltration of the free atmosphere into the PBL and exchanges at the top of the PBL also affect wind distribution within the PBL. The lowest part of the atmosphere, which is about one tenth of the height of the PBL, is the SL. Dynamics and thermodynamics of this layer are governed by surface fluxes of energy and momentum. The vertical profiles of wind are defined by Monin-Obukhov similarity theory. LSM schemes combine atmospheric information from the SL scheme with land surface properties (dependent on land use)

to evaluate the vertical transport in the PBL schemes, which has a direct influence on the estimation of the PBL height (Han et al., 2008).

Skamarock et al. (2008) described several schemes available for various parameterization of the boundary layer. The WRF model handles SL, PBL and LSM parameterizations individually but, since there is a strong interaction between them, selecting one scheme will dictate the selection of the other schemes. The inter-relationship between these schemes is described in detail in Skamarock et al. (2008). In published literature, one can find an extensive list of different parameterization schemes representing the same physical process. Several studies were conducted aiming to investigate the model's performance under different physical parameterization schemes (Awan et al., 2011; Gilliam and Pleim, 2009; Kim et al., 2011; Shin and Hong, 2011).

The MM5 Similarity Scheme uses stability functions described in Skamarock et al. (2008) for computing surface exchange coefficients for heat, moisture, and momentum. This surface layer scheme must be run in conjunction with the Medium Range Forecast Model (MRF) or Yonsei University scheme (YSU) PBL schemes. The YSU PBL is a first-order closure representing entrainment at the top of the PBL explicitly. It is capable of more accurately simulating deeper vertical mixing in buoyancy-driven PBLs with shallower mixing in strong-wind regimes. It has been shown by Challa et al. (2007) that surface wind speed and direction are better simulated by the YSU PBL and NOAH LSM schemes. These provide realistic meteorological predictions in the lower atmosphere. Borge et al. (2008) concluded that, since the option involving the YSU PBL simulation of turbulence transport in the boundary layer ameliorates the appended SL and LSM schemes, it is important to conduct a sensitivity study for obtaining an appropriate model configuration. The above combination of SL, LSM and PBL has been utilized in this study and it proved to be better of the other available schemes in WRF. Also winds, temperature and mixing height near the coast are better simulated with this combination (Carvalho et al., 2012), therefore, it was also used for the experiment in WA.

The NOAH LSM was developed jointly by NCAR and NCEP and has 4-layer soil temperature and moisture model with canopy moisture and snow cover prediction. The scheme provides sensible and latent heat fluxes to the boundary-layer scheme and has

the benefit of being consistent with the time-dependent soil fields provided in the analysis datasets.

SL PleimeXiu (PX) scheme has to be used with the PBL Asymmetric Convective Model (ACM2) scheme. In addition, the SL PX and PBL ACM2 schemes have to be used together with the LSM PX scheme (Carvalho et al., 2012). The central benefit of the P-X LSM lies in the indirect soil temperature and moisture nudging algorithm that significantly improves error and bias of near-surface meteorology as long as accurate 2-m temperature and moisture analyses are provided as input. But due to the absence of these analyses, use of this scheme in East Africa did not improve wind speed compared with the *in situ* wind speed

Rapid Radiative Transfer Model (RRTM) is a spectral-band scheme using pre-set tables to accurately represent longwave processes due to water vapour, ozone, CO2, and trace gases. RRTM scheme is used for Long Wave (LW) radiation in combination with the Dudhia Short Wave (SW) scheme which has a simple downward integration of solar flux, accounting for clear-air scattering, water vapour absorption. RRTM/Dudhia radiation suite has been in MM5 and WRF for years and has been well tested therefore it is chosen for all the numerical experiments conducted in this study (Rogers et al., 2013).

The Kaine-Fritsch (Kain, 1993) scheme is used by the model to parameterize cumulus physics. It should be noted that the cumulus physics option was used only with large domains (greater than 10 km) as vertical fluxes due to cloud related updrafts and downdrafts and compensating motion outside the clouds can be resolved explicitly until grid sizes of approximately 5-10 km (Skamarock et al., 2008).

Microphysics in WRF help to account for fine scale structures (formed by radiative, dynamical or convective processes) not resolved by the model. The Eta or Eta Ferrier scheme is capable of predicting changes in water vapor and condensate in the forms of cloud water, rain, cloud ice, and precipitation ice microphysics. It is a simple efficient scheme with diagnostic mixed-phase processes used in NCEP models and has been used in most simulations in this study as it is well tested for WRF-NMM, used operationally at NCEP (Skamarock et al., 2008). WRF Single-Moment 6-class scheme with ice, snow and graupel processes has also been tested in this study. The

graupel scheme was not used on domains with grid size larger than 10 km because the updrafts producing graupel are not resolved.

Considering the guidelines mentioned in the above mentioned studies for WRF sensitivity analysis, three experiments were conducted using the parametrization schemes mentioned in Table 4.3. It should be noted here that, before commencing the tests on the physical options, WRF's performance validation was established in WA using the "A1" parameterizations (see Table 4.3). In the next step, the tests were performed on the East African terrain starting with the "A1" set of physical options then altering them progressively to obtain the best match with *in situ* observations. Furthermore, selections described in Table 4.3 have also been utilized in further investigations and the final best choice was selected after conducting these tests.

Parameterization	**SL**		**PBL**		**LSM**		**Long-wave radiation**	**Short-wave radiation**	**Cumulus**	**Microphysics**	
	MM5	PX	YSU	ACM2	NOAH	PX	Rapid Radiative Transfer Model	Dudhia	Kain-Fritsch	WRF Single-Moment 6-class	Eta microphysics
A1	✓	☒	✓	☒	✓	☒	✓	✓	✓	☒	✓
B1	✓	☒	✓	☒	✓	☒	✓	✓	✓	✓	☒
C1	☒	✓	☒	✓	☒	✓	✓	✓	✓	☒	✓

Table 4.3 Physical Selections for Simulations (where ☑ means accepted and ☒ means ignored)

4.3.12 Influence of Different Initialization Fields

WRF's performance has been evaluated using different meteorological initial and boundary conditions in order to bring the model outputs to agreement with the *in situ* surface measurements. Often WRF is initialized using reanalysis data which are produced by a NWP initialized using observations from satellites, aircraft, radiosondes and surface stations. Hence, it becomes possible to hind cast meteorological variables including wind speeds extending back several years. Such data sets include NCEP's reanalysis data and some third generation reanalyses, such as the Climate Forecast System Reanalysis (CFSR), the Modern-Era Retrospective Analysis for Research and Applications (MERRA) and the ERA-interim data. Testing the model with different sources of initial and boundary conditions will identify the best performing reanalyses data for a particular terrain (M. Giannakopoulou 2014, personal. comm., 02 April). Reanalyses may vary as they utilize diverse observational databases and may run at

assorted resolutions using different model dynamics and physics. In data sparse areas, such as East Africa, the analyses will depend heavily on the first guess supplied by the forecast model. This, in turn, will be sensitive to the diabatic heating distribution produced by the physical parameterizations used in the model. It is important that the reanalysis products, such as precipitation, are compared with independent surface and satellite-based observations where appropriate (Annamalai et al., 1999).

The following describes the implementation of a sequence of WRF executions utilising the enhanced surface information to evaluate the impact on forecast accuracy. Primarily the data from NCEP FNL (Final) Operational Global Analysis data (National Centers for Environmental Prediction/National Weather Service/NOAA/U.S. Department of Commerce, 2000) on a 1° by 1° grid, prepared operationally every six hours, has been utilized for initialization of domains with different grid resolutions both for the East Africa and for WA sites. However, this reanalysis had consistency problems in its wind products in some locations, presumably due to challenges of assimilating data from a changing observational system (Brower, 2006). In the NCEP Reanalysis 2, some issues were corrected with an improved parameterization of the physical processes but grid configuration remained unchanged (Brower et al., 2013). The ERA-Interim reanalysis data, having a horizontal resolution of 70 km and 60 model vertical levels with a 6 hourly temporal resolution (ECMWF, 2009) has been utilized in parent and nested domains in the final analysis of the East African study. The ERA-interim reanalysis data, extending from 1989 onward, is basically a third generation reanalysis that makes use of a much improved atmospheric model and an assimilation scheme based on that used in ERA-40 (Uppala et al., 2005). In comparison with the operational analyses, the ERA-interim was the best of the newer reanalyses for the year 2007 (Wesley et al. 2012). On average, except for temperature at upper levels, both the newer-generation reanalyses (CFSR and ERA-Interim) yield smaller RMS error and biases than their predecessors (NNRP and ERA-40) (Bao and Zhang, 2013). Considering these facts, the ERA-interim data set was utilized in the current study to force the initial and boundary conditions in all domains and it produced lower RMS and higher correlation coefficients, as will be explained in section 5.2.5.

4.3.13 Ingesting Satellite Data

In order to achieve a precise forecast, in the case of a complex terrain, it is essential to achieve realistic simulations to initialize the domain with high resolution surface data (Beezley et al., 2011). Access to high spatial resolution terrain data, such as held by the USGS, has increased the interest in initializing WRF simulations using customised data sets. These data sets are read by WRF's pre-processing system, WPS, using a simple binary format. More effort should be applied in writing to this format which permits the utilization of such data. The effort on the WRF Fire module (Mandel et al., 2011) has led to small utilities being developed that can assist writing GeoTIFF files directly into GEOGRID's binary file. GEOGRID is a component of the WRF pre-processor WPS that is responsible for interpolating surface data onto the simulation's computational grid. It reads surface data from a simple binary format consisting of a single text file specifying metadata and provides a number of binary files containing a rectangular block of data known as a tile.

In order to add support for the use of the georeferenced data, the GeoTIFF image specification is utilized. It is an extension to the Tagged Image File Format (TIFF).

GeoTIFF files from ASTER are often stored in contiguous tiles much like the GEOGRID format, except that rows and tiles are ordered from top to bottom. Beezley et al. (2011) defines the method for converting ASTER data (in GeoTIFF format) to GEOGRID readable format. After successful conversion GEOGRID is able to read and interpolate the data which then can be ingested into WRF for completing the simulation. The results of this simulation will be explained in the next chapter.

4.3.14 Terrain complexity

A primary source of error in meteorological modelling arises because the models assume the terrain to be much smoother than it is in reality. Significant terrain features, including valleys and mountains are drivers for the change in wind speed, direction and turbulence. In early versions of WRF, a high bias in predicting surface winds over plains and valleys occurred due to the drag exerted by unresolved topography (Cheng and Steenburgh, 2005). The new parameterization scheme introduced in WRF version 3.4.1 corrects for this high wind speed bias over plains and valleys. The scheme also

corrects for the low wind speed bias found over the mountains and hills (Jiménez and Dudhia, 2012;2013). The impact of this feature on accuracy, however, will be limited by the resolution of the orographic height provided to the model. The higher the spatial resolution, the more the bias will be reduced and the forecast improved.

In order to assess the sensitivity of WRF to terrain complexity, the location of mast A is included within the WRF's nested domains but with different spatial resolution grids[10] ranging from a spatial resolution of ten arc minutes to thirty arc seconds. The model also has been tested with 30-meter resolution digital elevation data from ASTER[11].

4.4 Model Validation

The results of any prediction model should be verified because of inherent uncertainty in wind power forecasting model implementation for a specific site. Generally, for assessing the performance of forecasting algorithms, several different aspects have to be taken into account (Perez et al., 2013) and the percentage error is determined through various uncertainty analyses. The difference between the measured and predicted values is defined as model prediction error. Point forecast models usually are assessed and compared through MAE, mean square error (MSE), root mean square error (RMSE), the histograms of the frequency distribution of the error, the CC, normalized RMSE and MAE, bias, skill score and standard deviation. Three error measures are applied here to explore prediction uncertainty. While prediction for an individual site may be in error the overall prediction error is reduced by the grouping into an extensive area wind farms (Foley et al., 2012). The power generation RMSE for most modelling exercises is usually 10% of installed capacity. Wind farm operators have quoted individual wind farm modelling accuracy to be in the range of 10-20% (Foley et al., 2012). The RMSE increases as the forecasting horizon (hours) increases (Shiu et al., 2010).

It is intended to validate the model using observations that represent the true state of key variables hence three statistical parameters, i.e. RMSE, CC and percentage bias

[10] http://rda.ucar.edu/datasets/ds083.2 accessed 01/04/2013
[11] (http://gdem.ersdac.jspacesystems.or.jp/agreement.jsp accessed 06/01/2014).

will be used. The difference of simulated wind speeds (v_i^x) and the observed wind speeds (v_i^{obs}) for the same place and time instant is expressed by equation 4.16.

$$v_i^{/} = v_i^x - v_i^{obs}. \tag{4.16}$$

Since the wind direction is a circular variable, equation 4.16 is redefined as,

$$\Phi_i^{/} = \left(\Phi_i^x - \Phi_i^{obs}\right) \left| \left[1 - \left(\frac{360}{\left|\Phi_i^x - \Phi_i^{obs}\right|}\right)\right] \right| \; if \; \left|\Phi_i^x - \Phi_i^{obs}\right| > 180^{\circ}, \tag{4.17}$$

to accommodate the fact that the absolute deviation of wind direction cannot exceed 180°. In equation 4.17 Φ_i^x and Φ_i^{obs} are the simulated and the observed wind directions respectively.

Nemes (2013) concludes that the Weibull distribution (with two parameters) may be successfully utilized to describe the principal wind speed variation. The Weibull probability density is given by equation 4.18,

$$f_w\,(v) = \frac{\beta}{\alpha}\left(\frac{v}{\alpha}\right)^{\beta-1} exp\left[-\left(\frac{v}{\alpha}\right)^{\beta}\right]. \tag{4.18}$$

The corresponding probability function of the Weibull distribution is expressed in equation 4.19,

$$F_w\,(v) = 1\text{-}exp\left[-\left(\frac{v}{\alpha}\right)^{\beta}\right] \tag{4.19}$$

where α (m/s) is the scale parameter and β (dimensionless) is the shape parameter of the Weibull distribution. The scale parameter α provides information about the average of the wind speed profile while the shape parameter β provides information about the deviation of the wind speed values around the mean as well as the features of the Probability Distribution Function (PDF). α and β are interconnected through analytical expressions of mean and variance of the Weibull PDF. In this study, Weibull PDFs are used to assess forecast accuracy by comparing PDFs derived from modelled and measured wind speeds. The PDFs are calculated for the final experiment only and the distributions are calculated at the positions of all three masts.

4.5 WRF Post Processing Software

The most important variable to be deduced form the WRF output data files is wind speed with respect to location and time. Other important data include pressure, temperature, precipitation etc. WRF ARW files are mostly in the netCDF format where the data is stored in the form of arrays. There are a number of visualization tools available to display WRF-ARW products including NCL, GRADS, IDV, Plot_WRF etc.

4.5.1 Plot_WRF

Plot_WRF is a program developed by Dr. Peter Rye, DER, Perth, Western Australia in 2012. This program is capable of plotting data from both WRF input and output files. It has numerous options and can plot any variables likely to be needed from produced by the WRF. It is capable of interpolating the output variables from WRF at any desirable height and location. It also has the capability of reading multiple WRF output files at one time and products can be adjusted either to local time or UTC. It can cross compare measurements and modelled values with appropriate availability of the necessary databases. Its graphical output includes GIF files (which can be displayed on screen), plots within a separate X-window (using the Cairo graphics library) and, Windows Metafiles that can be read directly by Microsoft Office or OpenOffice software.

The program was compatible with the WRF 3.4.1 version and has been used extensively in this research to obtain wind speed and direction time series plots. But with the introduction of WRF 3.6.1, the current version of Plot_WRF is now incompatible. The developer is no longer providing software support. Alternative code had to be developed in NCL to compare wind speed output from WRF.

4.5.2 NCAR Command Language (NCL)

The NCAR Command Language (NCL) is a programming language designed specifically for the analysis and visualization of data. NCL can be run in interactive mode or in batch mode as an interpreter of complete scripts. NCL has robust file input and output. It can read in netCDF, HDF4, HDF4-EOS, GRIB, binary and ASCII data.

The graphics are world-class and highly customizable. The power and utility of the language are evident in three areas:

- File input and output
- Data processing
- Graphical display.

NCL can readily read and process WRF ARW netCDF files. In July 2007, the WRF-NCL processing scripts have been incorporated into the NCL Libraries, thus only the NCL Libraries are now needed.

This language has been utilized to develop two indigenous codes, one of which is used for interpreting wind speed and direction time series output from WRF. The other code can retrieve radial wind speeds from CDL and can compare them with the WRF output spatially at any desired location and at any instant of time.

4.5.3 Grid Analysis and Display System (GRADS)

The Grid Analysis and Display System (GRADS) is an interactive desktop tool to display earth science data and is freely available on the internet. It has two data models for handling gridded and station data and supports many data file formats, including binary, GRIB (version 1 and 2), NetCDF, HDF (version 4 and 5), and BUFR.

GRADS uses a 5-Dimensional data environment: the four conventional dimensions (longitude, latitude, vertical level, and time) plus an optional 5th dimension for grids that are generally implemented but designed to be used for ensembles. Data sets are placed within the 5-D space by use of a data descriptor file. GRADS handles grids that are regular, non-linearly spaced, gaussian, or of variable resolution. Data from different data sets may be graphically overlaid, with correct spatial and time registration. Operations are executed interactively by entering FORTRAN-like expressions at the command line. A rich set of built-in functions are provided, but users may also add their own functions as external routines written in any programming language. It can run in interactive or batch mode and can be used to produce scatter plots, time series and other plots.

In the current research the use of GRADS was particularly useful in acquiring the time series output from the NCEP data and comparing it with the WRF output.

4.5.4 Integrated Data Viewer (IDV)

The Integrated Data Viewer (IDV) from Unidata is a Java™-based software framework for analysing and visualizing geoscience data. The IDV is developed at the Unidata Program Center (UPC), part of the University Corporation for Atmospheric Research, Boulder, Colorado, which is funded by the National Science Foundation.

It brings together the ability to display and work with satellite imagery, gridded, surface observations, balloon soundings, etc., all within a unified interface. It also provides 3-D views of the earth system and allows users to interactively slice, dice, and probe the data, creating cross-sections, profiles, animations and value read-outs of multi-dimensional data sets.

Initially IDV was utilized in this study. The problem with using IDV is that it cannot retrieve the vertical coordinate correctly. The GUI requires the user to enter probe height interactively even using 10 m wind speed variable which already has vertical height specified. It also rounds off the latitude and longitude to one decimal place and hence it is not possible to obtain precise location of mast and compare that to WRF output. It is unable to handle large amount of data and therefore is not able to manipulate 3D wind vectors over a large period of time. Therefore, Plot_WRF and NCL were used for more precision.

4.6 Summary

This chapter provides a comprehensive review of the WRF software, its flexibility and how it has been implemented for this study. This chapter explains the architecture of the WRF software and its two main components i.e. WPS and WRF ARW. The chapter first explains the structure of these two packages and how they are integrated and their usage for running the simulations. It also explains the physical and parametrization models used in the software. An introduction to sensitivity testing has been discussed and it has been shown how an optimal configuration may be achieved for the Lake Turkana site in East Africa using WSDSA. It explains why a certain set of physical

and parametrization schemes, grid configurations, as well as the influence of different initialization fields and terrain complexity were utilized for this research. It also explains the criteria for model validation between masts and WRF output. The results of this sensitivity analysis along with the detail of model validation are presented in the next chapter.

Chapter 5 WRF Implementation and Sensitivity Analysis

5.1 Introduction

WRF model has been described comprehensively in the previous chapter. The options concerned with a sensitivity analysis have also been discussed in detail. This chapter is more concerned with describing the results obtained using WSDSA and discussing how an optimized configuration of WRF has been achieved. After completing a sensitivity analysis, the results from the optimized WRF model applied to the complex terrain in East Africa are compared with wind speed time series data from the CDL. The CDL data has also been compared spatially with the WRF model. It is pertinent to mention here that most of these comparisons were possible due to development of two indigenous codes in NCL for retrieving and comparing the data sets.

5.1.1 Design of Simulations

The initial design of the simulations has been focused on validating WRF performance in a well-defined meteorological environment in the knowledge that data sparseness and hence the quality of the assimilated analysis can affect the accuracy of model performance. Once the confidence in WRF performance was gained, the next step was testing physical options including; influence of the terrain complexity, the influence of the simulation domain resolution and, finally, the influence of different initialization fields. The model prediction accuracy for this WA site, using 2 weeks of *in situ* observations, was used to compare with prediction accuracy achieved for the East African site. To compare the simulated wind time series at the points that coincide with the locations of the meteorological stations, horizontal and vertical interpolations were employed. The methodologies followed to perform the various comparisons are described in the next sub-sections.

5.1.2 Establishing WRF Performance in a Well-Defined Meteorological Environment

WRF assimilates pre-processed initialization fields from the reanalyses data provided by the NCEP and ERA-Interim. These initialization fields are objective combination of observations and a numerical model that simulates one or more aspects of the Earth system for generating a synthesized estimate of the state of the system. These

initialization fields are dependent on the abundance of constraining *in situ* observations. The significance of their impact on model output fields decreases with the increase in the sparseness of observational data. Henceforth, in order to establish the validity of WRF's performance it was initially tested in a well characterised meteorological environment in WA with ample availability of observational data.

5.2 Results and Discussion

5.2.1 Establishing the Performance WRF in a Well-Defined Meteorological Environment

Before the commencement of WSDSA, it was important to test the performance of WRF in a region where ample validation data was available. NWPs initial conditions are determined by applying data assimilation techniques to optimally blend observational data with short range model forecast to produce an analysis. 'Imperfect' observations and approximations in the data assimilation process may be diagnosed as a reason for the uncertainties in the initial conditions (Dow, 2004). In addition, further complications arise when the terrain is complex and it becomes difficult to establish *a priori* a model's precision. Therefore, WRF was tested in a simple coastal site in WA during a sea breeze event and with abundant available observational data. Wind statistics, between WRF and measurements from the DER 10 m operated meteorological mast for a period of 16 days, are presented in Table 5.1. Comparison of wind speed and direction time series from WRF and the DER mast observations are presented in Figure 5.1 and 5.2. Note that the sea breeze is initially from the SW and, as expected, it backs southerly throughout the day. WRF captures this feature very well as the sea breeze weakens in the evening and the prevailing easterly wind are re-established at the surface.

There is a slight under-prediction of the strength of the sea breeze when compared to the onsite anemometer. However, this could be due to the anemometer being installed on a sand dune in which case it is possible there could be some over-reading of the wind speeds at the anemometer location compared to the WRF predicted wind.

It should also be noted that the predicted sea breeze arrival time for the 12 March is around 1-2 hours later than when it actually arrived. The model did not identify the formation of a weak temperature inversion leading to a weakening of the easterly

overnight from the 12 to the 13 March. The spike in the observed wind speeds from the easterly also was not identified in the model. However, it is very likely that these small scale features would not be picked up by any other simulation model (B. Buckley 2013, personal. comm., 29 November).

The meteorology occurring on the 12th of March 2011 at 8:00 am (local time) is identified in Figure 5.3. Since the value of CC is high ~ 0.7 / 0.8 respectively for wind speed and direction it was concluded that WRF can perform efficiently in a well-defined meteorological and topographical environment. This validation formed the base for the next step in the sensitivity analysis as the procedure for defining the correct configuration and positioning of domains, grid resolution, level of nesting, physical parameterization etc. were developed and because of the high value of CC, confidence in WRF performance was established.

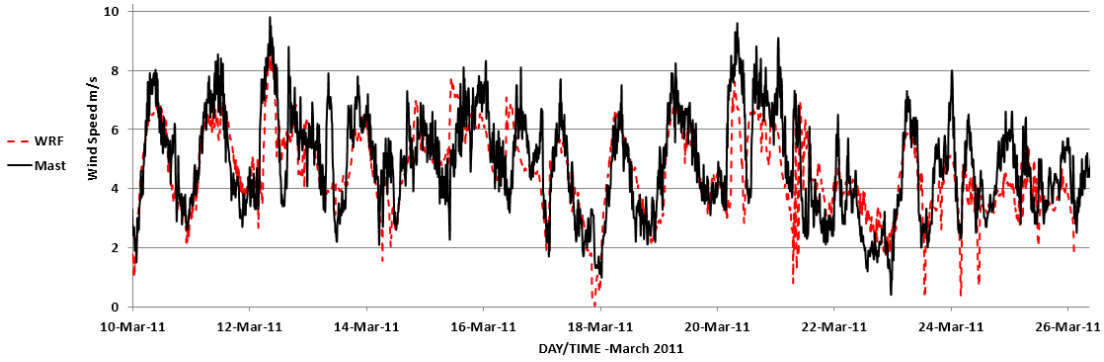

Figure 5.1 Comparison of wind speed between DER 10 m mast at Swanbourne (10 min sampling) and WRF predicted wind at 10 m (5 min sampling) from 10 to 26 March 2011 (time in UTC)

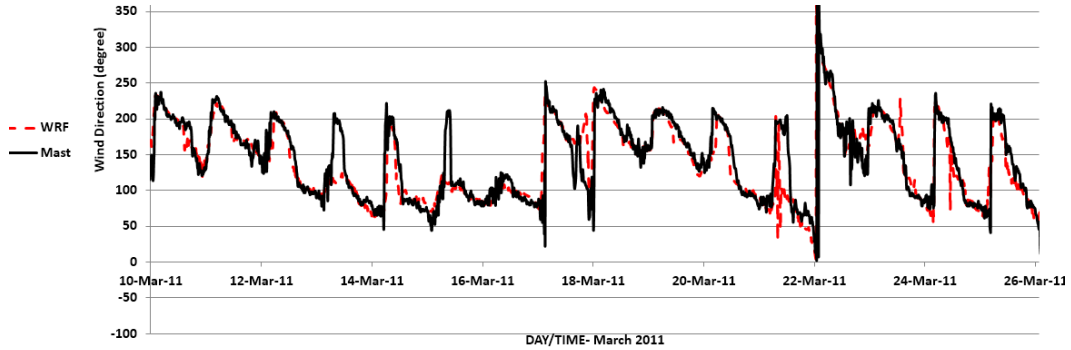

Figure 5.2 Comparison of wind direction between DER 10 mast at Swanbourne (10 min sampling) and WRF predicted wind at 10 m (5 min sampling) from 10 to 26 March 2011 (time in UTC)

NCEP initialization fields	Wind speed					Wind direction				
Set A1	**Modelled mean (m/s)**	**RMSE (m/s)**	**CC**	**BIAS (m/s)**	**%BIAS**	**Modelled mean (degree)**	**RMSE (degree)**	**CC**	**BIAS (degree)**	**%BIAS**
Swanbourne mast	4.4	1.27	0.7	-0.35	-7.4	137.7	32	0.78	+6.63	+4.5

Table 5.1 Wind speed and direction statistics between the Swanbourne Mast and WRF modelled winds from 10 to 26 March 2011

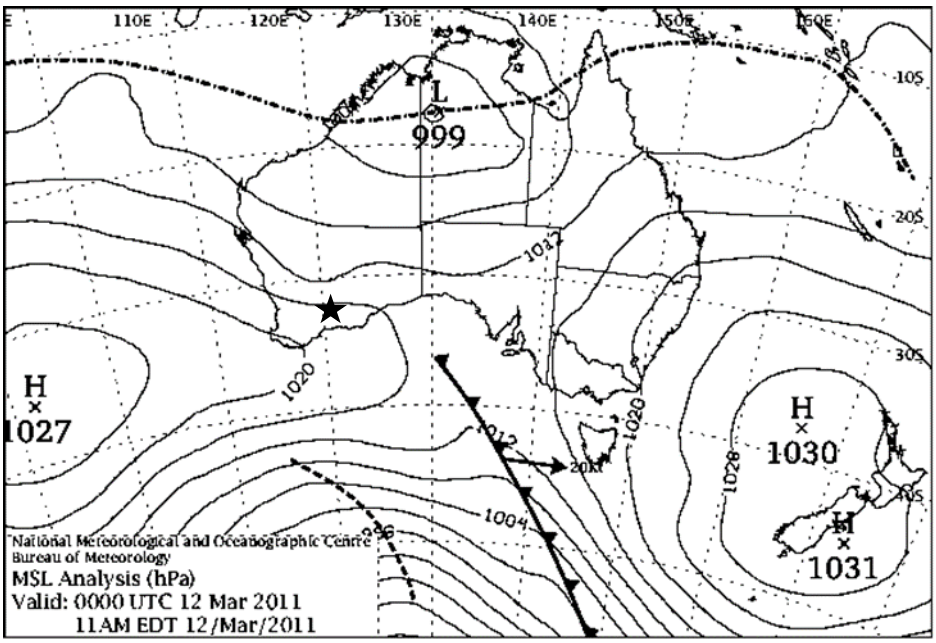

Figure 5.3 The MSP meteorology shows a high pressure system to the west of the continent maintaining E to SE winds. The local sea breeze cell strengthens during the morning into the afternoon and backs southerly as shown in Figure 5.2 (courtesy Australian Bureau of Meteorology; http://www.bom.gov.au/cgi-bin/charts/charts.browse.pl). Swanbourne's location ★ is at lat. -31.96°, long. 115.5°.

5.2.2 WRF Implementation

After optimising WRF's performance using set A1 of physical options given in section 4.3.11, the research focussed on the East African site's terrain. The WSDSA in this region was initiated using the set A1 of the physical options because this set tends to deliver better results according to our experience (reported in section 5.4.1) and the literature surveyed in section 4.3.11. The grid and nesting configurations for this experiment is shown in Table 5.2.

Configuration 4 domains 38 model levels	**Domain size (km x km)**	**Geographic resolution**	**Grid resolution (km)**	**Time step (s)**
1	1593 x 1593	10'	27	150
2	540 x540	5'	9	50
3	180 x 180	2'	3	16.66
4	87 x 78	2'	1	5.55

Table 5.2 Domain configuration and associated nesting parameters for the East African Model run using WRF

Due to instabilities in the numerical methods and the use of physical parametrization schemes that require short time steps to adequately simulate smaller scale processes[12], the time step has been reduced to 150 s rather than using 162 s as reported in section 4.3.10.

The results reported below for these experiments were achieved using these nestings. For comparison purposes, the WSDSA also utilized set B1 and C1 reported in Table 4.3 and the results of these modelling experiments using WRF, (which was executed using NCEP initialization fields), are shown in Figure 5.4 and 5.5 while the complete statistics shown in Table 5.3.

[12] http://www.dca.ufcg.edu.br/mna/Anexo-MNA-modulo02d.pdf

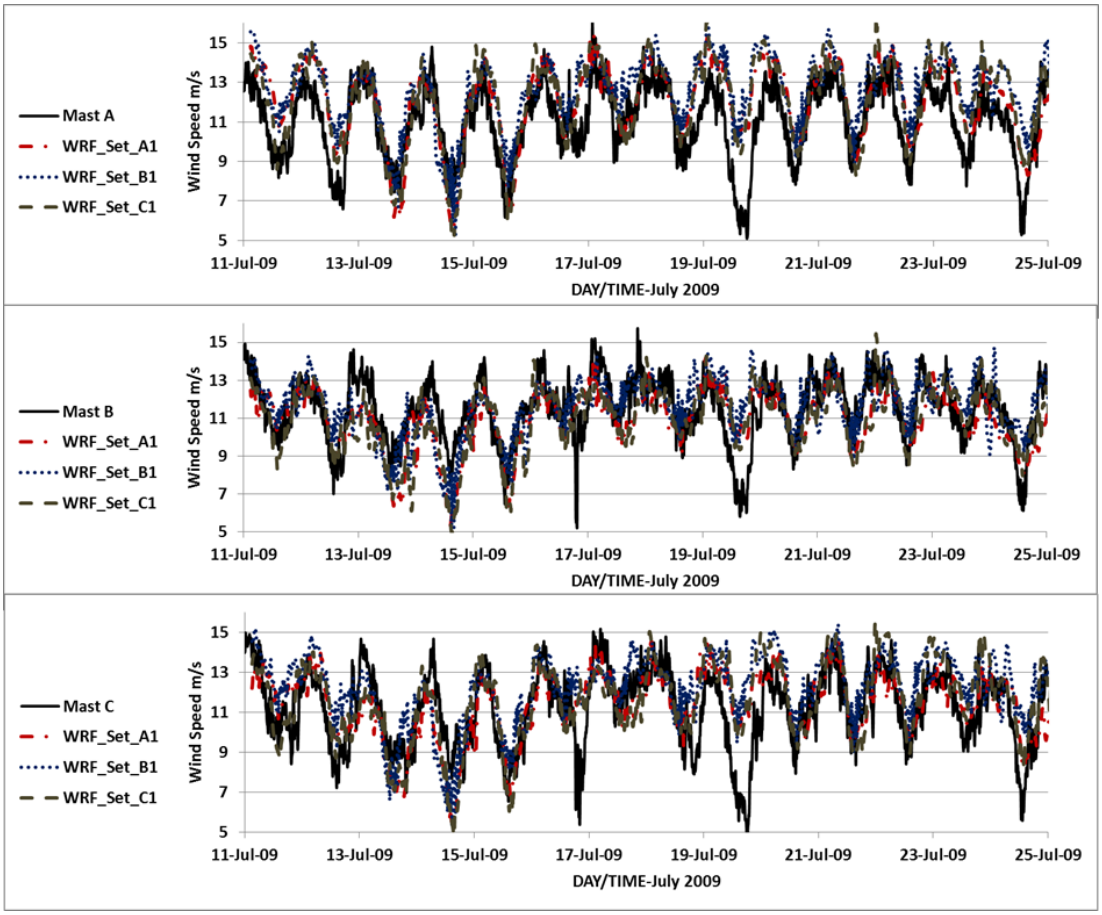

Figure 5.4 Comparison of wind speed between mast (A, B and C) observations and WRF output at 39 m, 38 m and 46 m above the surface for mast A, B and C respectively

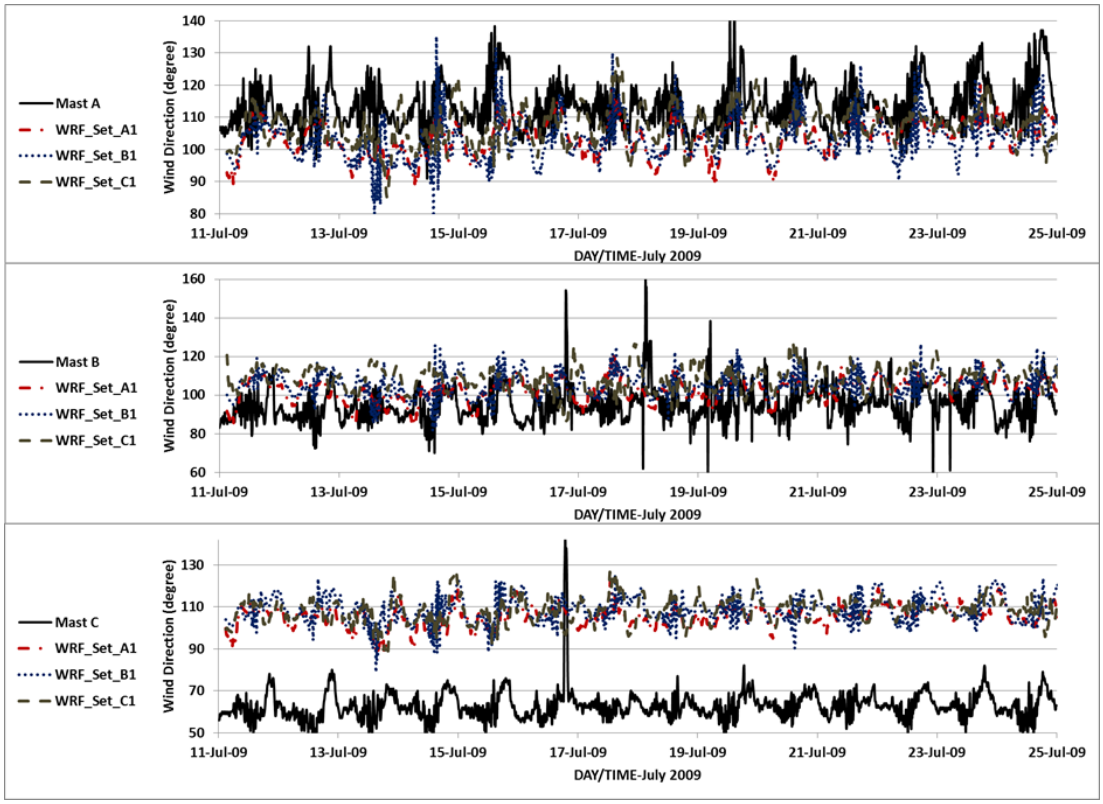

Figure 5.5 Comparison of wind direction between mast (A, B and C) observations and WRF output at 39 m, 38 m and 46 m above the surface for mast A, B and C respectively

NCEP initialization Fields	**Wind speed**					**Wind direction**				
Set A1	**Modelled mean (m/s)**	**RMSE (m/s)**	**CC**	**Model BIAS (m/s)**	**Model %BIAS**	**Modelled mean (degree)**	**RMSE (degree)**	**CC**	**Model BIAS (degree)**	**Model %BIAS**
Mast A	11.31	1.7	0.56	+0.28	+2.54	108.7	12.15	0.27	-9.54	-8.4
Mast B	10.94	1.82	0.48	-0.5	-4.4	102.9	13.73	0.05	+17.87	+8.3
Mast C	11.35	1.89	0.45	+0.15	+1.28	105.6	-----	-----	-----	-----
Set B1										
Mast A	12.59	2.4	0.47	+1.56	+14.13	103.3	13.87	0.19	-9.75	-8.6
Mast B	11.59	1.93	0.3	+0.15	+1.3	105.3	14.6	0.10	+10.48	+11.05
Mast C	12.22	2.32	0.33	+1.02	+9.1	108.6	-----	-----	-----	-----
Set C1										
Mast A	12.08	2.1	0.58	+1.05	+9.4	107.3	11.50	0.09	-5.7	-5.04
Mast B	10.94	1.81	0.47	-0.5	-4.3	108.3	17.39	-0.06	+13.50	+14.23
Mast C	11.62	2.11	0.42	+0.42	+3.7	108.3	------	-----	------	-----

Table 5.3 Wind speed and direction comparison statistics between the 14-day means of WRF output and mast anemometer observations at a height of 45 m above surface. The numerical experiments are using physical selection schemes from Table 4.3. There exists a calibration bias in the mast C wind direction which accounts for the offset from observed wind direction.

The mean wind speeds observed from 11th to 24th of July 2009 for masts A, B and C anemometers at height 45 m are 11.03, 11.44 and 11.20 m/s respectively. The results of analysing this set of three experiments using bias from Table 5.3 reveals that WRF over predicts the mean wind speed for masts A and C. The mean wind speed for mast B however, is under predicted in experiments 1 and 3 while it is over predicted in experiment 2. The RMSE values are higher for mast A and C and lower for mast B. The two data sets correlated well in case of mast A but not as well in case of mast B and C. Lower values of percent bias indicate satisfactory model simulation (Srivastava et al., 2015). The large values of the wind direction RMSE evident in Table 5.3 may reflect large uncertainties associated with the relevant measurements in gusty wind conditions (Keevallik and Soomere, 2010). The model wind direction discrepancy with the measurements of mast C are present because mast C was incorrectly calibrated (Sutton et al., 2010) with a directional offset of order 40°.

These set of experiments revealed that on the 19th of July 2009, in the afternoon, a "level error" (Pinson, 2006) is investigated between predicted and measured wind speed which persists for 4 hours in the forecast. There is a difference of 4 m/s between the predicted and measured wind speed which will cause a 40 % error in power estimation (Parkes and Tindal, 2004) and for a 325 MW facility this will cause a loss of 130 MW per day and 285 GWh loss per year. It was necessary to remove this error for an efficient forecast suitable for short term forecasting.

Atmospheric pressure is affected by temperature which in turn affects the wind speed. A low pressure is created in an area which is heated more than its surrounding and ultimately strong winds are developed in that area. Therefore, it was necessary to study the fact that whether a change in surface temperature is causing the level error in WRF's prediction of wind speed on 19^{th} of July 2009. The land surface temperature (LST) was retrieved (Figure 5.6) for East African site for a period of 14 days using the MODIS data base at National Aeronautics and Space Administration (NASA) for LST.

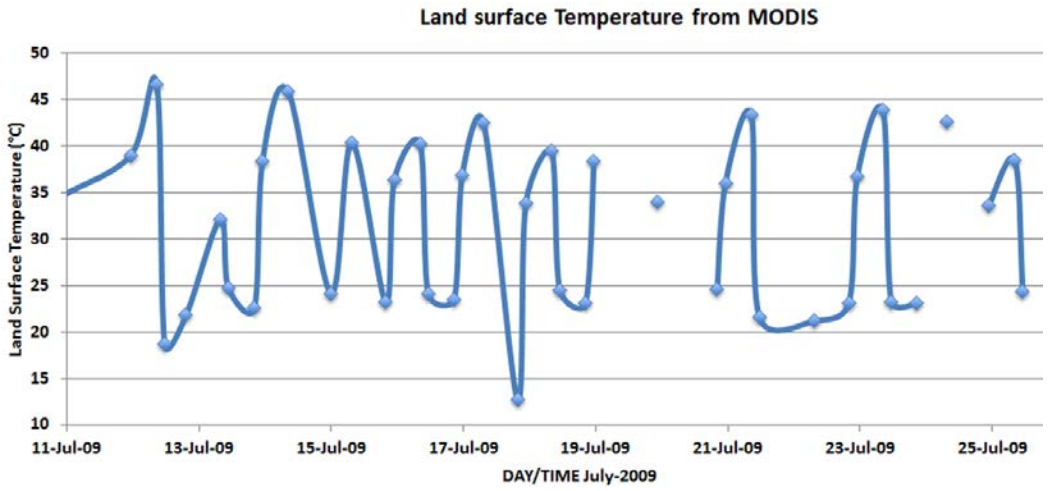

Figure 5.6 Diurnal Variations in LST at Lake Turkana wind farm site derived from MODIS

MODIS has two thermal bands [at ~ 11 and 12 microns] that are used to correct the estimate of LST for atmospheric water vapour absorption. These bands were processed using support at RSSRG Curtin. The temperature day night fluctuations are typically from ~ 23 °C to 42 °C with the minimum and maximum during the period of 12 °C and 47 °C. From the inspection of Figure 5.4 and 5.6 it seems that these changes are not causing much of impact on wind speed prediction of WRF. This conclusion is drawn on the fact that even with the day-night variability exhibited in Figure 5.6, WRF model is closely following mast observations on all days except 19th of July 2009. Therefore, this variability in temperature is not the cause of level error.

To further evaluate WRF's performance we experiment using higher spatial resolution terrain data and alternative initialization fields. The intention was to obtain a higher horizontal and vertical resolution to capture the level error occurring on 19th of July 2009.

5.2.3 Terrain Complexity

The terrain complexity experiment considers the impact of topography on wind speed and direction. WRF was tested with four different spatial resolution grids provided by NCAR as indicated in Table 5.2. Grid interpolated terrain height for each domain were compared with actual topographic heights above sea level (from Google Earth) and the surveyed height at the base of mast A. When varying the grid resolution with the size of the domain it was found that at mast A location, a difference Δz existed between the actual topographic heights above sea level compared to the value of surveyed

height at the base of mast A and the grid interpolated topographic heights at the same location, as shown in Figure 5.7. The actual height of the anemometer on mast A (39 m) is therefore measured from topographic height above sea level for each domain configuration with its particular geographic resolution. A positive Δz indicates grid interpolated height above while negative Δz indicates it below the actual height.

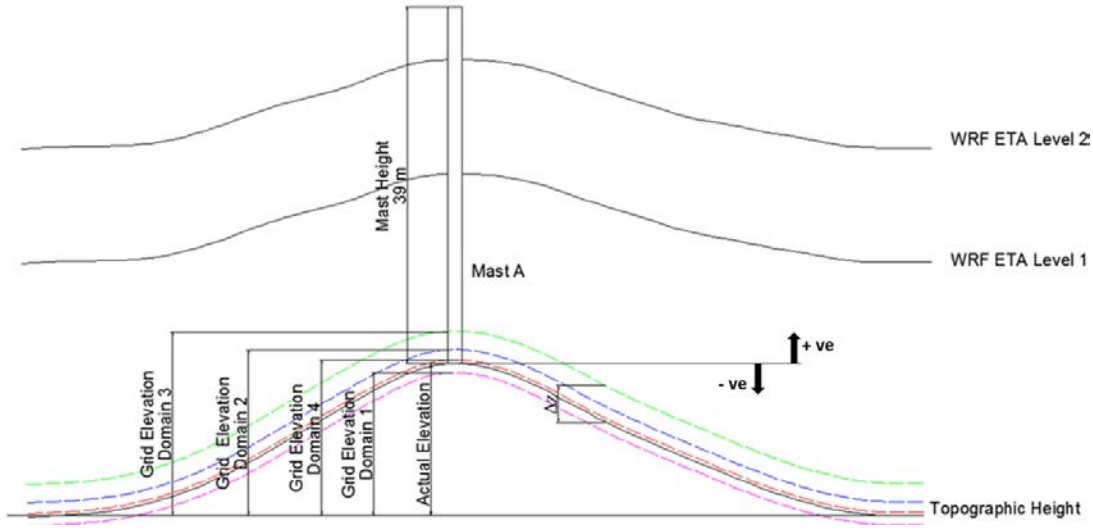

Figure 5.7 Representation of the differences between the grid and the actual elevation of the terrain at the location of mast A referenced to sea level for the different resolution domain (The value of Δz (in m) shown in the figure)

The WRF predicted wind at pressure level (eta level) closest to the mast anemometer is then compared with wind measured by mast A. The wind speed time series comparison of four domains with mast A measurement is shown in Figure 5.8.

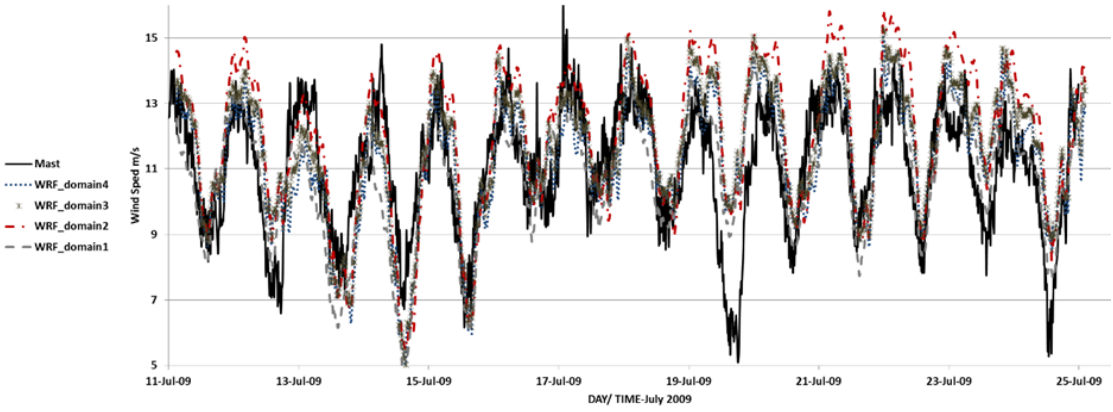

Figure 5.8 Comparison of wind speed between mast A observations and WRF model above the surface using the different model-resolved topographic heights at mast A

The resolutions of the domains, the surveyed and grid interpolated topographic heights, the offsets Δz, and mean wind speed are shown in Table 5.4. This table also shows RMSE and CC between *in situ* and WRF-predicted wind speed at a mast height of 39 m. Due to the increase in geographic and grid resolution, Δz is reduced, consequently the difference between WRF predicted and the *in situ* wind speed is reduced.

A weak terrain representation will cause the model to consider the terrain smoother and with lower topography than it is in reality which will induce an underestimation of wind speed in simulations. Places with lower elevation are typically characterized by a lower wind speed therefore if the model considers the simulation point lower than it is in reality, the computed wind speed will be lower than in reality also. The coarser geographic resolutions caused the topographic heights in domain 1 to be lower than the actual height. The simulation point of mast A is lying lower than in reality and therefore the mean wind speed (11.03 m/s from mast A) is under predicted at this point.

A simulation point lying at a higher elevation than the actual elevation will cause the wind to speed up and will overestimate the wind speed at that point. The simulation point of mast A is lying at higher elevation in the other three domains and therefore over predicted winds are observed in these domains.

Set A1	**Geographic resolution**	**Grid elevation above sea level (m)**	**Actual height above sea level (m)**	**|Δz| (m)**	**WRF Mean Wind speed (m/s)**	**RMSE (m/s)**	**CC**
Domain 1 (1593 km x 1593 km)	10'	653.12	804	150.88	10.84	1.93	0.48
Domain 2 (540 km x 540 km)	5'	1135.22	804	331.22	12.02	2.01	0.65
Domain 3 (180 km x 180 km)	2'	901.15	804	97.15	11.63	1.87	0.57
Domain 4 (87 km x 78 km)	2'	832	804	28	11.99	1.7	0.56

Table 5.4 Comparison of wind speed between mast A measured wind at 39 m and WRF modelled wind above the surface using different model resolved topographic heights at base of mast A

A logical way to try a better terrain representation in the model is to consider a new simulation with a higher resolution and test the model performance. This new simulation domain with a higher resolution should have, in theory, a better representation of terrain and thus a lower Δz. The new simulation used the same configuration as in Table 5.2 except the 4^{th} domain has geographic resolution of 30 arc second and horizontal grid resolution was increased to 54 km x 63 km. Three simulation points are considered in 3^{rd} and 4^{th} domain near to mast A. The location of the points with respect to mast A are given in Table 5.5. Wind speed retrieved by the model at each of these points is compared with the mast A wind speed measurement. It is seen is Table 5.5 that due to a more accurate representation of the terrain better CC and RMSE are achieved at all three points due to lower differences between real and model grid terrain characteristics. The complexity of the terrain in the simulation domains is ranked according to Δz i.e. as Δz increases the terrain complexity also increases resulting in higher RMSE and lower CC. We find that as spatial resolution is improved the difference Δz also decreases. Since point 1 has a higher value of Δz in both domains therefore it is considered to be in the most complex region. Therefore, the values of RMSE obtained at this point are higher as compared to other two locations

Carvalho et al. (2012) reported that increasing horizontal and vertical grid resolution may lead to better reproduction of fine-scale meteorological processes but this may necessarily may not be true due to uncertainties in the performance of the various physical parameterizations and their responses to grid resolution. Increasing grid resolution, increases computational costs, therefore, it is important to perform a careful "results improvement vs. computational cost" analysis when choosing the simulation domain resolution.

Latitude and longitude of WRF predicted points	Actual elevation above sea level (m)	Horizontal distance of point from mast A (km)	Direction of offset from the mast	Grid elevation above sea level (m)	Geographic resolution 2' (3.7 km)			Geographic resolution 30" (900 m)		
					|Δz| (m)	RMSE (m/s)	CC	|Δz| (m)	RMSE (m/s)	CC
Point 1 (2.53246 N 36.86150 E)	806	0.48	N	846.6	40.6	2.1	0.63	19.1	1.7	0.62
Point 2 (2.5236 N 36.8615 E)	811	1	SE	832.5	21.5	1.93	0.62	14.1	1.92	0.64
Point 3 (2.53245 N 36.8522 E)	794	0.55	NW	808.8	14	2	0.63	9.8	1.84	0.62

Table 5.5 Comparison of wind speed statistics generated by WRF at a mast height of 39 m and for selected locations (points) adjacent to mast A (lat.2.531 N; long.36.856 E) with their respective RMSE and CC

5.2.4 Ingesting Satellite Data

The complexity of the terrain in the East African region required the ingestion of satellite data in order to improve wind speed and direction compared to the *in situ* mast measurements. However, it should be kept in mind that although increased spatial resolution improves WRF's ability to capture surface variability, it does not seem to ameliorate regionally averaged simulation outputs or bulk ABL properties. Increased resolution allows the model to capture heterogeneous surface fluxes of importance in hydrometeorological applications but it was found that for bulk ABL dynamics (e.g., ABL height) the mesoscale simulations gave better agreement with measurements than the LES with increasing resolutions (Talbot et al., 2012). In the following, ASTER DEM data is used to improve the terrain representation in the WRF model. The procedure adopted for this approach has been explained in section 4.3.13 and can also be found at (Smith, 2010). The domain configuration and the associated details are provided in Table 5.6. The spatial resolution of ASTER data was 30 m therefore it was more meaningful to use it in the final nested domain. In addition, the MODIS 20 category land-cover classification of the International Geosphere-Biosphere Programme (IGBP) (Justice et al., 1998) has been used instead of the 24 category USGS data because the MODIS product was able to handle the lateral boundary effects correctly. The topographic heights of all the domains are shown in Figure 5.9. Due to the higher resolution of the 5th domain (30 m), the existence of a mountain at a boundary of the domain caused the model to become unstable. This problem was circumvented by removing the fifth domain from the configuration and using the 30 m ASTER data in the 4th domain. Figure 5.9 also signifies that code used to interpolate

the 5th domain was smoothing out the topographic height at top left of the domain. The existence of mountain (Mount Kulal[13]) at this end of the domain having prominence of 1552 m is represented as ~1000 m. Therefore, a different MATLAB algorithm developed by DER was applied to get a better approximation of the topographic heights as shown in Figure 5.9 (f). Figure 5.10 shows the comparison of wind speed for mast A and the corresponding WRF output. It is concluded that the WRF output utilizing the smoothed satellite data was able to predict the wind speed better than the WRF output using the set A1. The RMSE has been improved by 9.7 % while the average wind speed is reduced by 5.0 % which is 3.4% closer to mast measurements. It is pertinent to mention here that the model had also been configured to smooth the model topography for matching with the low resolution topography coming with the source data. This approach, however, was not able to solve the problem of wind speed deviation between mast measurements and the WRF model on 19th July 2009. Accordingly, it was decided to continue the experimentations using different model initialization.

Configuration 5 domains 36 model levels	Domain Size km x km	Geographic Resolution	Grid Resolution km	Time Step s	Domain Configuration
do1	1593 x 1593	10'	27	50	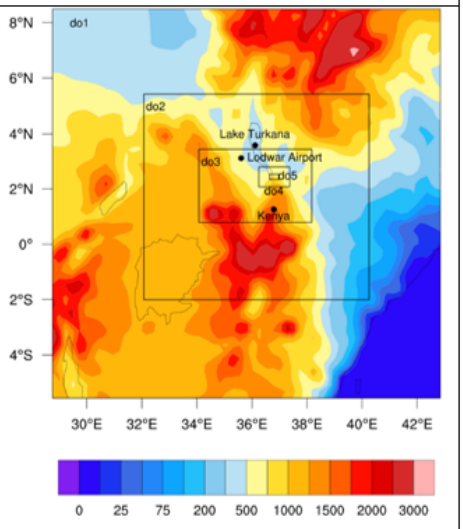
do2	918 x837	5'	9	16.66	
do3	459 x 297	2'	3	5.55	
do4	126 x 81	30"	1	1.85	
do5	36 x 21	1'	0.33	0.612	

Table 5.6 Domain configuration and associated parameters for East African site WRF model runs using improved spatial resolution topographic data derived from satellite

[13] https://en.wikipedia.org/wiki/Mount_Kulal

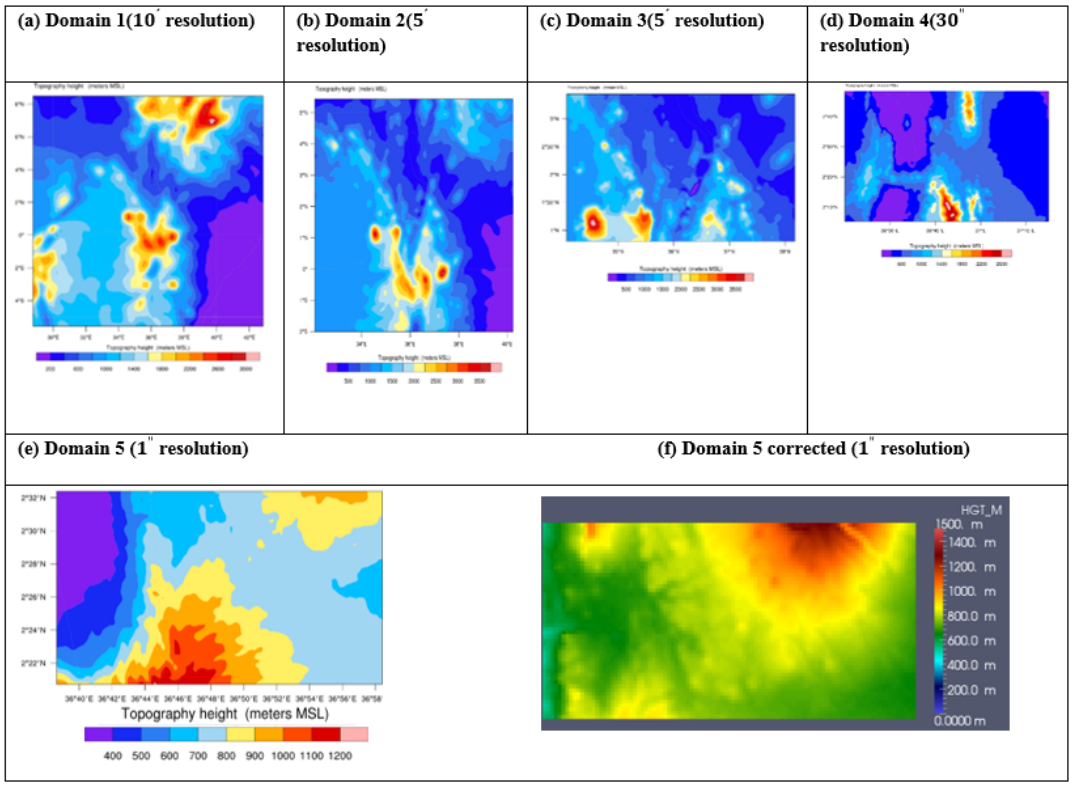

Figure 5.9 Topographic domain heights (meter) obtained using MODIS land cover (1 km) and ASTER DEM data (30 m) for panels (a) through (e). Panel (f) shows the topographic domain height (meter) using MODIS land cover (1 km) and ASTER DEM (30 m) data with cosine correction

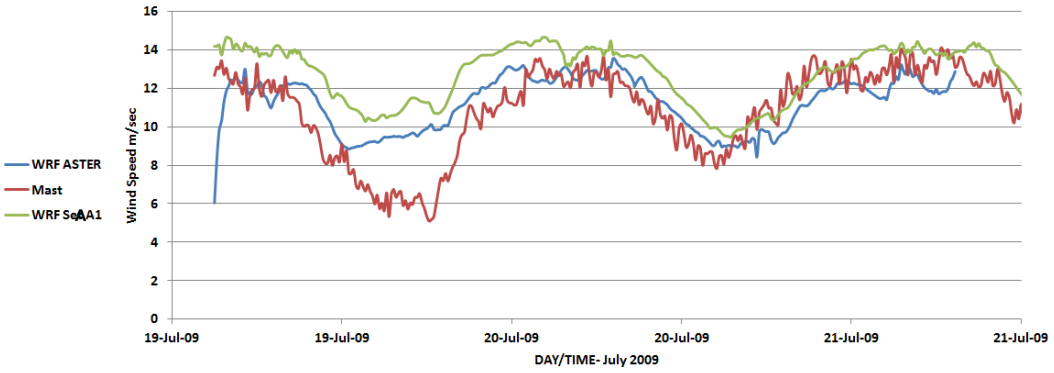

Figure 5.10 Wind speed comparison between mast A observations and WRF output at 39 m above the surface using data from ASTER DEM (30 m) and MODIS land cover data (1 km) with WRF grid spatial resolution of 1 km.

5.2.5 Influence of Different Initialization Fields

The WRF model has also been tested with different initialization fields from different sources specified in section 4.3.12. In addition to these data sets, the model has also been tested with the Global Forecast System's (GFS) 0.5° data (National Centers for Environmental Prediction 2007) using the configuration in Table 5.2 but there were

no significant differences in wind speed and direction compared with the results of WRF using set A1.

Considering the facts mentioned in section in 4.3.12, the assimilation of ERA-Interim data was selected to conduct several additional numerical experiments. The configuration used for these experiments along with the relative positions of the domains with respect to the masts are shown in Table 4.1 and Figure 4.11 respectively. Table 4.1 is reproduced for the convenience of the reader.

Configuration 4 domains 36 model levels	**Domain size (km x km)**	**Geographic resolution**	**Grid resolution (km)**	**Time step (s)**
1	1593 x 1593	10'	27	30
2	918 x837	5'	9	10
3	459 x 297	2'	3	3.33
4	126 x 82	30"	1	1.11

It should be noted here that both grid and geographic resolution were changed in domain 4 compared to Table 5.2. The terrain complexity suggested to use a smaller geographic resolution for improved surface wind prediction. The resolution of the inner most domain was increased to avoid the presence of a mountain at the edge of the domain and allow three masts to exit in the inner most domain. This will require the resolution in vertical level to be increased. In the final configuration of the WRF model over East Africa the vertical resolution was not increased therefore time step had to be adjusted to fulfil the Courant-Friedrichs-Lewy (CFL) criteria[14]. A highly resolved boundary layer (say ~15-20 levels below sigma=0.9) may require a smaller time step since it will be easier to violate this criteria[15].

The comparison of wind speed and direction obtained from these data sets are shown in Figure 5.11 and Figure 5.12, while the complete set of measured and modelled mean values and associated statistics are provided in Table 5.7. It is evident from these results that the wind speed deviation from the *in-situ* measurements occurring on the 19th of July 2009 was improved at all three masts. Predicted wind speed RMSE was improved by 13 % in case of mast A, 3.8% in case of mast B and 0.5 % in case of mast C when using ERA Interim data. Wind direction RMSE was improved by 1 % in case

[14] https://en.wikipedia.org/wiki/Courant%E2%80%93Friedrichs%E2%80%93Lewy_condition
[15] http://forum.wrfforum.com/viewtopic.php?f=8&t=357

of mast A and 3.8 % in case of mast B. However, the wind speed bias between measured and observed wind speed, compared between ERA-Interim data and NCEP data, reduced by 62 % in case of mast A and 6.8 % in case of mast B. Additionally, using ERA-Interim data instead of NCEP data, a 40 % reduction in error between observed and modelled wind speeds is achieved. In practical terms, this improvement corresponds to an estimated potential annual power generation improvement of 285GWh for a 1625 GWh per annum facility under construction at Lake Turkana.

The primary reason for this improvement is that ERA-Interim data set has a higher horizontal and vertical resolution compared to any other data sets evaluated[16]. The data set has improved physical parameterization schemes, being a third generation reanalysis, and is therefore considered to be reliable for predicting near surface winds. It was found to be the superior source of reanalysis data alternatives when judged by correlation with high-quality wind speed measurements from tall towers (Brower et al., 2013)

[16] http://rda.ucar.edu/index.html#!lfd?cmp=083.2&cmp=627.0 accessed 08/08/2014

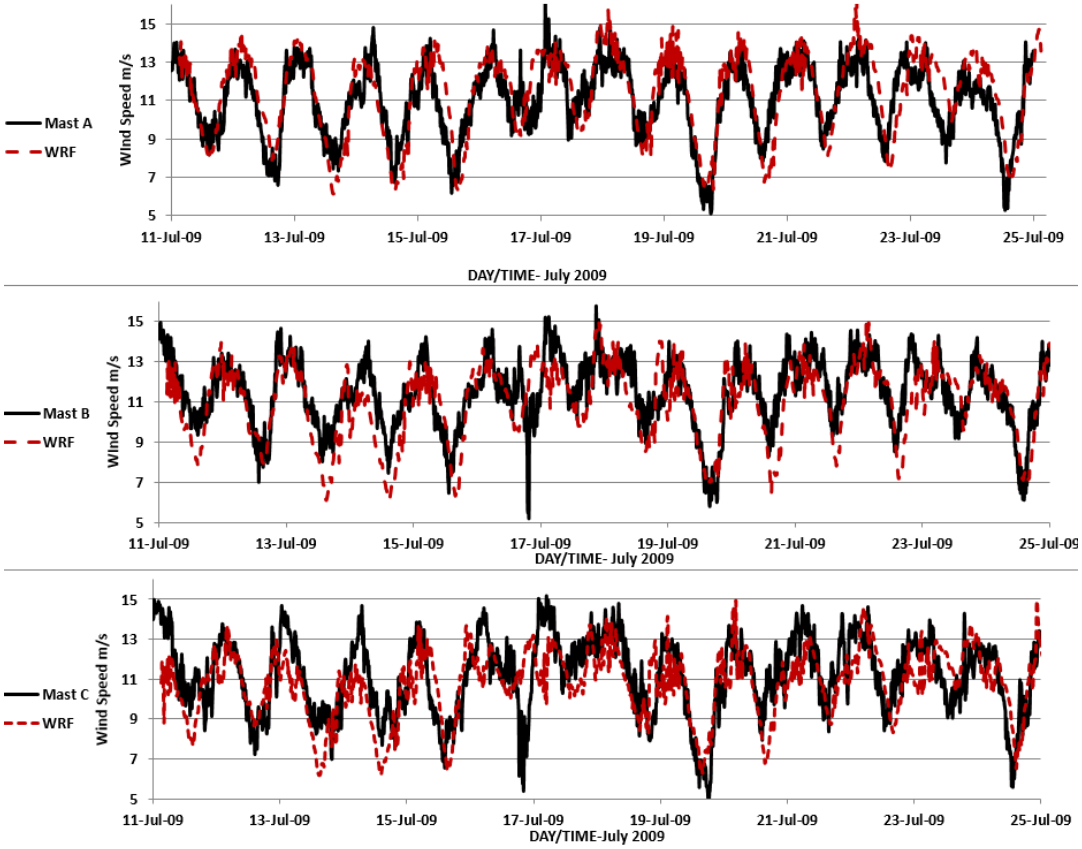

Figure 5.11 Comparison of wind speed observations for the masts (A, B and C) with WRF predictions at 39 m, 38 m and 46 m above the surface respectively using ERA-Interim initialization fields

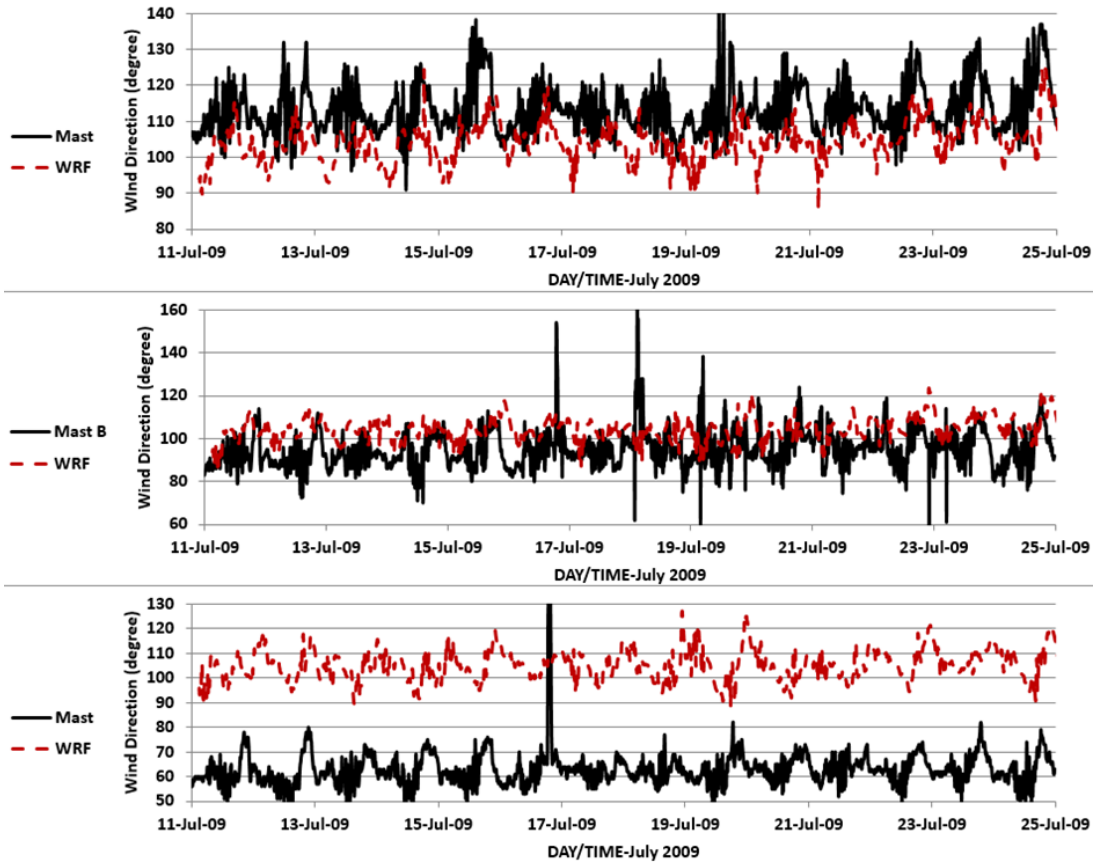

Figure 5.12 Comparison of wind direction observations for the masts (A, B and C) with WRF predictions at 39 m, 38 m and 46 m above the surface respectively using ERA-Interim initialization fields (the wind direction in calibration of mast C was in error by ~ 40 degree)

	Wind speed					Wind direction				
Mast A vs WRF	**Modelled mean (m/s)**	**RMSE (m/s)**	**CC**	**BIAS (m/s)**	**%BIAS**	**Modelled mean (degree)**	**RMSE (degree)**	**CC**	**BIAS (degree)**	**%BIAS**
NCEP initialization fields	11.31	1.7	0.56	+0.28	+2.54	103.7	12.1	0.2	-9.54	-8.4
ERA-Interim initialization fields	11.38	1.66	0.69	+0.35	+3.2	104.3	12	0.4	-8.7	-7.6
Mast B vs WRF										
NCEP initialization fields	10.94	1.82	0.48	-0.5	-4.4	102.95	13.73	0.05	+17.87	+8.3
ERA-Interim initialization fields	10.96	1.75	0.57	-0.47	-4.1	104.47	13.23	0.24	+9.6	+10.13
Mast C vs WRF										
NCEP initialization fields	11.35	1.89	0.45	+0.14	+1.28	105.6	43.57	0.17	+42.6	+67.8
ERA-Interim initialization fields	10.75	1.9	0.48	-0.44	-3.9	105.15	42.96	0.37	+42.3	+14.8

Table 5.7 Wind speed and direction comparison statistics for mast (A, B and C) observations and WRF predictions at 39 m, 38 m and 46 m respectively using NCEP and ERA-Interim initialization fields

The comparison of Weibull distributions for masts A, B and C and WRF's output at these locations is shown in Figure 5.13. Considering Weibull distribution are merely cumulative and are independent of temporal simultaneity of the measured and simulated wind speeds, the simulation with a lower error in mean wind speed tends to yield a Weibull PDF curve closest to the observations. When the simulated wind speeds are overestimated by the model there is a visible shift of the model's PDF towards the right side of the wind speed axis relative to the observed values. This means that the low wind speeds are underestimated by the model while high winds are overestimated by simulations as has occurred for mast A observations. At mast B the shift is towards left and the model is overestimating lower wind speeds while underestimating high winds. Similarly, at mast C, the model is shifted towards the left and the model is overestimating low winds compared to mast B observations. Table 5.8 shows the average of the wind speed profile α and the deviation of the wind speed β around the mean for modelled and observed wind speeds (α and β are defined in section 2.5). Mean wind speeds are also provided while, separately, the wind power density is calculated to show that a difference of 10-12 % is observed between predicted power and the actual power available for these locations on this site [see Figure 3.6].

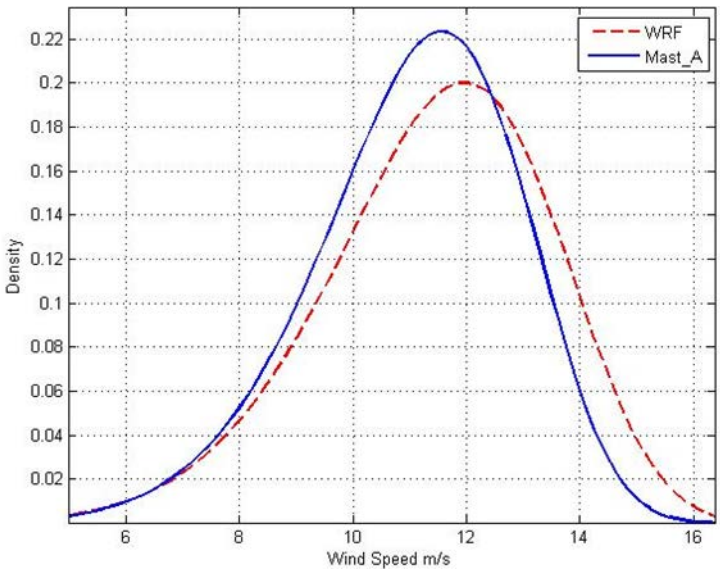

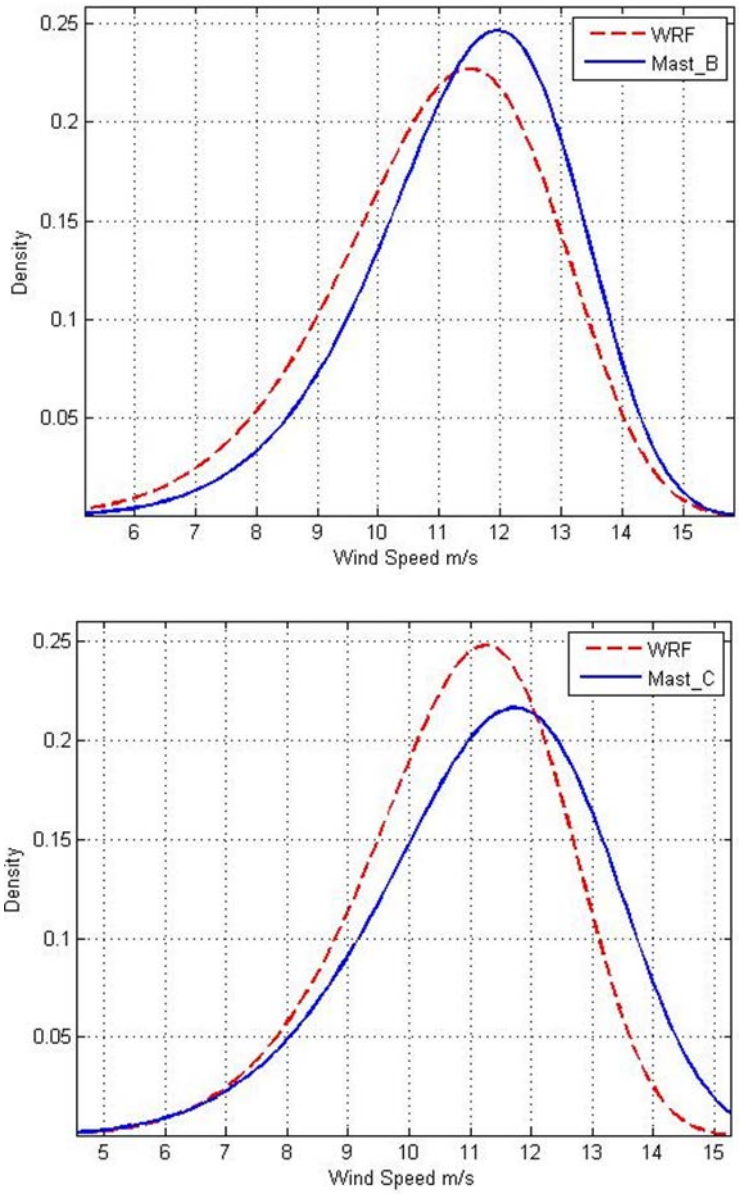

Figure 5.13 Comparison of Weibull distribution for mast (A, B and C) observations and WRF output respectively at 39 m, 38 m and 46 m above the surface using ERA-Interim initialization fields

	α (m/s)	**β**	**Mean wind speed (m/s)**	**Wind power density (W/m^2)**
Mast A	11.81	7.09	11.03	907.27
Mast B	12.15	8.07	11.44	888.84
Mast C	11.99	6.98	11.20	931.58
WRF A	12.25	6.58	11.38	813.51
WRF B	11.73	7.17	10.96	798.58
WRF C	11.45	7.66	10.75	817.71

Table 5.8 Weibull PDF parameters, mean wind speed, wind power density and wind speed bias averaged for mast (A, B and C) observations and WRF output respectively at 39 m, 38 m and 46 m above the surface using ERA-Interim initialization fields

5.2.6 Comparison of Wind Speed Time Series from Optimized WRF model Configuration and CDL at Lake Turkana Site

The results obtained from optimized WRF configuration were compared with the data from CDL to further strengthen the postulates presented in the modelling exercise. Figure 5.14 shows the comparison of wind speed between masts, WRF optimized output and CDL while a statistical analysis of the comparisons is tabulated in Table 5.9.

Generally, a poor correlation won't just relate to amplitude (i.e. two in-phase signals that have a constant relationship in amplitude will have a CC of 1.0) but maybe could arise from possibly a phase offset or just an uncorrelated model output.

It is observed that mast A has CC of 0.6 and RMSE of 1.27 m/s, which compared to other masts, is rather better comparison. The reason for inferior correlation between CDL and WRF model output at mast A location is that CDL retrieved vectors may have larger deviations at perpendicular directions as the fact that it measures only radial component. Therefore, this deviation from the WRF model output could be due to the fact that mast A site is quite near perpendicular direction. Though the error in the forecast at the location of mast A has been improved through terrain complexity, ingesting satellite data and ERA-Interim initialization fields experiments but still there is deviation compared to CDL measurements. The model, when using set A1 parametrizations, is overestimating high winds at the location of mast A (Figure 5.13) which might be a source of deviation from CDL measurements.

Mast B is located, roughly 2 km south west of CDL on a narrow ridgeline running approximately north south. The unusual shape and orientation of the ridge line is a reason for the problems in modelling and data collection by CDL as it can subject to sporadic wind gusts and rapidly changing wind directions. CDL derived wind speed measurement is not located exactly at the mast, both in the horizontal and vertical planes. As a result, there is the potential for differences in measured values arising from landscape induced turbulence and windshear. These effects were evident in the comparison of the low level Lidar scans and mast anemometer analysis at the mast B. Due to sporadic wind gusts, a poor correlation is seen between CDL and WRF output at mast B.

Sutton et al. (2010) reported that the direction correlation coefficients between mast A and B, and A and C, are much lower than between A and C, at only 0.78 each. This means the fraction of the variance from other influences is 39%. Overall, it appears that measurements at mast C site are sampling a significantly different wind regime. This factor should be considered in any model validation analysis. The WRF implementation using ERA-Interim experiments also revealed that the wind direction in calibration of mast C was in error by ~ 40 degree. The WRF model overestimated low winds at this location compared to mast B observations, for which we see the poor CC and RMSE between WRF and CDL.

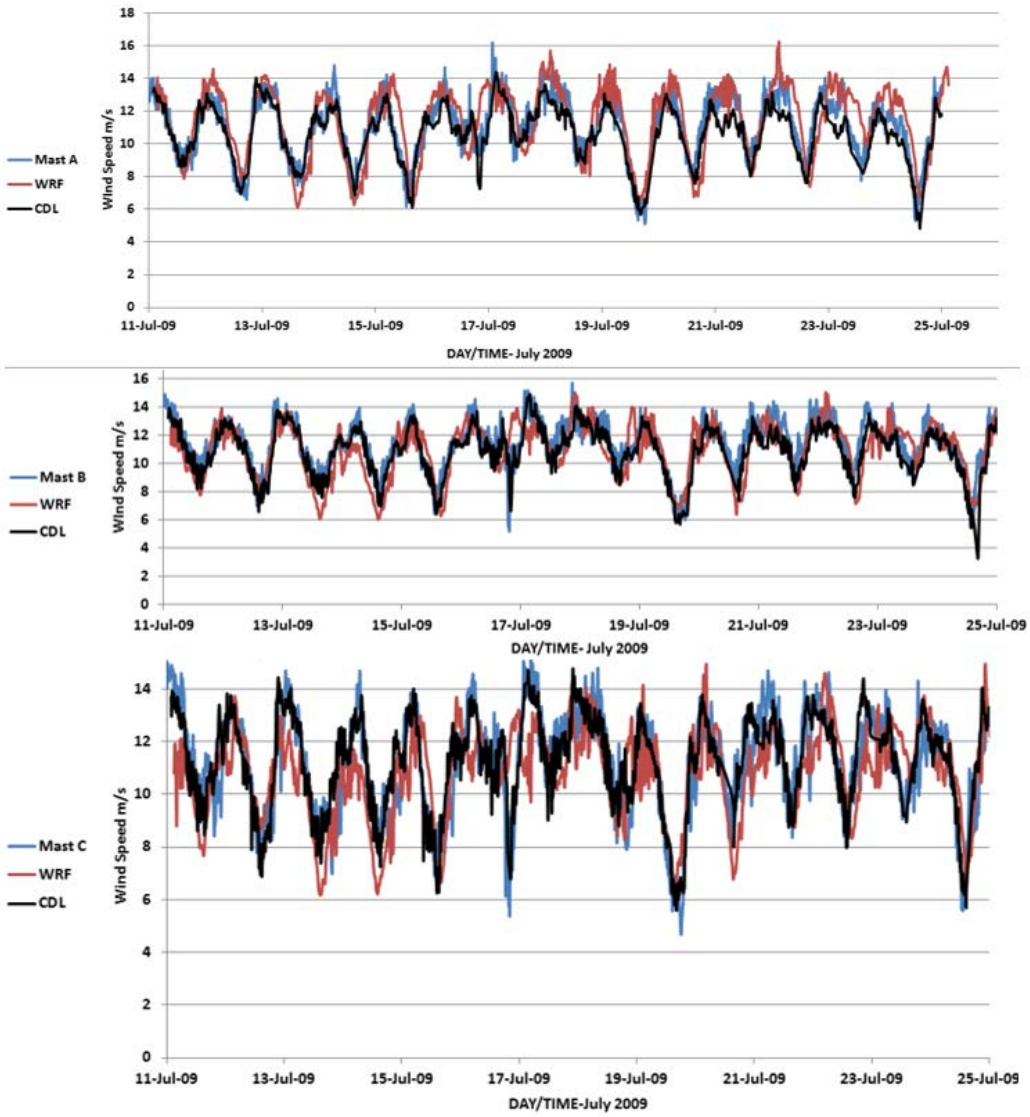

Figure 5.14 Comparison of wind speed observations for mast (A, B and C), with WRF and CDL outputs at 39 m, 38 m and 46 m above the surface respectively using ERA-Interim initialization fields

WRF modelled wind speed vs CDL observed field	WRF mean (m/s)	CDL mean (m/s)	RMSE (m/s)	CC
Mast A location	11.38	10.5	1.27	0.6
Mast B location	10.96	10.85	1.87	0.53
Mast C location	10.75	11.19	1.65	0.57

Table 5.9 Wind speed statistics for WRF output at 39 m, 38 m and 46 m above the surface using ERA-Interim initialization fields and CDL at 45 m

At the Lake Turkana site, the CDL generated a hub height terrain following layer wind map that was compared with the WRF model generated wind map. Such a spatially resolved wind map comparison may aid developers to gain a more complete understanding of the spatial variation of winds within a prospective wind farm. The regions of high wind speeds may be easily located and compared via visual inspection.

In Figure 5.15 a comparison of CDL terrain following wind map and a wind magnitude map generated by WRF is presented. The magnitude of wind vector on both these maps is expressed in m/s. The direction of wind on the WRF generated map is identified with wind barbs. Figure 5.15 (b) expresses the detail of this comparison, where the CDL generated wind is expressed as arrows. The colours of the arrows display the magnitude of wind vector which is indicated using the legend in Figure 5.15 (c). The colours in the matrix in Figure 5.15 (b) represent the wind speed magnitude determined using WRF and is clarified by the legend. It is obvious from visual inspection that since WRF is looking into a coarser resolution with less detail of topography, the magnitude of wind shown by CDL is a bit higher at point 1 in Figure 5.15 (b) while there is more agreement between the two at point 2 and 3. It is worth mentioning here that these plots were generated with convolved code developed in NCL.

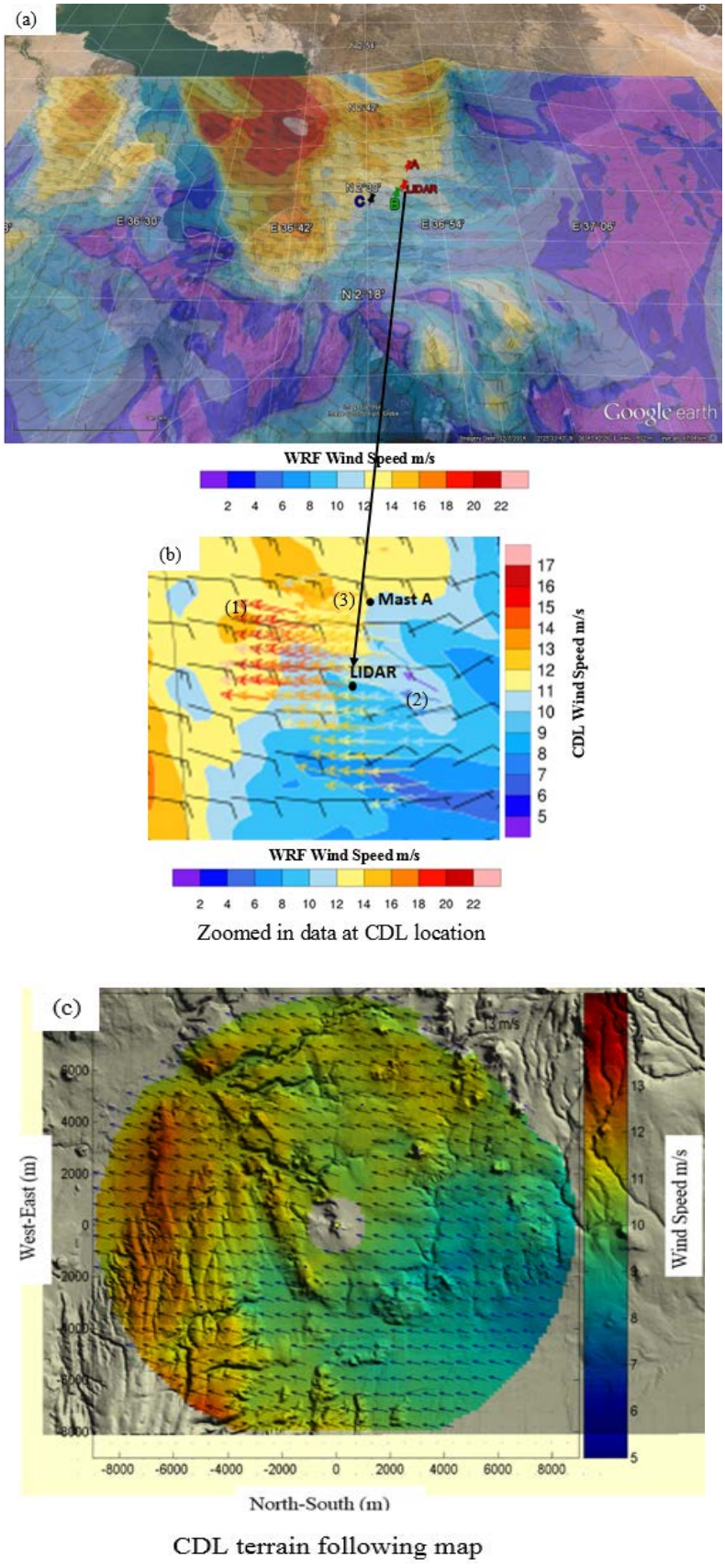

Figure 5.15 (a) Comparison of CDL scan with the model generated wind map (time UTC 11/07/2009 00:00) (b) CDL location is zoomed to clarify comparison; CDL terrain following map Figure 5.15 (c) overlayed on model generated wind map; arrows represent wind vectors while directions are shown by wind barbs (c) CDL generated wind map on a terrain following layer at hub height

The second suite of code developed in NCL helped to specify the discrepancies in the wind speed CDL data which were not evident in the retrieval from the MATLAB® code developed at DER. At the location of mast A, there existed errors at three points in the wind speed data retrieved from software developed in NCL code which caused an erroneous percentage increase of 23.65 % in the wind speed RMSE and a reduction of 13.41 % in CC when compared with the wind speed from MATLAB® code. These problems occurred due to a change in the scanning strategy and the existence of clouds on 21/09/2009 (point 2 in Figure 5.16) and 23/09/2009 (point 3 in Figure 5.16). The CDL was restarted on 16/09/2009 which caused the loss of observations for some hours on this day. Figure 5.16 presents the wind speed data at the mast A location with and without the use of linear interpolation.

It was believed that interpolation of the data might solve the problem but subsequently, it was agreed to break up the CDL data into three points where problems are occurring and then compare them with the wind speed predicted by WRF at the coordinates of some of the proposed turbine locations. These turbine locations were extracted from site source material prepared by Papadopoulos, (2010) and are shown in Figure 5.17. Four of these locations in the vicinity of CDL location were selected for comparison between CDL-observed and WRF-predicted wind speeds. These comparisons are shown in the form of time series plots of wind speed in Figure 5.18 to 5.21. Each of these figures is distributed into three events (identified as events 1, 2 and 3) shown in Figure 5.16. The statistics of the comparisons at the turbine locations between CDL-observed and WRF-predicted wind speeds are shown in Table 5.10.

What is learnt from this experiment is that removing unnecessary data from CDL data set has actually improved the CC to 0.86. The RMSE increased to 1.9 m/s at locations which are at a higher altitude. This establishes that the RMSE in the WRF simulation increases with an increase in altitude (Walterscheid, 2009).

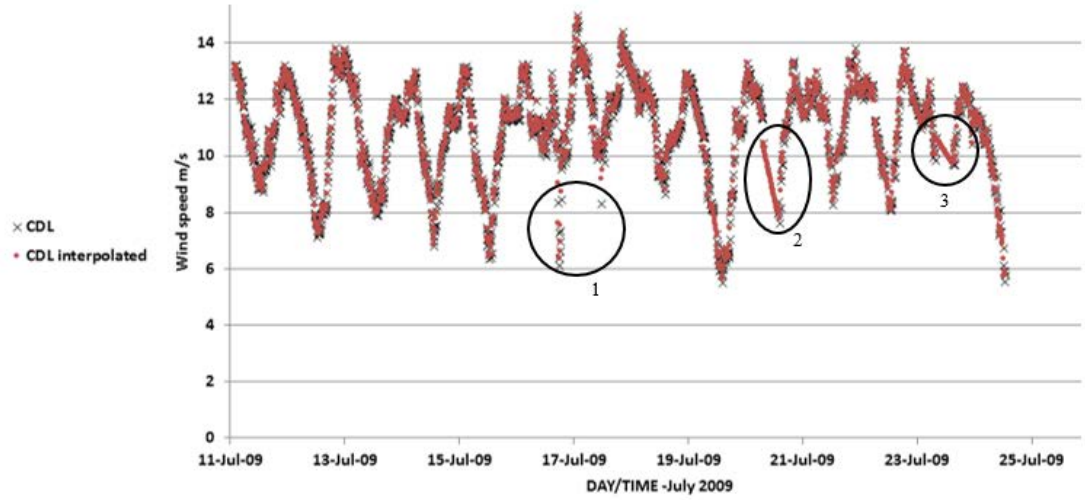

Figure 5.16 Comparison of CDL wind speed at mast A location with and without the use of interpolation with the NCL script. The events identified at the times shown (and identified here as 1, 2 and 3) represent the problematic areas

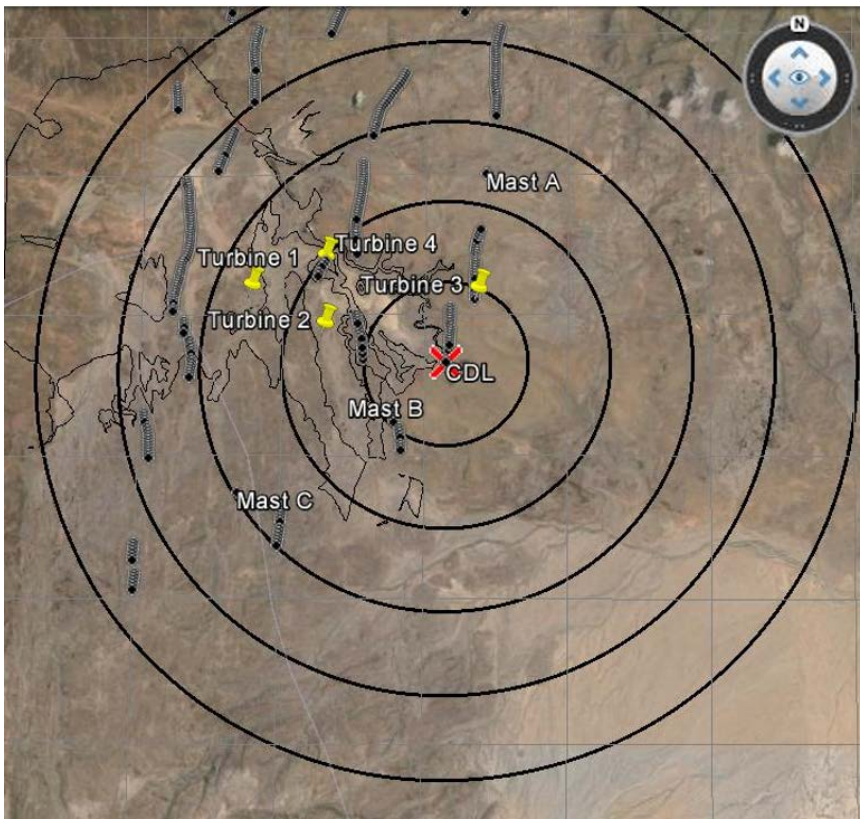

Figure 5.17 Locations of the turbines with respect to the CDL's location at Lake Turkana Wind Farm

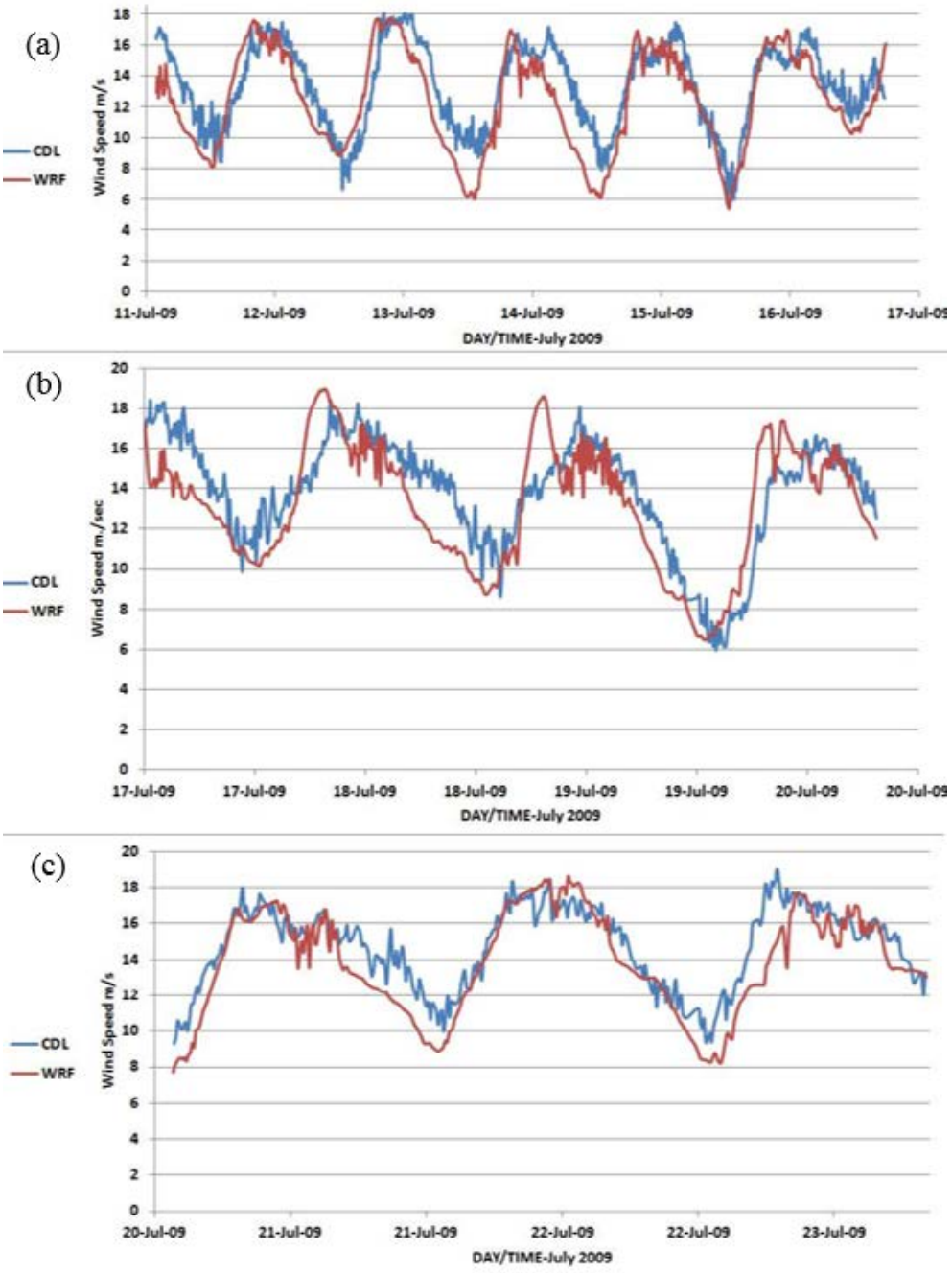

Figure 5.18 Comparison of CDL observed and WRF predicted wind speed at Turbine 1 location (lat 2.50392, lon 36.80472). (a), (b) and (c) refer to the CDL observed and WRF predicted wind speeds comparisons extracted at events (1), (2) and (3) identified in Figure 5.17

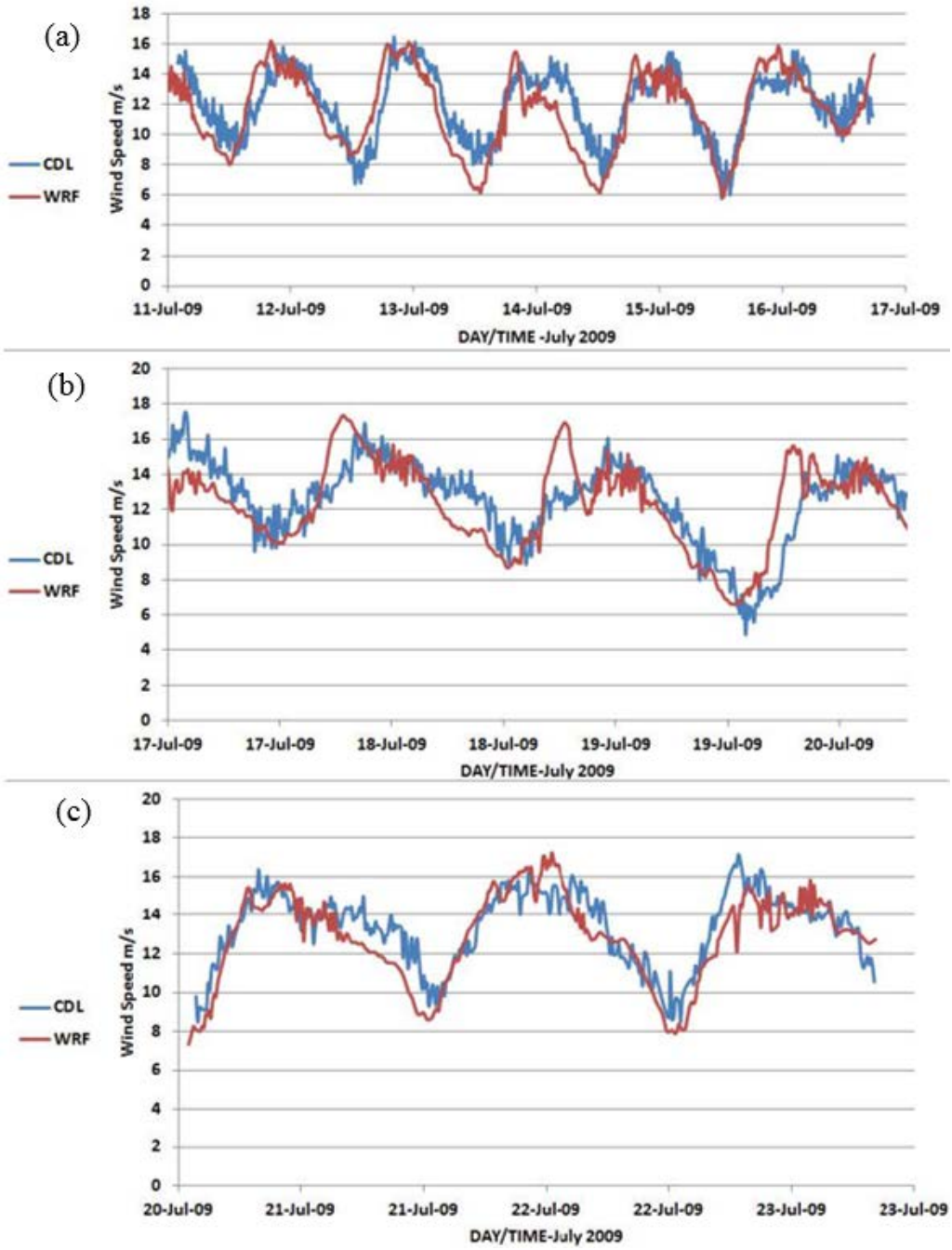

Figure 5.19 Comparison of CDL observed and WRF predicted wind speed at Turbine 2 location (lat 2.495347, lon 36.820832). (a), (b) and (c) refer to the CDL observed and WRF predicted wind speeds comparisons extracted at events (1), (2) and (3) identified in Figure 5.17

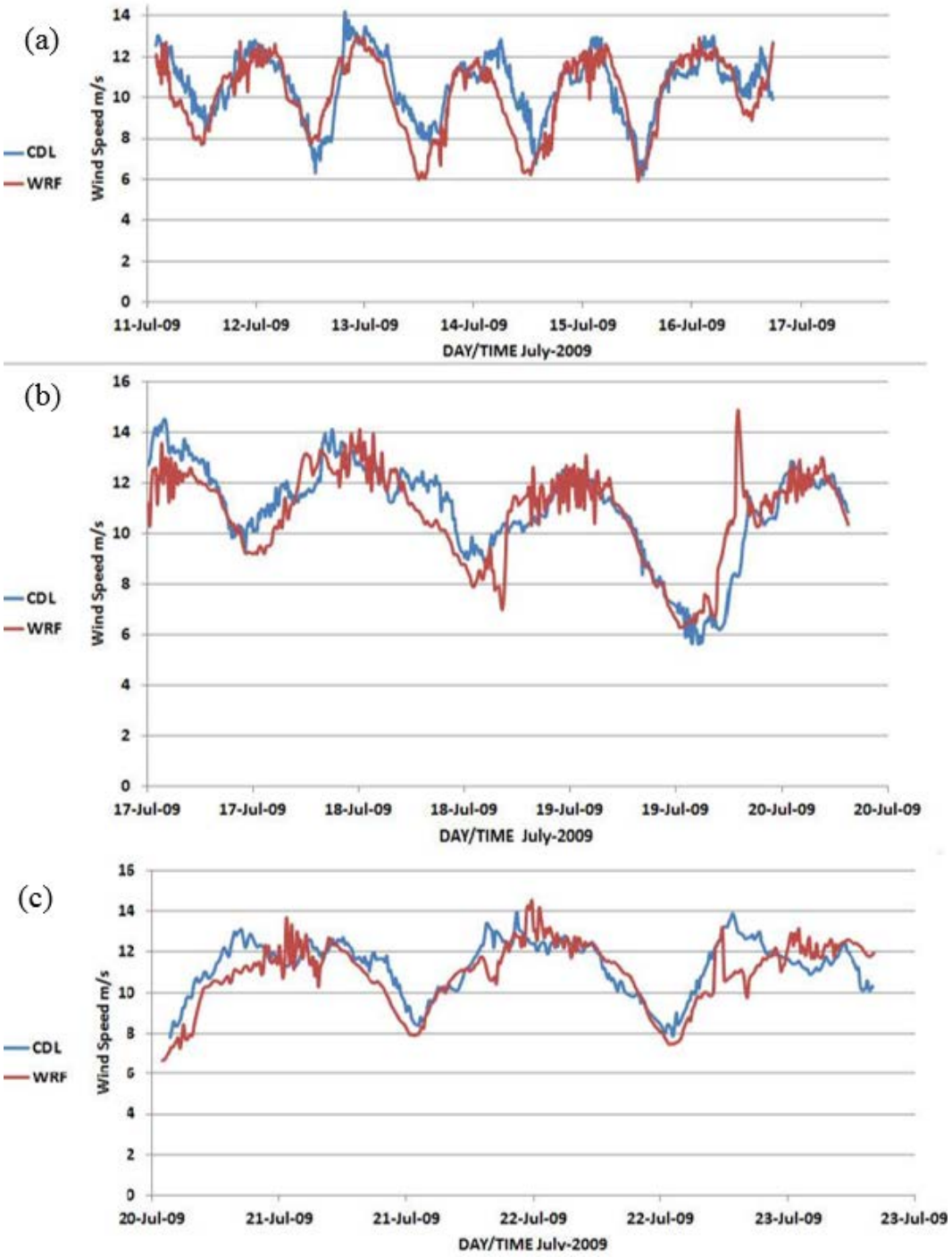

Figure 5.20 Comparison of CDL observed and WRF predicted wind speed at Turbine 3 location (lat 2.50303, lon 36.85451). (a), (b) and (c) refer to the CDL observed and WRF predicted wind speeds comparisons extracted at events (1), (2) and (3) identified in Figure 5.17

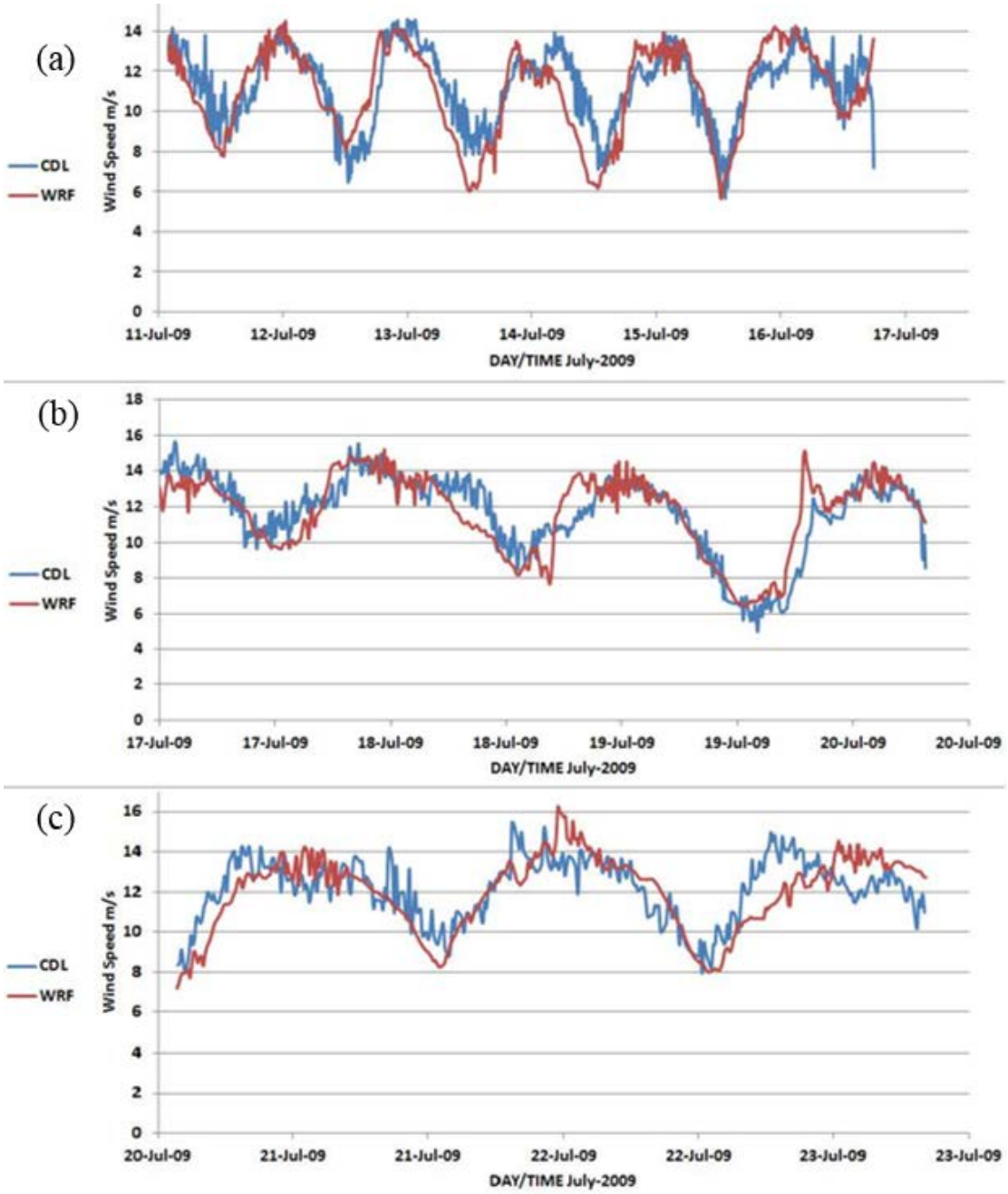

Figure 5.21 Comparison of CDL observed and WRF predicted wind speed at Turbine 4 location (lat 2.51037, lon 36.820843). (a), (b) and (c) refer to the CDL observed and WRF predicted wind speeds comparisons extracted at events (1), (2) and (3) identified in Figure 5.17

WRF modelled wind speed vs CDL observed field	Turbine 1 45 m (a.g.l)[17] [lat 2.50392, lon 36.80472]		
	height (m) above sea level	RMSE (m/s)	CC
Set 1	1016	1.93	0.84
Set 2	1016	1.98	0.79
Set 3	1016	1.5	0.9
	Turbine 2 45 m (a.g.l) [lat 2.495347, lon 36.820832]		
Set 1	814	1.59	0.81
Set 2	814	1.76	0.73
Set 3	814	1.23	0.86
	Turbine 3 45 m (a.g.l) [lat 2.50303, lon 36.85451		
Set 1	831	1.18	0.79
Set 2	831	1.14	0.81
Set 3	831	1.07	0.77
	Turbine 4 45 m (a.g.l) [lat 2.51037, lon 36.820843]		
Set 1	792	1.35	0.8
Set 2	792	1.23	0.84
Set 3	792	1.28	0.73

Table 5.10 Statistics of the comparison of wind speeds between CDL observed and WRF predicted winds at four of proposed locations of Turbines at the Lake Turkana wind farm. Set 1, 2 and 3 refer to the events identified as (1), (2) and (3) in Figure 5.17.

5.3 Summary

This chapter describes in complete detail the sensitivity study undertaken at Lake Turkana wind farm in order to optimize WRF's configuration for this particular region characterised by complex terrain. The experiments were directed at answering several of the research questions, specifically c, d, e and g that were posed in Chapter 1.

This study showed that it is possible to tune WRF in a given region (complex terrain in Lake Turkana) using particular set of physical and parametrization schemes. Consequently, the accuracy of the WRF model is improved when compared to both masts observations and CDL measurements. These conclusions are significant for

[17] a.g.l stands for above ground level

development of an efficient short term forecasting system in the sense that once an optimal configuration is achieved for a particular location it may be used as an input to a microscale model. It was learnt through the WSDSA analyses that WRF is most influenced by the initialization fields. In the East African region, the particular use could provide up to a 40 % improvement in wind prediction.

CDL has proven to perform better than meteorological masts in supporting short term forecasting due to its capability to both, capture the complete spatial and temporal structure of wind field and its large area coverage (including model constraining elevated winds). The spatial and time series comparisons of CDL data with WRF predictions established further confidence in WRF-predicted wind fields through WSDSA. The effect of the wind speed magnitude and direction sensitivity to assimilated meteorological information was judged in section 5.2.2 to 5.2.5. The WRF implementation experiment established suitable set of parametrization and physical schemes for the complex site at Lake Turkana. The terrain complexity and satellite ingestion experiments provided the suitable grid and geographic resolutions while suitable initialization schemes were found to be ERA-Interim for this site. Consequently, the RMSE between mast observed and model predicted wind improved to 1.7 m/s and CC was improved to ~0.7 at mast A location. Emery et al. (2001) suggested that good model performance refers to RMSE $\leq$ 2 m/s between observed and modelled wind speeds. Even in complex terrain, like the current site, where this value could easily be contaminated by a relatively small number of larger errors, an RMSE of 1.7 m/s points the level accuracy archived for modelling of near surface wind speed.

A method for reducing the error in the forecast and validating it using the CDL data is presented in section 5.2.6. The method not only reduced the forecast error by improving the CC to 0.86 but it also pointed out the discrepancies in data retrieved by the CDL.

Chapter 6 . Meso and Micro Scale Model Coupling

6.1 Introduction

Short term forecasting is strictly related to the wind field within the wind farm's spatial scale. A decisive factor for determining the uncertainties in the expected wind energy production is the accuracy of wind flow field prediction. In case of a complex terrain, where the wind field varies extensively locally, realistic simulations of the wind require analysis on a spatial scale that is much smaller than those used in meteorological models. Numerical representation of the wind field in such an area is extremely challenging thus integration of a suitably parameterized microclimatic model into a forecasting system is necessary. Microclimatic or CFD models run at a higher spatial resolution representing in full detail the wind field within the wind farm scale.

This chapter describes WRF model's optimized configuration for predicting the spatial and temporal variability of the wind field at the Lake Turkana wind farm coupled with the specialized CFD code developed in OpenFOAM version 2.1.1. This coupling serves for improvement of wind field prediction in a small temporal scale and thus supports short term forecasting accuracy. The downscaling procedure from WRF to OpenFOAM is complex and is achieved through one-way interaction. It is a two-step procedure where WRF's three-dimensional output provides the necessary boundary conditions (i.e. wind velocity profiles) across the boundaries of the computational domain of the CFD model, OpenFOAM.

The first step involves converting WRF's pressure coordinate system to OpenFOAM's consistent Cartesian coordinate system. In the second step the fields are mapped from the pressure coordinate system to the Cartesian coordinate system i.e. the mesh points are moved to exact x, y and z coordinates and WRF's variables are unstaggered on a collocated grid. The term staggering, as used in this context, relates to the process of placing variables of a partial differential equation at different points in different grids; bringing them to one point is unstaggering This process generates the necessary input files for the OpenFOAM solver.

The OpenFOAM-based solver used in this study has been developed as part of a software package known as SOWFA (Simulator for On/Offshore Wind Farm

Applications) at the U.S. Department of Energy's National Renewable Energy Laboratory (NREL) for simulating wind energy generating plants. It is capable of performing LES and computing the atmospheric boundary layer flow and is known as Atmospheric Boundary Layer Terrain Solver (ABLTerrainSolver). The solver has the flexibility to use any of the OpenFOAM standard subgrid-scale models to simulate flow over the complex terrain.

Appropriate statistical methods have been implemented to correlate WRF output to three reference positions in the wind farm site at Lake Turkana. During this correlation procedure, a number of important parameters are included: wind direction, wind speed bias, diurnal variations and forecast horizon. Apparently, forecasts produced by WRF require a systematic correlation analysis between mast/CDL and reference position in the model. However, this strategy can be reversed, determining the appropriate inflow boundary conditions to the CFD model to match those at the reference positions in the wind farm. The output of this meso microscale coupling includes local predictions of wind speed within a time window of up to 30 minutes to 2 hours which can be directly used for short term wind farm power generation forecasting.

6.2 Boundary Layer Meteorology

Boundary layer meteorology includes the study of all types of surface–atmosphere boundary, including ocean, lake, urban land and non-urban land for the study of meteorology. Above this layer the free atmosphere responds very slowly to the surface events. The wind turbines extract energy from boundary layer winds, therefore near surface simulations require understanding of the processes in the boundary layer. Technically the boundary layer represents 10 % of earth's atmosphere and responds to the earth surface forcing within one hour.

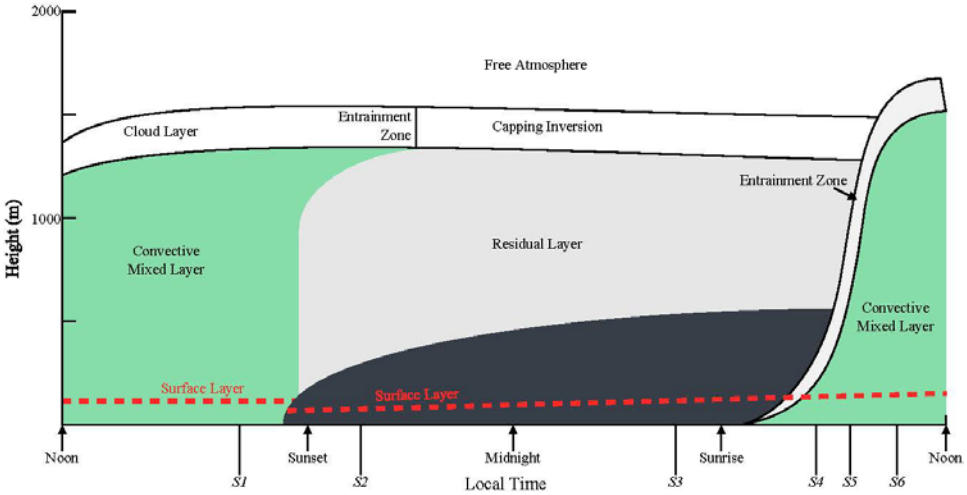

Figure 6.1 Components of the boundary layer near Earth's surface (Stull, 1988)

There are various sub-layers associated with boundary layer as depicted in Figure 6.1. The entrainment zone is a buffer region and the air from the free atmosphere enters the boundary layer through this region. A statically stable layer at the top of the boundary layer is called capping inversion which traps surface induced turbulence and causes the free atmosphere not to respond to the Earth's surface conditions. The mixed layer is characterised by uniform wind speeds and temperature plus turbulence in this region is determined by convection driven air parcels rising from the surface. The residual layer is the remaining part of mixed layer that forms shortly before the Sun sets and has much less turbulence. The stable boundary layer grows as the day ends and wind speeds near the surface are reduced. The lowest part of the boundary layer that most interests the wind modellers is the surface layer as it is the region of operation of wind turbines. The upper level winds are slowed down by the surface drag creating a wind shear i.e. the change of wind speed with height and causes mechanical turbulence (turbulence from physical contact with ground, vegetation, buildings, etc.). The intermolecular forces between the molecules stuck to the surface and the molecules adjacent to them are known as viscosity and this property combined with surface drag that slows the upper level winds through the entire surface layer creating the wind velocity profile characteristic of surface layer. The bottom of the surface layer is the microlayer which extends a few centimetres above the surface. The top of this layer has zero wind speed and is equivalent to the roughness height (Stull, 1988). Apart from mechanical turbulence the other source of surface layer turbulence is convective heat transfer and the variance of turbulence is approximately 10 % of the

overall magnitude of day time turbulence which is another defining surface layer characteristic.

If the atmosphere is considered to be comprised of parcels of air with different densities, the tendency is for those of lower density to ascend and those of higher density to descend and the fluid, in the absence of turbulent mixing is said to be stratified. The boundary layer stability refers to the response of the air parcels that have been displaced vertically. The boundary layer is statically stable if a parcel of air returns to its original height, is unstable if the parcel keeps moving in the direction of the original displacement and is neutral if there is very little convective turbulence. The static part of the definition refers to the absence of horizontal wind.

In order to quantify stability, a term called potential temperature is used in meteorology. This is the temperature a parcel of fluid at pressure P would acquire if adiabatically bought to a standard reference pressure P_0 usually 1000 hPa. The potential temperature is denoted by θ and for an air parcel at temperature T and pressure P in a given atmosphere, it is determined using:

$$\theta = T\left(\frac{P_0}{P}\right)^{\frac{R}{c_p}}. \tag{6.1}$$

where: P_0 = reference pressure level (1000 hPa)

R = universal gas constant, and

c_p = specific heat at constant pressure.

In terms of potential temperature, the stability of boundary layer is expressed as

Unstable $\frac{\partial\theta}{\partial z} < 0$ (6.2)

Neutral $\frac{\partial\theta}{\partial z} = 0$ (6.3)

Stable $\frac{\partial\theta}{\partial z} > 0$ (6.4)

6.2.1 Surface Layer Modelling

A fundamental model for external flow is flow over a smooth, flat plate (Figure 6.2). Boundary layer forms downstream from the leading edge of the plate and increases in height over its length where this height is a function of u_∞ (free stream velocity). The top of the boundary layer is the height, δ, above the plate where the velocity u of the air is:

$$u = 0.99 * u_\infty \tag{6.5}$$

There is no physical change to the flow near the top edge of the boundary layer and no-slip surface and a viscous force generates shear turbulence within the boundary layer. The increase in speed with height above the surface is shown by the velocity profile– see Figure 6.2.

Atmospheric flow is represented correctly with a rough wall boundary layer where mechanical turbulence is generated both by smooth wall shear and fixed objects on the surface. The ratio of the rough feature height to the boundary layer height, and the boundary layer turbulent structures are a function of rough wall features.

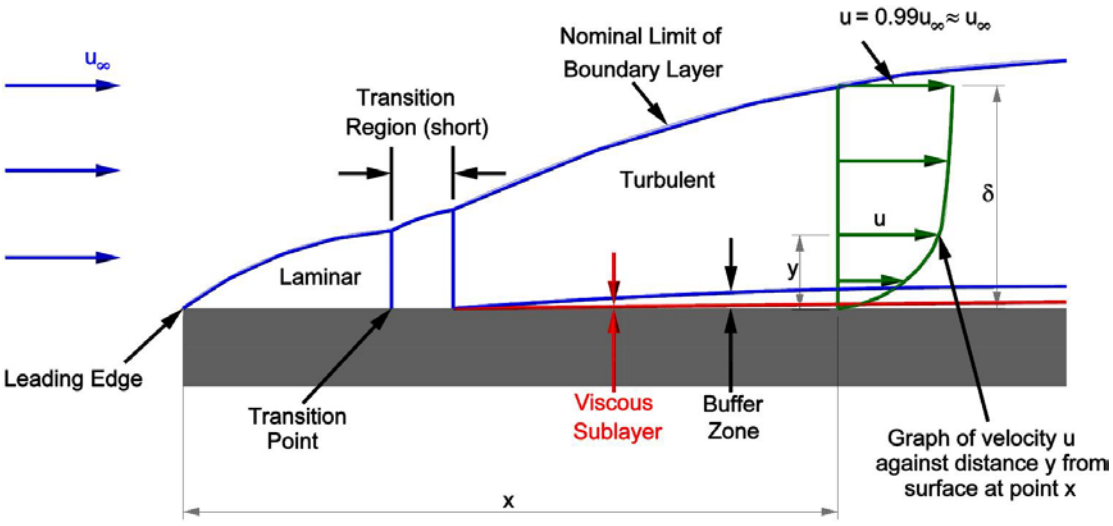

Figure 6.2 Schematic of boundary layer flow over a flat plate

Experimental and atmospheric boundary layer structure schematics are presented in Figure 6.3. If the wind farm site has significant roughness features, further investigation of rough wall turbulence would be of interest. The Lake Turkana wind farm, at regions where wind turbines are likely to be located, has relatively few

obstacles and therefore a roughness height of 0.02 m (Tapia, 2009) is appropriate. A day-time surface layer depth of 200 m is used in this study. The features to boundary layer height ratio, k/δ is therefore 10,000 while it is mentioned in Jiménez, (2004) that the critical value of this ratio for roughness to affect the entire boundary layer is 80. Hence, in this area, roughness does not affect turbulence through the entire boundary layer though there is certainly additional turbulence near the ground that diminishes rapidly with height in CFD simulations.

The structure of the atmospheric boundary layer is similar to that of a rough wall boundary layer. The surface layer depth is affected by surface topography and physical features like buildings and vegetation. Further, surface layer depth is altered by the upper part of the atmosphere and local weather systems.

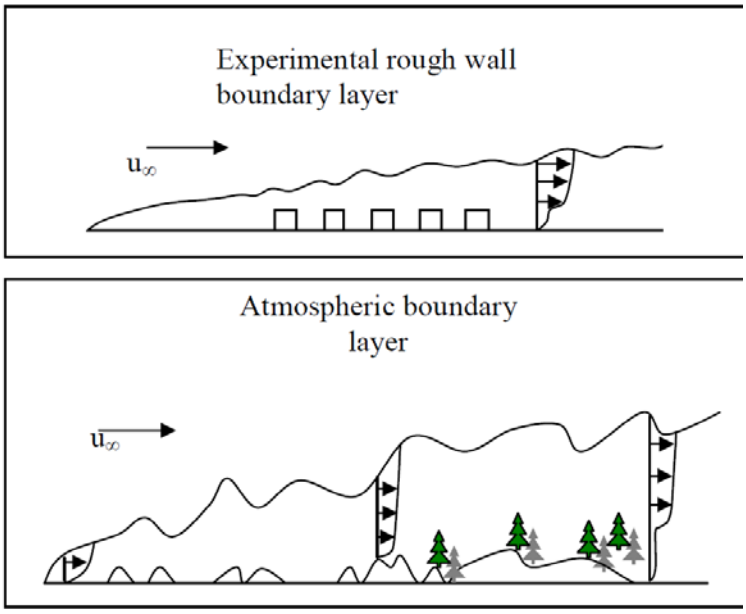

Figure 6.3 Rough wall and atmospheric boundary layer schematics (Russell, 2009)

6.2.2 Turbulence Modelling

Since real atmospheric flow is always turbulent, its modelling demands for the inclusion of turbulence. The set of partial differential equations describing turbulent motion are known as Navier-Stokes (NS) equations. NS equations govern the motion of the fluid and can be seen as Newton's second law of motion for fluids. NS equations represent the conservation of momentum and are solved together with continuity equation that represents the conservation of mass. These equations admit a limited number of analytical solutions and therefore, for complex geometries, they must be

solved numerically. Turbulence in the atmospheric boundary layer can either be modelled with Reynold's averaging (Stull, 1988). which decomposes turbulent terms into average and instantaneous components or through LES. The Reynold's Average NS (RANS) models turbulent structures as ensemble averages of the flow field. The equations for momentum and conservation of energy for atmospheric flows using RANS are derived in Stull, (1988).

The LES requires more computational power and directly resolves turbulent flow down to the large eddy level and models energy dissipation in small eddies. In LES the turbulent structures larger than mesh spacing are directly simulated while the structures smaller than this spacing are modelled with a sub-grid scale (SGS) model.

LES of the ABL requires the incompressible filtered NS equations to be solved using the Boussineq approximation for buoyancy along with the continuity equation, enforced usually through the solution of an elliptic equation for the pressure variable. The continuity and the momentum equations are

$$\frac{\partial \overline{U}}{\partial x_i} = 0 \tag{6.6}$$

$$\frac{\partial \overline{U_\iota}}{\partial t} + \frac{\partial\, \overline{U_j}\overline{U_\iota}}{\partial x_j} = -2\varepsilon_{ijk}\Omega_j\overline{U_k} - \frac{\partial \bar{p}}{\partial x_i} - \frac{\partial \tau_{ij}}{\partial x_j} + \rho_b \mathrm{g}_i \tag{6.7}$$

In these equations, the over bar denotes the LES filtering operation, $\overline{U_\iota}$ is the component of the resolved-scale velocity vector in the coordinate direction, x_i, ε_{ijk} is the alternating unit tensor, $\Omega_j$is the Earth's rotation rate vector at the point of interest on the Earth's surface (which is dependent on latitude), $\bar{p}$ is pressure, τ_{ij} is the SGS stress tensor, $\rho_b$is a scalar that dictates the sign and strength of the buoyancy force, and $g_i$is the gravitation vector (Churchfield et al., 2013).

Definition of $\Omega_j$arises from the fact that, due to planetary rotation, there is an apparent force called the Coriolis force and in Cartesian coordinates if positive x denotes east and positive y denotes north while z denotes the height of the domain then

$$\Omega_j = \omega \begin{bmatrix} 0 \\ \cos\varphi \\ \sin\varphi \end{bmatrix} \tag{6.8}$$

where ω(rad/s) is the Earth's rotation rate and φ is the appropriate latitude.

In order to computeρ_b, which is given by

$$\rho_b = 1 - \left(\frac{\bar{\theta} - \theta_0}{\theta_0}\right) \tag{6.9}$$

where $\bar{\theta}$ is the resolved-scale potential temperature and $\theta_0$is a reference temperature, a potential temperature transport equation must be solved and is given by equation 6.10.

$$\frac{\partial \bar{\theta}}{\partial t} + \frac{\partial \bar{U}_J \bar{\theta}}{\partial x_j} = -\frac{\tau\theta_i}{\partial x_i} \tag{6.10}$$

where $\tau\theta_i$ is the SGS temperature flux. In both momentum and potential temperature equations, the effects of molecular diffusion are not included because the SGS effects are much more dominant except extremely near to the surface. LES and ABL rely on appropriate surface model near the surface in which the temperature fluxes and viscous/SGS stresses are lumped together. This model will be discussed later in the study.

For turbulent flows, NS equations have more unknown variables than equations. This is known as closure problem. The closure problem requires model simplification for allowing the possibility of an algebraic solution or development of additional equations for turbulence and then using numerical methods for solving the closed equation set. Atmospheric flows require numerical solutions while closed form solutions exist only for laboratory models designed to fit the equations.

Closure methods are described by their order where the order refers to the level of approximation. Closure orders include zero, half, first, one and half and second orders and typical examples include the wind speed log law, lapse rate equation, k-ε models etc. LES is an example of higher order solution methods where the turbulent flow is directly resolved to the large eddy level.

Since the solver in this study is capable of handling both RANS and LES, where RANS uses the k-ε turbulence model and LES uses Smagorinsky, Dynamic

Smagorinsky and Langrangian-averaged scale-independent dynamic Smagorinsky (LASI) models [derived for atmospheric flows in (Russell, 2009) and (Churchfield et al., 2013) respectively]. It also includes a two wall shear stress model [(Schumann, 1975) and (Moeng, 1984)] as the surface of the Earth is covered with roughness elements (dirt, rocks, vegetation) that would be extremely expensive to resolve with a grid and it would be inappropriate to apply no-slip at the surface. It also includes volumetric symmetric tensor field that is zero on the interior and only takes on a value on patches in which the wall shear stress boundary condition is applied. The surface stress model predicts total stress at the surface and assumes that first cell centre away from surface lie within surface layer of the ABL. So at the surface

$$\begin{bmatrix} 0 & 0 & \tau_{13}^{tot} \\ 0 & 0 & \tau_{23}^{tot} \\ \tau_{13}^{tot} & \tau_{23}^{tot} & 0 \end{bmatrix} \tag{6.11}$$

Therefore, the wall models τ_{13}^{tot} andτ_{23}^{tot}.

The total temperature flux at the surface is modelled using a similar approach using

$$\begin{bmatrix} 0 \\ 0 \\ q_3^{tot} \end{bmatrix} \tag{6.12}$$

Total average temperature flux, Q_s, is specified and the wall model creates the fluctuating temperature flux q_3^{tot} or the surface heating/cooling rate is specified and q_3^{tot} is calculated (Basu et al., 2008).

6.3 Buoyancy Effects in Atmospheric Flow Modelling

Surface heat flux during the day affects the boundary layer flow significantly. Thermal energy is transferred into the air near the surface as the sun heats the ground, consequently the near surface air becomes more buoyant and tends to rise adding significant turbulence and changing the wind profile in the surface layer (Figure 6.1). The patterns of wind changes between night and day because of local surface heating. Seasonal and diurnal variations are contained by heat flux variations. The low surface

heating in winter completely changes the makeup of the boundary layer. The buoyancy effects are incorporated into the simulation in this study by term ρ_b in equation 6.7.

6.4 Methodology

The methodology adopted to conduct the coupling experiment is a combination of the standard CFD procedure and unstagerring the WRF grid to provide boundary conditions to the CFD model. The final CFD model for this project is the LES model, including the buoyancy and Coriolis forces, using Smagorinsky turbulence closure with modified constants for the atmosphere and Boussinesq approximation for density. The selection of the parameters for the experiment will be discussed in the relevant sections while the general steps followed are listed below. The goal is to provide enough information so that someone with a basic understanding of fluid dynamics and some background in atmospheric science can make a surface map mesh and gather and process wind data and have all of it to run in OpenFOAM.

- Pre processing
- Mesh generation and discretization
- Coordinate conversion
- Unstaggering WRF variables on a collocated grid
- Solver
- Post processing

6.4.1 Work Flow in OpenFOAM

It is important to provide a brief introduction to the work flow in OpenFOAM (Open Field Operation and Manipulation) before the process of coupling is explained. OpenFOAM was developed at imperial college in the 1980s and is C++ based and was released under GNU's Not Unix (GNU) General Public License in 2004. The overall workflow is explained in Figure 6.4.

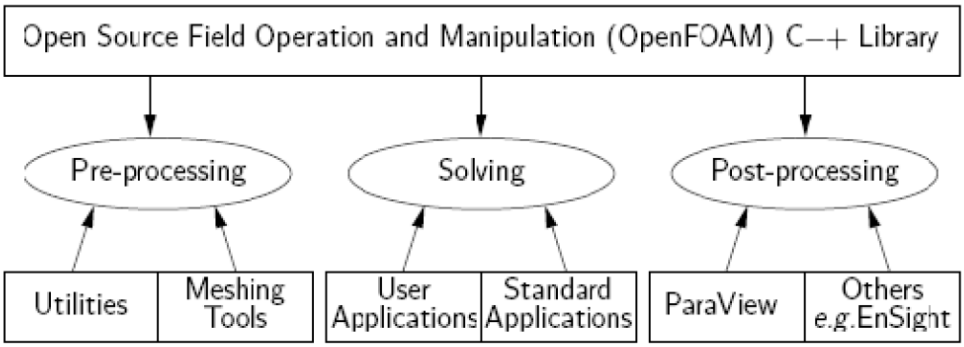

Figure 6.4 OpenFoam structure. [Source: OpenFOAM User Guide]

A typical case is setup in OpenFOAM using the directory structure shown in Figure 6.5. The System folder contains three files; controlDict controls I/O data and running parameters, the fvSchemes file includes the laplacian, divergence and so on are solved numerically while algorithm controls are set in fvSolution. The Constant folder contains two files and two folders. The fluid properties are included in the transportProperties file while the turbulence model and its parameters are set in the turbulenceProperties file. The Polymesh folder contain all the data for the mesh while the information about a complex 3D geometry is stored in TriSurface folder. The boundary conditions for the simulation are defined in the 0 folder. The Time directories contain the data for the particular fields such as initial values and boundary conditions or results.

Name	Size	Type
H	3 items	folder
0	7 items	folder
epsilon	1.4 KB	C source code
k	1.4 KB	C source code
nut	1.4 KB	C source code
nuTilda	1.3 KB	C source code
p	1.3 KB	C source code
R	1.4 KB	C source code
U	1.4 KB	C source code
constant	4 items	folder
polyMesh	1 item	folder
blockMeshDict	1.4 KB	C source code
triSurface	1 item	folder
terrain.stl	1.1 GB	plain text document
RASProperties	935 bytes	C source code
transportProperties	1.3 KB	C source code
system	5 items	folder
controlDict	1.3 KB	C source code
fvSchemes	1.8 KB	C source code
fvSolution	1.9 KB	C source code
sampleDict	1.2 KB	C source code
snappyHexMeshDict	10.4 KB	C source code

Figure 6.5 Directory tree and contents of an OpenFOAM case where H is the user defined name of the case.

6.4.2 Pre Processing

The subsequent transformation of the input to a suitable format for the solver is provided to CFD program by means of an operator-friendly interface is known as the Pre-processing. Generally, the user activities at this stage involves:

- Definition of the region of interest known as the computational domain.
- Dividing the domain into a number of smaller cells and subsequently into nodes (point where two vertices intersect) is knowns as grid generation or mesh definition.
- Selection of physical and chemical phenomena that need to be modelled.
- Definition of the fluid's properties.
- Specifications of appropriate boundary conditions at cells which coincide with or touch the domain boundary.

At each node inside each cell, the solution to the flow problem is defined. CFD accuracy is dominated by the number of cells in the grid and obviously a larger number of cells will increase CFD accuracy. Solution accuracy and its computational cost are dependent on the fineness of the grid. An optimal mesh is supposed to be non-uniform, finer in areas where large variations occur from point to point and coarser in regions with relatively little change. Over 50% of time spent in industry on a CFD project is spent on domain geometry definition and grid generation.

6.4.2.1 Surface Model Generation

Atmospheric modelling over variable surface terrain requires a reasonable process for transforming a topographical map into a surface mesh. The data from Shuttle Radar Topography Mission (SRTM) (Jarvis et al., 2008) was downloaded for the Lake Turkana Wind Farm region. This data is available in TIFF format on the USGS website with a resolution of approximately 90 meters with the user providing the latitude and longitude of the area (Figure 6.6).

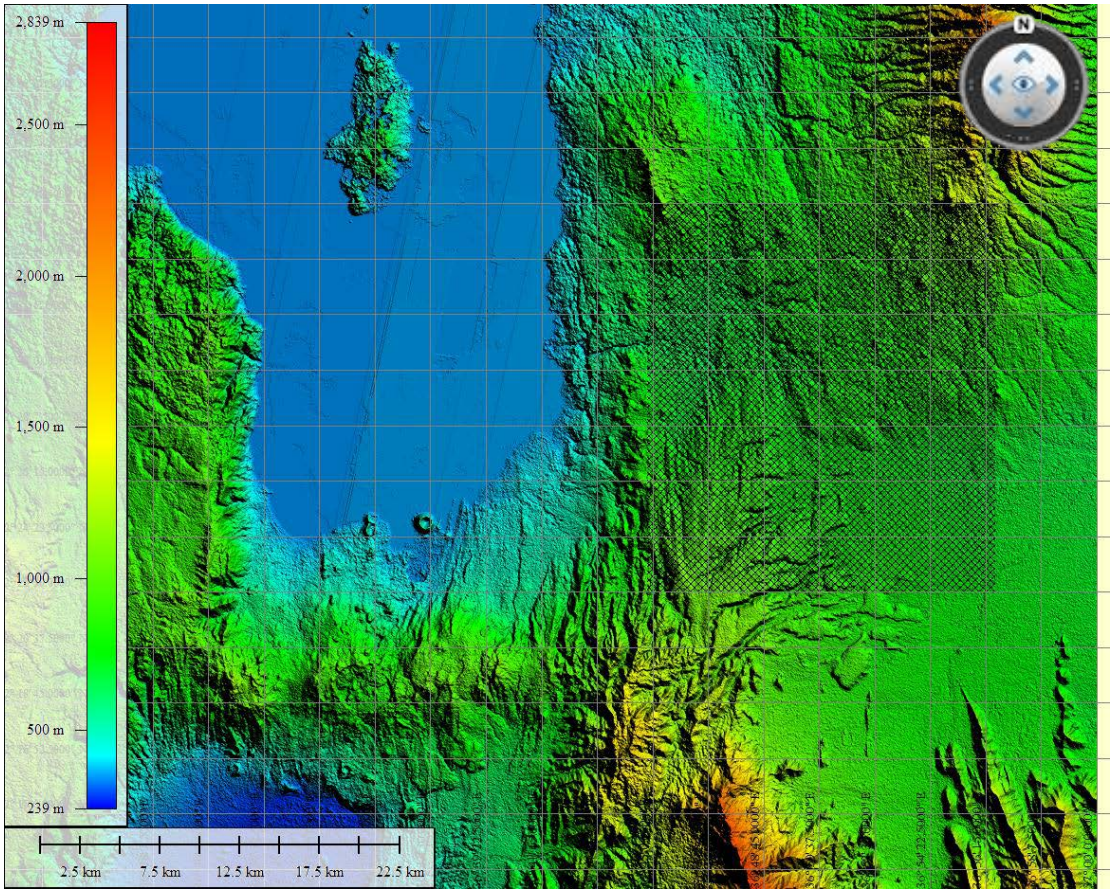

Figure 6.6 SRTM data downloaded from http://dds.cr.usgs.gov/srtm/version2_1/SRTM3/Africa/N02E036.hgt.zip. The checkered rectangle shows the Lake Turkana Wind Farm location

This data is imported into the Global Mapper software which generates the stereolithographic (STL) file required for the surface model. Since OpenFOAM uses a Cartesian coordinate system, the coordinates are changed from Geographic to the Universal Transverse Mercator (UTM) coordinates. The datum selected is WGS 84 and the zone selected is 37 N. The initial size of the domain selected for this experiment was 17 km x 20 km similar to the DEM generated by the LIDAR. The final model after treatment of edges in Rhinoceros 5 software is shown in Figure 6.7.

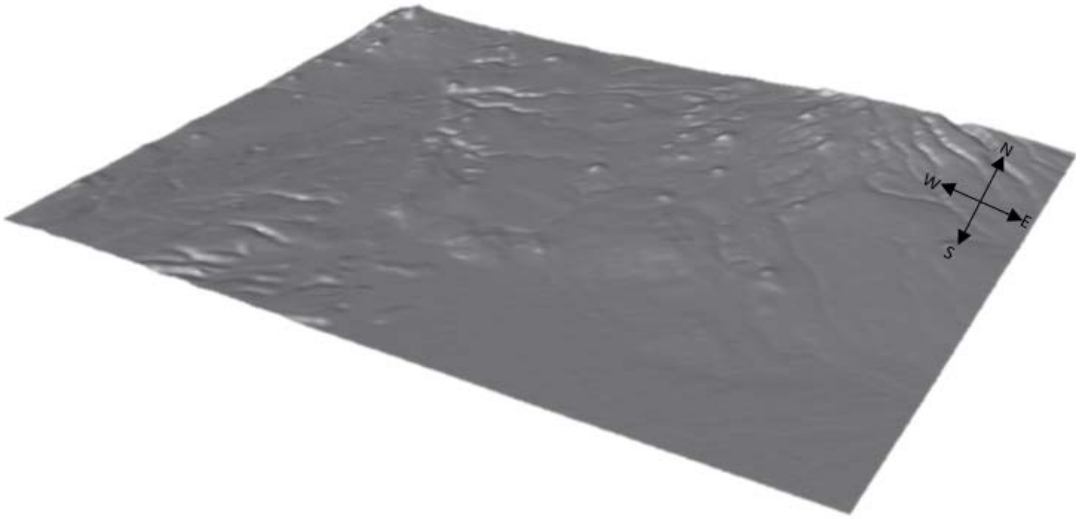

Figure 6.7 Surface model for Lake Turkana Wind Farm

It was decided to reduce the size of the surface model to 7 km x 7 km with the LIDAR location as the centre in order to reduce computation time in LES. OpenFOAM is capable of reading the STL file and then generating the mesh. The process of creating the mesh is explained in the section to follow.

6.4.2.2 Mesh Generation

Generation of a good quality mesh is essential for reliable CFD computations in a complex terrain. Factors to consider is the shape of the mesh element, surface grid spatial resolution, boundary layer resolution and the overall number of elements. It is necessary to resolve areas near the surface where a large velocity gradient is present due to surface friction. It is highly advisable to massage terrain (increase the sides of the domain by 1 m) terrain towards the domain boundaries ensuring homogenous inlet and outlet conditions (Richards and Hoxey, 1993). Further inlet, outlet and top boundaries should be kept at a considerable distance from the area of interest. For the top boundary this distance will generally depend on the type of boundary chosen.

Mesh cells are made up of connected flat faces; 3D cells can be an unstructured mix of tetragonal and hexagonal shapes or a structured group of hexagonal cells. Unstructured meshes help meshing irregular surfaces while the structured meshes helps to run and converge solutions faster due to equal time steps across the model surface.

OpenFOAM offers structured and unstructured meshing via the blockMesh and SnappyHexMesh respectively. Another tool is the moveDynamicMesh utility. In addition to these three libraries, a custom library for meshing has also been developed at Institute for Wind energy and Energy Systems (IWES), Fraunhofer Laboratory called terrainBlockMesher (Schmidt et al., 2012).

SnappyHexMesh is interesting for flow-over-terrain modelling as it has the ability to snap (adjust the nodes of the mesh so that they adopt the shape of the terrain) irregular surfaces and generate surface cell layers. The main downside of this utility is that it requires a background mesh with an aspect ratio close to one. The background structured mesh in this case is generated using blockMesh, which in process, helps to develop the 3D geometry serving as the domain for wind flow. This will generally lead to an excessive number of cells, thereby increasing, the computational cost. In addition, the generation of unstructured cells requires more computational time than for a structured domain limiting its use in serial mode. The experiment of coupling WRF to OpenFOAM expects the first node of the terrain mesh to start from coordinate (0,0,0); but using SnappyHexMesh, the lowest point in the z positive direction is 40 m. The consequence is that it becomes incompatible with the collocated grid for OpenFOAM and permits the usage of certain velocity boundary conditions causing solver to “crash” (cease execution) earlier than expected. The preliminary mesh, without the mesh density experiment, was coarse and was comprised of 38,190 cells. The number of cells, however, was improved to about 70,000 as shown in Figure 6.8.

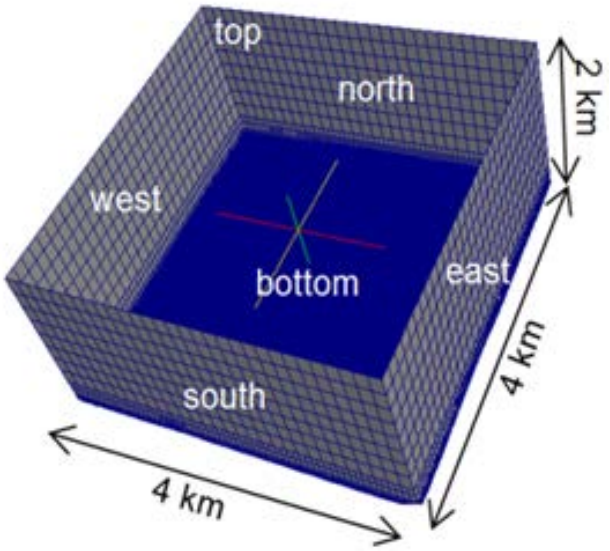

Figure 6.8 Domain and mesh generated using SnappyHexMesh with specified patches (boundary of the mesh is broken into different regions called patches)

The mesh generated with terrainBlockMesh is structured itself and does not require blockMesh. This utility is very useful and efficient in generating meshes for complex topography. It can handle domains with large size and can overcome the problems associated with smoothing the terrain at the edges and bringing them to the reference coordinate (0,0,0) for efficient coupling. Since this is a custom library, some of its features such as the structure of the blockMeshDict, are incompatible with the solver used in this study.

moveDynamicMesh is preferable as it allows the mesh cells to move and adhere to the complex shape of the topography. Further, it allows the terrain to be located at exactly the zero coordinate location suitable for coupling WRF with the OpenFOAM grid. The mesh generated with moveDynamicMesh is shown in Figure 6.9.

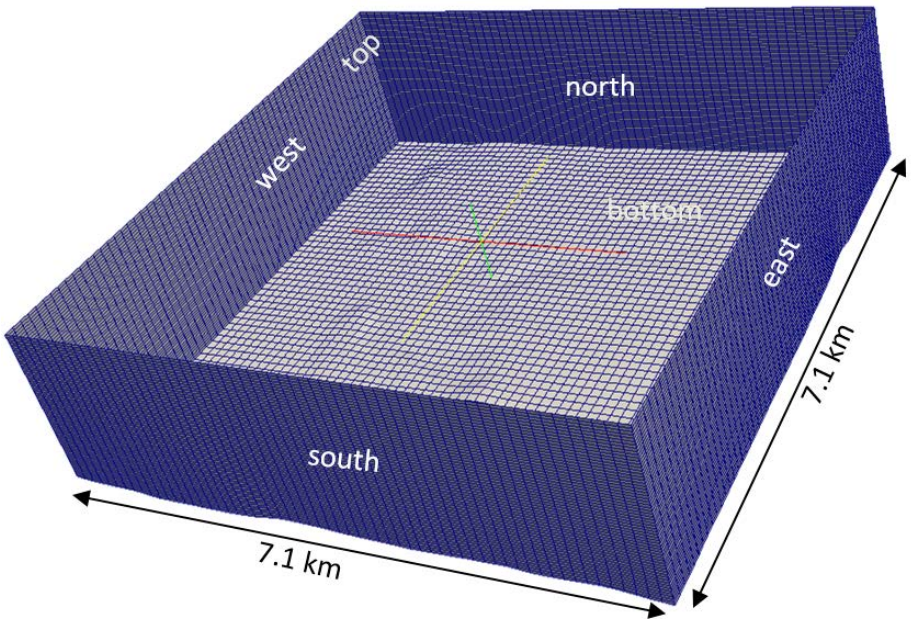

Figure 6.9 Domain and mesh generated using moveDynamicMesh with specified patches

The dimensions of the surface model in this simulation have been changed and the new dimensions of the computational domain are 7.1 km x 7.2 km x 2 km. This strategy was adopted to allow the point of interest, the CDL location, to be distant from the boundaries. The total number of hexahedral cells is 216000 as tetrahedral cells are unsuitable for LES. The average first cell height is 25 m and the surface layer has 8 cells. The horizontal resolution of the domain is 117 m and the vertical resolution is 33 m. The terrain has been massaged at the edges, using a MATLAB® script, to prevent the formation of flat cells at the edges. This shows that the grid resolution is not constant in all directions but is small enough to capture the boundary layer dynamics.

One of the critical aspects of the mesh cell design is the first mesh cell height and vertical resolution. It is important have mesh cells in the boundary layer to model surface drag forces. Dimensional analysis provides the log law which helps determining the height of the boundary layer. The log law is a graph plotted between the dimensionless height (y^+) and dimensionless velocity (u^+). For a smooth surface and external flow, the first mesh cell should have a y^+ value between 20 and 300 while for LES $y^+ \sim 1$. Another requirement of the first mesh cell height is that the roughness element cannot be higher than the top of the cell.

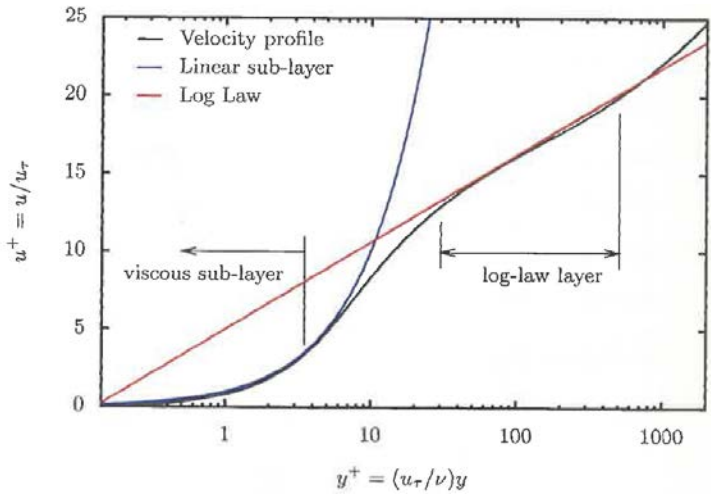

Figure 6.10 Wall Boundary Layers

The law of the wall-y^+ method is not compatible with the atmospheric roughness, since atmospheric roughness elements are objects such as shrubs, trees or buildings etc., and relatively tall first mesh cell height is required. The y^+ values are on an order of magnitude above the recommended range when the first cell height is of the order of one or two meters tall. The aim is to have a better resolution of mesh. A meteorological mast or a remote sensing instrument such as a LIDAR or SODAR can be used to measure the height of the surface layer. The roughness elements can be accounted for by setting the first cell height appropriately and while the higher cells will account for good surface layer resolution. In this study the first cell height is set to 2 m above surface (Alinot and Masson, 2002; Alinot and Masson, 2005).

Gaitonde et al. (2006) explains that grid independence cannot exist in LES as a grid independent LES is actually a Direct Numerical Simulation (DNS) and therefore the 'systematic grid-convergence' studies offer no great benefit. The LES will no longer have economical computational efficiency than DNS on account of resolving the most energetic eddies. Some studies, however, explore filtering techniques to attempts to demonstrate grid-independence in LES. The total number of cells in the mesh were increased until the solver was able to detect key processes in the boundary layer.

6.4.2.3 Coordinate Conversion

In order to extract required meteorological variables from WRF and initialize OpenFOAM's domain, Geographic to Cartesian coordinate conversion is required. This is done with the help of a MATLAB® script which prepares the input files for the

OpenFOAM domain boundaries. The domain boundaries are designated according to cardinal direction (cardinal directions are the four main points of a compass: north, south, east, and west) with a top boundary and a bottom terrain surface. The UTM coordinates of two opposite corners of the terrain STL file, with sufficient height, are provided as an input to the code which interprets the size of the domain. The number of cells are kept the same as the number of hexahedral cells in the mesh created in OpenFOAM. The geographical coordinates of the WRF domain from which the variables of interest are to be extracted are also defined in the code. Grid spacing of how far apart the points should be placed in three dimensions is set by dividing the domain size with the number of cells in each direction. The position of the centres of the cells are also defined in the code. These positions are defined for all of the six boundaries of the domain and the interior of the domain. The variables from the WRF output file will be extracted at these locations. These positions are saved for all the six boundaries as separate files and for the interior of the domain. This code plots the spatial comparison of the WRF grid with respect to the OpenFOAM domain and also assists plotting of the locations of the masts and the CDL.

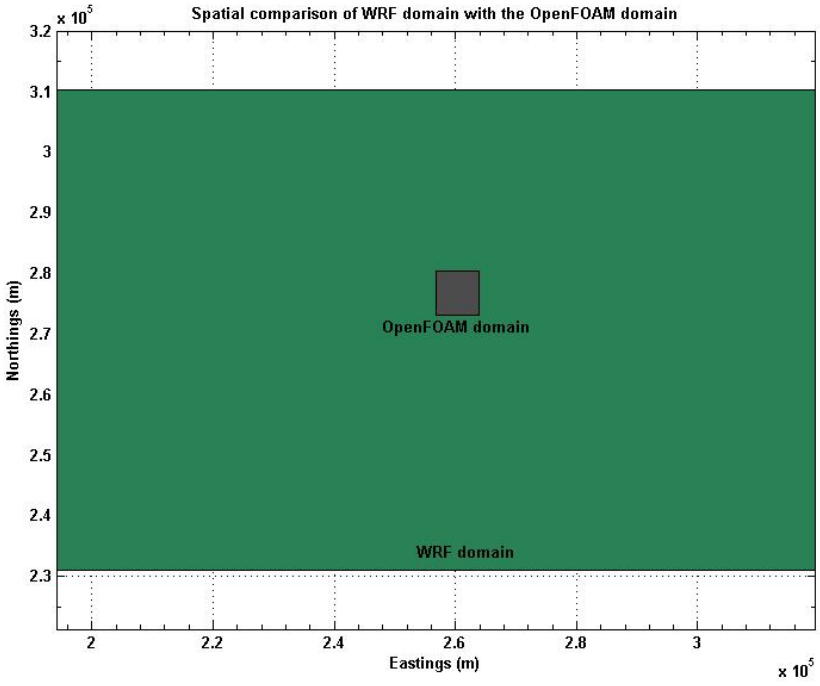

Figure 6.11 Spatial comparison of WRF domain with the OpenFOAM domain

6.4.2.4 Un-staggering WRF Variables on a Collocated Grid

The primary procedure to couple WRF with OpenFOAM involves un-staggering the WRF variables on a collocated grid. On a staggered grid the scalar variables (pressure, density, total enthalpy etc.) are stored in the cell centres of the control volumes, whereas the velocity or momentum variables are located at the cell faces. In a collocated grid, all variables are stored in the same position as shown in Figure 6.12.

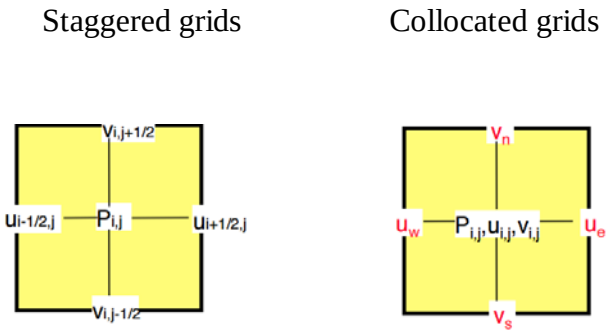

Figure 6.12 Collocated vs staggered grid

Before explaining the code, it is important to correctly interpret the WRF grid and associated variables that, require extraction in order, to initialize OpenFOAM. WRF grids are logically rectilinear and the variables for WRF cell indexed as (i, j, k) can be located at one of four possible points (Figure 4.9). The position of these variables can be determined from WRF registry. Briefly

- at the centre of the cell-theta points are not staggered
- at the centre of left face-U point are staggered in X
- at the centre of front face-V point are staggered in Y
- at the centre of the bottom face-W point are staggered in Z.

Thermodynamic variables such as pressure and temperature generally reside at theta points only with the exception of geopotential which resides at W-points. Wind velocity vectors are stored as U, V and W at their corresponding locations, hence the point names. Since they are on different staggered grids the code expects them to be at a single point for which they are interpolated to theta points. The latitude and longitudes are fixed while the elevation is computed from geopotential height.

The WRF to OpenFOAM processor helps to un-stagger velocity, pressure and temperature to centres of the cells in the OpenFOAM domain. It reads in WRF output files and yields OpenFOAM boundary conditions. WRF output file (2009-07-15_00:00:00 UTC) for the fourth domain (900 m resolution) deduced from the optimized WRF procedure for Lake Turkana has been used in this study. The points created for the interior and for the sides of the domain generated in MATLAB® script serve to locate the centre of cells. Since a straight forward application discretization on collocated grids results in a very wide stencil for the pressure. Since pressure points are also uncoupled and the pressure field can develop oscillations, a Rhie and Chow (1983) like flux interpolation is used. This helps to avoid pressure velocity decoupling. Once the interpolation is complete the processor prepares the boundary condition files in OpenFOAM format for all sides of the domain. The code reads each time stamp stored in the WRF output files and generates the boundary condition files for that respective time. The code is also able to change the date format of the time stamp to the "no of elapsed seconds" format and stores the files for each time stamp under designated seconds. It is also possible to create the initial condition files separately. These files are stored under the first time stamp converted into second.

6.4.2.5 Boundary Conditions

CFD modelling requires that information on the dependent (flow) variables on the boundaries must be specified. The process of defining the boundary conditions involve identifying the location of the boundaries (e.g., inlets, walls, symmetry) and supplying information at the boundaries. The boundary condition type and the physical models employed are driven by the data required at the boundary. Incorrect definition of boundary conditions can lead to a poor solution. Generally, the selected boundary location and shape should allow either fluid to enter or leave for better convergence. A large gradient in a direction normal to the boundary should be prevented and grid skewness near the boundary should be minimized. Typical boundary conditions include inlet, outlet, wall, prescribed pressure, symmetry and periodicity. A few of these used in this study will be defined

- **Inlet Boundary Condition**

The distribution of all flow variables need to be specified at the inlet boundaries. Flow velocity is an essential variable.

- **Outlet Boundary Condition**

This also requires the specification of all flow variables mainly flow velocity. It is used in conjunction to inlet boundary condition and is used where outlet velocity is known. In a region where the flow becomes fully developed with no change in flow direction far away from geometrical boundaries, outlet boundary condition could be defined and gradient of all variables could be equated to zero except the flow velocity.

- **Wall Boundary Condition**

The wall boundary condition or more specifically, the no-slip boundary condition is appropriate for velocity components at the wall. The normal components of velocity are zero at this boundary while the tangential components are set to velocity of the wall. Heat transfer could also be specified across the wall.

- **Prescribed Pressure Boundary Condition**

It is appropriate for atmospheric flow where boundary values of pressure are known and the exact details of the flow are unknown. It includes a pressure inlet and outlet condition.

- **Neumann and Dirichlet Boundary Conditions**

A Dirichlet boundary condition refers to a fixed value or constant value of the dependent variable prescribed on the boundary of the domain. A Neuman condition, on the other hand refers to the prescribed gradient of a variable normal to the boundary and is defined as a fixed gradient.

In OpenFOAM defining pressure and velocity for a known flow behaviour includes a Dirichlet and a Neumann condition which should be defined to connect the mathematical model with the required boundary conditions for the model. Their implementation will affect the respective mathematical operator. The definitions of

boundary conditions in OpenFOAM are described in fvPatchFields. It contains the general class definition of the boundary condition, which represent the base class. This class defines main functions and data structures that will be used by the genuine classes. The basic mathematically defined boundary conditions i.e. Dirichlet, Neumann and Robin type boundary conditions are saved in a basic directory.

In this study the OpenFOAM domain has Dirichlet conditions for velocity U, temperature T and pressure p at the south, top and east boundaries. These boundaries are considered as inlets and are fed from WRF via a "timeVaryingMappedFixedValue" boundary condition. The west and north boundaries are considered to be outlets and Neumann conditions apply for U, T and p. The bottom boundary or the terrain's surface has a Dirichlet surface T flux from WRF, a Neumann condition for p and a surface stress model. The wind was considered to enter the domain from the south-east specified by an angle of 135° from North with the simulation taking place at longitude 37° E. In order to bring the fluxes up to the right values at processing boundaries, the solver reads some initial values from the setABLField's dictionary and the initial conditions file. These contain the initial values of velocity to be 12 m/sec while the reference temperature was set to 300 K. The height of the capping inversion was assumed to be 1050 m (a.g.l) and the depth of inversion was 100 m. The virtual potential temperature was initialized at 300 K from surface up to 100 m height. In addition, a vertical profile table was provided which derived values from the global ERA-Interim data for values of height, U, V and T for day 20090715 at 0010 UTC. The drive wind is set to false because the intention is to couple the model with WRF and not generate precursor fields. The statistical information for the boundary layer is collected at a frequency of 1 every n time steps. The kinematic viscosity is set to 0 as the solver reads it but does not solve it. This is a software "bug" that needs fixing in the future. The standard Smagorinsky model with Cs= 0.168 was used as the surface stress model for LES (Churchfield et al., 2013). The von Karman constant is set to 0.4 (Beare et al., 2006). For calculating friction velocity in non-neutral flow, the Monin-Obuhkov universal constants (betaM and gammaM) are set to 15 and 4.9 respectively (M. Churchfield 2015, personal. comm., 20 April). The aerodynamic roughness height as stated before is set to 0.02 m (see section 6.2) and mean surface temperature flux is set to -0.27 K-m/s (assimilated from WRF). The turbulence Prandtl number is fixed uniformly throughout the field at a

value of 1 (Churchfield et al., 2013). The wall model selected is “Moeng”. Since this simulation is designed for East Africa, lying very near to the equator, the Coriolis effects will be negligible but they still have been accounted for in the simulation. The planetary rotation period is 24 hr which yields 7.2 E-5 and 4.54E-6 rad/s at 3.58 °N latitude.

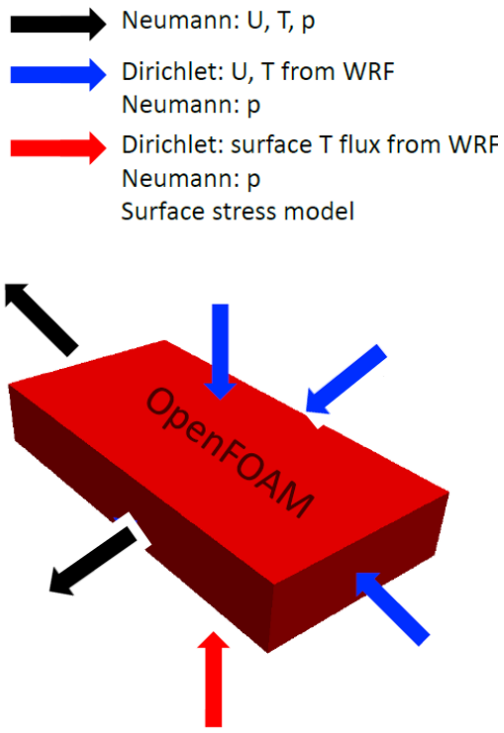

Figure 6.13 Boundary Conditions for the OpenFOAM Domain (courtesy NREL)

6.4.3 Solver

The finite volume method, central to most established CFD codes, requires the numerical algorithm to run in the following sequence of steps:

- Assimilation of the governing equations of fluid flow between all the cells of the entire domain.
- The process of conversion of the resulting integral equations into a system of algebraic equations known as discretization.
- Solution of the algebraic equations by an iterative method.

The first step is based on the law of conservation of momentum where the flow variable within a finite control volume can be expressed as a balance between the various processes tending to increase or decrease momentum.

The solver used in this study is a customized version of OpenFOAM 2.1. x's [x meaning compatible with the onward versions], namely buoyantBoussinesqPimpleFOAM that includes the modification to include Coriolis forces, a largescale driving pressure gradient to achieve a desired wind speed at a given height, and specified surface stresses and temperature fluxes. Rearranging equations 6.7 gives,

$$\frac{\partial \overline{U_\iota}}{\partial t} + \frac{\partial\, \overline{U_J}\overline{U_\iota}}{\partial x_j} = -2\varepsilon_{ijk}\Omega_j \overline{U_k} - \frac{\partial \bar{p}}{\partial x_i} - \frac{1}{\rho_0}\frac{\partial}{\partial x_i}\overline{p_0}(x,y) - \frac{\partial}{\partial x_j}\left(\tau_{ij}{}^{D}\right) - \frac{\mathrm{g}z}{\rho_0}\frac{\partial}{\partial x_i}\rho_b + \frac{1}{\rho_0} f_i^T \tag{6.13}$$

In equation 6.13 the pressure variable computed is the deviation from the hydrostatic pressure and is added to the isotropic part of the SGS stress tensor, an elliptic pressure equation to enforce continuity, and the potential temperature in equation 6.10. The Samgorinsky is used in this study and a temperature predictor along with correctors is added to the solver to achieve a better temperature velocity coupling (Churchfield et al., 2013).

Discretization schemes

If a flow domain is modelled as a continuous medium throughout which a non-linear set of equations relate various fluid dynamic quantities; the process of subdividing this continuous domain into discrete segments and linearizing these equations is called discretization. The emerging equations are finite and linear, solutions to which can be achieved numerically. There are several discretization methods, including:

- Finite difference method
- Finite area method
- Finite volume method
- Finite element method

There are several discretization schemes, including:

- Euler
- Gauss linear.

The finite volume method subdivides the volume into a finite number of contiguous control volumes and solves the integral forms of the equations as a starting point. The midpoint rule for integrating these equations is used, though higher order schemes are available. Gauss' theorem is often applied to the equations as well. The result is a finite number of linear equations that can be solved using matrix methods. The flow quantities may be collocated or staggered; collocated grids have these quantities defined at a single location in the control volume while staggered grids define volume based quantities at the centre of an elemental volume while the flux base values are defined on the faces. Values at other locations in space are obtained from interpolation. There are several schemes that may be used in order to interpolate, but in this section only those used in this study are defined as:

- The Time derivative schemes or ddt schemes that use backward differencing, Crank Nicholson spatial derivative treatment with and offset 1, ideal for LES modelling.
- Gauss linear divergence and gradient schemes (ideal for LES) that are used for convective and gradient terms
- Laplacian terms are treated with Gauss linear corrected schemes.
- An interpolation scheme that is linear.

All interpolation to faces is linear (second-order central) to avoid dissipation associated with upwind schemes when doing LES.

- The non-orthogonal correction to the surface normal gradient calculation, evaluated by interpolating the gradients at the adjacent cell centres through a differencing operation that is defined in snGradSchemes sub directory. The non-orthogonal correction is set to “corrected”.
- The numerical flux generated after solving the pressure equation, is defined in fluxRequired sub-dictionary with p_rgh keyword.
- The spatial discretization can be specified in the system/fvSchemes file. 2nd-order central differencing on the convective scheme for the momentum equation is used in this research. Central differencing is best because it has no artificial diffusion associated with it, meaning if there is a steep gradient in the flow, it won’t artificially smooth it. It does have artificial dispersion, though,

meaning that in a wave equation, waves will pile up on each other (i.e., at steep gradients, oscillations occur). Central differencing is good for LES because it doesn't artificially smooth out resolved turbulence. But, especially on really fine meshes, or those applied over terrain, sometimes central differencing gets too much dispersion and the solution field gets polluted with spurious oscillations. Therefore, a blend of central differencing and upwind differencing can be applied (upwind has lots of artificial dissipation). The blend can also be specified to vary spatially.

Since, on finer grids more oscillation occur, more upwinding is added to control it. On grids which have a local refinement, the amount of upwinding is based on the cell face size. The smaller the face, the more upwinding. Same goes for the temperature equation. That is what the list in fvSchemes states faceSize1-4 are a list of different face sizes. The blending only happens if the div (phi, U) is set to "Gauss localBlended linear upwind;" or "Gauss localBlended midPoint upwind;" The difference between "linear" and "midpoint" is that linear does central differencing where the difference weights take into account cell length.

6.4.3.1 ABL Terrain Solver

ABLSolver is an atmospheric solver developed out of the buoyantBoussinesqPimpleFoam. It can be run in PISO or SIMPLE mode for either LES or RANS (or a blend). It can simulate a variety of atmospheric stabilities. In the current research it has been used in LES mode to compute the wind speeds and compare them with mast and CDL observations and WRF forecast scenario while it is used compute turbulence intensity, recirculation regions and vertical wind profile in resource assessment scenarios.

Their exits different algorithms for solving the NS equations with a coupled velocity and pressure field. One of the most common approaches is to derive an equation for the pressure by taking the divergence of the momentum equation and by substituting it into the continuity equation. This is known as the SIMPLE algorithm developed in 1970's by Prof. Brian Spalding from Imperial College London. Since PISO solver is an expansion of SIMPLE therefore both will be explained here.

SIMPLE (Semi-Implicit Method for Pressure-Linked Equations)

Linear pressure velocity coupling does not need to be resolved fully, if a steady state process is being solved iteratively, since the changes between the consecutive solutions are not small. Therefore, the SIMPLE algorithm is utilized and its major steps are clarified by Figure 6.14

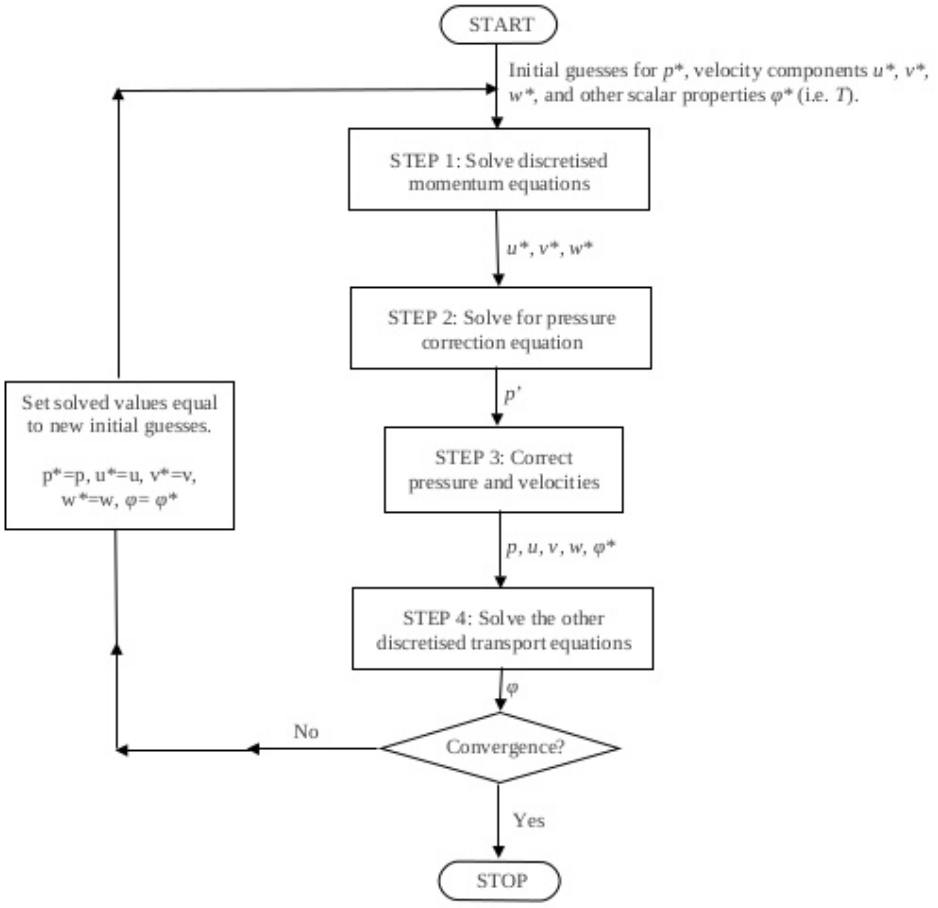

Figure 6.14 SIMPLE algorithm

PISO (Pressure Implicit with Splitting of Operators)

The first three steps, coefficients and pressure corrections of the PISO algorithm are same as the SIMPLE algorithm. PISO however, is equipped with two pressure corrections compared with SIMPLE algorithm.

Both of these algorithms are based on evaluating some initial solution and correcting them. SIMPLE, however only makes 1 correction whereas PISO requires more than 1, but typically not more than 4. Extended details of both algorithms are presented in Figure 6.15.

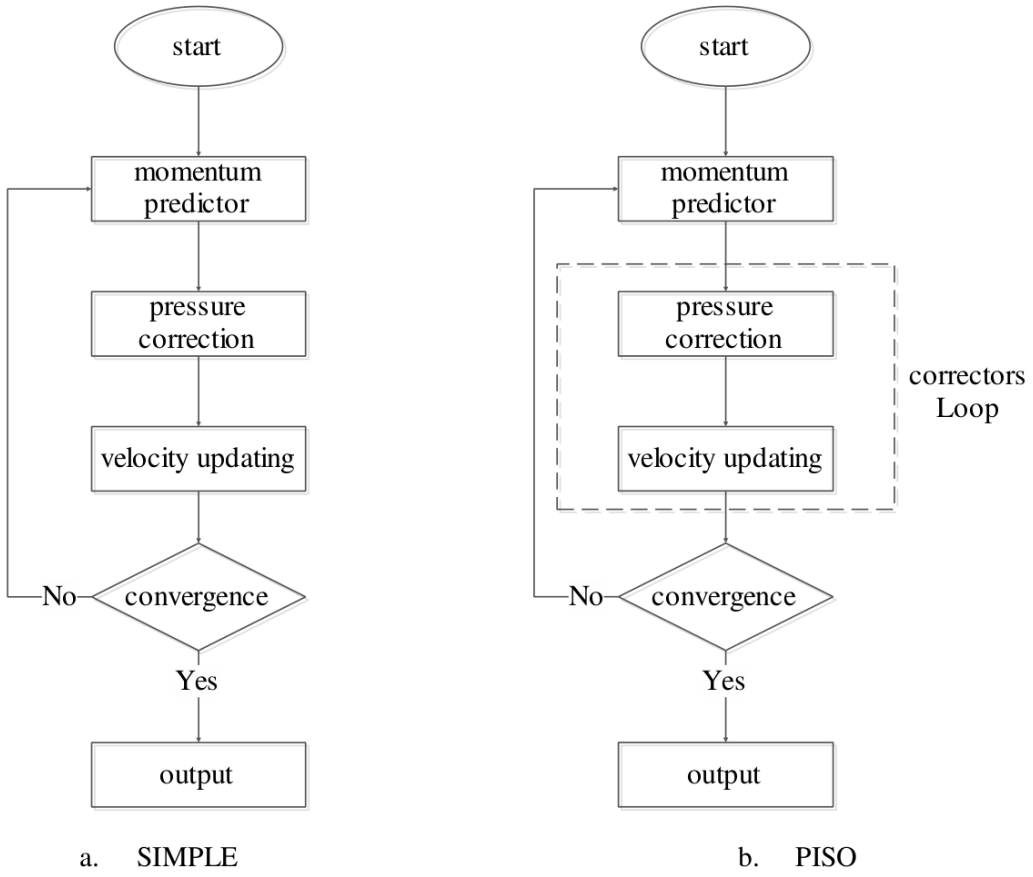

Figure 6.15 Detail of SIMPLE and PISO algorithms

Another Solver used in this research is the PIMPLE algorithm which is nothing but a PISO procedure with two (eventual) additions:

1. outer correction loops (i.e. multiple cycling over the same time step using the last iteration final value as initial guess for the next iteration).
2. under-relaxation of the variables between consequent outer iterations.

In order to compute the set of linear discretised equations, linear solver methods are used. Two commonly known methods used in OpenFOAM are preconditioned conjugate gradient (PCG) (for symmetric matrices), preconditioned (bi-)conjugate gradient (PBiCG) (for non-symmetric matrices). Other methods include solver using a smoother, generalised geometric-algebraic multi-grid (GAMG) and diagonal Solver for explicit systems.

PBiCG is used for the temperature, velocity, turbulent properties k-ε and the Reynolds stress. A preconditioner transforms the set linear equations into a form that fits better

for numerical calculations. Several options for preconditioning of matrices in the conjugate gradient solvers exist but in this study diagonal incomplete-LU (asymmetric) is used. GAMG on the other hand is used for pressure p, and it first perform calculations on a coarse grid, and then map this solution onto a finer grid as an initial guess for the calculation. One PISO predictor is followed by three correctors in this study. The refinement may take one or more steps until a final solution on the desired grid is obtained.

The simulation start time is chosen on the basis of the fact that mean wind speed remains stable from this start time for the next couple of days. The observational data available from the mast and CDL is consistent at this time and the modelled output from WRF is also in phase with the observed wind speed. The simulation start time is 20090715 00 10 UTC which is extracted from the WRF output file and then it runs for 12 hours real time on an CRAY XC40 with 14 nodes and 144 processes for computing 12 hours with 216000 cells. This gives a threshold value of ~30,000 cells per core per 7 cores. Anything above this value will be exceedingly slow. The simulation is run at a constant Courant number and an adjustable run time.

Since LES is transient, it always depends on the previous set of time steps. So, in theory, LES never "stabilises" as such. However, that being said it is usually expected to observe eddies form a repeating pattern. Therefore, a monitor point is set up for whichever variable "Ux" is tracked and plotted to the GUI during the Solver's execution. Once it is observed that the pattern is relatively consistent, it is considered to be stable (see Figure 6.16). Assuming the domain is large enough, it is expected that the pattern would have stabilised by the time the fluid in the domain has travelled 1 to 2 times the distance between the structure generating the eddies and the outlet boundary. It's just a rule of thumb but it tends to work reasonably well.

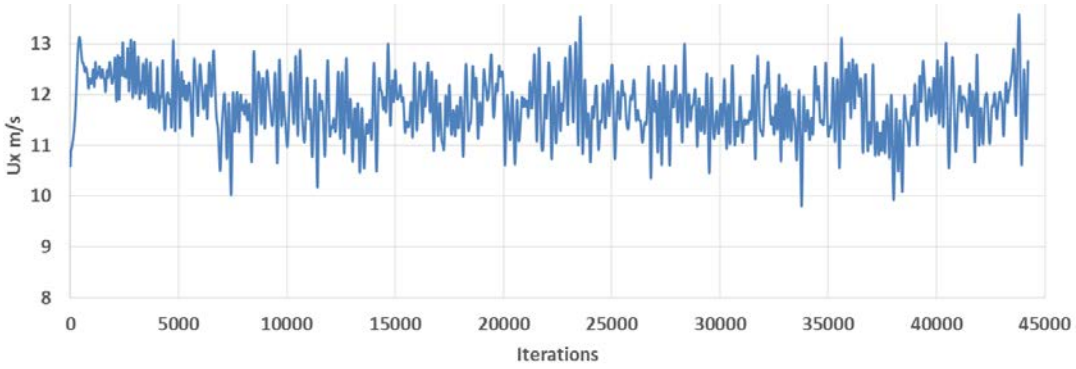

Figure 6.16 Solver Stability at the location of mast B

6.4.4 Post Processing

The process of examining and exhibiting the results from Solver is known as Post Processing. Development of outstanding Graphical Processing Unit (GPU) processing capabilities has improved the graphic capabilities of workstations therefore CFD packages are now equipped with versatile graphic visualization tools. Paraview is a third party software that can be used in conjunction with OpenFOAM. Paraview capabilities include

- Domain geometry and grid display
- Vector plots
- Line and shaded contour plots
- 2D and 3D surface plots
- View manipulation
- GPU compatibility
- Colour post script output and
- Animation

These capabilities have revolutionised the communications of ideas developed in CFD to the non-specialists. In the present study Paraview generates velocity panel plots and streamline plots at the location of mast A. The time series data was obtained using the probe function in OpenFOAM at mast location and using it to generate wind speed time series comparison plots.

6.5 Results and Discussions

The objective of the meso microscale coupling activity was to support short term forecasting at higher spatial resolution. The coupled model not only serves as a reliable forecasting tool but can also be employed effectively as a resource assessment tool.

The CDL measurement campaigns at Lake Turkana in 2009 and 2010 were designed with the aim to support wind modelling through the use of precise *in situ* measurements. These campaigns supported the meso scale wind modelling and micro scale modelling in the context of providing virtual masts to the WASP software but were unable to provide useful observations for atmospheric boundary layer CFD modelling over a complex terrain. These useful observations include the turbulence intensity, vertical temperature and wind profiles etc. In addition, time averaged standard deviations from mast observations at 10 m weren't available for comparing with model-predicted turbulence intensities. Thus the modelling exercise was limited to wind speed time series comparison between masts, CDL, WRF and coupled OpenFOAM. The average height of the masts is ~40 m and the forecasts are in excellent agreement at these heights. The comparison of hub height measurements are useful for micro siting in terms of positioning the turbines. The wind speeds observed by masts and CDL are compared with the WRF and OpenFOAM modelled wind speed at the location of mast B and mast C at ~ 40 m above ground level in Figure 6.17 and their associated statistics are presented in Table 6.1. The simulation time is limited to 12 hours keeping in view the changes in the atmospheric boundary layer with the changes in air temperature. The position of the mast in the domain is the key factor for determining correct wind speeds. Since the mast C is located 7 grid points away from the south boundary while mast A is 1 grid point away from the north boundary, wind speeds are under predicted at these two locations by ~ 1 m/s. The position of mast B is much deeper into the domain and therefore RMSE values at mast B are lower as compared to mast A and B. To further strengthen this conclusion was a mesh that was constructed placing mast A as the centre. The size of the grid is 3.2 x 3.1 x 2 km and its boundary conditions are kept similar to the previous simulation. The resolution of the mesh is 54 m in the x direction, 52 m in the y direction and 33 m in the z direction Reasonable improvements in wind speed RMSE and percentage bias are achieved as shown in Figure 6.18 and Table 6.1 respectively.

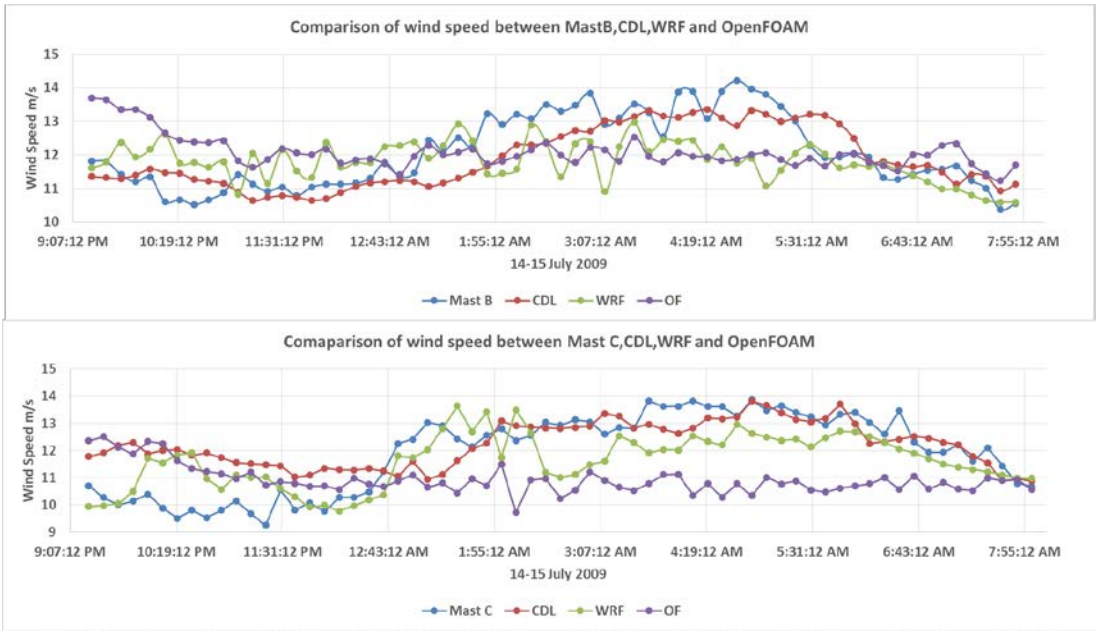

Figure 6.17 Comparison of Mast and CDL measured wind speeds with modelled wind speed from WRF and OpenFOAM at location of Mast B and C (time is in Kenyan local time (KST))

OpenFoam and WRF modelled wind speed vs Mast and CDL observed field	**RMSE (m/s) OF modelled Vs Mast**	**RMSE (m/s) OF modelled Vs CDL**	**% BIAS OF modelled Vs Mast**	**% BIAS OF modelled Vs CDL**
Mast A location	1.07	0.81	-3.41	+0.404
Mast B location	1.25	1.08	+0.35	+1.8
Mast C location	1.77	1.06	-5.8	+5.3

Table 6.1 Wind speed statistics at the location of the masts using OpenFOAM

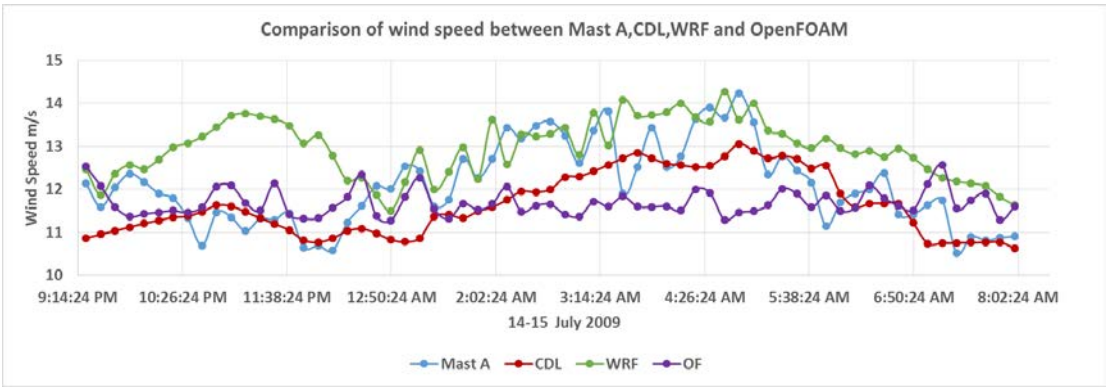

Figure 6.18 Comparison of Mast and CDL measured wind speeds with modelled wind speed from WRF and OpenFOAM at location of Mast A (time is in Kenyan local time (KST))

Since the experiments at mast A produced better results, the velocity magnitude and streamline of the flow field at mast A location were plotted as an aid to specifying the prospective positions of the wind turbines at the at Lake Turkana wind farm. The spatial variability of wind is represented by Figure 6.19 while its complete structure is shown in Figure 6.21. These plots are extracted 12 hours after the simulation period when the solver has become relatively stable. The major portion of wind is coming from the east side and is increasing in magnitude towards the west side with the increase in simulation time as the turbulence fields are becoming dominant. In Figure 6.22 it is noted that the wind speed plots are agreeing with the statistics present in Table 6.1. It is further expected that as the turbulence will mature in OpenFOAM after 24 hr simulation time, the agreement in the plots in Figure 6.22 will strengthen Mast A location. It is confirmed from these plots that the ideal location of the turbines should be in the vicinity of mast A.

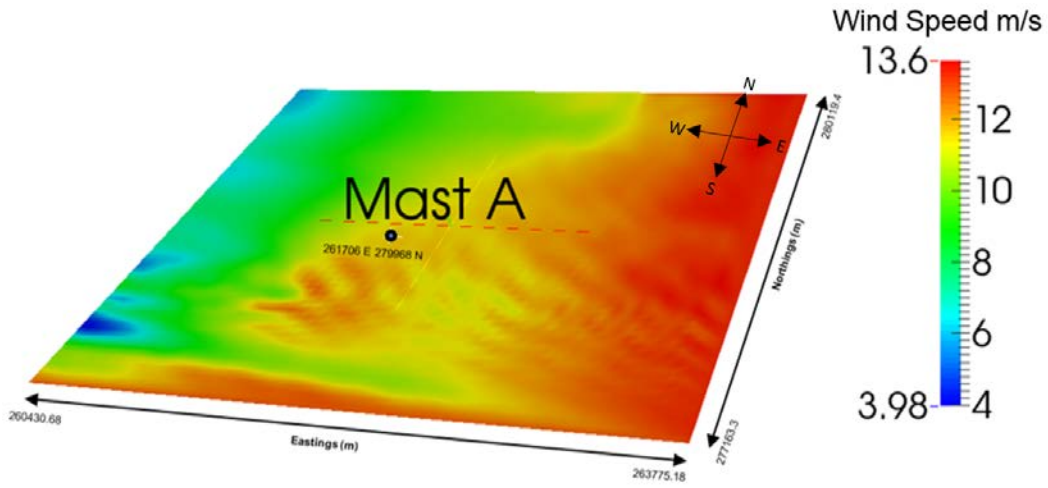

Figure 6.19 Velocity cut plane (XY) at mast A location at a height of 39 m above surface

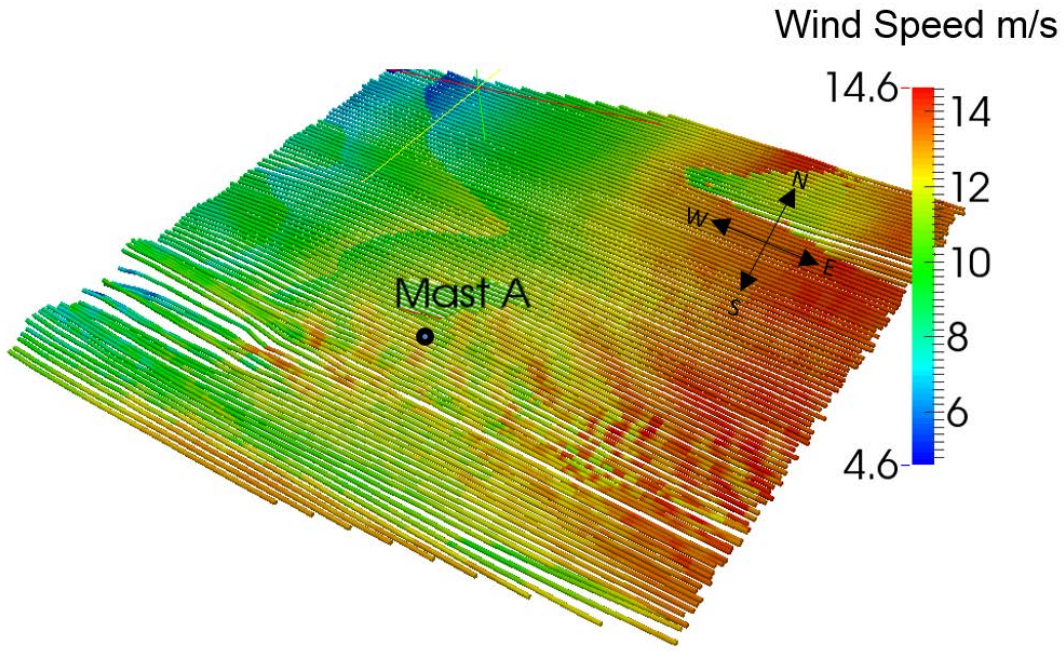

Figure 6.20 Streamlines in the form of stream tubes coloured by the magnitude of velocity at the location of mast A at a height of 39 m above surface

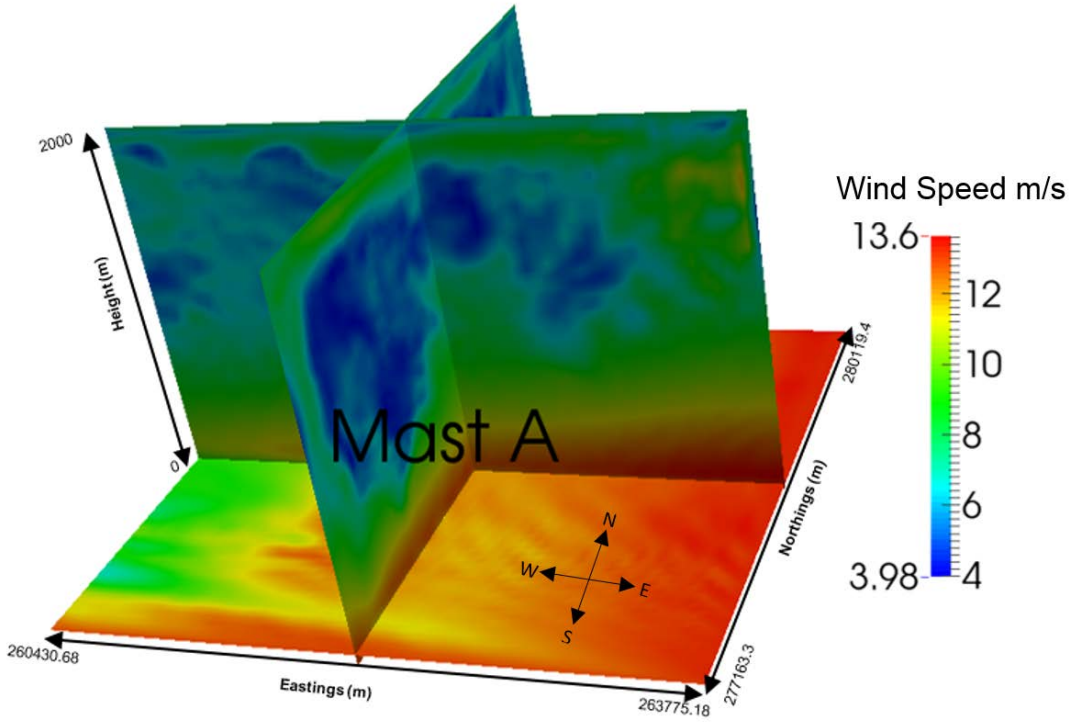

Figure 6.21 Full velocity field at the location of mast A

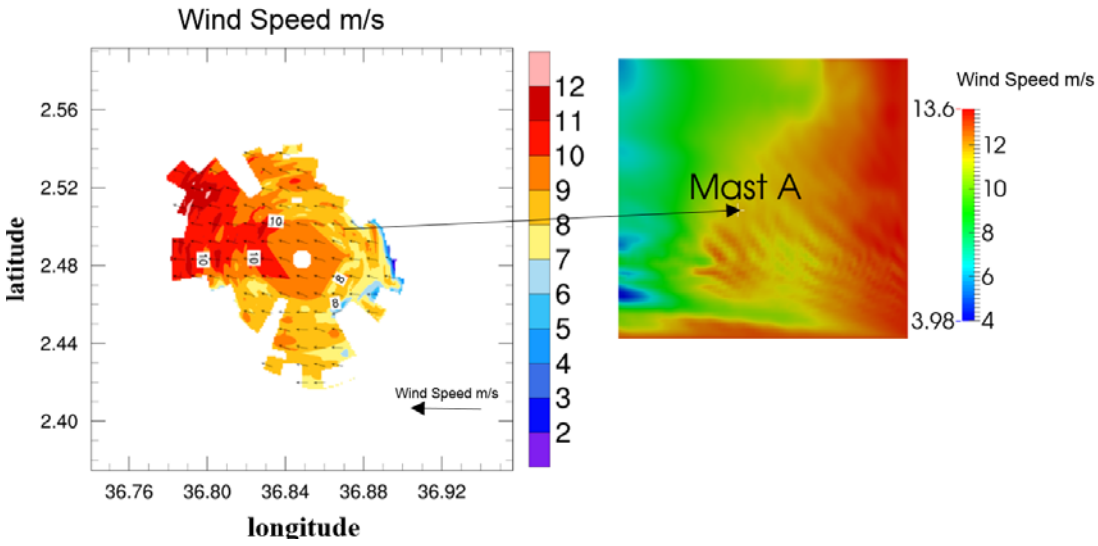

Figure 6.22 Comparison of CDL observed wind field (left panel) with OpenFOAM (right panel) after 12 hours simulation (time is in Kenyan local time (KST) 20090715 08:00)

Error inducing factors in the simulation include assumptions of the surface layer height, the aerodynamic roughness height and capping inversion height and thickness. Since the vertical temperature profile for initialization and the associated velocities are interpolated from ERA-Interim data a further improvement in the analysis is expected if these values are derived from the measuring instruments such as CDL and SODAR. Another important factor is to include more pressure levels near the surface in the WRF simulation. This would allow OpenFOAM to have an improved representation of the vertical wind profile when used in coupling. Increasing the spatial resolution of the domain from WRF to be used as input must also be increased for improved forecasting.

6.6 Summary

This chapter describes in detail the process of coupling the mesoscale model WRF with OpenFOAM modified as a microclimatic model. The chapter not only presents the theoretical background based on which OpenFOAM was modified to simulate the atmospheric boundary layer but also focuses on the boundary conditions necessary to initialize and conduct the simulations The chapter is structured according to typical CFD guidelines for conducting simulations and then details the procedure of model coupling under this standard framework. The results of simulation confirm the effective role of CFD to improve wind forecasting in a shorter time scale at higher

spatial resolution; important for management of wind farm infrastructure and other applications. This investigation has contributed to solving the research questions e and f (see Chapter 1) as CFD has been proven as a potentially beneficial tool for resource assessment and helpful for wind farm design and establishing design criteria.

Chapter 7 Conclusions Recommendations & Future Work

7.1 Conclusions

The aim of this thesis was to contribute effectively to the wind energy community by developing novel wind prediction, modelling and validation technique using *in situ* data supporting short term wind forecasting and wind resource assessment funded and supported by CRC CARE and Curtin University. Provided below are the conclusions from this study including recommendations for designing a field validation program to constrain and tune the model and hence enhance the validation. Suggested opportunities for future research are also provided.

The elevated terrain in the Rift Valley region of Africa which is the site of a developing wind farm is the goal of this research. A near ideal formation for an enhancement of the local winds is created by the large scale terrain. The site however, is relatively remote meaning that there was little infrastructure in place to support a field campaign. Further, and not ideal for this project, was that there was no routine source of meteorological information such as a WMO-linked weather station. As a result, upper air data (from radiosondes) and land surface observations were not available. The field campaigns involving CDL were designed focussing primarily on improving the wind retrieval technique. Therefore, little consideration was given to vertical observations from CDL supporting boundary layer study. These would have been beneficial in supporting the research undertaken.

The research is novel as it not only involved refining the modelling with WRF using validation observations to tune the performance in the elevated terrain. The coupling of WRF to the CFD model OpenFOAM and assessment of the impact on modelled winds has also been a challenging but beneficial activity since there is no open source software available to users who wish to pursue this evaluation.

The validation program has also offered a quite novel opportunity to utilise two validation data sets including the meteorological data from the 3 high masts installed on the site. The inclusion in the field deployment of the unique capability of a Doppler LIDAR to measure wind speed and direction, in-principle over 2π sr and with a range typically of 15 to 20 km, provide sampling of an area ~ 800 km^2 from a single location; certainly adequate for sampling over the spatial extent of a large wind farm

1. WRF is a generalized numerical modelling software package that continues to evolve for a number of applications ranging from weather forecasting to, modelling severe weather system (tornados, typhoons,). The sensitivity of power generation to wind speed has motivated this research for Lake Turkana Wind Farm, (Kenya East Africa) site and its varying topography. The performance and sensitivity of WRF's forecast products were evaluated using a number of numerical experiments which were used to attempt to optimize its performance for application at this site. The validation has employed a number of tall meteorological masts that provided wind speed and direction observations heights of order 40 meter.
2. WRF model capability may be limited in wind farm applications by the sparseness of constraining observational data and the number of vertical levels required in the initialization fields. It is also dependent on the detail and resolution of the geographical static data. A comprehensive 13 % improvement was achieved in wind speed RMSE whereas bias is reduced by 62 % when utilizing these initialization and geographical fields. Additionally, a 40 % reduction in error between observed and modelled wind speed was achieved, using ERA-Interim data instead of NCEP data. This advantage corresponded to an estimated potential improvement in annual power generation of 285 GWh for a 1625 GWh per annum facility at the planned Lake Turkana wind farm
3. The knowledge of boundary layer structure and microphysics plays a decisive role in the accuracy of predictions of wind speed and direction using the WRF model. Additionally, for sub-grid scale processes, realistic parameterization schemes are necessary.
4. The grid configuration and level of nesting along with the positioning of grids on this site, significantly affects the prediction of wind speed and direction at a specific location within the wind farm domain. The spatial resolution of geographic data chosen at each nested level also significantly affects the predicted wind speed.
5. The terrain height offset, Δz and proximity of a location of interest to complex terrain also significantly affects the wind speed and direction predictions.

6. WRF was tested initially at a simple coastal site in WA during a sea breeze event and with abundant and *in situ* supporting observational data. A low RMSE of 1.7 m/s and high CC 0.7 established WRF's performance in a well-defined environment. The slight under prediction in wind speed was confirmed with a bias of -0.35 m/s.
7. These modelled results confirm that the errors in wind simulation may be reduced by conducting WSDSA to achieve a suitable model configuration for the site under assessment. After an optimal configuration is achieved with the least possible errors (requiring of reasonable computational resources) the output from the model can serve as a valuable tool for short-term wind forecasting.
8. The comparison of WRF predictions with CDL demonstrates an improved performance of the model with RMSE in wind speed of 1.2 m/s, and correlation coefficient 0.84 respectively when validated against meteorological observations; a 25% improvement in wind prediction and a 22% improvement in the correlation coefficient (against *in situ* mast data).
9. A spatial verification of the WRF model outputs with that of CDL was performed in order to identify the areas of maximum wind speed which can be effectively employed as a resource assessment tool.
10. At the location of mast A, there existed errors at three points in the wind speed data retrieved from our locally developed NCL code and CDL which caused a percentage decrease of 23.65 % in the wind speed RMSE and an increase of 13.41 % in CC.
11. The output of the optimised WRF model configuration were supplied as an input to the microclimatic model developed in OpenFOAM. The microclimatic model predictions agreed better than the mesoscale model predicted winds in short temporal scales at a high resolution.
12. The microclimatic model outputs reduced RMSE to 1.07 m/s at the location of mast A, 1.25 m/s at the location of mast B and even mast C with its associated problems showed and improvement of 1.77 m/s.
13. The major improvement in predicted wind speed is expected by placing the specific location of interest deeper into the domain at a sufficient distance away from the boundaries.

14. The model predicted winds at hub height provided valuable data for placement of wind turbines and hence demonstrated the capacity to contribute to wind farm design.

7.2 Recommendations

1. WRF model performance is significantly affected by the sparseness of local meteorological observations and specifically, the number of vertical information levels provided in the observations. Therefore, for complex wind farm applications characterised by high diurnal variability, initialization with ERA-Interim data is suggested as the preferred option. The measurement campaigns should be designed to avoid data sparseness by considering the use of CDL to achieve high spatial coverage and avoid the high costs of installing multiple meteorological masts.
2. For high spatial resolution, near-surface wind simulations, it is recommended to use WRF set A1 of the physical options in order to achieve a low RMSE and high CC (e.g. this study achieved as low as 1.6 m/s as high as 0.69 respectively) for elevated complex terrain modelling such as encountered on the East Africa site.
3. The elevation error that arises due to differences in grid interpolated and actual surveyed height and from overlaying of the model's nested grid relative to the coordinates of the location of interest (e.g. a wind turbine) can give rise to significant model errors.
4. Further improvements in the model's predictions may be achieved by using the outputs of the WSDSA as input to a micro scale model and comparing the results with a site-based observational instrument such as a LIDAR or SODAR.
5. The placement of CDL is very important as its line of sight shouldn't be affected by the upwind topography.
6. It is important to maintain a consistent scanning strategy with CDL and to account for presence of clouds.
7. The atmospheric surface layer must be measured using CDL or low level meteorological tower instruments to ensure effective microclimatic modelling.

Land surface infrared sensors should be installed on site for validating satellite-derived land surface temperature.

8. Added pressure levels and increased vertical resolution in OpenFOAM should improve the predicted wind speeds from OpenFOAM.
9. Radiosondes should be deployed to determine the vertical atmospheric temperature profile and RHI scans with CDL should be used to determine the vertical wind profile.

7.3 Future Work

The research that has been undertaken has not exhausted all possible experiments that could beneficially be performed. We suggest the following could provide insights and possibly lead to improvements to the performance of numerical modelling of the boundary layer.

1. Promote the advantages of CDL in wind farm research particularly in their potential operational role in enhancing the prediction of winds for improved infrastructure protection (e.g. turbulence, severe wind gusts) and for improved lead time to support energy generation management.
2. Integration of CDL observations (wind speed and direction, precipitation, heat flux etc.) to improve the initialization fields for WRF
3. Explore the impact of integrating expanded CDL data sets: for example, perhaps exploring the capture of CDL observation upwind of the wind farm and assessing its impact on wind speed and direction prediction and the potential benefits to wind farm power generation management
4. For boundary layer studies, the standard deviation of wind speed for each recording interval can be obtained for CDL and mast to calculate the turbulence intensity, which can be used frequently to determine the suitability of the site for wind energy production. Most turbine manufacturers set a maximum limit of the turbulence intensity to protect wind turbine at highly turbulent sites
5. Using NREL's actuator line model embedded in SOWFA to determine the location of the turbines at Lake Turkana site (Churchfield et al., 2012).

6. A full wind power production software could be incorporated in this project. It would need to be capable of (a) calculating the mean power and annual energy output as a function of mean wind speed, (b) determining the level of wind variability, (c) providing estimates of the economics of the wind farm based on information provided by a validated numerical model and (d) estimating how much energy will be used locally and how much will be exported to the grid.
7. Curtin University does not have an instrumented wind turbine field research laboratory. Its research will therefore focus on advances in modelling, model coupling and LIDAR wind technology combined with the extensive expertise in field deployment of instrumentation and test facilities.

References

Aitken, Matthew L., Michael E. Rhodes, and Julie K. Lundquist. 2012. "Performance of a Wind-Profiling Lidar in the Region of Wind Turbine Rotor Disks." Journal of Atmospheric and Oceanic Technology 29 (3): 347-355. doi: 10.1175/jtech-d-11-00033.1.

Albers, A. 2006. "Evaluation of Zephir." Deutsche WindGuard Consulting GmbH Report, Germany.

Alinot, Cedric, and Christian Masson. 2002. Aerodynamic Simulations of Wind Turbines Operating in Atmospheric Boundary Layer with Various Thermal Stratifications: American Society of Mechanical Engineers.

Alinot, Cédric, and Christian Masson. 2005. "K-ϵ Model for the Atmospheric Boundary Layer under Various Thermal Stratifications." Journal of Solar Energy Engineering 127 (4): 438-443.

Annamalai, H., J. M. Slingo, K. R. Sperber, and K. Hodges. 1999. "The Mean Evolution and Variability of the Asian Summer Monsoon: Comparison of ECMWF and NCEP-NCAR Reanalyses." Monthly Weather Review. 127 (6): 1157-1186.

Antoniou, Ioannis, Mike Courtney, Hans E. Jørgensen, Torben Mikkelsen, Sabine Von Hunerbein, Stuart Bradley, Ben Piper, Michael Harris, Ignacio Marti, and Mariano Aristu. 2007. "Remote Sensing the Wind Using Lidars and Sodars." In EWEC, Milan, Italy.

Archer, Cristina L., and Ken Caldeira. 2009. "Global Assessment of High-Altitude Wind Power." Energies 2 (2): 307-319.

Awan, Nauman K, H Truhetz, and A Gobiet. 2011. "Parameterization-Induced Error Characteristics of MM5 and WRF Operated in Climate Mode over the Alpine Region: An Ensemble-Based Analysis." Journal of Climate 24 (12): 3107-3123.

Bailey, Bruce H., Scott L. McDonald, D. W. Bernadett, M. J. Markus, and K. V. Elsholz. 1997. "Wind Resource Assessment Handbook." Albany-New York: AWS Scientific Inc.

Bao, Xinghua, and Fuqing Zhang. 2013. "Evaluation of NCEP–CFSR, NCEP–NCAR, ERA-Interim, and ERA-40 Reanalysis Datasets against Independent Sounding Observations over the Tibetan Plateau." Journal of Climate 26 (1): 206-214.

Barker, Dale, Xiang-Yu Huang, Zhiquan Liu, Tom Auligné, Xin Zhang, Steven Rugg, Raji Ajjaji, Al Bourgeois, John Bray, and Yongsheng Chen. 2012. "The Weather Research and Forecasting Model's Community Variational/Ensemble Data Assimilation System: WRFDA." Bulletin of the American Meteorological Society 93 (6): 831-843.

Barker, D. M., W Huang, Y. R Guo, and A.Bourgeois. 2003. A Three-Dimensional Variational (3DVAR) Data Assimilation System for Use with MM5. NCAR Tech. Note NCAR/TN-453STR.

Basu, Sukanta, Albert A. M. Holtslag, Bas J. H. Van De Wiel, Arnold F. Moene, and Gert-Jan Steeneveld. 2008. "An Inconvenient “Truth” About Using Sensible Heat Flux as a Surface Boundary Condition in Models under Stably Stratified Regimes." Acta Geophysica 56 (1): 88-99.

Beare, Robert J, Malcolm K Macvean, Albert AM Holtslag, Joan Cuxart, Igor Esau, Jean-Christophe Golaz, Maria A Jimenez, Marat Khairoutdinov, Branko Kosovic, and David Lewellen. 2006. "An Intercomparison of Large-Eddy Simulations of the Stable Boundary Layer." Boundary-Layer Meteorology 118 (2): 247-272.

Beezley, Jonathan D, Adam K Kochanski, and Jan Mandel. 2011. "Integrating High-Resolution Static Data into WRF for Real Fire Simulations." In 12th WRF Users’ Workshop, National Center for Atmospheric Research.

Boccippio, Dennis J. 1995. "A Diagnostic Analysis of the VVP Single-Doppler Retrieval Technique." Journal of Atmospheric and Oceanic Technology 12 (2): 230-248.

Boquet, M., Parmentier, R., Sauvage, L., Cariou, J., 2010. Theoretical and CFD Analysis of Pulsed Doppler Lidar Wind Profile Measurement Process in Complex Terrain, Proceedings of the EWEA European Wind Energy Conference: Warsaw, Poland.

Borge, Rafael, Vassil Alexandrov, Juan José del Vas, Julio Lumbreras, and Encarnacion Rodríguez. 2008. "A Comprehensive Sensitivity Analysis of the WRF Model for Air Quality Applications over the Iberian Peninsula." Atmospheric Environment 42 (37): 8560-8574.

Boutanios, Z, C Miller, and H Hangan. 2010. Computational Analysis of the Manitoba September 5 1996 Storm: Mesoscale WRF-ARW Simulations Coupled with Microscale Openfoam CFD Simulations The 5th International Symposium on Computational Wind Engineering, Chapel Hill, North Carolina, USA (to be submitted),

Brower, M. C., M. S. Barton, L. Lledó, and J. Dubois. 2013. A Study of Wind Speed Variability Using Global Reanalysis Data. Technical report, AWS True Power.

Brower, Michael C. 2006. "The Use of NCEP/NCAR Reanalysis Data in MCP." In Proceedings of the European wind energy conference & exhibition, Athens, Greece.

Byrkjedal, O., and E. Berge. 2009. "The Use of WRF for Wind Resource Mapping in Norway. 9th WRF User's Workshop." Boulder, CO., NCAR P 9.

Carpenter, Richard L, Brent L Shaw, Michael Margulis, Keith S Barr, Tahllee Baynard, Rod Munson, Pete Wanninger, Devon Yates, Stanton L Thomas, and Justin Sharp. 2013. "Short Term Numerical Forecasts Using Wind Tracer Lidar Data " In Fourth Conference on Weather, Climate, and the New Energy Economy, Austin Texas United States. American Meteorological Society.

Carvalho, David, Alfredo Rocha, Moncho Gómez-Gesteira, and Carlos Santos. 2012. "A Sensitivity Study of the WRF Model in Wind Simulation for an Area of High Wind Energy." Environmental Modelling & Software 33 (0): 23-34. doi: http://dx.doi.org/10.1016/j.envsoft.2012.01.019.

Castro, F. A., C. S. Santos, and C. Costa. 2010. Development of a Meso-Microscale Coupling Procedure for Site Assessment in Complex Terrain EWEC 2010-European Wind Energy Conference & Exhibition: EWEA-European Wind Energy Association.

Cattin, René, Beat Schaffner, and Stefan Kunz. 2006. Validation of CFD Wind Resource Modeling in Highly Complex Terrain 2006 European Wind Energy Conference and Exhibition, Athens, Greece: Citeseer.

Challa, V.S, Jayakumar Indracanti, Monika K.Rabarison, John Young, Chuck Patrick, Julius M.Baham, Robert Hughes, and Anjaneyulu Yerramilli. 2007. "Numerical Experiments on the Sensitivity of WRF-CMAQ Simulations of Air Quality in the Mississippi Gulf Coastal Region to Pbl and Land Surface Models." In Community Modeling & Analysis Systems Conference, Chapel Hill, North Carolina, USA. http://www.cmascenter.org/conference/2007/agenda.cfm.

Chang, Wen-Yeau. 2014. "A Literature Review of Wind Forecasting Methods." Journal of Power and Energy Engineering 2 (04): 161.

Cheng, William YY, and W James Steenburgh. 2005. "Evaluation of Surface Sensible Weather Forecasts by the WRF and the Eta Models over the Western United States." Weather Forecasting 20 (5): 812-821.

Churchfield, Matthew J, Sang Lee, and Patrick J Moriarty. 2013. "Adding Complex Terrain and Stable Atmospheric Condition Capability to the Openfoam-Based Flow Solver of the Simulator for on/Offshore Wind Farm Applications (SOWFA)." In in Proc.1st Symposium on OpenFOAM in Wind Energy, Oldenburg, Germany.

Churchfield, Matthew J., Sang Lee, Patrick J. Moriarty, Luis A. Martinez, Stefano Leonardi, Ganesh Vijayakumar, and James G. Brasseur. 2012. "A Large-Eddy Simulation of Wind-Plant Aerodynamics." AIAA Paper 537.

Costa, Alexandre, Antonio Crespo, Jorge Navarro, Gil Lizcano, Henrik Madsen, and Everaldo Feitosa. 2008. "A Review on the Young History of the Wind Power

Short-Term Prediction." Renewable and Sustainable Energy Reviews 12 (6): 1725-1744.

Courtney, M.; Lindelöw, P ; Wagner, R. 2009. Lidar Profilers for Wind Energy—the Current Status In Proceedings of the European Wind Energy Conference, Marseille, France,

Crescenti, Gennaro H. 1997. "A Look Back on Two Decades of Doppler Sodar Comparison Studies." Bulletin of the American Meteorological Society 78 (4): 651-673. doi: 10.1175/1520-0477(1997)078<0651:albotd>2.0.co;2.

Crook, N. Andrew, A. Didlake, J. Sun, and Y. Zhang. 2005 "Evaluating Various Lidar-Based Wind Analysis Schemes against Independent Observations." In 2nd Symposium on Lidar Atmospheric Applications 85th AMS Annual Meeting, San Diego, CA.

DIMET, FRANÇOIS-XAVIER LE, and Olivier Talagrand. 1986. "Variational Algorithms for Analysis and Assimilation of Meteorological Observations: Theoretical Aspects." Tellus A 38 (2): 97-110.

Dow, Gareth. 2004. "Developments in Observational Requirements for Global Numerical Weather Prediction ". MSc diss, Department of Meteorology University of Reading.

ECMWF. 2009. "ERA-Interim Project." Shinfield Park, Reading, RG2 9AX, United Kingdom: The European Centre For Medium-Range Weather Forecasts (ECMWF)

Emery, Chris, Edward Tai, and Greg Yarwood. 2001. "Enhanced Meteorological Modeling and Performance Evaluation for Two Texas Ozone Episodes." prepared for the Texas Near Non-Attainment Areas through the Alamo Area Council of Governments", by ENVIRON International Corp, Novato, CA., http://www. tnrcc. state. tx. us/air/aqp/airquality_contracts. html# met01.

Finardi, S., M.G. Morselli, and P. Jeannet. 1997. "Wind Flow Models over Complex Terrain for Dispersion Calculations." COST Action 710, Preprocessing of

meteorological data for dispersion modelling.Report of Working Group 4,: 12-25.

Foley, Aoife M, Paul G Leahy, Antonino Marvuglia, and Eamon J McKeogh. 2012. "Current Methods and Advances in Forecasting of Wind Power Generation." Renewable Energy 37 (1): 1-8.

Foussekis, Dimitri, T Georgakopoulos, and I Karga. 2009. "Investigating Wind Flow Properties in Complex Terrain Using 3 Lidars and a Meteorological Mast." EWEC proceedings.

Frehlich, Rod. 2013. "Scanning Doppler Lidar for Input into Short-Term Wind Power Forecasts." Journal of Atmospheric and Oceanic Technology 30 (2): 230-244.

Frehlich, Rod, and Neil Kelley. 2008. "Measurements of Wind and Turbulence Profiles with Scanning Doppler Lidar for Wind Energy Applications." Selected Topics in Applied Earth Observations and Remote Sensing, IEEE Journal of 1 (1): 42-47.

Gabisch, M., Duru, U., 2011. Lake Turkana Wind Power Project. African Development Bank: Kenya, p. 38.

Gaitonde, Ulka, Dominique Laurence, and Alistair Revell. 2006. Quality Criteria for Large Eddy Simulation: University of Manchester.

Gardner, P., A. Garrad, P. Jamieson, H. Snodin, G. Nicholls, and A. Tindal. 2004. "Wind Energy—the Facts—Technology, Vol. 1." European Wind Energy Association Report.

Gilliam, Robert C., and Jonathan E. Pleim. 2009. "Performance Assessment of New Land Surface and Planetary Boundary Layer Physics in the WRF-ARW." Journal of Applied Meteorology and Climatology. 49 (4): 760-774. doi: 10.1175/2009jamc2126.1.

Golding, Edward William. 1956. "The Generation of Electricity by Wind Power." Soil Science 82 (4): 345.

Gregor Giebel, Richard Brownsword, George Kariniotakis, Michael Denhard, and Caroline Draxl. 2011. The State-of-the-Art in Short-Term Prediction of Wind Power "a Literature Overview". ANEMOS. plus.

Han, Zhiwei, Hiromasa Ueda, and Junling An. 2008. "Evaluation and Intercomparison of Meteorological Predictions by Five MM5-PBL Parameterizations in Combination with Three Land-Surface Models." Atmospheric Environment 42 (2): 233-249.

Hanna, Steven R., and Ruixin Yang. 2001. "Evaluations of Mesoscale Models' Simulations of near-Surface Winds, Temperature Gradients, and Mixing Depths." Journal of Applied Meteorology 40 (6): 1095-1104.

Hannon, Stephen, Keith Barr, John Novotny, Jeremy Bass, Andrew Oliver, and Mike Anderson. 2008. Large Scale Wind Resource Mapping Using a State-of-the-Art 3D Scanning Lidar European Wind Energy Conference.

Harris, M., Locker, I., Douglas, N., Girault, R., Abiven, C., Brady, O. 2010. "Validated Adjustment of Remote Sensing Bias in Complex Terrain Using CFD." In European Wind Energy Conference Warsaw Poland, 7.

Hellmann, G. 1919. "Über Die Bewegung Der Luft in Den Untersten Schichten Der Atmosphäre, Dritte Mitteilung." Sitzungsber. Akad. d. Wiss. Berlin: 404-416.

Hirabayashi, Satoshi, Charles N Kroll, and David J Nowak. 2011. "Component-Based Development and Sensitivity Analyses of an Air Pollutant Dry Deposition Model." Environmental Modelling & Software 26 (6): 804-816.

Indeje, Matayo, Fredrick HM Semazzi, Lian Xie, and Laban J Ogallo. 2001. "Mechanistic Model Simulations of the East African Climate Using NCAR Regional Climate Model: Influence of Large-Scale Orography on the Turkana Low-Level Jet." Journal of Climate 14 (12): 2710-2724.

Jacobson, Mark Z. 2005. Fundamentals of Atmospheric Modeling: Cambridge University Press.

Jarraud, M. 2008. "Guide to Meteorological Instruments and Methods of Observation (WMO-No. 8)." World Meteorological Organisation: Geneva, Switzerland.

Jarvis, Andy, Hannes Isaak Reuter, Andrew Nelson, and Edward Guevara. 2008. "Hole-Filled Srtm for the Globe Version 4." available from the CGIAR-CSI SRTM 90 m Database (http://srtm. csi. cgiar. org).

Jaynes, Daniel W., James F. Manwell, Jon G. McGowan, William M. Stein, and Anthony L. Rogers. 2007. "MTC Final Progress Report: Lidar." Renewable Energy Research Laboratory, Department of Mechanical and Industrial Engineering, University of Massachusetts.

Jiménez, Javier. 2004. "Turbulent Flows over Rough Walls." Annual Review of Fluid Mechanics 36 (1): 173-196. doi: 10.1146/annurev.fluid.36.050802.122103.

Jiménez, Pedro A, and Jimy Dudhia. 2012. "Improving the Representation of Resolved and Unresolved Topographic Effects on Surface Wind in the WRF Model." Journal of Applied Meteorology and Climatology. 51 (2): 300-316.

Jiménez, Pedro A, and Jimy Dudhia. 2013. "On the Ability of the WRF Model to Reproduce the Surface Wind Direction over Complex Terrain." Journal of Applied Meteorology and Climatology. 52 (7): 1610-1617.

Jiménez, Pedro A, J Fidel González-Rouco, Elena García-Bustamante, Jorge Navarro, Juan P Montávez, Jordi Vilà-Guerau de Arellano, Jimy Dudhia, and Antonio Muñoz-Roldan. 2010. "Surface Wind Regionalization over Complex Terrain: Evaluation and Analysis of a High-Resolution WRF Simulation." Journal of Applied Meteorology and Climatology. 49 (2): 268-287.

Jung, Jaesung, and Robert P. Broadwater. 2014. "Current Status and Future Advances for Wind Speed and Power Forecasting." Renewable and Sustainable Energy Reviews 31: 762-777.

Justice, C. O., E. Vermote, J. R. G. Townshend, R. DeFries, D. P. Roy, D. K. Hall, V. V. Salomonson et al. 1998. "The Moderate Resolution Imaging Spectroradiometer (MODIS): Land Remote Sensing for Global Change

Research." IEEE Trans.Geosci.Remote.Sens 36 (4): 1228-1249. doi: 10.1109/36.701075.

Kain, John S. 1993. "Convective Parameterization for Mesoscale Models: The Kain-Fritsch Scheme." The representation of cumulus convection in numerical models, Meteorological Monographs 24 (46): 165-170.

Kalnay, Eugenia, Stephen J Lord, and Ronald D McPherson. 1998. "Maturity of Operational Numerical Weather Prediction: Medium Range." Bulletin of the American Meteorological Society 79 (12): 2753-2769.

Kariniotakis, Georges, Pierre Pinson, Nils Siebert, Gregor Giebel, and Rebecca Barthelmie. 2004. "The State of the Art in Short-Term Prediction of Wind Power-from an Offshore Perspective." In Proceedings of SeaTechWeek, Brest, France, 20-21.

Kármán, Th v. 1921. "Über Laminare Und Turbulente Reibung." ZAMM-Journal of Applied Mathematics and Mechanics/Zeitschrift für Angewandte Mathematik und Mechanik 1 (4): 233-252.

Käsler, Yvonne, Stephan Rahm, Rudolf Simmet, and Martin Kühn. 2010. "Wake Measurements of a Multi-MW Wind Turbine with Coherent Long-Range Pulsed Doppler Wind Lidar." Journal of Atmospheric and Oceanic Technology 27 (9): 1529-1532.

Keevallik, Sirje, and Tarmo Soomere. 2010. "Towards Quantifying Variations in Wind Parameters across the Gulf of Finland." Estonian Journal of Earth Sciences. 59 (4): 288.

Kelley, Neil Davis, Bonnie J Jonkman, George N Scott, and Yelena L Pichugina. 2007. Comparing Pulsed Doppler Lidar with Sodar and Direct Measurements for Wind Assessment: National Renewable Energy Laboratory.

Kim, Jea-Chul, Chong Bum Lee, Miloslav Belorid, and Peng Zhao. 2011. "A Study of Sensitivity of WRF Simulation to Microphysics Parameterizations, Slope Option and Analysis Nudging in Haean Basin, South Korea." In TERRECO

Science Conference, Karlsruhe Institute of Technology, Garmisch-Partenkirchen, Germany.

Kindler, Detlef, Andrew Oldroyd, Allan MacAskill, and Danny Finch. 2007. "An Eight Month Test Campaign of the Qinetiq Zephir System: Preliminary Results." Meteorologische Zeitschrift 16 (5): 479-489.

Kinuthia, J. H., and G. C. Asnani. 1982. "A Newly Found Jet in North Kenya (Turkana Channel)." Monthly Weather Review 110 (11): 1722-1728.

Kinuthia, Joseph Hiri. 1992. "Horizontal and Vertical Structure of the Lake Turkana Jet." Journal of Applied Meteorology 31 (11): 1248-1274.

Koscielny, Albert J., R. J. Doviak, and R. Rabin. 1982. "Statistical Considerations in the Estimation of Divergence from Single-Doppler Radar and Application to Prestorm Boundary-Layer Observations." Journal of Applied Meteorology 21 (2): 197-210.

Krishnamurthy, Raghavendra. 2013. "Wind Farm Characterization and Control Using Coherent Doppler Lidar." PhD diss, Arizona State University.

Lackner, Matthew A, Anthony L Rogers, and James F Manwell. 2007. Uncertainty Analysis in Wind Resource Assessment and Wind Energy Production Estimation 45th AIAA Aerospace Sciences Meeting and Exhibit, AIAA-2007-1222,

Lackner, Matthew A. 2008. The Streamlined Site Assessment Methodology: A New Approach for Wind Energy Site Assessment: ProQuest.

Laks, Jason H, Lucy Y Pao, and Alan D Wright. 2009. Control of Wind Turbines: Past, Present, and Future American Control Conference, 2009. ACC'09.: IEEE.

Lalas, D. P., Ratto, C. F. & Walmsley, J. L. 1996. Modelling of Atmostpheric Flow Fields: World Scientific Publishing Co Pte Ltd.

Landberg, Lars. 1999. "Short-Term Prediction of the Power Production from Wind Farms." Journal of Wind Engineering and Industrial Aerodynamics 80 (1): 207-220.

Laprise, R., 1992. The Euler equations of motion with hydrostatic pressure as an independent variable. Monthly Weather Review 120(1) 197-207.

Lee, Sang-Mi, and Harindra J. S. Fernando. 2004. "Evaluation of Meteorological Models MM5 and Hotmac Using Pafex-I Data." Journal of Applied Meteorology 43 (8): 1133-1148.

Lei, Ma, Luan Shiyan, Jiang Chuanwen, Liu Hongling, and Zhang Yan. 2009. "A Review on the Forecasting of Wind Speed and Generated Power." Renewable and Sustainable Energy Reviews 13 (4): 915-920.

Lindelöw-Marsden, Petter. 2009. Uncertainties in Wind Assessment with Lidar Risø-R-1681(En). Denmark.

Lions, Jacques Louis. 1971. Optimal Control of Systems Governed by Partial Differential Equations. Vol. 170: Springer Verlag.

Liu, Yubao, Tom Warner, Yuewei Liu, Claire Vincent, Wanli Wu, Bill Mahoney, Scott Swerdlin, Keith Parks, and Jennifer Boehnert. 2011. "Simultaneous Nested Modeling from the Synoptic Scale to the LES Scale for Wind Energy Applications." Journal of Wind Engineering and Industrial Aerodynamics 99 (4): 308-319.

Lorenc, Andrew C. 1986. "Analysis Methods for Numerical Weather Prediction." Quarterly Journal of the Royal Meteorological Society 112 (474): 1177-1194.

Lorenzo Claveri, Francesco Durante, and Dr. Kai Mönnich. 2010. "Site-Related Wind Potential Analysis and Energy Yield Assessment at the Site Lake Turkana, Kenya." DEWI Wilhelmshaven, Germany 77.

Mandel, Jan, Jonathan D Beezley, and Adam K Kochanski. 2011. "Coupled Atmosphere-Wildland Fire Modeling with WRF 3.3 and Sfire 2011." Geoscientific Model Development 4 (3): 591-610.

Manwell, James F, Jon G McGowan, and Anthony L Rogers. 2010. Wind Energy Explained: Theory, Design and Application: John Wiley & Sons.

Marseille, Gert-Jan. 2014. "Improved Forecasts of Extreme Weather Events by Future Space Borne Doppler Wind Lidar."

Milligan, M, M Schwartz, and Y Wan. 2003. "Statistical Wind Power Forecasting Models: Results for US Wind Farms." National Renewable Energy Laboratory, Golden, CO.

Moeng, Chin-Hoh. 1984. "A Large-Eddy-Simulation Model for the Study of Planetary Boundary-Layer Turbulence." Journal of the Atmospheric Sciences 41 (13): 2052-2062.

Mylne, Ken. 2013. "Anticipated Advances in Numerical Weather Prediction (NWP), and the Growing Technology Gap in Weather Forecasting " In A workshop to assist in sustaining national meteorological services strengthening WMO regional and global centres, Washington DC, U.S.A. World Meteorological Organization.

Nakayama, Hiromasa, Tetsuya Takemi, and Haruyasu Nagai. 2011. "LES Analysis of the Aerodynamic Surface Properties for Turbulent Flows over Building Arrays with Various Geometries." Journal of Applied Meteorology and Climatology 50 (8): 1692-1712. doi: 10.1175/2011jamc2567.1.

Nakayama, Hiromasa, Tetsuya Takemi, and Haruyasu Nagai. 2011/2012. Coupling of WRF and Building-Resolving Urban CFD Models for Analysis of Strong Winds over an Urban Area. Japan.

National Centers for Environmental Prediction, National Weather Service Noaa U. S. Department of Commerce. 2007. NCEP Global Forecast System (GFS) Analyses and Forecasts. Boulder, CO. http://rda.ucar.edu/datasets/ds084.6/.

National Centers for Environmental Prediction/National Weather Service/NOAA/U. S. Department of Commerce. 2000. "NCEP FNL Operational Model Global Tropospheric Analyses." Boulder, CO: Research Data Archive at the National Center for Atmospheric Research, Computational and Information Systems Laboratory.

Nemes, Ciprian-Mircea. 2013. "Statistical Analysis of Wind Speed Profile: A Case Study from Iasi Region, Romania." International Journal of Energy Engineering 3 (6): 261.

Newsom, Rob K., and Robert M. Banta. 2004. "Assimilating Coherent Doppler Lidar Measurements into a Model of the Atmospheric Boundary Layer. Part I: Algorithm Development and Sensitivity to Measurement Error." Journal of Atmospheric and Oceanic Technology 21 (9): 1328-1345. doi: 10.1175/1520-0426(2004)021<1328:acdlmi>2.0.co;2.

Nicholls, M, R Pielke, and R Meroney. 1993. "Large Eddy Simulation of Microburst Winds Flowing around a Building." Journal of Wind Engineering and Industrial Aerodynamics 46: 229-237.

Nicholson, Sharon. "The Turkana Low-Level Jet: Mean Climatology and Association with Regional Aridity." International Journal of Climatology (2015).

Nossent, Jiri, Pieter Elsen, and Willy Bauwens. 2011. "Sobol'sensitivity Analysis of a Complex Environmental Model." Environmental Modelling & Software 26 (12): 1515-1525.

Ooyama, K.V., 1990. A thermodynamic foundation for modeling the moist atmosphere. Journal of the Atmospheric Sciences 47(21) 2580-2593.

Panofsky, Hans. 1976. "Adiabatic Atmospheric Boundary Layers: A Review and Analysis of Data from the Period 1880–1972." Atmospheric Environment (1967) 10 (3): 249-250.

Papadopoulos, Ioannis. 2010. Updated Assessment of the Energy Production of the Proposed Lake Turkana Wind Farm.

Parkes, Jermey , and Andrew Tindal. 2004. "Forecasting Short Term Wind Farm Production in Complex Terrain." In Proceedings of the 2004 European Wind Energy Conference EWEC'04, London,UK.

Parks, Keith, Yih-Huei Wan, Gerry Wiener, and Yubao Liu. 2011. "Wind Energy Forecasting: A Collaboration of the National Center for Atmospheric Research (NCAR) and XCEL Energy." Contract 303: 275-3000.

Pedersen, T. F. 2004. Power Curve Measurements under Influence of Skew Airflow and Turbulence. Risø National Laboratory Report.

Perez, Richard, Elke Lorenz, Sophie Pelland, Mark Beauharnois, Glenn Van Knowe, Karl Hemker Jr, Detlev Heinemann, Jan Remund, Stefan C Müller, and Wolfgang Traunmüller. 2013. "Comparison of Numerical Weather Prediction Solar Irradiance Forecasts in the US, Canada and Europe." Solar Energy 94: 305-326.

Perivolaris, Yiannis G., and Vasilis V. Alafouzos Anna N. Vougiouka, Dimitis G. Mourikis, Vaggelis P. Zagorakis, Kostas G. Rados, Dimitra S. Barkouta, Arthouros Zervos, and Quin Wang. 2006. "Coupling of a Mesoscale Atmospheric Prediction System with a CFD Microclimatic Model for Production Forecasting of Wind Farms in Complex Terrain " In Proceedings of European wind energy conference, Athens, Greece.

Peterson, Ernest W., and Joseph P. Hennessey Jr. 1978. "On the Use of Power Laws for Estimates of Wind Power Potential." Journal of Applied Meteorology 17 (3): 390-394. doi: doi:10.1175/1520-0450(1978)017<0390:OTUOPL>2.0.CO;2.

Philibert, Cédric, and Hannele Holttinen. 2013. Technology Roadmap-Wind Energy. France. www.iea.org.

Pinson, Pierre. 2006. "Estimation of the Uncertainty in Wind Power Forecasting." PhD diss, École Nationale Supérieure des Mines de Paris.

Piwko, R., D. Osborn, R. Gramlich, G. Jordan, D. Hawkins, and K. Porter. 2005. "Wind Energy Delivery Issues [Transmission Planning and Competitive Electricity Market Operation]." Power and Energy Magazine, IEEE 3 (6): 47-56. doi: 10.1109/mpae.2005.1524620.

Potter, C. W., and M. Negnevitsky. 2006. "Very Short-Term Wind Forecasting for Tasmanian Power Generation." Power Systems, IEEE Transactions on 21 (2): 965-972. doi: 10.1109/tpwrs.2006.873421.

Quail, Francis and Butler, Jonathan. 2012. "Comparison of 2nd Generation Lidar Wind Measurement Technique with CFD Numerical Modelling." In EWEA Oldenberg. Glassgow: Strathprints.

Quarton, D. 2004. "Wind Turbines—Part 121: Power Performance Measurements of Grid Connected Wind Turbines." IEC.

Reid, Steve J., and Richard Turner. 2001. "Correlation of Real and Model Wind Speeds in Different Terrains." Weather and Forecasting 16 (5): 620-627.

Retallack, Charles, Ron Calhoun, HJS Fernando, Ken Rayner, Anthony Stuart, John Sutton, and Mark F Hibberd. 2010. "Flow and Pollution Transport During Wagerup 2006: A Case Study." Meteorological Applications 17 (3): 269-278.

Rhie, C. M., and W. L. Chow. 1983. "Numerical Study of the Turbulent Flow Past an Airfoil with Trailing Edge Separation." AIAA Journal 21 (11): 1525-1532.

Richards, P. J., and R. P. Hoxey. 1993. "Appropriate Boundary Conditions for Computational Wind Engineering Models Using the K-ϵ Turbulence Model." Journal of Wind Engineering and Industrial Aerodynamics 46: 145-153.

Rife, Daran L., Christopher A. Davis, Yubao Liu, and Thomas T. Warner. 2004. "Predictability of Low-Level Winds by Mesoscale Meteorological Models." Monthly Weather Review 132 (11): 2553-2569.

Rogers, Raphael E, Aijun Deng, David R Stauffer, Brian J Gaudet, Yiqin Jia, Su-Tzai Soong, and Saffet Tanrikulu. 2013. "Application of the Weather Research and

Forecasting Model for Air Quality Modeling in the San Francisco Bay Area." Journal of Applied Meteorology and Climatology 52 (9): 1953-1973.

Roulston, M. S., D. T. Kaplan, J. Hardenberg, and L. A. Smith. 2003. "Using Medium-Range Weather Forcasts to Improve the Value of Wind Energy Production." Renewable Energy 28 (4): 585-602. doi: http://dx.doi.org/10.1016/S0960-1481(02)00054-X.

Russell, Alan. 2009. "Computational Fluid Dynamics Modeling of Atmospheric Flow Applied to Wind Energy Research." MSc diss, Boise State University Theses and Dissertations.

Satngroom, Paul. 2004. "CFD Modelling of Wind Flow over a Terrain." MEng diss, Department of civil engineering, University of Nottingham, United Kingdom.

Schmidt, J, C Peralta, and B Stoevesandt. 2012. Automated Generation of Structured Meshes for Wind Energy Applications Open Source CFD International Conference, London,

Schumann, Ulrich. 1975. "Subgrid Scale Model for Finite Difference Simulations of Turbulent Flows in Plane Channels and Annuli." Journal of Computational Physics 18 (4): 376-404.

Shin, Hyeyum Hailey, and Song-You Hong. 2011. "Intercomparison of Planetary Boundary-Layer Parametrizations in the WRF Model for a Single Day from Cases-99." Boundary Layer Meteorol. 139 (2): 261-281.

Shiu, Henry, Van Dam, and Junhui Huang. 2010. Wind Energy Forecasting: A Review of State-of-the-Art and Recommendations for Better Forecasts.

Simiu, E, and RH Scanlan. 1996. "Wind Effects on Structures: Fundamentals and Applications to Design."

Skamarock, William C, Joseph B Klemp, Jimy Dudhia, David O Gill, Dale M Barker, Wei Wang, and Jordan G Powers. 2008. A Description of the Advanced Research WRF Version 3.

Skamarock, William C. 2004. "Evaluating Mesoscale NWP Models Using Kinetic Energy Spectra." Monthly Weather Review 132 (12): 3019-3032.

Smith, David A., Michael Harris, Adrian S. Coffey, Torben Mikkelsen, Hans E. Jørgensen, Jakob Mann, and Régis Danielian. 2006. "Wind Lidar Evaluation at the Danish Wind Test Site in Høvsøre." Wind Energy 9 (1-2): 87-93.

Smith, Wesley. 2010. Topograbber Ver. 1.0. NOAA Earth Systems Research Laboratory. 2010 Accessed 08/12/, http://laps.NOAA.gov/topograbber/.

Soares, A., P. Pinto, and R. Pilão. 2010. Mesoscale Modelling for Wind Resource Evaluation Purposes: A Test Case in Complex Terrain

Soares, Carina C, Guilherme O Chagas, and Ricardo André Guedes. 2011. "Estimating Wind Resource Using Mesoscale Modeling." In European Wind Energy Conference (EWEC), Brussels, Belgium.

Soman, S. S., H. Zareipour, O. Malik, and P. Mandal. 2010. A Review of Wind Power and Wind Speed Forecasting Methods with Different Time Horizons North American Power Symposium (NAPS), 2010, doi: 10.1109/naps.2010.5619586.

Srivastava, Prashant K, Tanvir Islam, Manika Gupta, George Petropoulos, and Qiang Dai. 2015. "WRF Dynamical Downscaling and Bias Correction Schemes for NCEP Estimated Hydro-Meteorological Variables." Water Resources Management 29 (7): 2267-2284.

Stefan, Gsänger, and Pitteloud Jean-Daniel. 2013. "Wind Power Worldwide." In Wind Power for the World, 39-67. Pan Stanford Publishing.

Strack, M., Riedel, V., 2004. State of the art in application of flow models for micrositing, German Wind Energy Institute GmbH (DEWI) Wilhelmshaven. The international Technical Wind Energy Conference DEWEK.

Stull, Roland B. 1988. An Introduction to Boundary Layer Meteorology. Vol. 13: Springer Science & Business Media.

Sutton, John, F-L. YU, and Francois Jeanneret. 2010. Lake Turkana Lidar Wind Field Assessment. Perth, Australia.

Talbot, Charles, Elie Bou-Zeid, and Jim Smith. 2012. "Nested Mesoscale Large-Eddy Simulations with WRF: Performance in Real Test Cases." Journal of Hydrometeorology 13 (5): 1421-1441. doi: 10.1175/jhm-d-11-048.1.

Tapia, Xabier Pedruelo. 2009. "Modelling of Wind Flow over Complex Terrain Using Openfoam." MSc diss, Department of Technology and Built Enviroment, University of Gavle, Sweeden.

Theuri, Daniel. 2008. Solar and Wind Energy Resource Assessment in Kenya. Nairobi: Solar and Wind Energy Resource Assessment Project (SWERA).

Touma, Jawad S. 1977. "Dependence of the Wind Profile Power Law on Stability for Various Locations." Journal of the Air Pollution Control Association 27 (9): 863-866.

Treinish, L. A., Cipriani, J., Praino, A. P., Diaz, J., & Dorronsoro, J. R. 2013. "Precision Wind Power Forecasting Via Coupling of Turbulent-Scale Atmospheric Modelling with Machine Learning Methods." In Fourth Conference on Weather, Climate, and the New Energy Economy, Austin, TX. https://ams.confex.com/ams/93Annual/webprogram/Paper222876.html.

Uppala, Sakari M, PW Kållberg, AJ Simmons, U Andrae, V Bechtold, M Fiorino, JK Gibson, J Haseler, A Hernandez, and GA Kelly. 2005. "The ERA-40 Re-Analysis." Quarterly Journal of the Royal Meteorological Society. 131 (612): 2961-3012.

Waldteufel, P, and H Corbin. 1979. "On the Analysis of Single-Doppler Radar Data." Journal of Applied Meteorology 18 (4): 532-542.

Walterscheid, Richard L. 2009. "High-Altitude Wind Prediction and Measurement Technology Assessment." Report prepared for US Department of Transportation, Federal Aviation Administration, DOT-VNTSC-FAA-09-13 30.

Wang, Wei, Cindy Bruyere, Michael Duda, Jimy Dudhia, Dave Gill, HC Lin, J Michalakes, S Rizvi, X Zhang, and JD Beezley. 2010. "ARW Version 3 Modeling System User's Guide. Mesoscale & Miscroscale Meteorology Division." National Center for Atmospheric Research (July 2010), http://www. mmm. ucar. edu/wrf/users/docs/user_guide_V3/ARWUsersGuideV3. pdf.

Wang, Xiaochen, Peng Guo, and Xiaobin Huang. 2011. "A Review of Wind Power Forecasting Models." Energy Procedia 12: 770-778. doi: 10.1016/j.egypro.2011.10.103.

Wesley, Ebisuzaki , Zhang Li, Yang S. K., and Kumar Arun. 2012. "Assessing the Daily and Radiative Performence of the CFSR, ERA-Interim and MERRA " In 37th NOAA Annual Climate Diagnostics and Prediction Workshop, Fort Collins, CO, 22-25 October. NOAA's National Weather Service

Wilde, Martin. 2012. The Use of Real-Time Off-Site Observations as a Methodology for Increasing Forecast Skill in Prediction of Large Wind Power Ramps One or More Hours Ahead of their Impact on a Wind Plant.

Wu, Yuan-Kang, and Jing-Shan Hong. 2007. A Literature Review of Wind Forecasting Technology in the World Power Tech, 2007 IEEE Lausanne: IEEE.

World Wind Energy Association (WWEA). 2014 WWEA Half-Year Report 2014. Bonn, Germany.

Yamada, Tetsuji. 2004. "Merging CFD and Atmospheric Modeling Capabilities to Simulate Airflows and Dispersion in Urban Areas." Computational Fluid Dynamics Journal 13 (2): 47.

Yamada, Tetsuji, and Katsuyuki Koike. 2011. "Downscaling Mesoscale Meteorological Models for Computational Wind Engineering Applications." Journal of Wind Engineering and Industrial Aerodynamics 99 (4): 199-216. doi: http://dx.doi.org/10.1016/j.jweia.2011.01.024.

Yamadaa, Tetsuji, and Katsuyuki Koikeb. 2010. "The A2C Mesoscale Meteorological Modeling System for Computational Wind Engineering Applications." In The Fifth International Symposium on Computational Wind Engineering (CWE2010), Chapel Hill, North Carolina, USA. ftp://ftp.atdd.NOAA.gov/pub/cwe2010/Files/Papers/147_yamada.pdf.

Zehnder, Alan T, and Zellman Warhaft. 2011. "University Collaboration on Wind Energy." Cornell University

Zhang, Yao, Jianxue Wang, and Xifan Wang. 2014. "Review on Probabilistic Forecasting of Wind Power Generation." Renewable and Sustainable Energy Reviews 32: 255-270.

Every reasonable effort has been made to acknowledge the owners of copyright material. I would be pleased to hear from any copyright owner who has been omitted or incorrectly acknowledged.